The Application of Continuum Mechanics to the Stochastic Modeling of Fracture in Fiber-Fiber Composites

by

Julie Chen

B.S. Massachusetts Institute of Technology
(1986)

M.S.M.E. Massachusetts Institute of Technology
(1988)

Submitted to the Department of
Mechanical Engineering
in Partial Fulfillment of the Requirements
for the Degree of

DOCTOR OF PHILOSOPHY IN MECHANICAL ENGINEERING

at the
Massachusetts Institute of Technology
September 1991

Signature of Author _____
Department of Mechanical Engineering
September, 1991

Certified by _____
Professor Stanley Backer, Department of Mechanical Engineering
Thesis Supervisor

Accepted by _____
Professor Ain A. Sonin, Chairman
Department Graduate Committee, Department of Mechanical Engineering

The Application of Continuum Mechanics to the Stochastic Modeling of Fracture in Fiber-Fiber Composites

by

Julie Chen

Submitted to the Department of Mechanical Engineering on August 27, 1991
in partial fulfillment of the requirements for the Degree of
Doctor of Philosophy in Mechanical Engineering

ABSTRACT

The fracture behavior of paper can be a key component in successful production or converting operations and in desirable end-use performance. Frequent failures in the paper web can translate to $10,000 per hour of lost production, and with the heightened interest in using recycled fibers, the frequency of breaks is likely to increase. A proposed solution to improving the fracture resistance of paper has been the addition of ductile reinforcing fibers, thus creating a fiber-fiber composite.

In order to optimize this technology, a better understanding of the fracture process in these materials is needed. Because of the fairly dense matting of moderate to heavy basis weight papers, it has been hypothesized that the fracture behavior of this "quasi-continuous" material can be modeled as a local, statistically represented response of the material to underlying continuum strain fields. Pullout of the reinforcing fibers is considered in an additive manner.

The focus of this study is the development of this new method of analysis for these materials and the evaluation of its potential for success. Experimental evidence supporting this hypothesis has been obtained through direct observation of the fracture process and direct measurement of the crack-tip strain fields using a scanning electron microscope tensile stage setup.

Implementation of the quasi-continuous model was based on a theoretical analysis for plane stress steady state crack propagation in an elastic-plastic material. This model predicts the relative effects of parameters such as reinforcing fiber pullout and the statistical distribution of small area sheet properties (e.g., critical strains) on fracture behavior. Results have been encouraging, indicating the possibility of using this new method to realistically predict fracture, a complex process dependent on weak spots and stress concentrations rather than means.

Thesis Supervisor: Dr. Stanley Backer, Professor of Mechanical Engineering

Acknowledgements

The initiation and completion of this endeavor would not have been possible without the continued support of many people. While it is impossible to recognize individually all of those who have helped me at various points along this trek, I would like to acknowledge at least a few of those people here.

First of all, I would like to thank my thesis advisor, Professor Stanley Backer, for his support and guidance, and for the perspective he has given me on doing research and on life, in general. I would also like to thank the other members of my committee – Professor Rohan Abeyaratne and Professor Timothy Gutowski – for their many valuable suggestions and interest.

Financial support for this project was generously provided by Westvaco Corporation — along with ideas, materials, and time contributed specifically by Robert Beran, Ed Seames, and Wayne Ogden. In addition, the project has benefitted from an unrestricted grant and donated materials from the DuPont Company.

I have also greatly enjoyed the environment created by my colleagues, both those in the not too distant past — Moon Hwo Seo, Hwai-Chung Wu, Youjiang Wang, and Shipeng Li — and those who remain to inhabit 3-335 — Mary Lynn Realff, Bill Scelzo, Lata Misra, and Omar Hasan. Thanks also to Travis Hein and Soo Lee who contributed their efforts to this project through the UROP program.

And, of course, the two people who help to keep everyone away from the administrative pitfalls and just generally on our toes....Dorothy Eastman and Debbie Blanchard.

To my family — my mom and dad (Yuki and Inan), and my brother (Mike) and Magda — thanks for always being there.

Finally, a note to the people who have helped me to keep a balance in my life. Carol Cantwell (C^2, you made it 3 for 3!)...my roommates, Ellen Sullivan and Lisa Gabel, who put up with the last few crazy months and more...Sharon Spittle and all the Women in Black (the perpetual student is done!). And, a special thanks to Jennifer Lewis, with whom this doctoral venture was essentially a shared experience (except that she beat me out by a year!), no regrets.

Contents

List of Figures

List of Tables

Chapter 1

Introduction

Often taken for granted because of its omnipresence in today's world, paper has been a key component in the development of our society. A lightweight means of communication over distance and time, paper has propelled the spread of knowledge and ideas without the obvious limitations of cave walls and stone tablets. Communication and packaging – the transfer of ideas and goods – have been vital to our society's evolution and revolutions (Figure 1.1 [53]).

With the advent of the computer age, many people were ready to sound the death knell for paper. Visions of the "paperless" office with computer files and data communications replacing manila file folders and letters filled the imaginations of the public. Yet, as we approach the next century, the annual consumption of paper has increased to almost *100 million tons* !! [47] Instead of making paper obsolete, the FAX machine, the copier, and the desktop publisher have created easy access to and easy production of printed information. Computers have also transformed the face of papermaking with the introduction of highly sophisticated, high speed, automated systems. The result has been an increase in the demands on paper as a material – both during production (e.g., higher processing speeds and stresses) and during end-

Figure 1.1: Paper as a Medium for Communication and Packaging

use (e.g., lightweight for economic transport; strong and durable for use in faster and higher capacity machines; aesthetic features for quality printing and image scanning).

The mechanical demands on paper and paperboard are many. In the production side, wet-end processing at speeds exceeding 1000 ft/min can put incredible stresses on the web as it is being formed. Operations such as coating, calendering, winding, printing, and converting require similar processing speeds. Because the large capital investments required can translate to a cost of $10,000 per hour of lost production [39], economic considerations make the continuous operation of these machines extremely desirable. Thus, it is often of greater benefit to produce extra yards of lower-quality paper that can be recycled back into the process if necessary, rather than having to stop a 900ft long x 30ft wide machine in order to cut and hand-feed a broken edge back into the system. Similarly, failures in converting machines and end-use machines can cause stoppages and jamming which can damage expensive machinery.

Is the goal then to create a stronger paper? Not necessarily. Certainly, a degree of strength is needed, i.e., some lower limit or threshold. Nevertheless, it has been shown in runnability studies that failures are often caused by sporadic peak loads which exceed the paper strength despite this strength being well above the expected average loads [39]. However, designing for paper strengths which far exceed any possible peak load is economically not practical. The solution then is to either (1) attempt to eliminate these peak loads, or (2) prevent the total disruption of the operation should a peak load occur. The work discussed in this thesis will focus on the latter.

Upon exposure to a peak load, it is expected that some damage will occur. Especially because the raw material is a natural material (i.e., wood fibers), it is virtually impossible to avoid the presence of flaws in the sheet. A peak load combined with the concentration of stresses at a flaw may thus result in the formation of a crack or tear. Preventing total disruption of the operation then requires that this damage

be prevented from progressing to the point where the sheet becomes separated into two halves. Since some damage has already occurred, aesthetic qualities of the sheet are no longer a primary consideration. This section of the sheet will be discarded or recycled. What is key is that the integrity of the sheet remains to permit continuous operation of the machine.

So the question remains – what method can be used to slow down or halt the progress of the crack? One possible scheme is the addition of longer fibers to the sheet during production. This method has actually been used to some extent for decades by many plant managers. In order to temporarily eliminate a succession of web breaks, a higher percentage of longer pine fibers (3mm vs. 1mm) is added until the cause of the web breaks can be determined. This is a temporary solution, however, as other properties of the sheet can be negatively affected.

The development of the synthetic fiber and its multitude of possible compositions, lengths, and strengths has suggested its use in the papermaking process. The result is what could be considered a fiber-fiber composite — cellulose fiber matrix and synthetic fiber reinforcement. Again, since the goals here are retardation of crack growth, increased elongation to failure, and increased fracture energies, we are looking at more ductile reinforcing fibers rather than the typical high stiffness carbon or kevlar fibers considered for most composites applications.

The precedent here has been demonstrated in another composite – fiber-reinforced concrete. Designed to take primarily compressive loads, concrete is highly susceptible to low tensile stresses. The fibers in fiber-reinforced concrete add insignificant strength to its designed load-bearing capacity. However, should the concrete be exposed to an unexpected tensile load, the fibers act to retard cracking and hold the concrete together until it can be replaced [50]. In a similar manner, ductile fibers inserted into paper can hold the web/sheet together until it either makes it through the machine, or an operator has time to halt the operation to prevent machine damage.

The question is how to implement this potential solution. There are hundreds of synthetic fibers currently being produced and hundreds more that have yet to be developed. Certainly, a trial and error method is likely to be time-consuming, costly, and limited in its success. In addition, with the current state of the environment, questions of recyclability must also be addressed. These may be related to the "environmental friendliness" of the composite sheets or to the use of this technology to reinforce sheets made from waste fibers. Clearly, more knowledge is needed as to the driving mechanisms of crack propagation in paper sheets and similar materials, along with a more detailed definition of the key factors needed from reinforcing fibers to retard crack growth.

In developing a fracture model, we make assumptions about the dominant factors. A successful model thus not only serves to predict the behavior of other suitable materials, but also lends support to the importance of the factors accounted for in the model. It is with this in mind that we propose and evaluate the following hypothesis.

The continued development of man-made fibrous materials such as composites, papers, and nonwovens has led to the rapid growth of this class of materials that falls somewhere in between the traditional continuous materials (e.g., metals, bulk polymers) and discrete materials (e.g., woven textiles) (Figures 1.2a,b and Figure 1.3). The hypothesis presented here is that in materials where the bonding is sufficiently homogeneous and the density of fibers is great enough, the fracture behavior can be approached as if the material is a continuum. That is, the crack-tip strain fields can be described using continuum fracture mechanics analyses. There is one key qualifier – the "discrete" nature of the material (e.g., fiber orientation, variation in fiber strength and bond strength) must be accounted for by statistically describing the local material response to these underlying continuum strain fields (Figure 1.4). This will be described later in more detail in section 2.5 and chapter 6.

In this study, the approach will be applied to the fracture of moderate basis weight

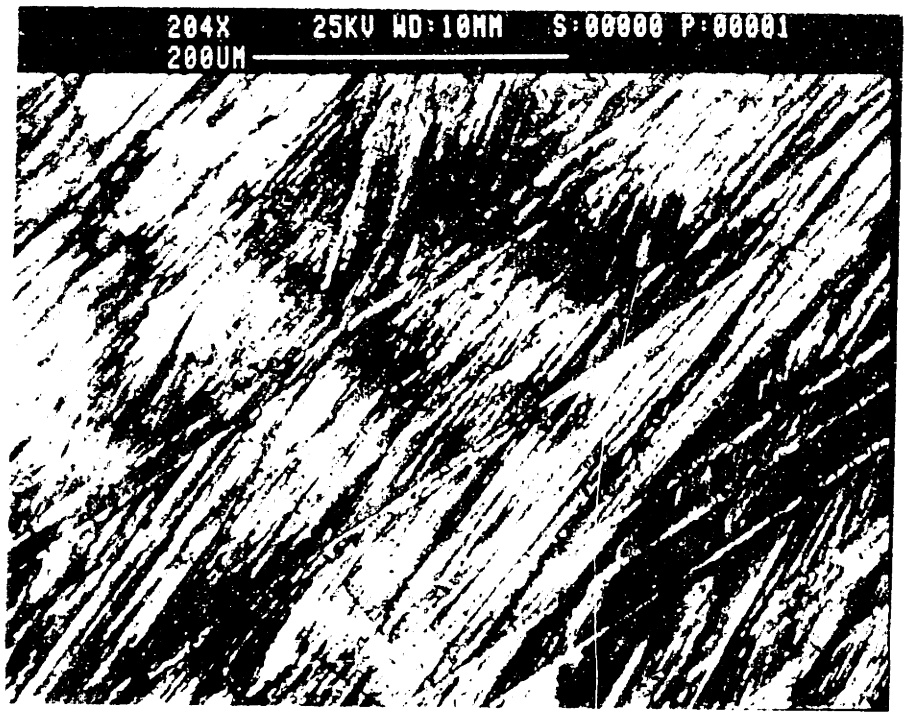

"Continuous"
Aluminum
Foil (200x)

"Discrete"
Woven
Fabric (50x)

Figure 1.2: Continuum – Discrete Spectrum of Materials

Figure 1.3: "Quasi-Continuous Cellulose Fiber Paper"

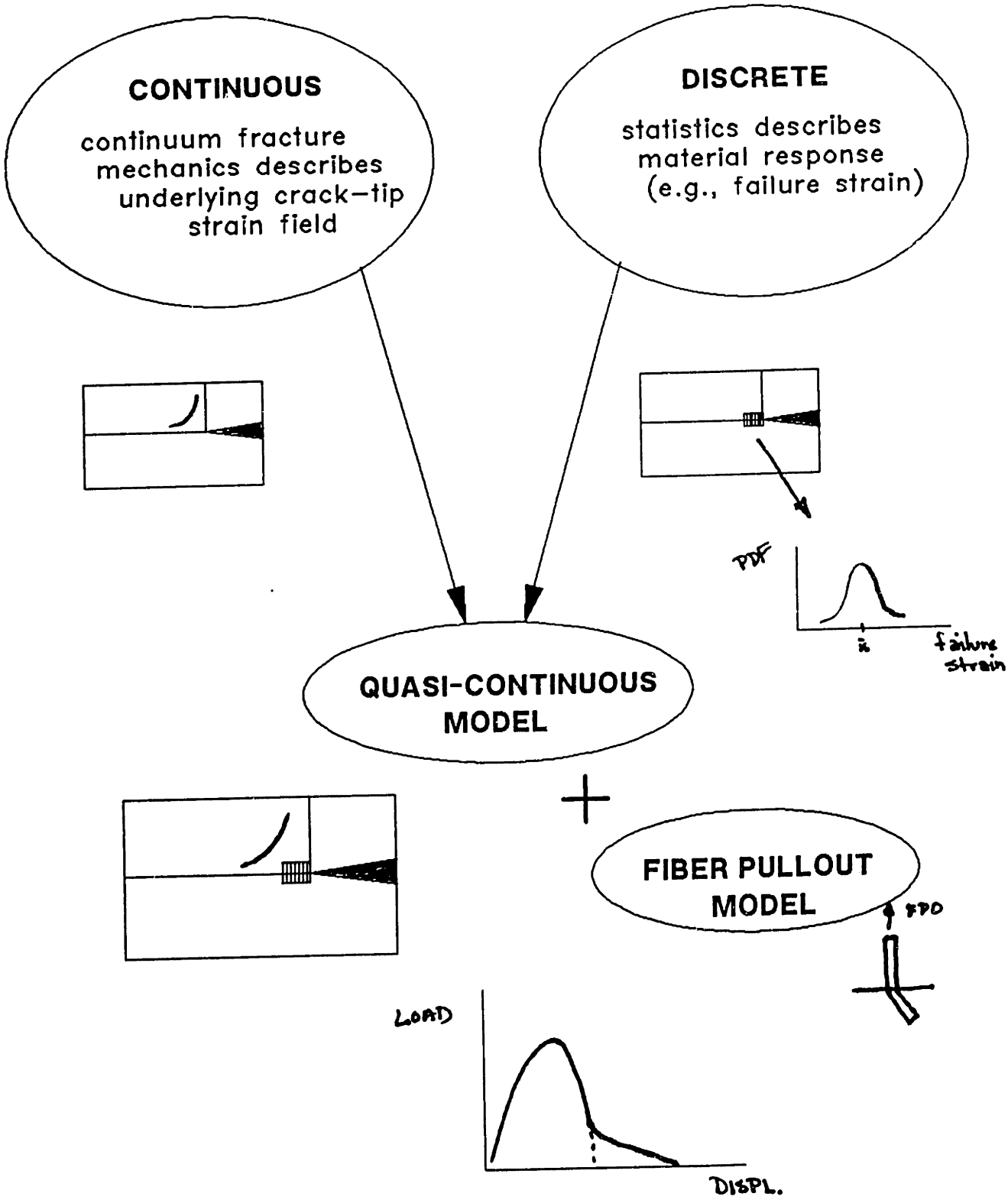

Figure 1.4: Quasi-Continuous Model

papers (e.g., $100g/m^2$). It is expected that application of the approach to denser materials (e.g., carton linerboard) will be successful; whereas the same is not true of less dense materials (e.g., tissue paper) where the bonding and the fiber interactions are not sufficient to simulate a continuum.

The scope of this work is not meant to be comprehensive. Rather, the objectives of this thesis are the proposal of this new method of analysis for these materials and the examination of its potential for success.

In keeping with these goals, chapter 2 will provide some background as to the unique characteristics of paper as a material and the current state of knowledge in paper fracture. Chapters 3,4, and 5 will each address a particular segment of the experimental study. Starting with a description of the general fracture behavior of paper in Chapter 3, some insights into the effects of factors such as fiber reinforcement, bonding, and compaction will be discussed. A quantitative characterization of the material behavior of the main paper types — in particular, Standard, Binder, Clupak, and PET — is given in Chapter 4. The quantitative results are linked to some qualitative observations about differences in fracture surface. Following this in the next chapter is a qualitative observation of the differing damage zone characteristics. Chapter 5 also describes the most novel experimental work — both procedure and results of *in-situ* measurements of the strain fields at the crack tip during a fracture test. The main theoretical and modeling work will be presented in chapter 6, including derivations of the fiber pullout loads and of the strain field for elastic-plastic steady state crack propagation. The model predictions for variability in fracture will also be discussed. Finally, the primary conclusions and recommendations for future work will be stated in chapter 7.

Chapter 2

Background

2.1 Paper History

There were many predecessors to paper as a medium for communication – e.g., palm leaves, papyrus, wood, clay, stone, metal, and animal skins. The distinction between these materials and paper is that paper consists of individual fibers that have been separated prior to being reformed into a sheet. The significance of this was the potential for development into a lightweight, inexpensive material which could be produced easily in large quantities and various dimensions. Making paper did not require the careful processing of single palm leaves or skins, nor did paper have the impractical weight of metal or stone.

Ts'ai Lun, a Chinese scholar and official in the court of Emperor Hu-Ti at Lei-Yang [54], is generally credited with the development of paper in 105 A.D.. Lun produced sheets of paper by mixing bark from the mulberry tree with rags and scraps of flax and hemp. Over a thousand years later, around 1150 A.D., the first mill in Europe was established in Xativa, Spain [54].

As with most technologies, gradual progression interspersed with periods of rapid growth has led to the current status of papermaking. One such growth period for papermaking occurred during the Renaissance period of the 14th through the 17th centuries. Key among the developments of this time was Johann Gutenberg's invention of the movable type [54]. With this invention, the demand for paper as a mass commodity rather than an expensive specialty product was established.

In the United States, the first paper mill was established near Philadelphia in 1690 by Wilhelm Rittinghuysen [54]. Fueled by the writings of revolutionists such as Franklin, Paine, and Adams, the demand for paper in the U.S. grew during the late 1700's.

Automation arrived in 1798 when Nicolas-Louis Robert, at the behest of St. Léger Didot, invented and patented the first paper machine. This machine introduced the concept of the endless screen, permitting the production of sheets of unlimited length. Soon after, in 1806, Henry Fourdrinier patented the first version of what is now referred to as the Fourdrinier type paper machine. Designed by Bryan Donkin, the slightly revised version of Robert's machine consisted of a flat screen onto which the fiber-water mixture would flow, with the water draining out and the subsequent sheet being pressed between felt rollers. A cylinder type paper machine was patented in 1809 by John Dickinson, but in large paper mills today, the flat Fourdrinier type machines are far more common. [54].

Advances in the paper industry over the past 200 years have been in the broad areas of chemical treatment and automation, resulting in an increase in uniformity, quality, and speed of production. A schematic of a typical modern papermaking process is shown in Figure 2.1 [52].

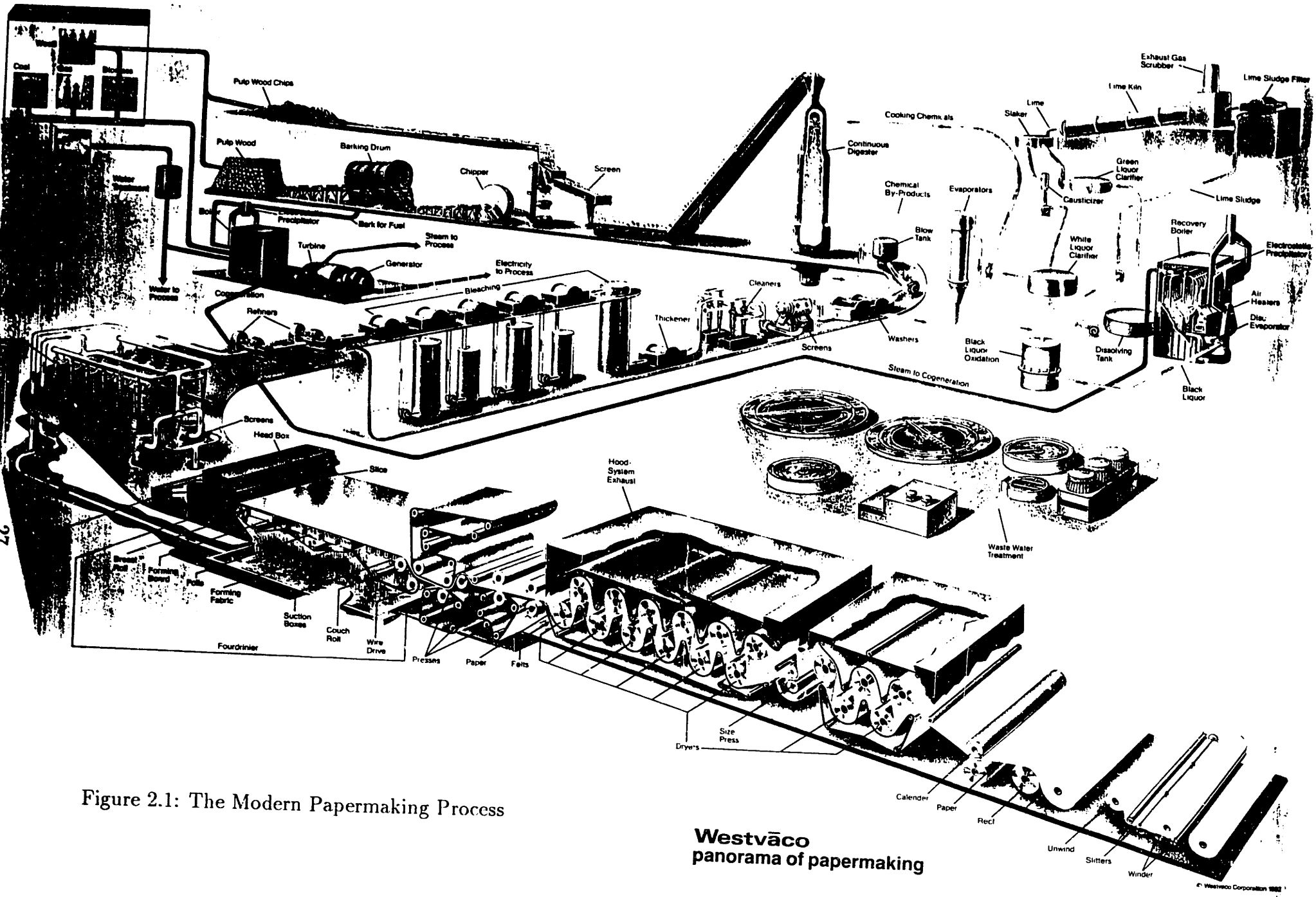

Figure 2.1: The Modern Papermaking Process

2.2 Cellulose Fibers and the Papermaking Process

Naturally, since its recorded inception almost 2000 years ago, people have been trying to improve both the properties of paper and the papermaking process. In the simplest terms, a sheet of paper is made by mixing some type of fiber with water, and then creating a consolidated sheet by allowing the water to drain or evaporate and by applying pressure.

Various types of vegetable matter have been used as the fiber source; the vast list has included reeds, leaves, straw, vines, kelp, hemp, cotton, and even wasp nests [12]. While a variety of materials are still being used in small handmade operations, often for artistic purposes, the primary source of fibers for today's consumer applications is wood pulp.

Wood cells are commonly referred to as a natural composite. Since the cells are hollow to allow transport of fluids and nutrients, the cell walls must be stiff enough to prevent collapse of the structure. These cell walls are composed primarily of a "crystalline, filamentous material (the microfibril)", an "extensively branched, three-dimensional, amorphous polymer (lignin)", and a "complex of relatively linear, partially branched, partially paracrystalline polymers (hemicelluloses)" [22]. The key structural component is the microfibril which acts as the fiber reinforcement in the lignin-hemicellulose matrix.

The chemical structure of the microfibrils is cellulose I (Figure 2.2). During drying of a paper sheet, surface tension will bring these fibrils closer together, furthering the formation of the hydrogen bond network which is basically responsible for keeping the sheet together. This dependence on the hydrogen bond has significant ramifications with regard to paper behavior when exposed to varying humidities and liquids. Liq-

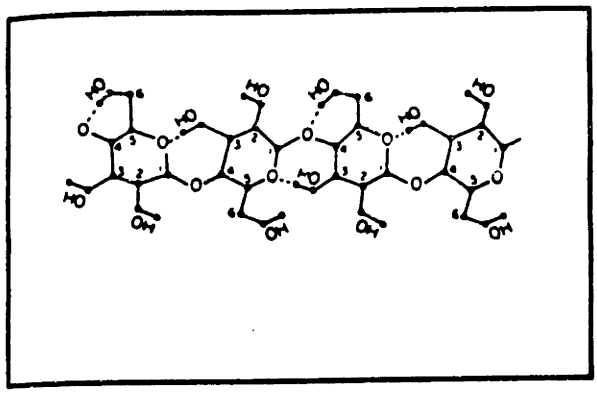

Figure 2.2: Chemical Structure of Cellulose

uids of high polarity such as water and high humidities can cause severe weakening of paper.

Taking a look at the next level, the wood fiber is composed of both a secondary and a primary cell wall. The secondary cell wall contains several layers — usually three layers referred to as S1, S2, and S3 (Figure 2.3 [22]). Each of these layers is made up of the fibrils helically wound and embedded in the lignin-hemicellulose matrix. It is interesting to note that the direction of the helix tends to alternate for adjacent layers.

In the process of papermaking, these fibers are separated from each other and formed into a sheet by a complex combination of mechanical and chemical means. A very simplified version of the commercial process is described here; most of the information is cited from Westvaco literature [52].

Initially, the wood is chipped into small pieces about the size of a quarter. There are several methods of separating the chips into fiber form – all involve some combination of chemical and mechanical breakdown of the material. Chemical processes

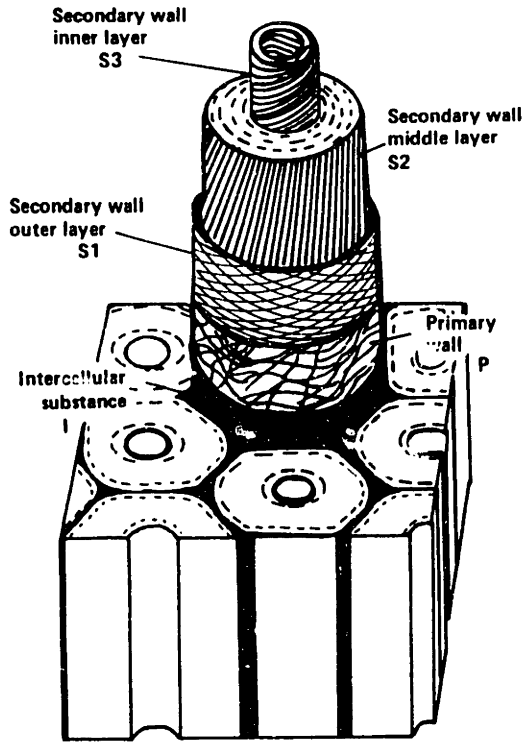

Figure 2.3: Typical Wood Fiber Structure

result in stronger fibers with lower yields (40-50%); mechanical processes result in weaker fibers but much higher yields (60-80%). The cellulose fibers then go through "several stages of washing, screening, cleaning, and, if necessary, bleaching [52]" in order to separate out the various undesirable chemicals and contaminants, the main culprit being lignin. While the presence of some lignin is useful, too much lignin will weaken the bonding in the sheet.

Beating or refining collapses and fibrillates the fibers to form a ribbonlike structure with more bonding surfaces — i.e., more exposed microfibrils. The fiber are then "combined with pigments, dyes, sizing, and resins" to form a mixture "more than 99% water and less than 1% fiber and other solids". The mixture or furnish flows onto a rapidly moving Fourdrinier screen, forming a mat as the water drains through the screen. Rollers and steam-heated cylinders further down the line help to remove more moisture from the paper web by pressing and evaporation. Pressing and the effects of surface tension during drying act to densify the sheet.

Note that the flow direction and the rollers tend to orient the fibers, giving rise to

a somewhat orthotropic structure commonly referred to in terms of a machine direction in the flow direction and a cross-machine direction. In contrast, the laboratory handsheet maker produces a single randomly oriented sheet by allowing the water to drain vertically through several screens (see Figure 3.15).

In many commercial applications, a coating may be applied to the sheet for improved printability. Finally, the continuous sheet is wound onto a large roll as wide as 30ft. This roll can be rewound onto smaller rolls that can be put through further operations such as additional coating, calendering, and converting.

2.3 Paper Modeling

Cox [11] is generally recognized as the first to attempt to model the elastic behavior of paper. This model treated paper as a plane of long, straight, thin fibers. Assuming that these fibers experience only small axial strains and that the strains were equivalent to the global strain in the fiber direction, Cox derived the nontrivial elastic constants $(E_x, E_y, \nu_{xy}, \nu_{yx}, G_{xy})$ for a planar matrix as a function of the fiber orientation distribution. Since Cox's pioneering work, several others have proposed variations and alternatives.

Kallmes and Corte [19] also applied probability theory to paper structure. However, instead of simply representing the fiber orientation, Kallmes and Corte considered both the fibers and the pores. The fundamental assumptions in their analysis of paper were that "its mechanical properties depend primarily on the number of fiber-fiber contacts; its porous properties on the number and size of the interfiber spaces; and its optical properties on its density and roughness". Thus, by deriving the distribution of various geometric properties such as the number of fiber crossings per fiber, the free fiber length, and the polygon (pore) area, a relationship can be established between the independent fiber and sheet properties (e.g., fiber length, fiber

width, sheet area, number of fibers) and the sheet structural properties (e.g., elastic modulus, breaking load).

In a related paper on nonwovens. Petterson [33] showed that the **elastic theory of orthotropic materials** satisfactorily predicted the effect of test angle (i.e., sheet orientation) on the material constants E_y and ν_{xy}. The treatment of paper as an orthotropic material has been suggested by many researchers – no doubt the influence of the machine direction/cross direction character of most machine-made sheets. Baum [4] chose to describe paper as a "three-dimensional homogeneous orthotropic plate" using wave theory. This was the basis for the application of ultrasonic techniques to determine the orthotropic elastic constants of paper.

Unfortunately, as Petterson states[33], the orthotropic theory assumes that "the stress-strain relationship is given for the two principal directions of the material...and the limitations of small elastic strains." Tackling these limitations, Petterson developed a **fiber web theory** which assumed only the stress-strain properties of the fiber and a fiber orientation distribution, similar to Cox's approach. Petterson derives the relationship between fabric strain and fiber strain and between fiber stress and fabric stress. The key addition made to the prediction of material failure is the idea of a rupture stress determined by the "weakest unit cell". The rupture strength for a given cell is defined in terms of the rupture elongation of the fibers, the area density of fibers, and the fiber orientation distribution. The rupture stress of the fabric is related to the probability that "minimum values of all three occur in the same unit cell." [34]

Perkins and Mark[31] further advanced Cox's theory to develop a **network model** which incorporated not only a fiber orientation distribution function, but also a fiber length distribution function and the effects of drying restraints and coupling efficiency. This model was supported by experiments performed by Rigdahl, et al.[38] who demonstrated that the ratio of E_x/E_y could be determined accurately by the

model for various orientation distributions.

Schulgasser[40,41] simplified the results from Perkins' network model by showing that of the four constants - $E_x, E_y, \nu_{xy}, G_{xy}$ - the latter two (Poisson's ratio and shear modulus) could be predicted from the two elastic moduli, values which are experimentally much more easily determined.

In a later paper, however, Schulgasser questioned the assumption of allowing only axial deformation in the fiber. He felt that in poorly bonded papers, it was reasonable to neglect transverse properties - i.e., the network theory was adequate. However, for well-bonded, dense papers, Schulgasser supported the use of a **laminate theory** which included transverse effects[42]. This laminate theory treats paper as a *continuous* composite of cell wall material with the soft hemicellulose/lignin acting as the matrix and the aligned cellulose microfibrils acting as the reinforcing fiber [28]. Page and Schulgasser showed further evidence for the laminate theory by demonstrating its ability to predict the effect of moisture content and strain rate on the in-plane elastic modulus anisotropy ratios and Poisson's ratios. These phenomena are not addressed by the network model.

In a somewhat different approach, Nissan [24,25] went down to the level of the critical bond in paper, the **hydrogen bond**. Based on the assumption that the mechanical properties of paper depend on the density and the characteristics of the H-bond, Nissan calculated the elastic modulus from the number of H-bonds per unit volume and the average force constant of stretching for a H-bond in cellulose. A statistical representation of the orientation of the H-bonds in cellulose was also included. While the importance of the H-bond in paper is without question, the practicality of modeling mechanical properties in paper directly from the H-bond level is suspect.

In an excellent series of experiments, Page and Seth[29] elucidated the effects of several factors on the elastic modulus of paper. By independently changing bonding

pressures, beating times, fiber lengths, and other processing conditions, Page and Seth were able to qualitatively analyze the effect of fiber modulus, fiber length, degree of bonding, and the presence of dislocations, microcompressions, curl, crimps, and kinks. From this work, they developed an expression for the elastic modulus of randomly oriented sheets as a function of fiber moduli, fiber dimensions, and relative bonded area of the sheet.

The most recent advancement in the modeling of the uniaxial elastic behavior of paper has been done by Ramasubramanian and Perkins [37]. Basically an extension of Perkins' network theory, Ramasubramanian contributes two major enhancements – (1) nonlinear elastic and deformation theory plastic behavior of the fibers and the bonds; and (2) different fiber behavior in tension and compression – in simulating the stress-strain behavior of paper.

All of these models have dealt with numerous aspects of paper behavior and with the effect of fiber and bond properties on this behavior, but ultimately the majority of models have only related this behavior to the prediction of elastic constants. With the exception of the work done by Petterson[34] who discussed the idea of a rupture stress governed by the weakest unit cell and the work done by Kallmes and Corte[19] who dealt with statistical distributions of pores and fiber contacts and its effect on breaking load, very little has been said about modeling the fracture of paper. The few papers gleaned from a literature search on paper fracture will be discussed in the next section.

2.4 Paper Fracture

Despite the obvious importance of predicting the failure of paper, models of paper fracture are almost nonexistent. Within the last decade, Britton [5] and Hansen [14] have both developed computer simulation models of the stress-strain curve to

failure of low density nonwovens. These simulation models rely on establishing a computer generated sheet and applying alternating strain and relaxation methods to this sheet while checking for local failures. Both of these models are geared to low density nonwovens. While these models may provide important information on general trends - e.g., effect of Poisson's ratio, elastic modulus, etc... - they tend to be limited because they often require extensive computer time and cannot easily be used to model denser materials where the number of fibers would be prohibitive. This makes reproduction or extension of the results difficult for other researchers.

On the experimental side, several parametric studies have been done on fracture of paper in an attempt to come up with some reliable measurement to characterize paper fracture behavior. In particular, Seth and Page [45,46] examined sample dimension effects and the effect of basis weight on fracture resistance. They defined fracture resistance as "the work required to propagate a crack through unit distance."

Heckers [15] did an extensive series of experiments on using the stress intensity factor to predict web breaks. As with the Seth and Page study, Heckers looked at the effects of sample dimensions as well as basis weight, thickness, fiber length, pH value, and stock composition. Of particular interest is Heckers' moderately successful attempt to correlate the stress intensity factor with other traditional strength measurements (e.g., breaking length, tearing resistance) and with actual records of the frequency of web breaks in a printing press.

Pouyet, et al. [35] did a survey of existing methods of measuring fracture toughness. These included J-integral methods (compliance, R.P.M.= Rice, Paris, and Merkle), quasi-static crack propagation (Seth and Page), and methods using specimens without pre-cracks (variations by Corte, Cavlin, and Goldschmidt). While the results from the compliance and Goldschmidt's methods were the most accurate, both require many tests; because of this drawback, Pouyet concluded that the R.P.M method was the most reasonable balance between accuracy and convenience.

It should be noted that both Pouyet and Heckers chose sample dimensions and strain rates that were significantly longer and faster, respectively, than those used by Seth and Page. This may be because they were looking primarily for the fracture toughness or stress intensity factor (i.e., the maximum load values) and did not require a quasi-static propagation condition.

While these studies have experimentally addressed the issue of using fracture toughness and fracture resistance values to quantify fracture behavior, there has been little or no attempt to model the fracture process.

2.5 Fracture Model

Part of the difficulty in modeling the fracture behavior of paper or other fiber matrix composites arises from the somewhat discrete nature of the material, which does not lend itself *directly* to the currently accepted fracture mechanics analyses. Yet, as suggested above, the use of fiber network simulations seems unwieldy and a nonportable use of computer time. This is especially apparent when one examines a scanning electron microscopy (SEM) photo of a typical sheet of paper (Figure 2.4); the number of fibers is enormous and the bonding is virtually continuous throughout.

Cox and others have done an excellent job of predicting the elastic constants in uniaxial tensile straining. Although not addressed directly, except perhaps somewhat by Petterson, these models could be extended to predict the stress-strain curve to failure, assuming a catastrophic type tensile failure when the adjusted sheet stress exceeded the failure stress of a critical number of component fibers. But in reality, failure of a sheet does not occur at an "average" point experiencing an "average" stress.

Failures initiate at a flaw, a cut, or other stress concentration. And, since we are

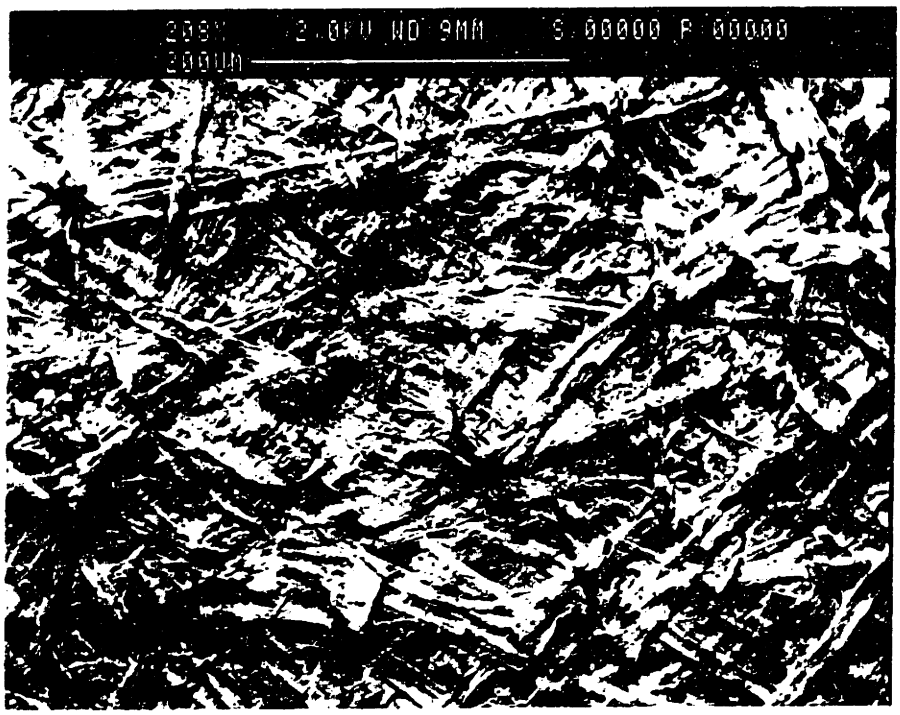

Figure 2.4: SEM photo of Standard Paper Sheet

dealing with natural materials, i.e. wood pulp fibers, it is reasonable to expect the existence of such flaws. In fact, flaws in the sheet can be caused by dirt or other contaminants. Shives, or fiber bundles which do not get separated properly, are also major sources of stress concentrations. Even nonuniform fiber distribution can cause weak spots which may result in premature failures.

Thus, in the failure of paper, cracks may develop at many of these flaws until one crack begins to dominate and propagates through the sheet, effectively freezing the growth of the other cracks. From fracture mechanics, we can surmise that the strain fields in the sheet are no longer uniform or homogeneous near these cracks. Unfortunately, one of the key assumptions of the network models is that the strain field in the sheet is uniform!! This would suggest another tack for modeling the fracture of paper.

The continuous nature of paper, especially of denser paper, has been suggested by other researchers. In fact, the laminate model is not far from this, using the idea of paper being a fibril-reinforced hemicellulose/lignin matrix. It should also be stated that our concept of continuous materials versus discrete materials is based on a given magnification level. At a distance of say 1 meter, one would be hard pressed to distinguish between a sheet of paper and a sheet of opaque polymer film. In a slightly different viewpoint, metals and bulk polymers, traditionally referred to as continuous, are obviously discrete at the molecular level. So, the key is the degree of discontinuity at the level of the controlling mechanism.

The hypothesis proposed here is that in moderate to heavy basis weight paper, the bonding is sufficiently homogeneous and the density of the fibers is great enough to treat the paper as a continuum material. That is, the crack-tip strain fields can be described using continuum fracture mechanics analyses. And, it is this underlying strain field which drives the propagation of the crack. The major difference between these "quasi-continuous" materials and continuous materials is that the response of

the material to these strain fields may not be uniform. That is, due to variations in local fiber orientation, fiber strength, or bond strength, a given section of paper may fail at lower strains while another section may better resist propagation of the crack. This is how the "discrete" nature of the material manifests itself. The expected variations must be accounted for by statistically describing the local material response to the underlying continuum fields. The experimental evidence supporting this hypothesis and the results from a computer implementation of this model will be examined in this thesis.

Chapter 3

Experimental Fracture Behavior of Paper

What are the controlling mechanisms in the fracture of paper? In order to identify how different fiber and bonding properties affect paper fracture, fracture tests were run on a variety of samples. The samples were handsheets, and therefore randomly oriented sheets, produced by Westvaco for this study. The test procedure, types of samples, and results will be discussed in this section.

3.1 Sample Preparation

The papers produced by Westvaco for these tests were prepared in three batches under the following basic conditions:

- All sheets were manufactured with bleached hardwood and 10% pine pulp.
- Hardwood pulp was additionally refined in a laboratory Valley beater to increase fiber/fiber bonding; pine was not.

- The target basis weight was 60lbs/3000ft^2 A.D. (air-dry) or approximately 100g/m^2.
- 30cm x 30cm rectangular sheets were formed, cut in half, and drum dried at 250°F on a felted, steam heated dryer drum. Binder treated and compacted sheets were subsequently drum dried.
- Treated sheets underwent a surface application of one of the two acrylic binders used in this study. The binder was diluted to 15% solids and applied to both sides of the sheets with a paint roller. Excess binder was removed with a blotter and a handsheet roller.
- Compacted sheets underwent the Clupak process in one direction only, adding extra stretch in that direction.
- Fiber reinforced sheets had synthetic fiber added to the cellulose pulp furnish prior to sheet formation.

Actual values for synthetic fiber volume fraction (%vol), binder uptake, compaction, and degree of beating are given in tables accompanying the respective discussion sections. Processing difficulties caused by the addition of synthetic fibers were significant in some cases, but not in others; the details will be discussed in the fiber reinforcement section.

All fracture test samples were stored at roughly 23°C and 50%RH for at least 20 hours before testing.

3.2 Procedure

A series of preliminary tests were run to determine the appropriate specimen dimensions and testing conditions for the fracture test. The main results will be mentioned,

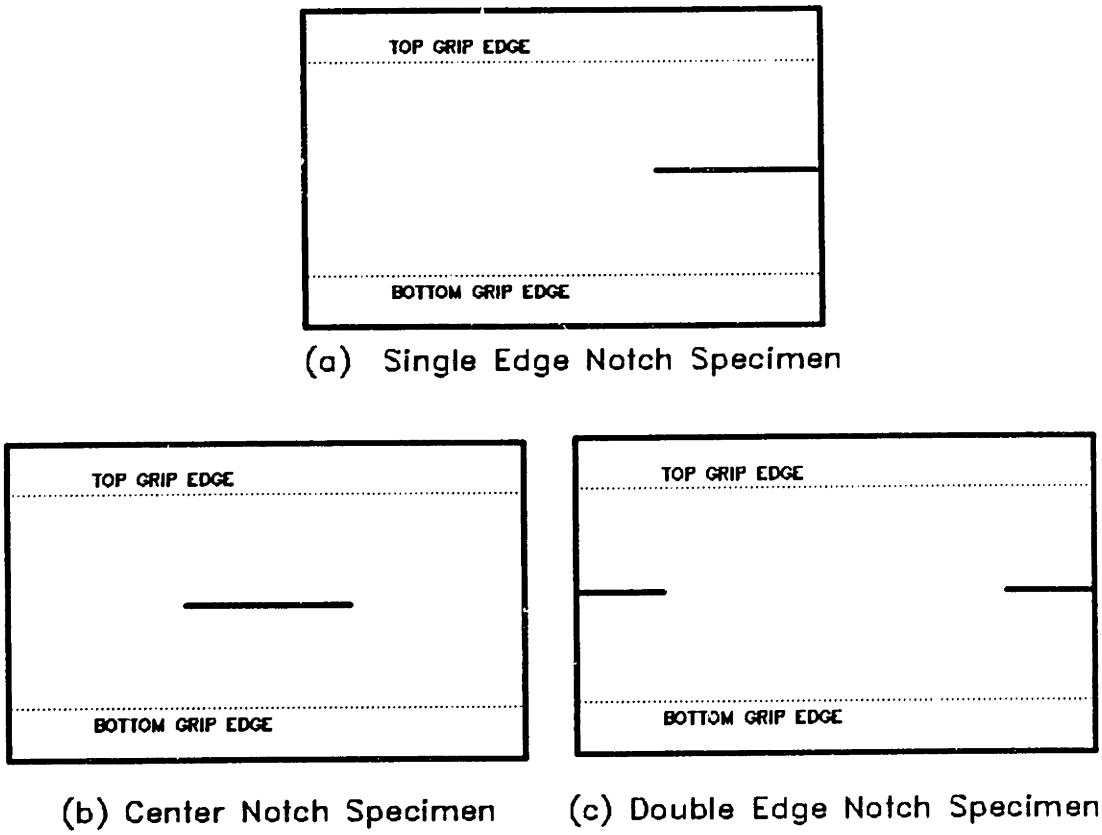

Figure 3.1: Notch Configurations

but details can be found in Appendix A.

The fracture test is an in-plane tensile test with a single-edge notch precut into the specimen with a razor blade. The double-edge notch generally led to the development of two cracks which do not meet, while the center cut tended to initiate on both sides, eventually cracking through one side only. Thus the single-edge notch gave us the most controlled test. The three test configurations are shown in Figure 3.1.

The chosen specimen dimensions were 5cm long x 12cm wide with a 4cm edge crack. In terms of specimen width, the widest sample which still gives satisfactory test results is desired; this expands the length of the crack propagation region, allowing for more accurate analysis. Precut length as a ratio of the width was chosen to be 1/3. This ratio has been shown experimentally to give the highest fracture toughness values. Length was minimized in order to induce quasistatic propagation. At longer

lengths, the stored energy builds up too rapidly, usually resulting in a catastrophic type failure.

Experimental results reported in the literature by Seth[45] indicated that for bleached softwood kraft handsheets and writing paper of approximate basis weight 60g/m^2 and for 45g/m^2 newsprint paper, fracture resistance values leveled off at widths greater than 10cm. Seth eventually chose specimen dimensions of 5cm x 15cm with a 5cm precut. We found that a slightly narrower specimen gave us more consistent fracture results.

Specimens were cut, avoiding any obvious flaws in the sheet (e.g., uneven binder application, fiber clumps, etc...), and the edge crack was cut with a razor, perpendicular to the length direction. All of the specimens also had an additional 1-1.25cm on the top and bottom edges for gripping. The selected fracture sample dimensions are shown in Figure 3.2.

In order to grip the paper, a special set of pneumatic grips with alignment rods was built for us by B&B Engineering (Stoughton, MA), similar to the grips developed by Paprican[45]. Figure 3.3 shows the fracture test setup. Air pressure of 50-70psi was supplied through a series of ball valves and foot valves to control opening and closing of the clamps. In addition to the pneumatic system, damage to the samples prior to the start of the test is reduced by use of clamp faces covered with a thin piece of rubber. The grips also have alignment rods to prevent rotation of the clamps during the test. This keeps the orientation of the sample, and concomitantly the stress fields, reasonably consistent in the Mode-I configuration throughout the test.

Data acquisition was via a Nicolet digital oscilloscope – Series 4094 with a dual disk drive – in conjunction with a Measurements Group 2100 system strain gage conditioner/amplifier. Amplification was set at 10mv=1lb. Sampling rate was $\approx$ 4000pts at 50ms/pt for the fracture tests. Load-jaw displacement (V-sec) curves were

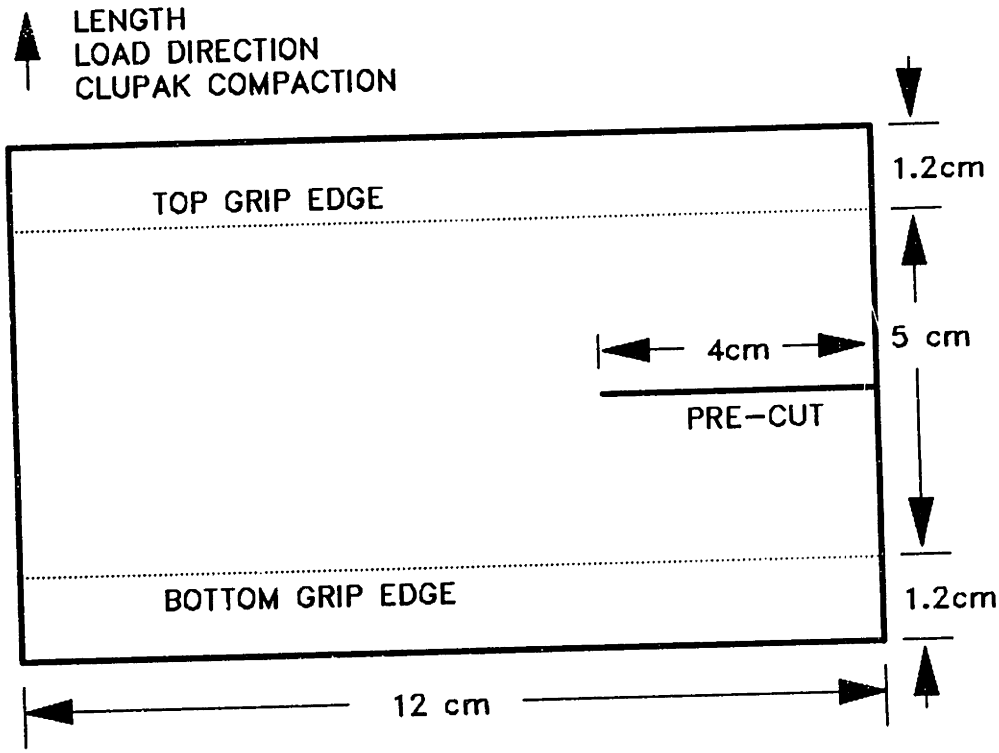

Figure 3.2: Fracture Specimen Dimensions

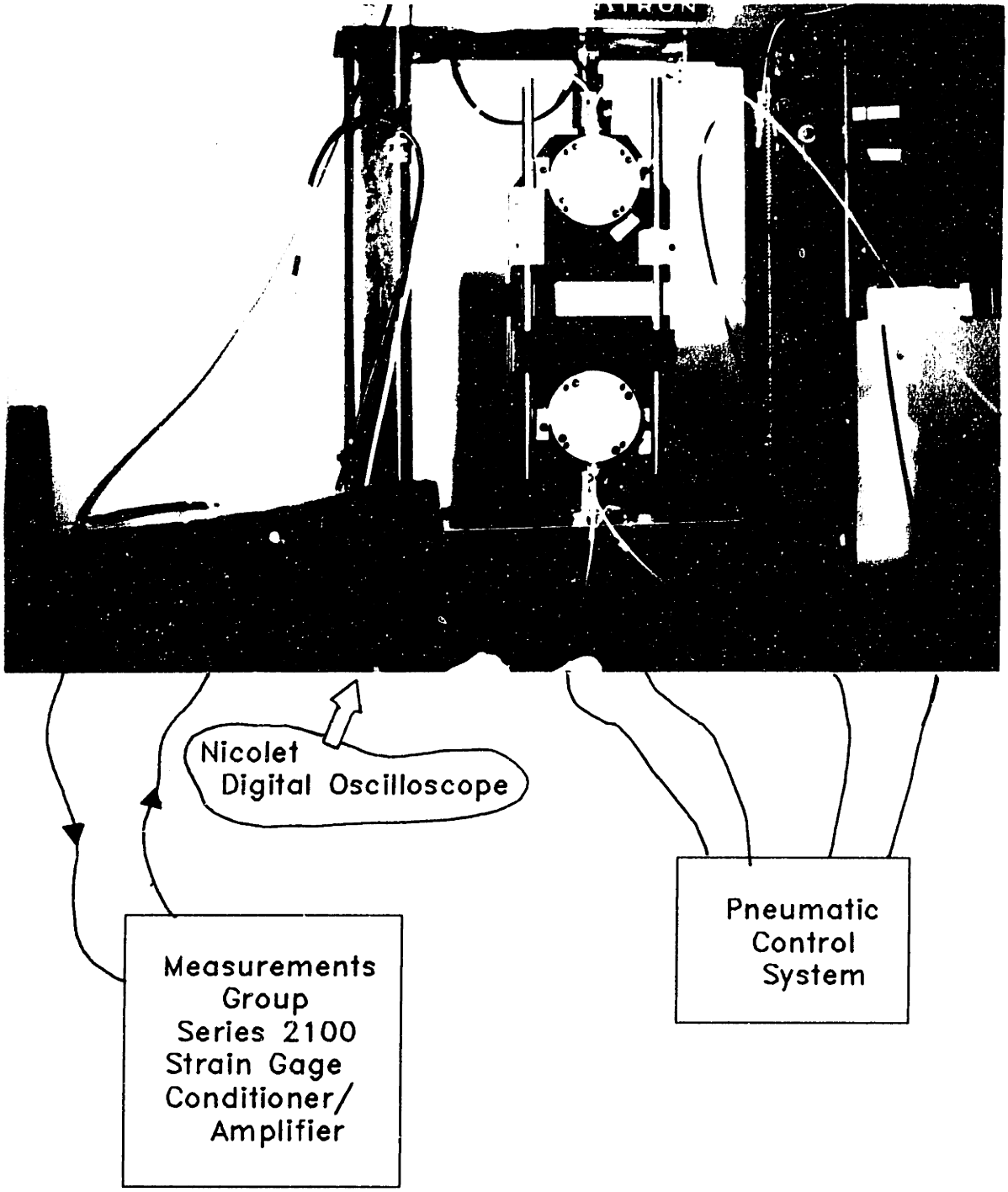

Figure 3.3: Fracture Test Setup

stored on high density $5\frac{1}{4}$in disks.

The fracture test is run at a very slow constant rate of displacement – 0.05in/min (0.00212 cm/sec) – to achieve quasistatic crack propagation conditions. During the main portion of the test, this is the case – i.e., if the crosshead is stopped, the crack will stop propagating. However, the failure of the last 1/8 or so ($\approx$ 1cm) of the cellulose matrix tends to occur very rapidly, resulting in a sharp load drop. The entire test takes roughly 150sec.

Analysis of the data was accomplished using Nicolet software with the oscilloscope, and Vu-Point and Lotus 1-2-3 software on an IBM compatible. Tested samples were saved and placed in plastic sheet protectors for further observation.

During a typical test, the fracture curve will consist of three regions, as shown in Figure 3.4. In the first region where there is no crack propagation, the load-displacement behavior is essentially linear-elastic. In the second region, the crack initiates from the precut (Figure 3.5a), and the load-displacement curve starts to soften, deviating from the linear behavior, until it reaches a peak value; the load then begins to drop as the crack continues to propagate across the specimen, leaving less material to carry the load. The peak value seems to occur when the increase in load carried by the existing material with each strain increment no longer offsets the loss of load-carrying material due to crack propagation.

In the third and final region, after the crack has propagated completely through the specimen (Figure 3.5b), there is a fiber bridging region for the reinforced samples. For the samples without fiber reinforcement, the curve simply drops to zero after the specimen has failed (dashed line, Figure 3.4).

The differences in fracture behavior for the various paper types will be discussed in the following sections. All experimental curves shown are typical curves selected out of a set of 5-10 tests for each sample type.

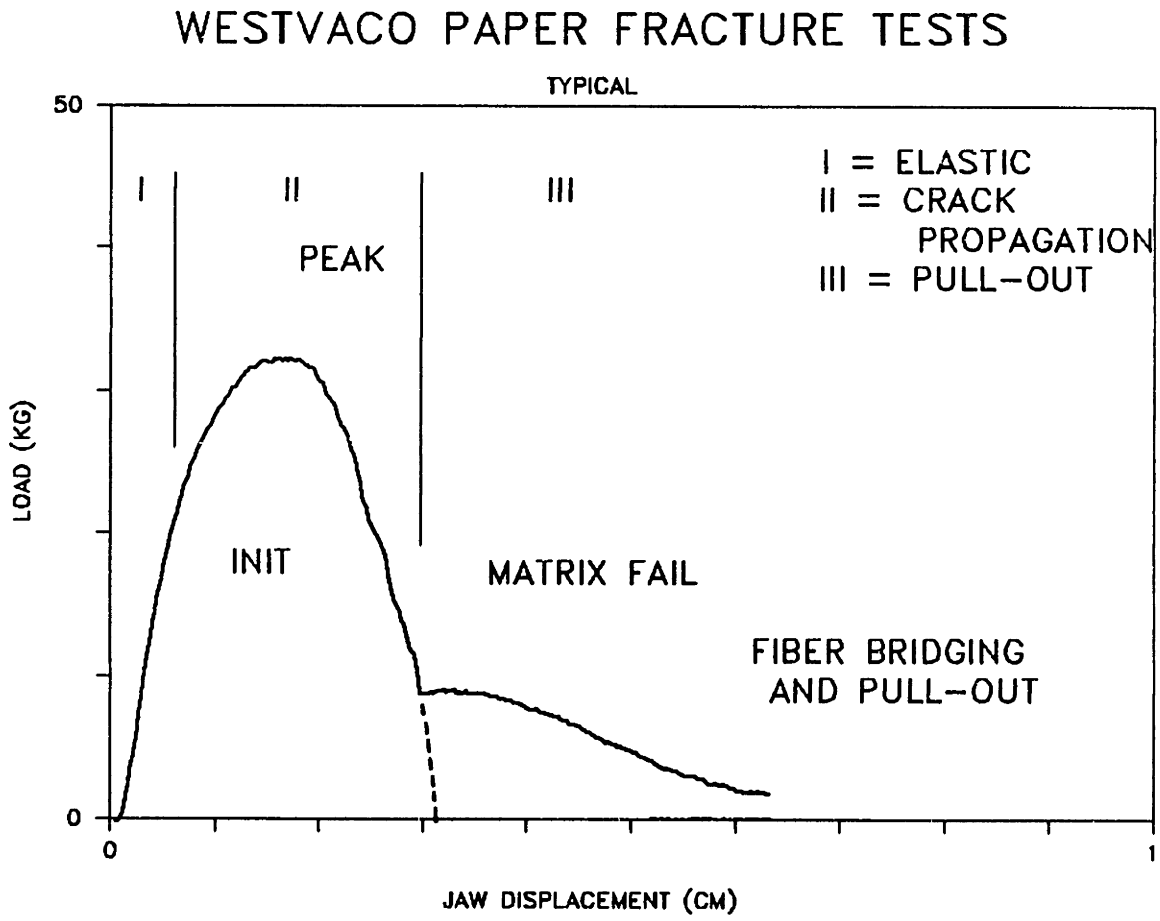

Figure 3.4: Typical Fracture Curve

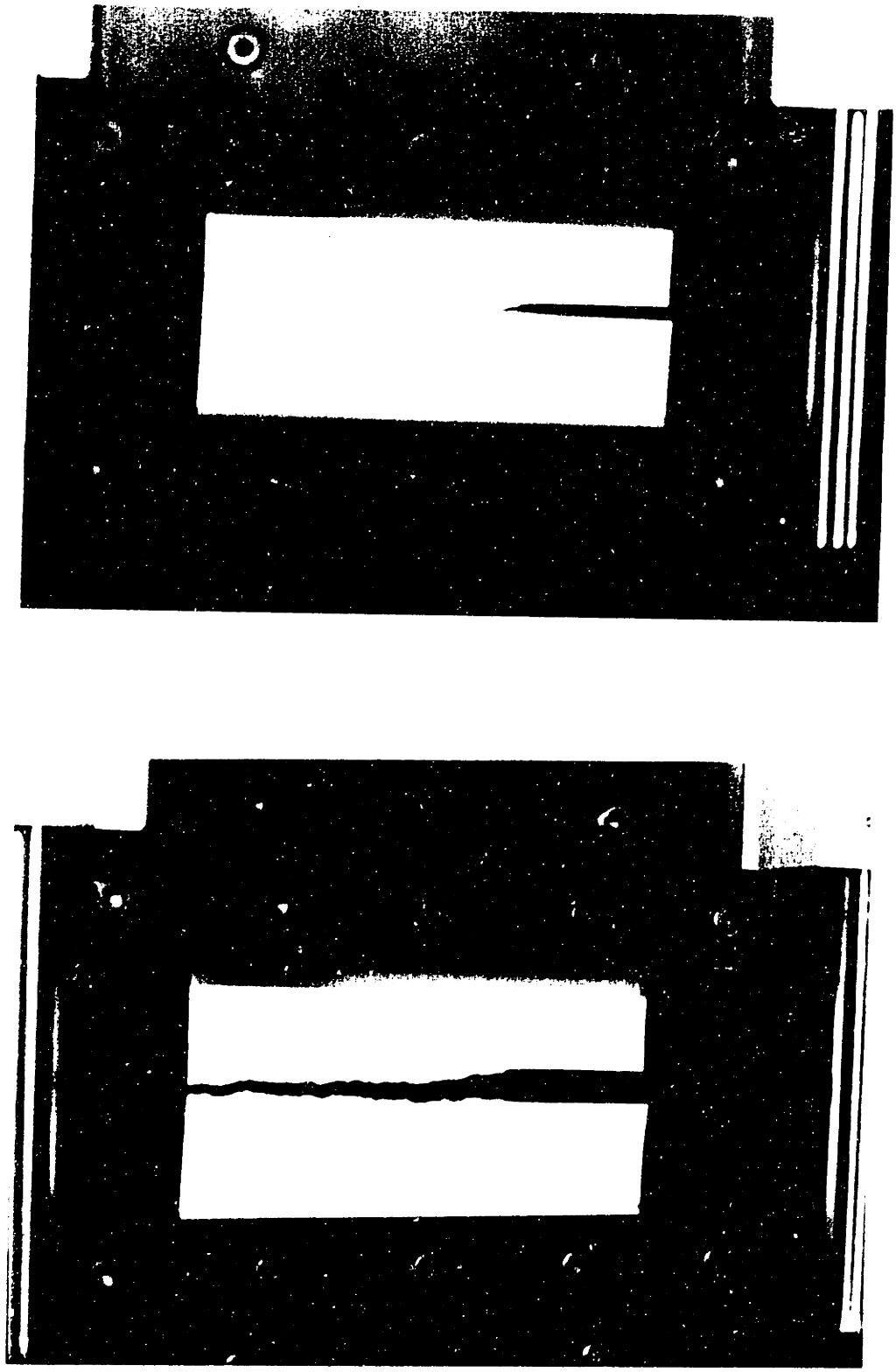

Figure 3.5: Typical Fracture Test Specimen

3.3 Effect of Fiber Reinforcement

One major point of interest in this study was the effect that synthetic fiber reinforcement would have on the fracture behavior of paper. As mentioned earlier, some success had been achieved with fiber-reinforced concrete using synthetic fibers such as polypropylene, nylon, and polyester[50]. In this case, we were concerned with improving the fracture toughness of the paper rather than the tensile strength or stiffness. Therefore, rather than using an expensive, high stiffness fiber such as carbon, graphite, or kevlar, a more ductile polyester(PET) fiber was chosen (Figure 3.6).

It is very difficult to measure the stress-strain curve of wood fibers, given their extremely short length (1-3mm). For this reason, we sought to determine a reasonable stress-strain curve from the literature. Unfortunately, the only curves found in the literature were obtained by Page[27] and by Jayne[18], all for softwood fibers. A stress-strain curve for the sprucewood fiber, from Page's paper, is presented in Figure 3.6, to give a rough idea of the cellulose fiber stress-strain curve. It is expected that the hardwood fibers in our samples would have a somewhat stiffer behavior; however, the pine fiber behavior should be similar to the curve shown. Polyester, of course, has a much higher elongation to break value than wood pulp fiber. Nevertheless, it should be noted that the initial elastic moduli and the failure loads are not that different.

3.3.1 Papermaker Staple

The reinforcement fibers, known as Papermaker Staple (D257), were supplied with a special hydrophilic finish applied to enhance dispersion with the cellulose fibers. The Dacron fibers were provided courtesy of Dr. J. S. Ahn and J. Weikel of DuPont (Kinston, NC). These fibers are 1.5 denier and were provided in cut lengths of 1/4in, 1/2in, and 3/4in (roughly 6mm, 12mm, 18mm).

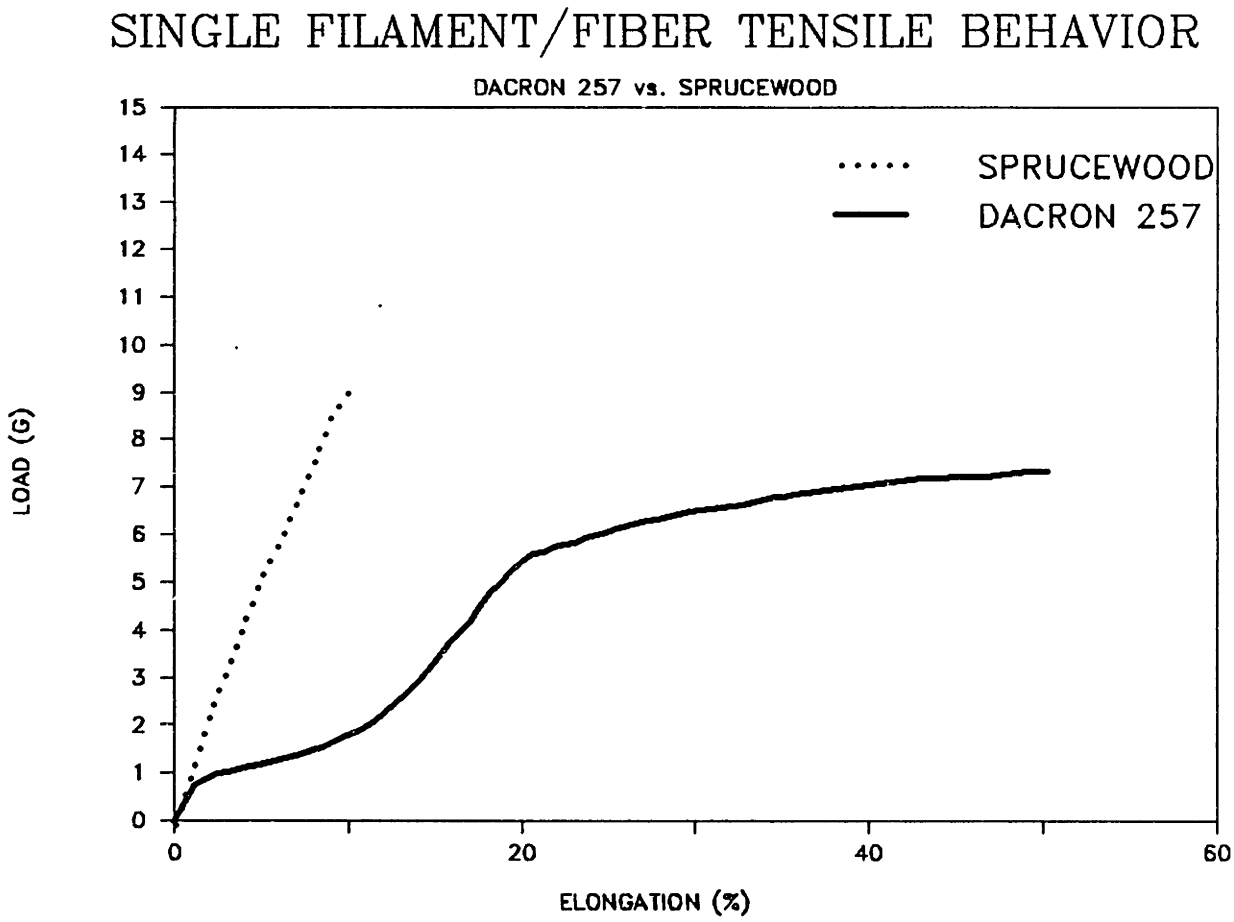

Figure 3.6: PET and Cellulose Fiber Stress-Strain Curves

Table 3.1: PET Volume Fractions in Test Samples

SERIES	PET TYPE	%PET	PET LEN (mm)	COMMENTS
I	—	0	—	
I	D257	5	18	
I	D257	5	6	
II	—	0	—	
II	—	0	—	less beating
II	D257	5	18	less beating
II	D257	10	18	
II	D257	10	12	
II	D269	10	18	
II	D269	10	12	
III	—	0	—	
III	D257	2.5	18	
III	D257	5	18	
III	D257	7.5	18	

Because of economic and practical reasons, we were looking at adding small volume fractions (e.g., 5%vol) of the synthetic fibers. The point was to reinforce cellulose paper not produce a blend or a polyester paper. Table 3.1 shows the volume fractions and lengths of PET fibers that were utilized. Note that D257 refers to the Papermaker Staple, and D269 refers to the bicomponent fiber which will be discussed later.

Despite the length of the PET fibers compared to the pulp fibers (e.g., 18mm vs. 1-3mm), dispersion of the Papermaker Staple was not a problem because of the hydrophilic finish. Only at the highest %vol tested (10%vol) was dispersion of the PET fibers a problem (Figures 3.7a,b). At the 10%vol level, the SEM photo shows significant bundling of the PET fibers. The unevenness can also be seen by simply holding a sheet up to the light; scattered light and dark patches are easily detected. In contrast, SEM photos of the 5%vol PET samples show well dispersed single PET fibers, and the sheet appears fairly uniform when held up to the light. The actual

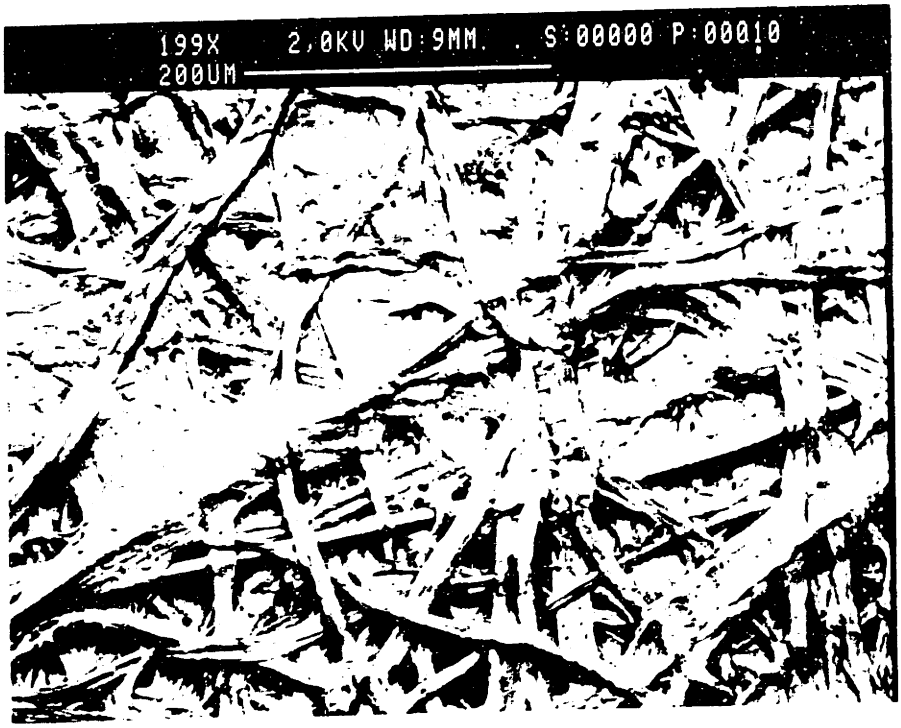

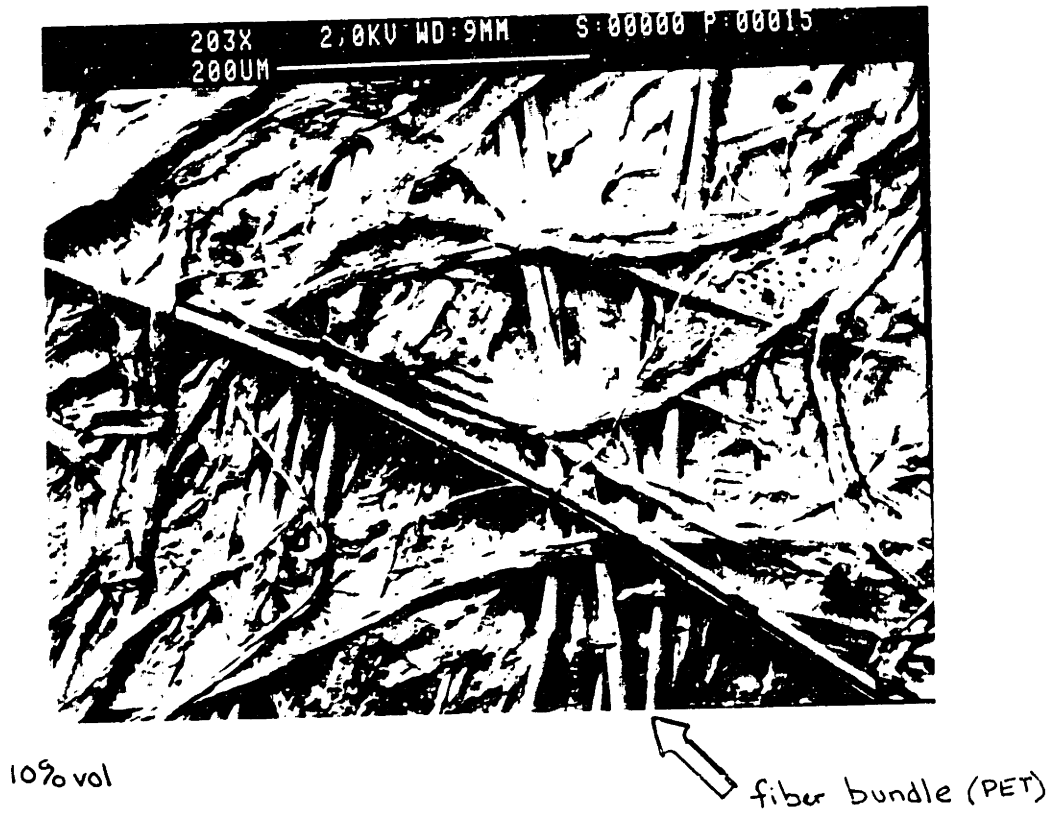

Figure 3.7: SEM photo – 5% and 10% PET

critical %vol will change depending on the fiber type, finish, and length. Beyond this level, increasing the %vol will result in more clumping of the fibers and poorer sheet uniformity. Thus, the cost of adding more fibers is unlikely to be offset by improved properties.

In the fiber-reinforced paper we tested, the PET fibers did not significantly affect the first two regions of the fracture curve (Figure 3.8). In fact, the only observable effect was an occasional slight decrease in post-crack initiation loads due perhaps to the diminished bonding of the PET fibers replacing the cellulose fibers. Because of the low volume fractions used and the relative closeness of the initial moduli, this is not surprising.

The positive effect of the PET fibers shows up clearly only after the crack has propagated through the cellulose matrix. At this point, only the PET fibers are holding the sample together. The load-displacement curve thus displays the load exerted to pull out the reinforcing PET fibers. It is assumed that this pull-out load contributes to the main part of the fracture curve also, but only once the crack has propagated through a given section. Since initially the crack size is small and thus the number of fibers being pulled out is few, the pullout loads tend to be masked by the loads carried by the cellulose fibers. However, after the cellulose fiber contribution ceases, the fiber pullout contribution is clear.

Since we cannot separate the fiber pullout from the cellulose matrix behavior in the main part of the fracture curve, we shall concentrate on the fiber pullout behavior in the third region, after the cellulose matrix has failed.

An example of the theoretical fiber pullout load contribution is given in Figure 3.9. As predicted from the fiber pullout analysis detailed later in Chapter 6, the pullout load will rise as the crack propagates and more fibers are involved. However, the average load/fiber contribution will decrease, since the average embedment length/fiber

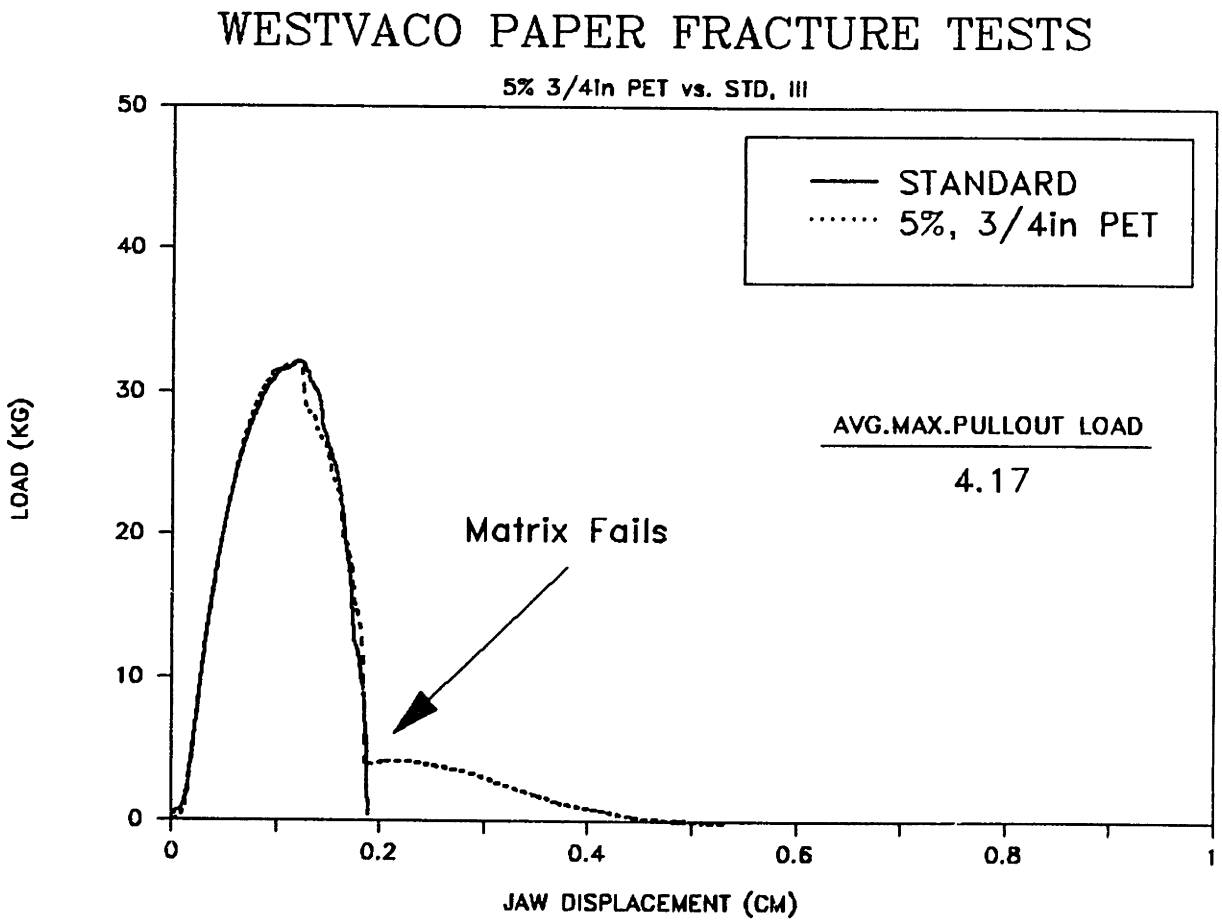

Figure 3.8: Fracture Curve – 5%vol 3/4in PET

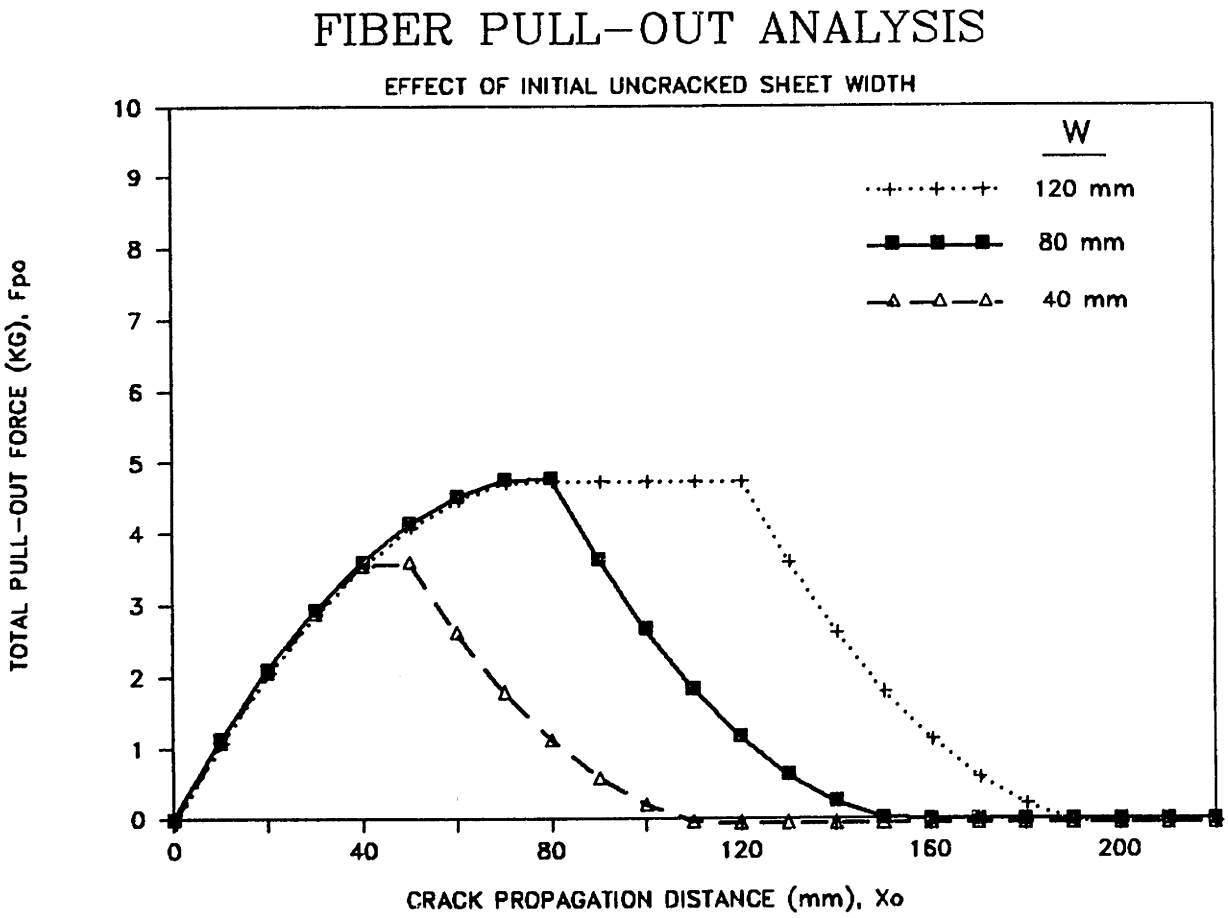

Figure 3.9: Theoretical Fiber Pullout Loads – Effect of Sheet Width

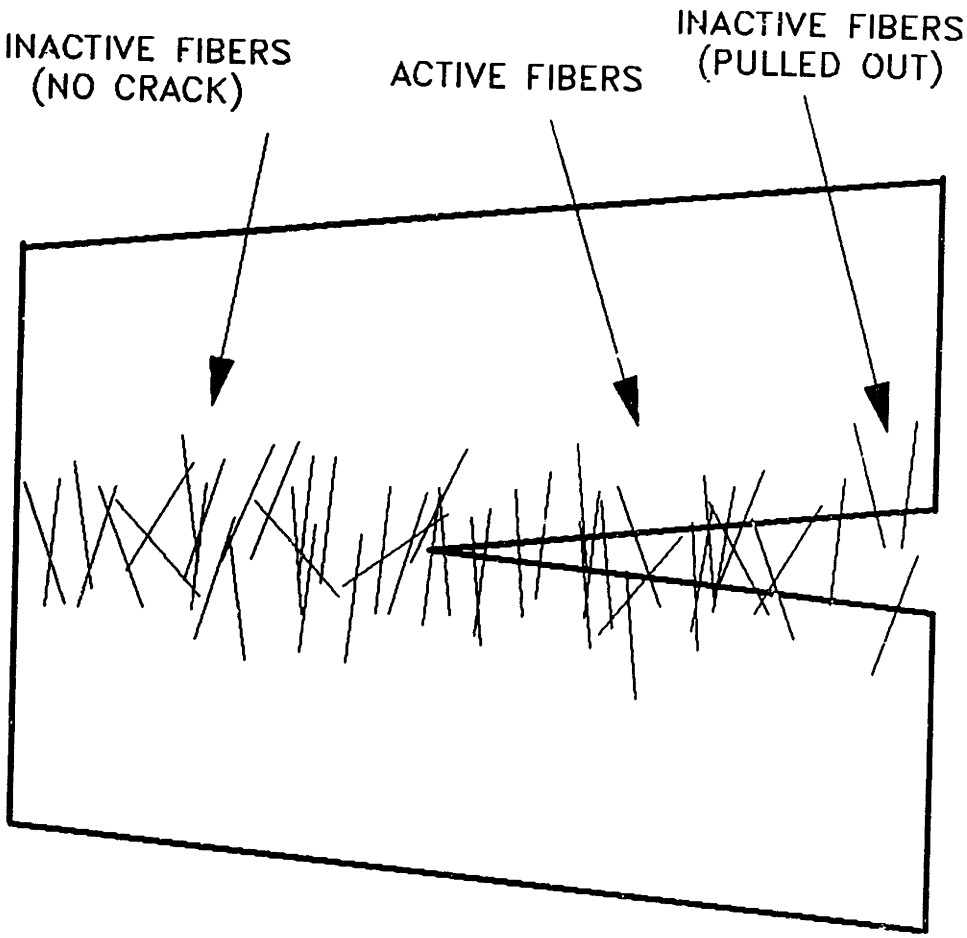

Figure 3.10: Inactive and Active Fibers in a Sheet Being Fractured

decreases. That is, as more fibers just start to be pulled out, the fibers behind them have already been pulled out some distance, reducing the average embedment length. This is the cause of the decreasing slope in the first portion of the curve.

At some point, if the sheet is wide enough, a pullout load plateau will be reached — as more active fibers are added at one end due to additional crack propagation, an equivalent number have been completely pulled out at the other end (becoming inactive fibers). This is shown schematically in Figure 3.10. The existence or duration of this plateau depends on the original uncracked width. Note that Figure 3.9 shows a long plateau for a 120mm sheet and a very short plateau for the 80mm sheet; the

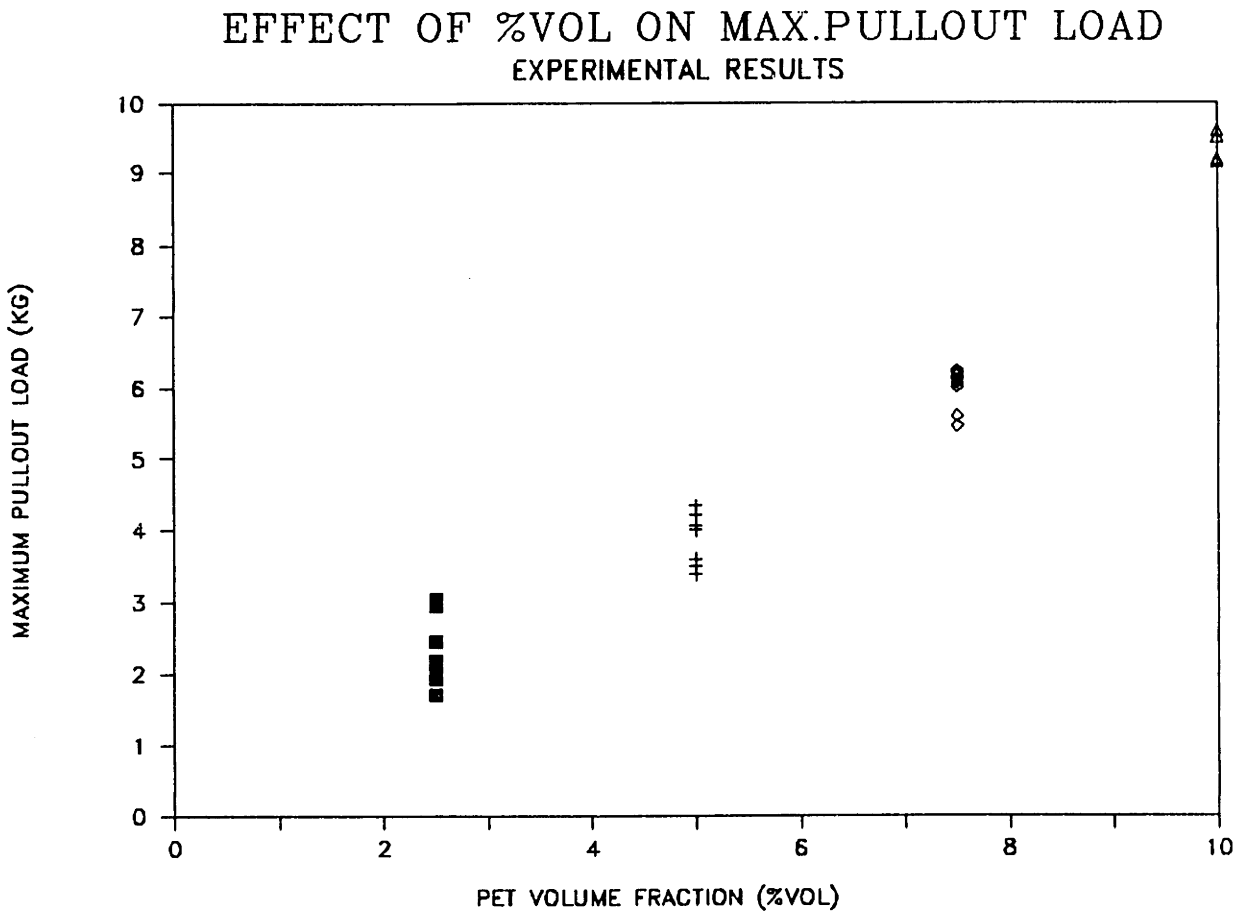

Figure 3.11: Measured Effect of PET %vol on Maximum Pullout Load

40mm sheet does not make it up to the plateau values.

Once the sheet has cracked completely through, new fibers are no longer being added to the pullout process; so, the pullout load gradually drops to zero as the remaining fibers are pulled out. Thus, the plateau value or the load value at the instant of complete matrix failure is the maximum pullout load attained. For all of the experimental fracture curves for fiber reinforced samples in this chapter, an average value (5-10 tests) for the maximum pullout load is given in the figure. This load varies somewhat linearly with %vol PET as expected (Figure 3.11). The effect of %vol in the theoretical analysis is shown in Figure 3.12 for comparison.

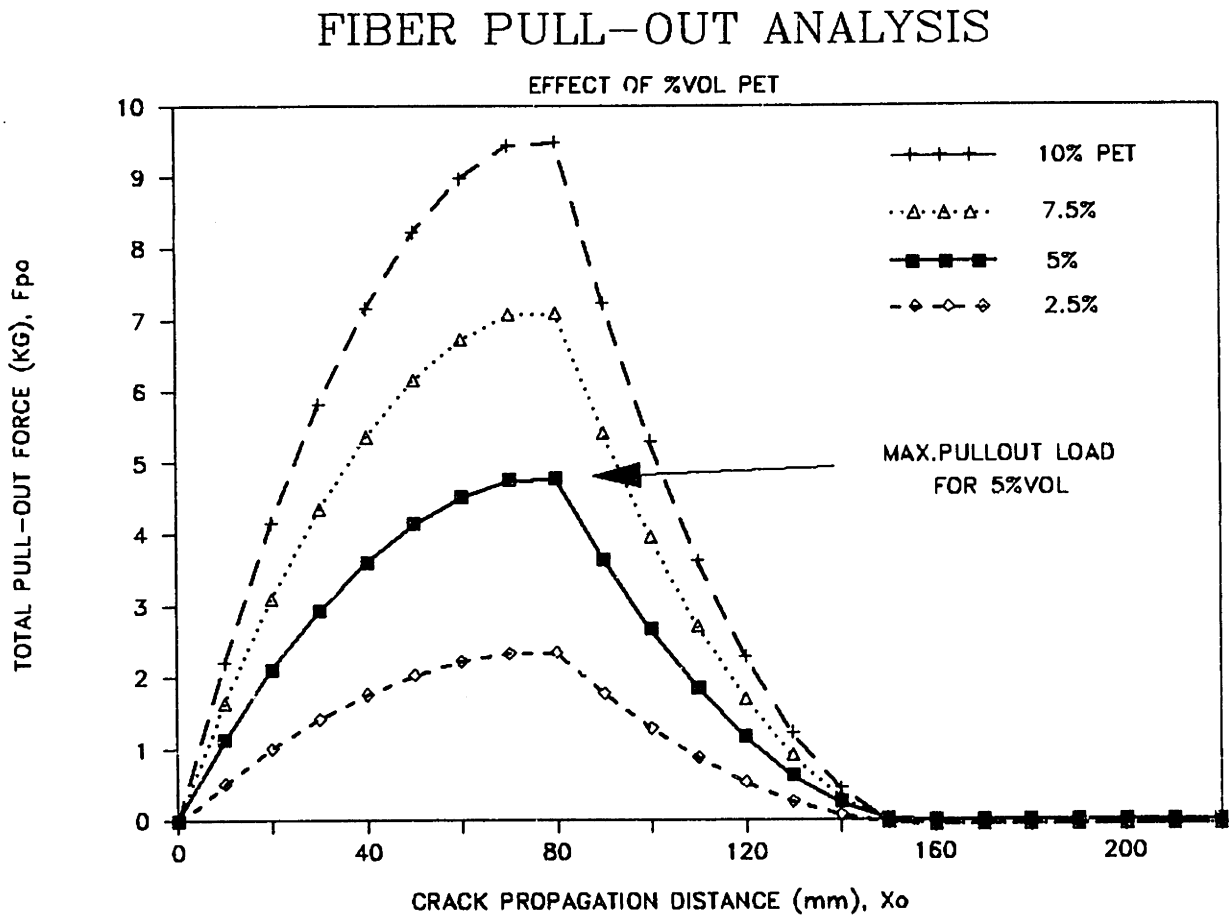

Figure 3.12: Theoretical Effect of PET %vol on Maximum Pullout Load

The %vol ranges tested were 2.5%, 5%, 7.5%, and 10%. Since the theoretical analysis assumes good dispersion at all volume fractions, the predicted pullout load vs. %vol curve is linear. However, at volume fractions much greater than 10%vol, we would expect the load/fiber to decrease for the experimental samples due to poorer bonding, and thus, the maximum load would not continue to increase linearly with %vol. Contradicting this prediction, the experimental curve appears to have an increasing slope. It is likely that the three lower volume fractions, which were all from the same sample series, are actually showing a linear relationship; while the 10%vol samples, which was made with a different pulp furnish, had slightly better bonding despite the poorer dispersion indicated by the SEM photos.

Fiber length is also a factor, as can be seen in Figures 3.13 and 3.14, displaying the experimental and theoretical results, respectively. Not surprisingly, increased length leads to higher pullout loads. In contrast to the volume fraction analysis, increasing length results in a greater than linear increase in pullout loads. This is due to the incorporation of more fibers into the pullout region, since the longer fibers do not cease contributing to the pullout load as quickly. Unfortunately, increased length generally also results in poorer dispersion. With the hydrophilic finish and at 10%vol, however, the increase in length from 1/2in to 3/4in showed no dispersion problems and no significant deterioration of gain in pullout load.

Independent experiments on PET fiber pullout from a cellulose matrix were run to support these observations. These results will be discussed in the next section.

3.3.2 Fiber Pullout Studies

In order to get some independent data on the pullout of synthetic fibers from a cellulose matrix, a separate set of experiments were run on special samples prepared in the M.I.T. Fibers and Polymers Laboratory. A homemade papermaker (Figure 3.15)

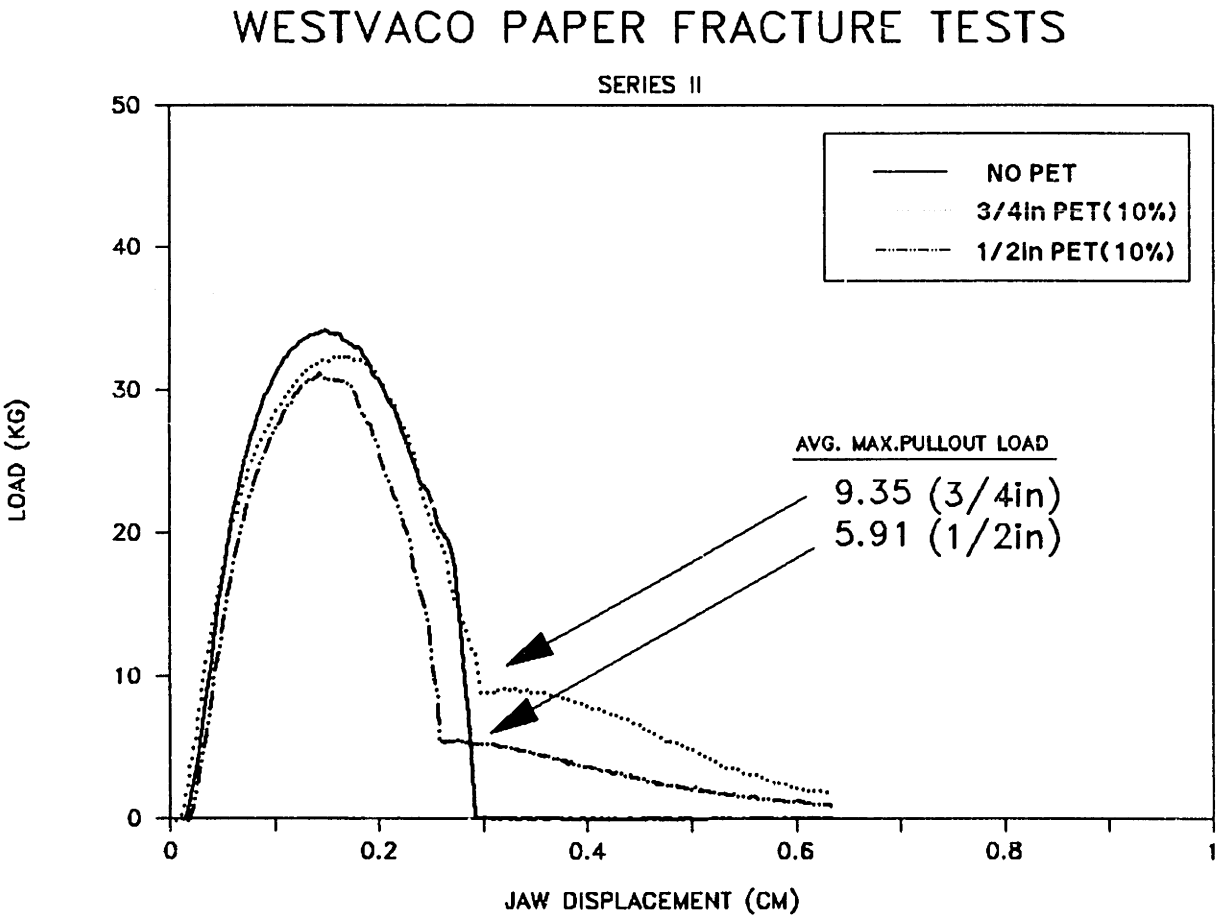

Figure 3.13: Measured Effect of PET Length on Maximum Pullout Load

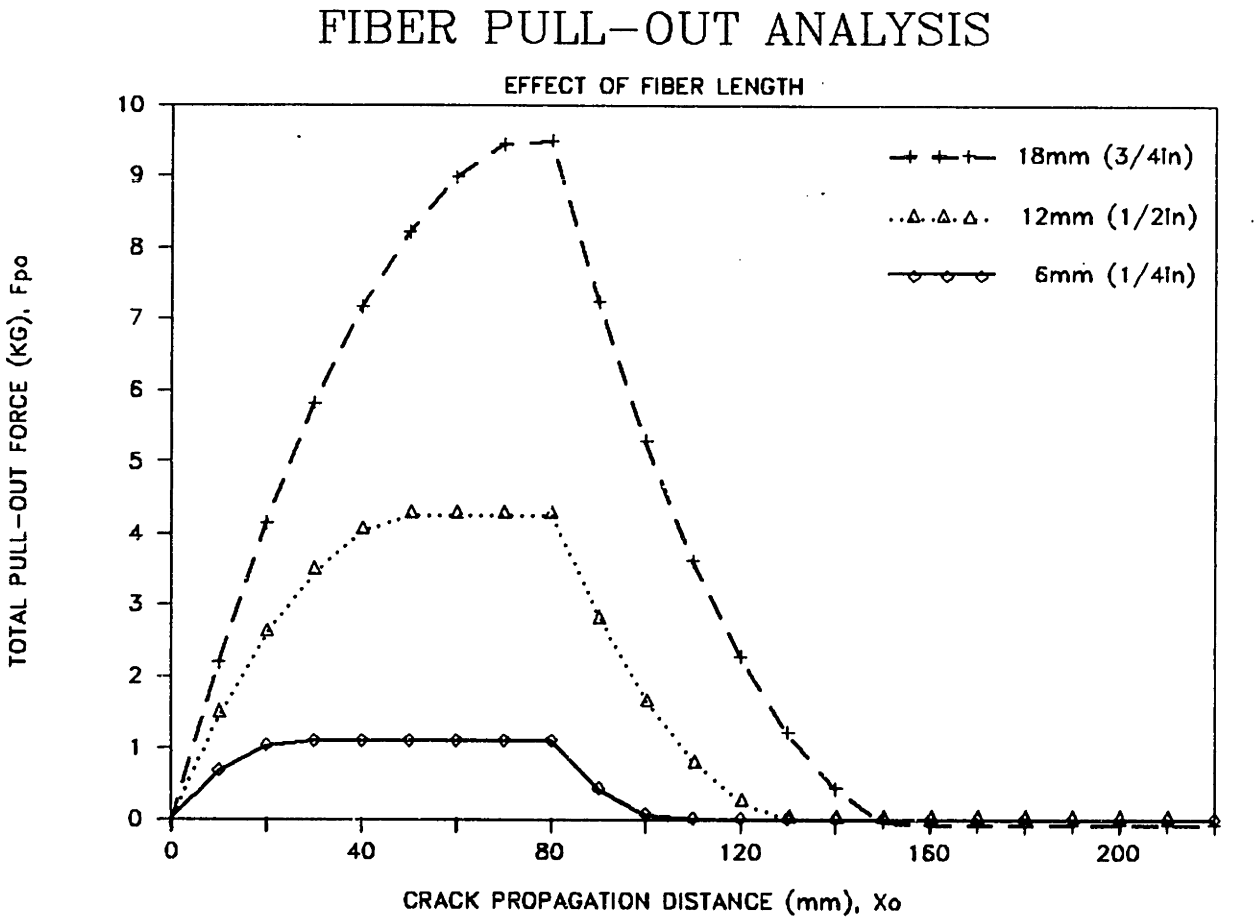

Figure 3.14: Theoretical Effect of PET Length on Maximum Pullout Load

was built, consisting of a 6.5in diameter bucket with a cork ring inserted about 1/3 of the way down to act as a support ledge. A piece of forming fabric was placed on top of the cork, followed by a plastic support plate with a multitude of drainage holes. A plastic tube was connected to the bottom of the bucket to supply water, and four holes were drilled to allow control of the drainage rate out of the bucket.

Production of paper sheets took only a few minutes. A piece of forming fabric was placed on top of the support plate and held in place by a large pvc tube. Water was supplied to the papermaker until the water level was about two inches above the forming fabric. Wood pulp supplied by Westvaco was mixed with water in a blender and then poured into the papermaker. After chaotically disturbing the flow pattern created by the pouring and waiting 5-10 seconds for the motion to cease, one or more of the drainage holes is opened. Once the water level is below the level of the support plate, the forming fabric and newly formed paper can be removed, placed under pressure ($\approx$ 3kg), and allowed to air-dry.

Several sheets were made and tested to determine the optimal pulp quantity and technique. Approximately 100ml of the pulp furnish supplied by Westvaco was sufficient to produce a 6in diameter sheet which weighed roughly 1.8g, giving a basis weight of approximately 100g/m^2, reasonably close to the Westvaco produced handsheets. Mixing the pulp furnish with plenty of water and allowing the mixture to equilibrate in the papermaker prior to "pulling the plug" proved to be positive influences on paper uniformity. The sheets were slightly weaker than the Westvaco produced sheets.

Once consistent cellulose sheets could be produced, synthetic fibers were introduced. A sandwich construction was used because bonding was too poor for bundles that were simply placed on top of the forming fabric prior to adding the pulp. To make the sandwich sheets, half of the pulp was set aside and the other half was used to make one sheet. This sheet was removed from the Papermaker. Using roughly

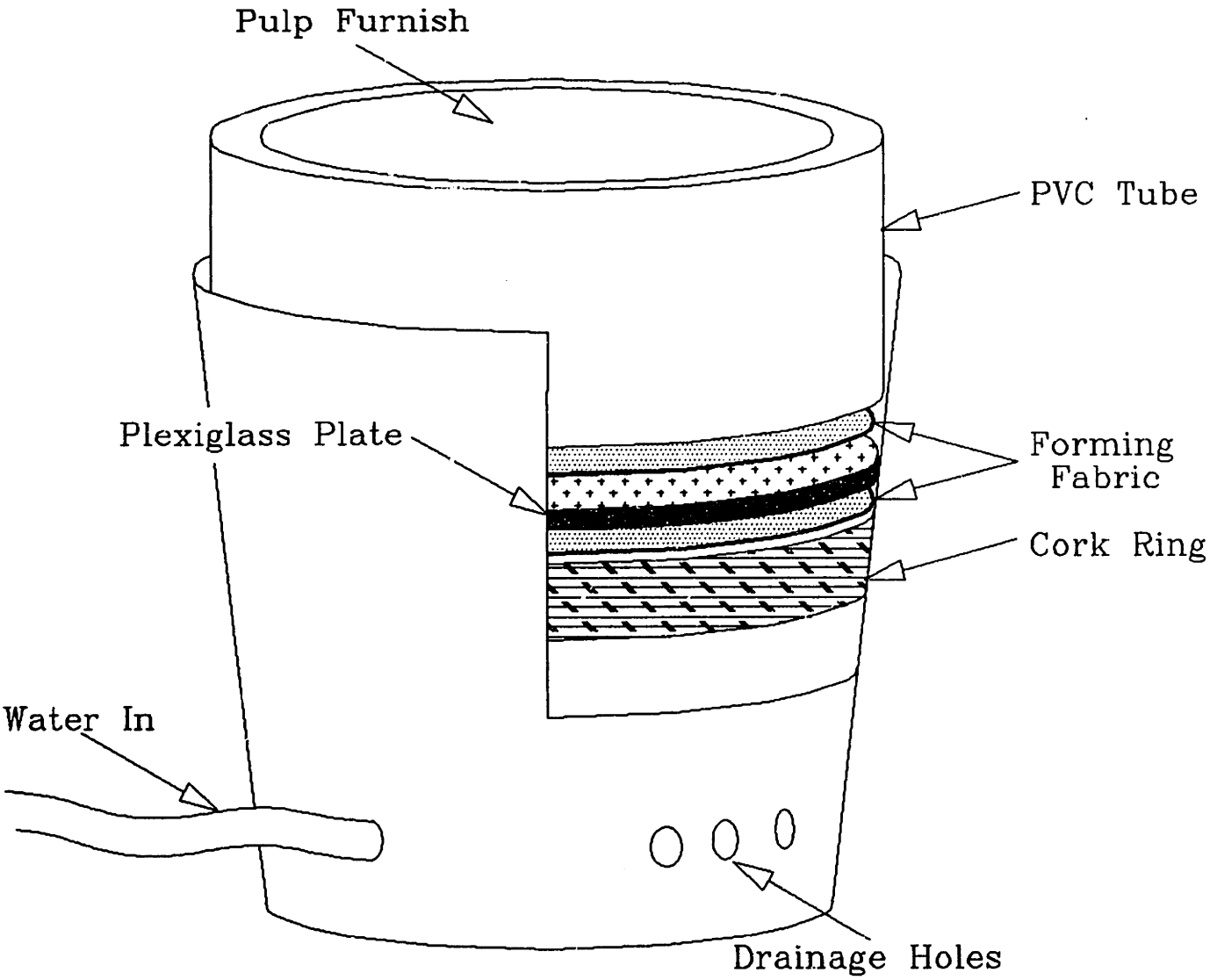

Figure 3.15: Papermaker Apparatus

8inch lengths of originally uncut Papermaker Staple, two bundles of the synthetic fiber were laid across the first sheet. A second sheet was made from the remaining half of the pulp and a second piece of forming fabric; it was then inverted on top of the PET fibers and the first sheet. Pressure was applied to consolidate the sheet. Fiber bundles were used because single fibers were too difficult to separate out without damage. Also, these bundles were not unlike the bundles we had seen in the 10%vol samples.

Double-sided pullout samples were also made to better reproduce the actual behavior of the PET fibers in bridging the crack. These samples were produced in a similar manner. The main alteration being the addition of a divider onto the pvc tube. Thus, instead of making two circular sheets, four half sheets were made, two at a time on each piece of forming fabric. The space between the sheets produced by the divider was bridged by the bundles and was approximately 1-2mm wide.

Tests run on these two types of samples confirmed three points of interest. First, in the case of a double-sided pullout, almost all the pullout occurs from the side (top or bottom) with the weakest bonding - the weakness of the bonding may be due to embedment length or actual bond strength. Therefore, when comparing the double-sided pullout curves with single-sided pullout curves from the opposite sides of the sheet, the double-sided curve tends to match the lower single curve more closely. The sample configuration and typical results are shown in Figure 3.16 [16].

Second, in terms of fiber bundle size, the pullout load per fiber exhibits a concave shape (Figure 3.17 [16]). The drop-off in load per fiber at the high fiber bundle size can be explained in terms of poor bonding of the fibers in the center of the bundle. However, it is unclear why at lower bundle sizes there is also a drop-off in load per fiber. Hein's results show a peak in load per fiber at bundle sizes of 25-40 fibers.

Third, using bundle sizes of 40 fibers, Hein demonstrated that the pullout load/fiber

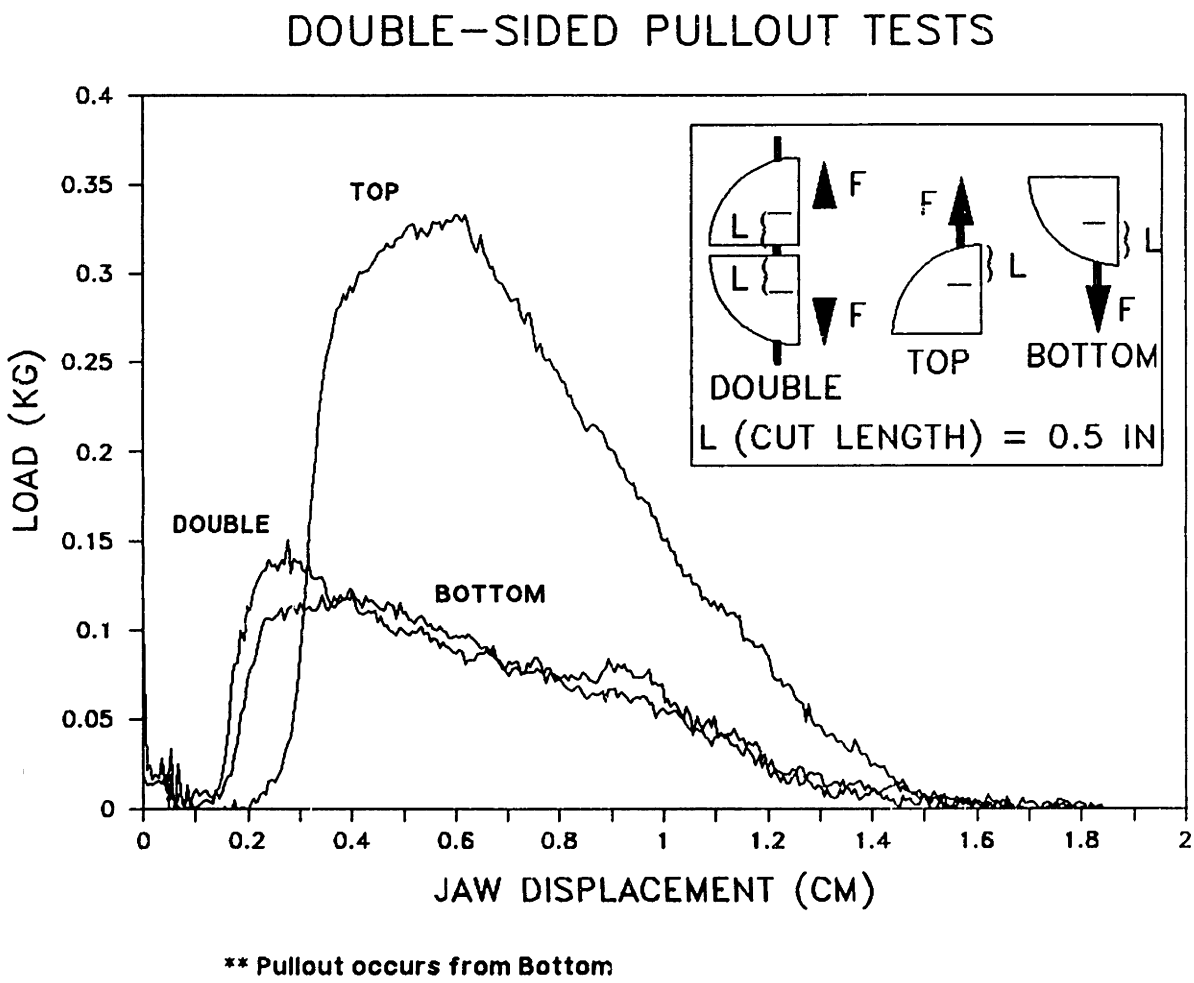

Figure 3.16: Double-Sided Pullout Test

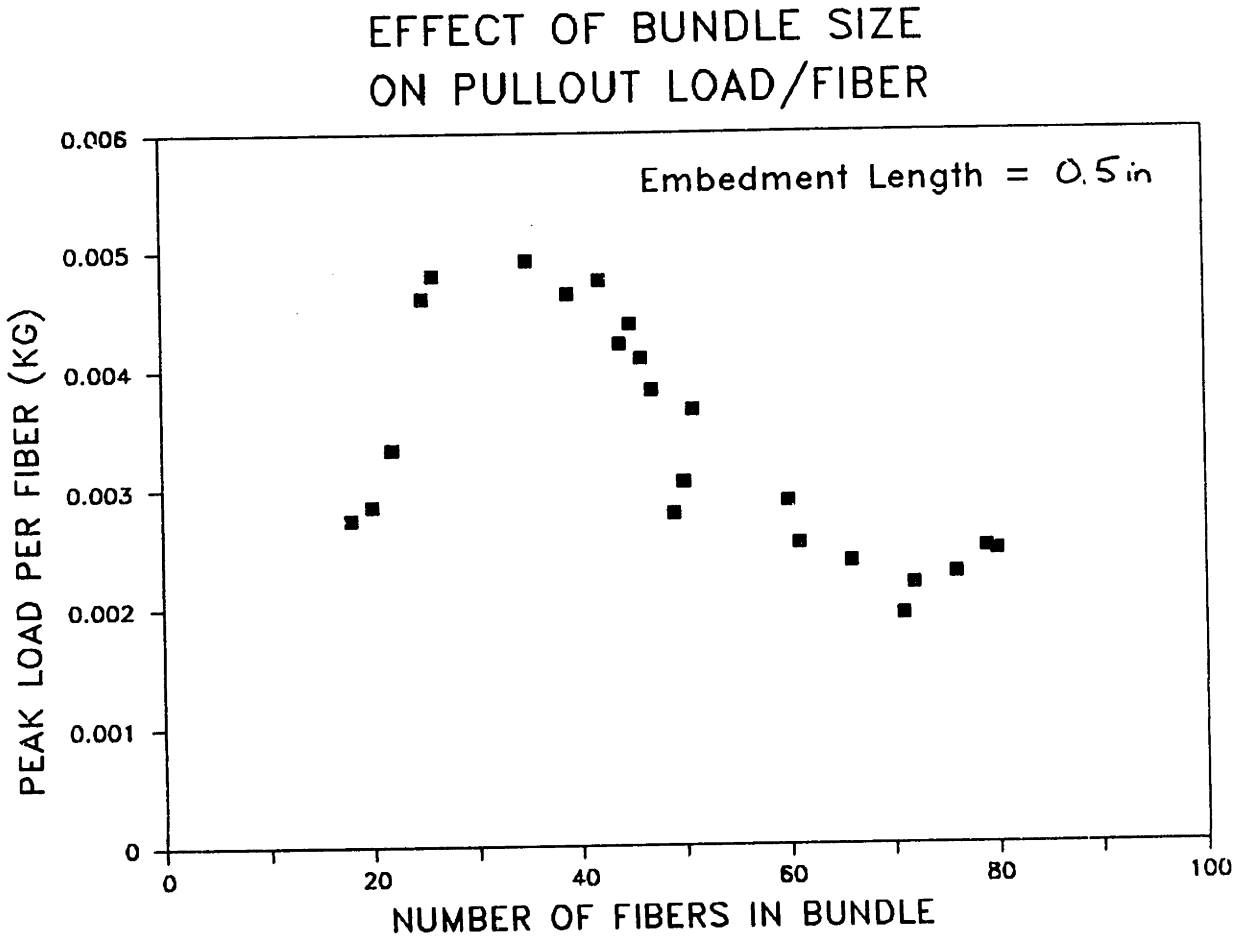

Figure 3.17: Effect of Bundle Size on Pullout Load/Fiber

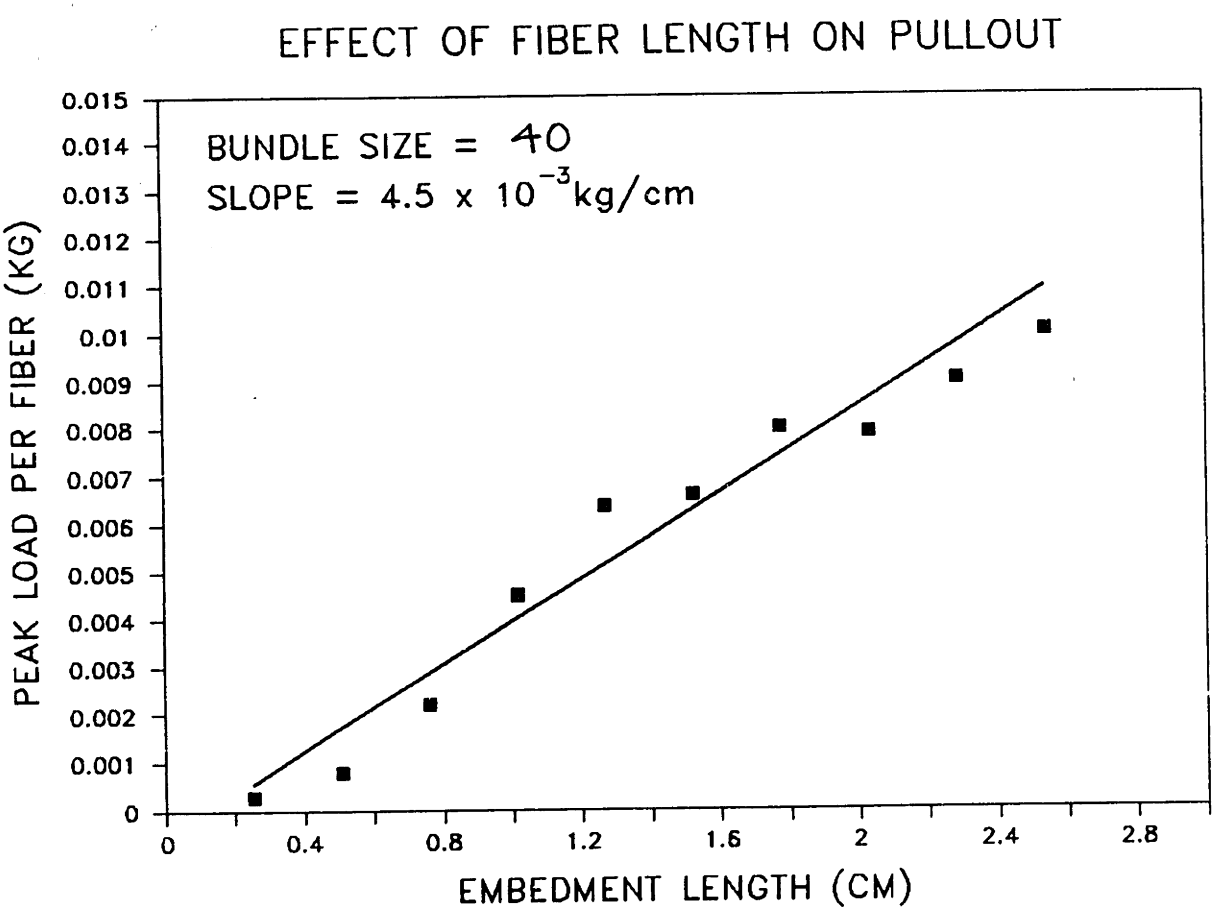

Figure 3.18: Effect of Fiber Length on Pullout Load/Fiber

does increase linearly with embedment length up to lengths of 2.6cm (Figure 3.18 [16]). A least-squares linear fit to the points provides the following equation

$$\text{Load per fiber (kg)} = C_0 + C_1 * \text{embedment length (cm)} \tag{3.1}$$

with

$$C_0 = -5.88\text{x}10^{-4}\ kg$$

$$C_1 = 4.51\text{x}10^{-3}\ kg/cm$$

Note that if we assume that the average embedment length is half the length of the fiber, we would expect to get a peak load contribution of approximately 4g/fiber for the 1.8cm fibers (0.9cm embedment length). Using some rough "back of the envelope" calculations, the fracture tests produced an average maximum pullout load of 4kg (5%vol, 3/4in). This would translate to a little over 1000 PET fibers, if all the fibers were being pulled out simultaneously. A quick look at an SEM photo (Figure 3.19) of the fiber pullout in the 5%vol and 10%vol samples displays approximately 12 and 30 fibers in a 500μm distance, respectively. Taken over the entire width of 2cm, this would translate to just about 2000 fibers (5%vol). However, in the actual fracture test, the maximum pullout load does not consist of all the fibers along the crack path being pulled out at an embedment length of half their length. Instead, some of the fibers have already been pulled out, rendering them inactive. And, many of the fibers are at much shorter embedment lengths. Taking all of this into account, it is not surprising that the 2000 fiber figure is somewhat higher than the predicted number of 1000. Therefore, the numbers fall in the range of reasonable values.

3.3.3 Bicomponent Fiber

There was some disappointment with the contribution of the reinforcing fibers, especially in the main part of the fracture curve. Several things were tried to improve this. One method included the use of bicomponent fibers. The bicomponent fibers are made of a higher melting temperature polymer core encircled by a lower melting temperature polymer sheath. Thus, with the application of the correct heating process, the sheath melts and bonds the core to the cellulose fibers in the matrix. This would, in theory, help strengthen the bond between the reinforcing fibers and the matrix.

The bicomponent fibers (D269) supplied by DuPont were 50/50 sheath/core fibers with an elongation to break of 20% and a tenacity of 3g/den. Binding temperature

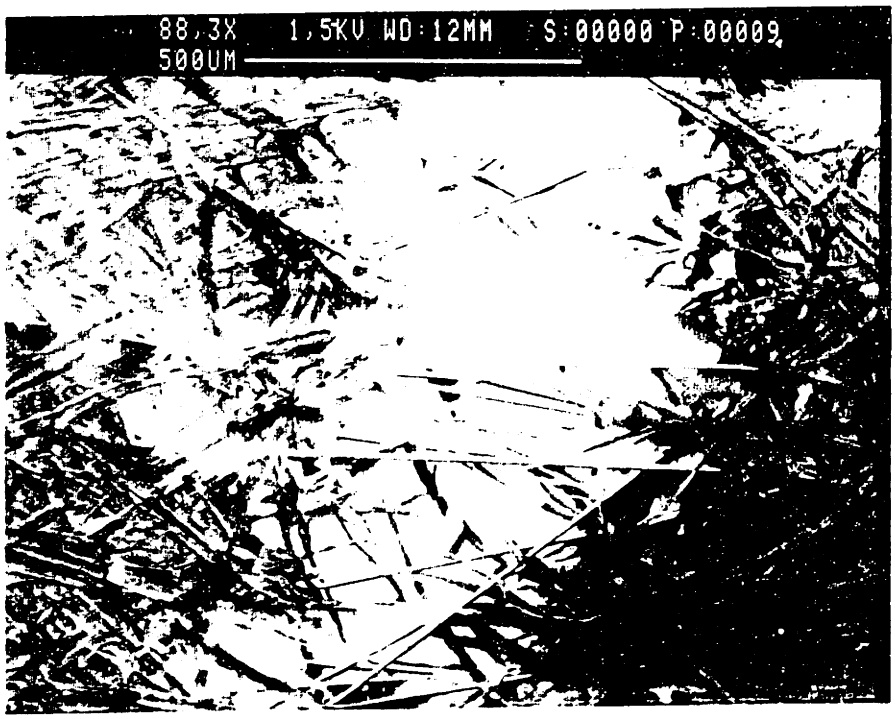

5%

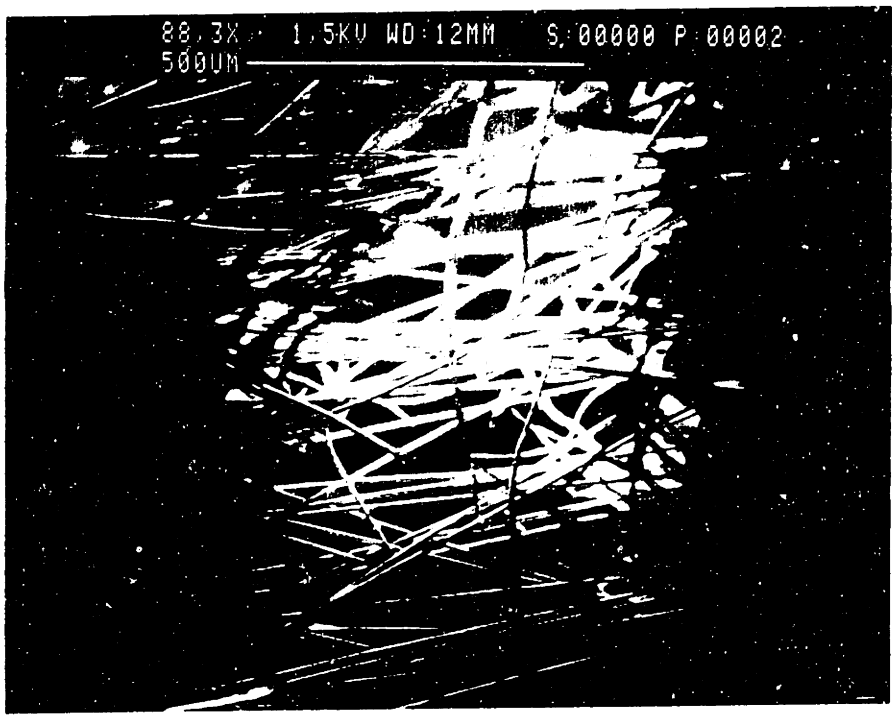

10%

Figure 3.19: Typical Number of Fibers Bridging the Crack

was $130°C$ without pressing. Unfortunately, the bicomponent fibers did not disperse well, exhibiting extremely hydrophobic behavior, as can been seen by the tendency of the fibers to curve and form bundles. This unevenness was also apparent through the visible variations in sheet opacity. SEM photos of surface bicomponent fibers indicated varying degrees of sheath melting (Figure 3.20a,b), which probably contributed to this effect. It is unclear if this is also occurring in the few interior layers of the sheet. However, this poor dispersion and uneven bonding may explain the results from the fracture tests (Figure 3.21). The loads are significantly lower and more erratic for the bicomponent samples than for the standard sheet and the Papermaker Staple sheet. An interesting point to note is that there is very little difference between the fiber pullout regions of the 3/4in and 1/2in Bicomponent fibers. This would support the idea that the curvature of the fibers is the same for both lengths, such that the effective lengths are also similar.

3.4 Effect of Binder Application

The mechanical properties of paper are governed by a combination of the fiber properties and the bond properties. The previous section examined the effect of mixing in fibers with different properties. Unfortunately, it became clear that for the samples tested, bonding between the cellulose fibers and the PET fibers was somewhat lacking. The use of bicomponent fibers was an attempt to improve the bond strengths. Unfortunately, due to dispersion problems, this solution was ineffective.

Two other methods were tried in order to improve the bonding of the reinforcing fibers and to also produce a sheet with a different fracture behavior to test the model. The first that will be discussed is the surface application of an acrylic emulsion binder; the second is the addition of binder fibers.

Figure 3.20: SEM photos of Bicomponent Fibers

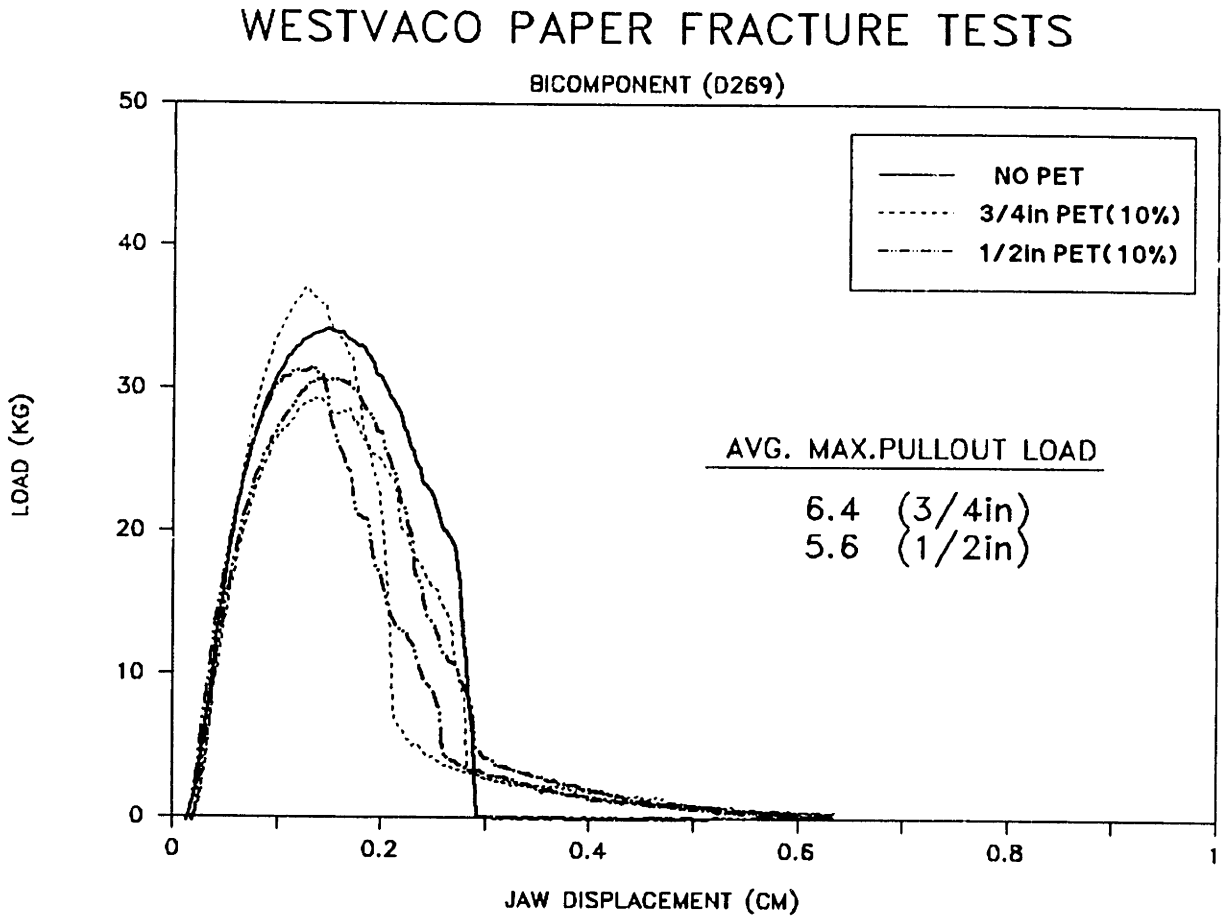

Figure 3.21: Fracture Curves – Bicomponent Fibers

3.4.1 Surface Application

The acrylic emulsion binder was supplied courtesy of W. Devry of the Rohm and Haas Company (Philadelphia, PA). Two binders, Rhoplex TR-407 and TR-934 were examined. Both binders are used in the paper industry as paper saturants to improve physical properties. While both are self-crosslinking, the TR-407 is stiffer than the TR-934. Specific properties are listed in Table 3.2 (from the Rohm and Haas brochure)

The binder was mixed with water to 15%solids and then applied to the surface of the already made sheets. The composition and the binder wet pickup for the different samples is given in Table 3.3.

Addition of the binder is obviously a significant change of the paper structure. The increase in stiffness from the Standard sheets is easily distinguishable by hand. SEM photos show the binder coating the surface of the sheet (Figure 3.22a,b). There is no obvious difference in appearance between the two binders.

The binder acts as an auxiliary to the hydrogen bonds between the cellulose fibers. In addition, the binder strengthens the primarily mechanical bond between the cellulose fibers and the PET fibers. The result of this additional bonding is that fiber pullout becomes less likely; instead, a very clean crack is produced where both cellulose fibers and PET fibers have fractured. This fracture surface observation will be discussed in the next chapter (section 4.1).

In terms of the load-displacement curve (Figure 3.23), the material tends to behave in a more brittle manner, with higher maximum loads and a sharp load drop for the main portion of matrix failure. Of course the exact behavior depends on the type of binder used. In our case, the softer binder did not change the fracture curve significantly from the Standard curve. However, the stiffer binder did exhibit the more brittle characteristics described above.

	Grade	% Total Solids	Density @ 25°C. lbs./U.S. gal.	Specific Gravity	pH (as packed)	Ionic Nature	T_{300} °C[1]	Minimum Film Formation Temp. °C.	Properties and Uses
Crosslinkable	RHOPLEX N-495	58.0	9.0	1.08	4.2	Anionic	- 3	0	High-speed packaging and laminating emulsion. Has excellent "wet grab", fast water release and quick rate of set. Good adhesion to paper and paperboard.
	RHOPLEX P-376	50.0	8.7	1.04	9.4	Anionic	14	8	Hydrophobic pigment binder. Recommended for paper and paperboard coatings when excellent wet and dry pick resistance is desired.
	RHOPLEX P-310	46.0	9.0	1.08	5.0	Anionic	25	14	Single component binder for use in pigmented paper and paperboard coatings. Yields high levels of opacity and brightness.
	RHOPLEX AR-74	45.0	9.0	1.08	5.0	Anionic	41	13	Alkali-reactive, highly swellable replacement for protein or casein in pigmented coatings for paper and paperboard. Provides high bonding strength and excellent ink receptivity
	RHOPLEX R-225	38.0	8.8	1.06	9.4	Anionic	28	16	Release coating for paperboard pigmented coatings masking tape.
	EMULSION E-581	46.0	8.8	1.05	8.3	Anionic	47	46	A pigment binder specifically designed to produce very high levels of gloss on paper and papberboard coatings.
Self-Crosslinking	RHOPLEX TR-934	44.5	8.7	1.04	8.5	Anionic	- 30	50	Forms soft flexible films. Used both alone and in combination with other polymers in paper saturation.
	EMULSION E-940	45	8.7	1.05	9.5	Anionic	- 20	125	Soft, hydrophobic polymer. Useful both as a pigment binder and a paper saturant.
	RHOPLEX K-87	46.0	8.6	1.03	3.0	Nonionic	- 18	0	A soft but tough resin used in saturation beater deposition of paper.
	RHOPLEX HA-8	45.5	8.7	1.04	3.0	Nonionic	- 14	0	General purpose binder, recommended for paper saturation.
	RHOPLEX E-32	46.0	8.7	1.04	3.0	Nonionic	- 2	0	Paper saturation. Excellent solvent resistance.
	RHOPLEX E-358	60.0	9.0	1.08	7.0	Nonionic	0	0	Paper saturation.
	RHOPLEX TR-621	55.0	8.9	1.07	3.5	Anionic	1	0	Beater deposition binder, also recommended for paper saturation; bookcover saturation.
	RHOPLEX HA-12	45.0	8.8	1.06	3.0	Nonionic	17	5	Paper saturation.
	RHOPLEX TR-407	45.5	8.9	1.07	3.5	Anionic	- 30	30	Anionic version of Rhoplex HA-16; used in pigmented specialty coatings and as a paper saturant.
	RHOPLEX HA-16	45.5	8.8	1.06	3.0	Nonionic	33	22	Clear coatings for wallcoverings, etc., paper saturation.
	RHOPLEX GL-655	46	8.7	1.04	8.5	Anionic	38	- 32	Anionic, low soap polymer; forms stiff films; hydrophobic. Useful in paper saturation and as a beater addition.

Table 3.2: Binder Properties

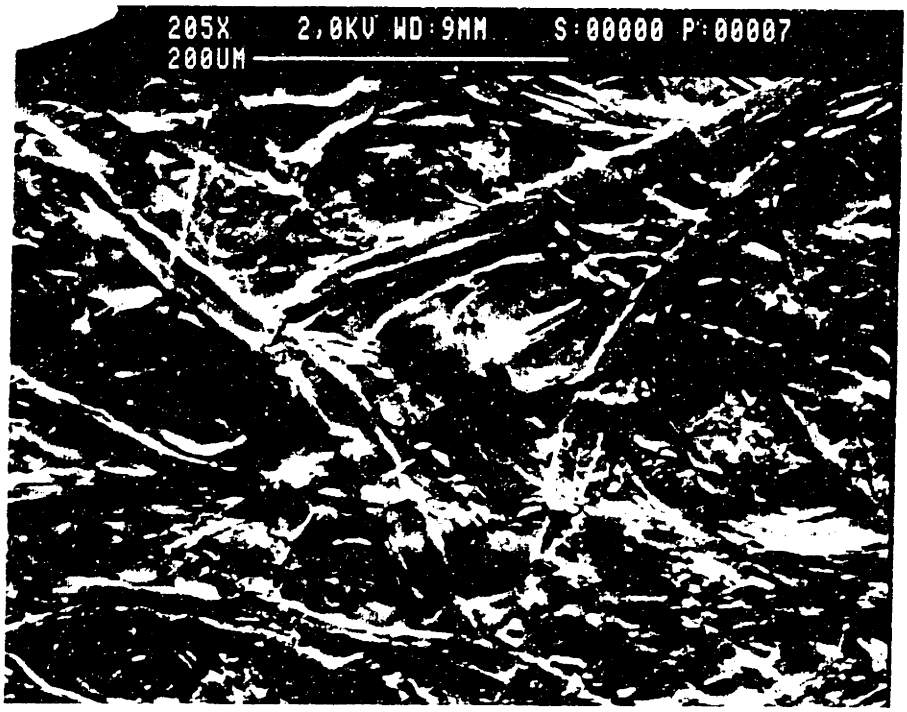

TR-407

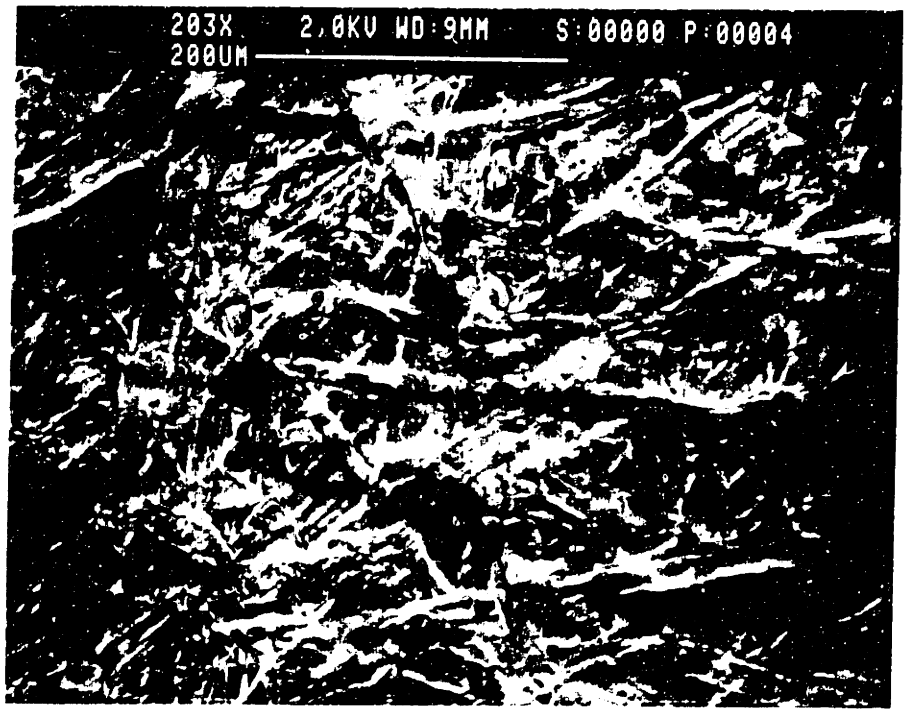

TR-934

Figure 3.22: SEM photos of Binder Sheets

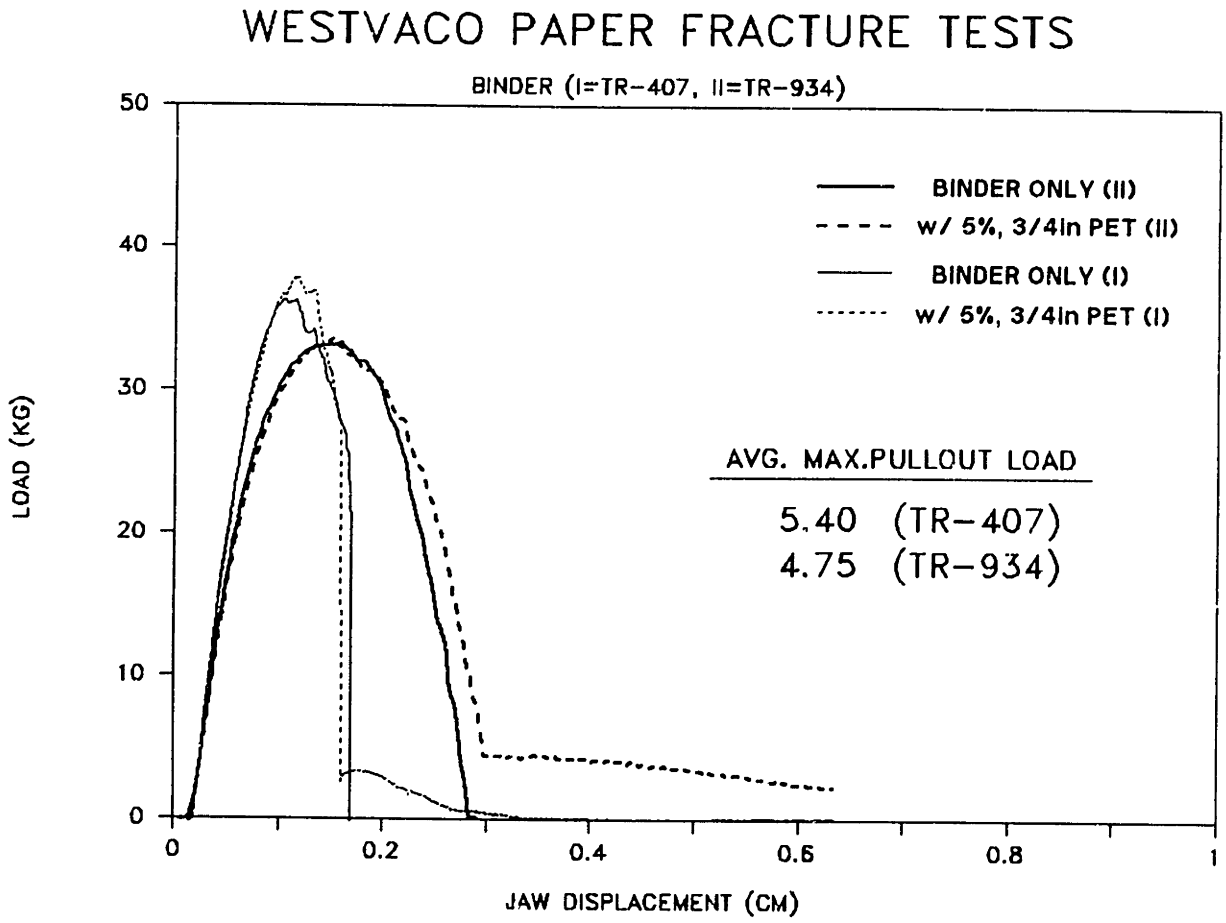

Figure 3.23: Fracture Curve – Binders: TR-407, TR-934

TABLE 3.3 Percentage of Binder in Test Samples

SERIES	BINDER TYPE	%BINDER	%PET	PET LEN (mm)
I	TR-407	15.8	—	—
I	TR-407	15.8	5	18
I	TR-407	15.7	5	6
II	TR-934	6.0	—	—
II	TR-934	7.0	5	18
III	TR-407	10.0	—	—
III	BINDER FIBERS	5.0	—	—
III	BINDER FIBERS	5.0	5	18

As it turns out, a stiff binder was not the ideal answer to improving the fracture toughness of the paper. The maximum pullout loads were only slightly higher than without the binder — 5.40kg, 4.75kg, and 4.17kg for the TR-407, TR-934, and Standard samples, respectively. In all three cases, there is very little influence on the PET contribution to the matrix fracture portion of the curve. A negative effect of the stiffer TR-407 binder is the rapid load drop-off of the pullout region. This can be explained by the failure of some of the PET fibers prior to and after the complete failure of the cellulose matrix. Since the PET fibers are not much stronger than the cellulose fibers, bonding them so that they fail instead of pull out provides little overall improvement, and it reduces the pullout contribution after matrix failure. Rather, the advantage of the PET fibers is that of holding the sheet together through its extra length and stretch. Thus, the ideal bond would connect the PET fibers to the cellulose matrix such that the PET fibers could carry some load and dissipate some of the input energy by stretching without failing or pulling out. Realistically, the easier solution is simply increasing the energy consumed during pullout of the fibers.

Because it was beyond the scope of this project, we did not attempt to try a

multitude of binders. Instead, we tried two distinct types to identify the major effect on the fracture behavior. From the results, the apparent direction of promise is the use of even softer binders. The main drawbacks to this method are that a separate step of adding the binder must be incorporated and that recycling also requires an extra step of binder removal. Both these mean additional expense and processing time.

3.4.2 Binder Fibers

A second method involves the use of separate binder fibers to bond the reinforcing PET fibers and the cellulose matrix fibers. The advantage of using binder fibers or bicomponent fibers that can be mixed in with the pulp furnish is that it eliminates the extra step of saturating or coating the sheet with a binder. The effect is also less dominating with the addition of moderate quantities, as will be seen later by comparing the fracture curves.

The binder fibers were also provided by DuPont. Designated as D262, the monocomponent binder fibers are designed to melt at $150^{o}C$. Similar to the bicomponent fibers, these fibers were mixed into the furnish both with and without the addition of the reinforcing PET fibers and then melted in the drying stage. The difference between the binder fibers and the bicomponent fibers is the precision of the bonding.

Obviously, the bicomponent fibers will bond only where the core reinforcing fibers are present. In contrast, the binder fibers are mixed throughout, coating cellulose-cellulose contacts, cellulose-PET contacts, and PET-PET contacts. Thus, if the binder fibers are dispersed uniformly, the end result is similar to a patterned application of binder to the entire sheet, through the thickness. If the goal is to improve the bonding between the reinforcing fibers and the matrix, then the bicomponent fibers are obviously more efficient. However, the binder fiber approach may be less

expensive and less complex.

Unfortunately, from the results it is difficult to judge. The binder fibers had the same dispersion and uneven melting problems as the bicomponent fibers (Figures 3.24 and 3.25). A brief attempt was made to apply a hydrophilic finish to the binder fibers, but the effort was unsuccessful.

It is interesting to note that there is a definite difference in appearance between the binder fibers and the PET fibers. The binder fibers seem to be larger in diameter, and the deformation of the binder fibers, while not as complete as desired, is clearly visible. Though from these photos, it is apparent that small volume fractions (e.g., 5%) of binder fibers are not sufficient to strengthen the reinforcing PET-cellulose fiber bond. The result is somewhat akin to watering one's lawn with a cup of water and a spritzer.

The fracture curves of the binder fiber and binder fiber + 5% PET samples were also not unlike the bicomponent fiber results (Figure 3.26). Generally, erratic crack propagation regions, lower crack propagation loads, and lower fiber pullout loads were found.

3.5 Effect of Clupak Compaction

The Clupak process is a method whereby the sheet is compacted, giving it extra stretch. The purpose of including this variation is not to suggest that compaction is the method of choice. There are, for instance, some obvious aesthetic and implementation problems. However, one of the goals of this study is to understand how significant differences in structure affect the fracture behavior.

In the Clupak process, the sheet is put through rollers running at different speeds (Figure 3.27) [?]. Because of the different speeds and the fact that one of the rollers

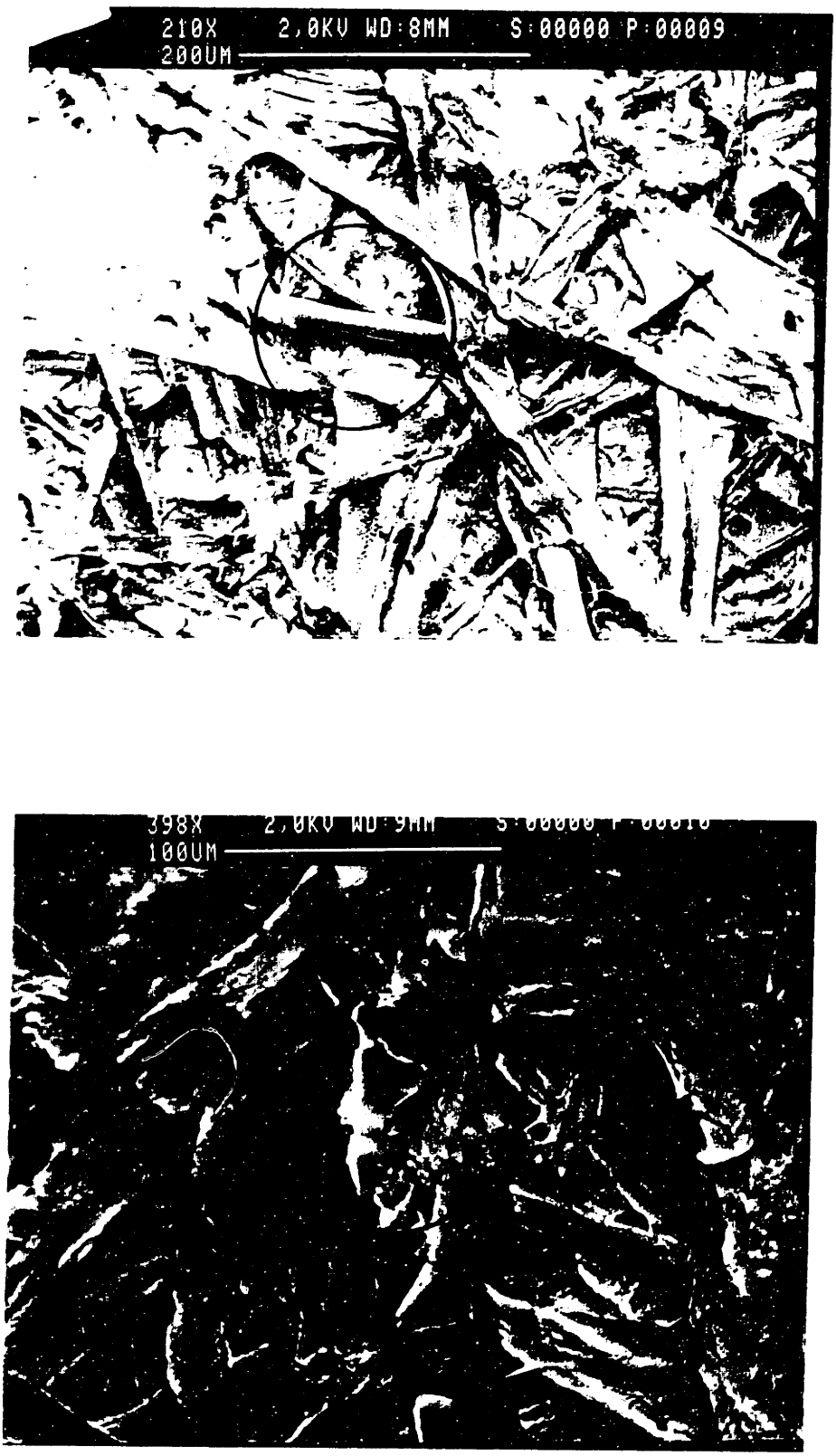

Figure 3.24: SEM photos of partially melted binder fibers

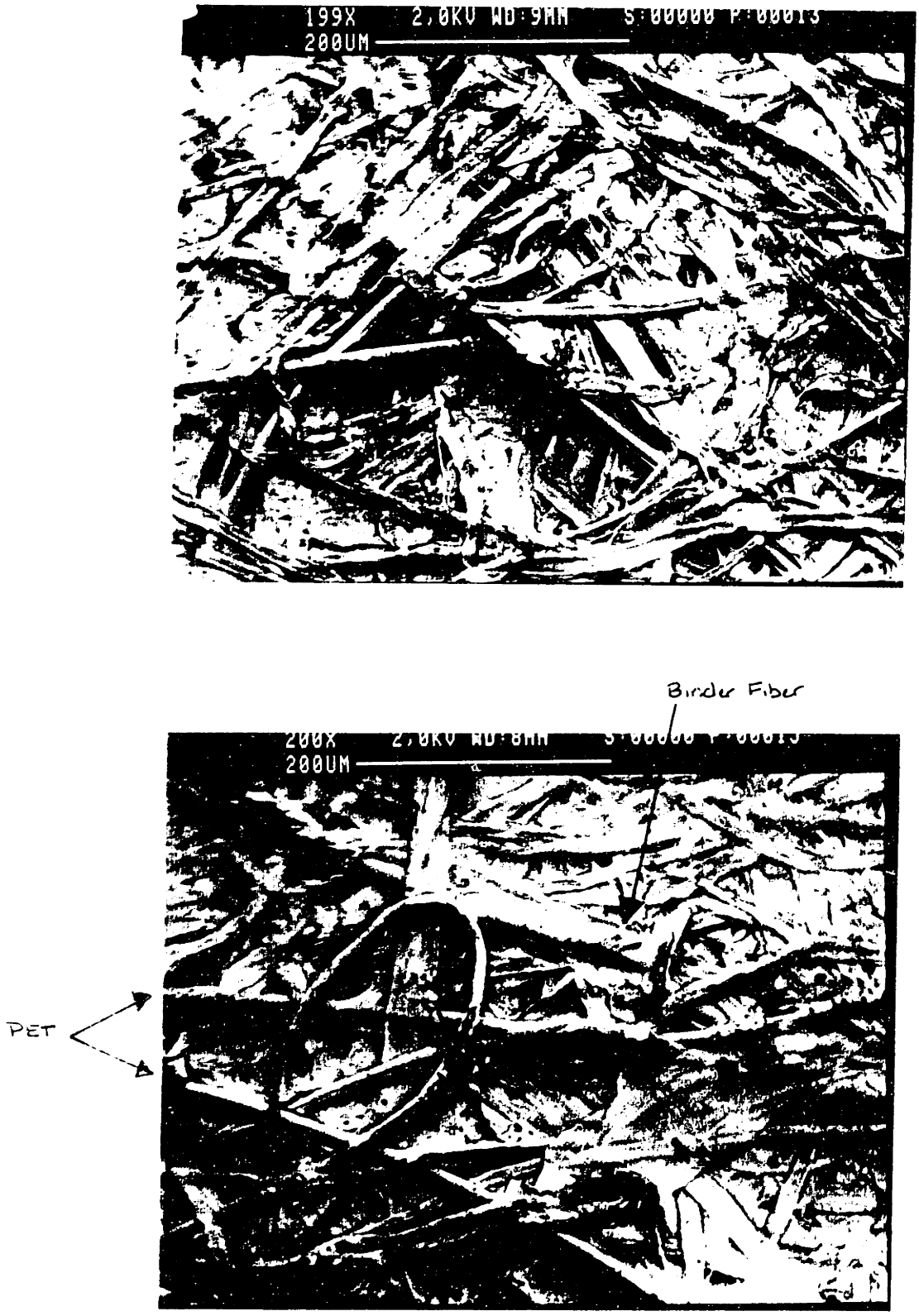

Figure 3.25: SEM photos of binder fiber/PET interaction

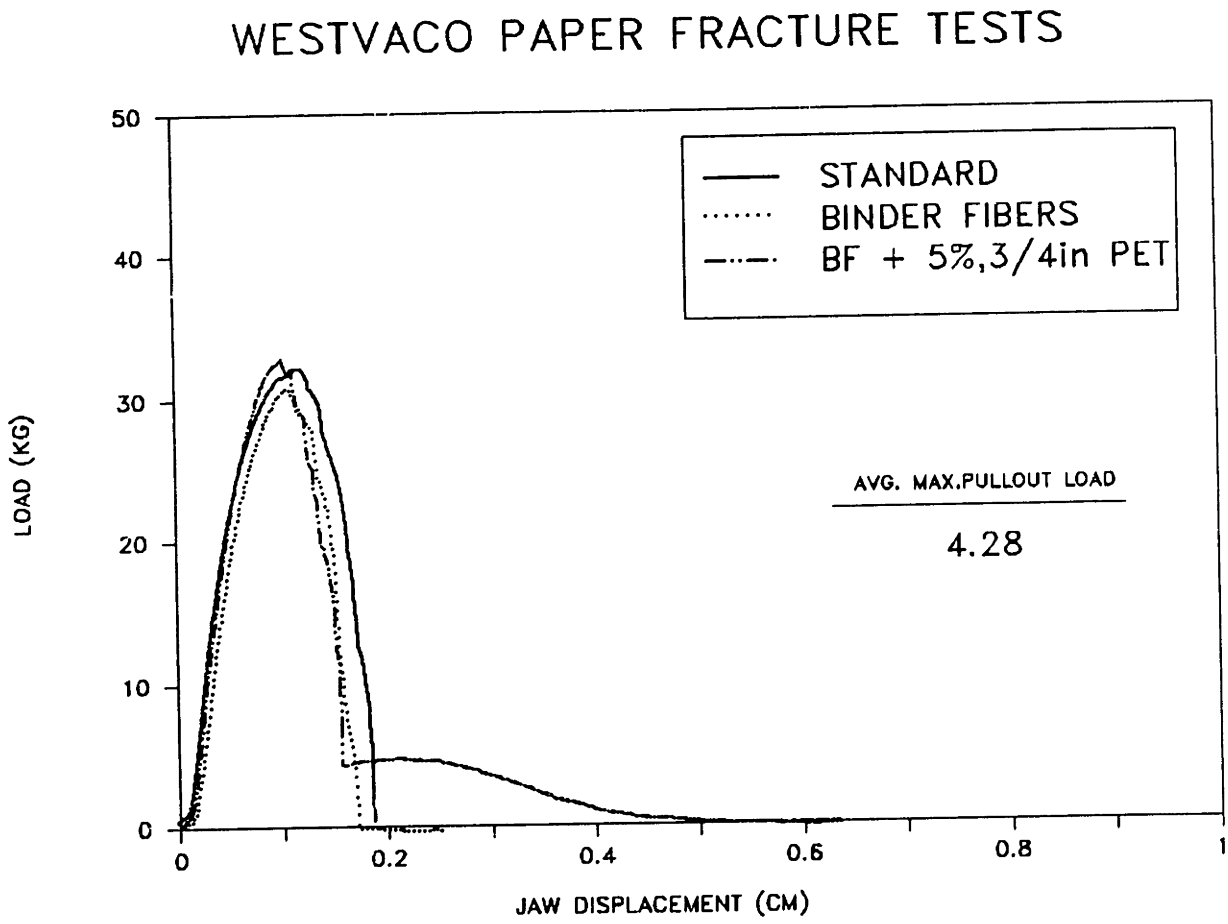

Figure 3.26: Fracture Curve - Binder Fibers

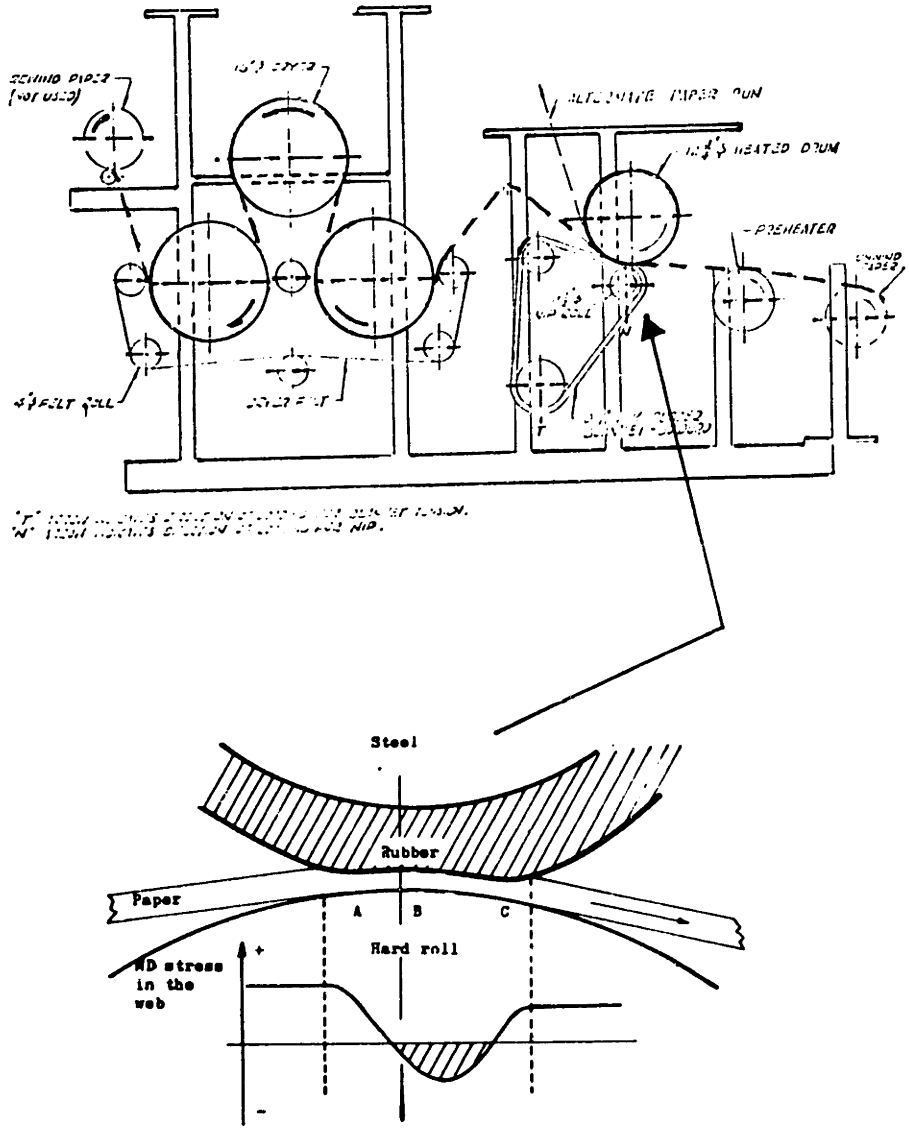

Figure 3.27: Clupak Compaction Process

Table 3.4: Percent Compaction of Clupak Sheets

SERIES	%COMPACTION	%PET	PET LEN (mm)
I	6.8	—	—
I	8.9	5	18
I	8.5	5	6
II	8.0	10	18
III	4.0	—	—
III	6.0	—	—
III	15.0	—	—

is a softer rubber material, buckling of the fibers in the sheet occurs as the sheet emerges from the rollers. This buckling occurs in one direction only, adding material and potential stretch in that direction. By changing the differential speeds, one can get different %compaction. The various %compaction examined were approximately 4%, 6%, 8%, 15%. The exact numbers are given in Table 3.4.

The effect of the compaction is one of softening the curve. The maximum load decreases while the curve itself is flattened significantly with a large extension to failure. Increasing the %compaction serves to flatten the curve even more (Figure 3.28). As can be seen in Figure 3.29, the flattening occurs in a way such that there is a somewhat linear relationship between the maximum load and the maximum strain; decreasing load is tied with a proportional increase in strain. The least-squares linear fit curve shown in the figure has a slope of -64.27 kg/strain and an offset of 26.68 kg.

As stated before, the compaction process results in buckling of both the cellulose and the PET fibers. SEM photos of the compacted sheets show ridges where the cellulose fibers have buckled and bonds have been broken in response to the compaction

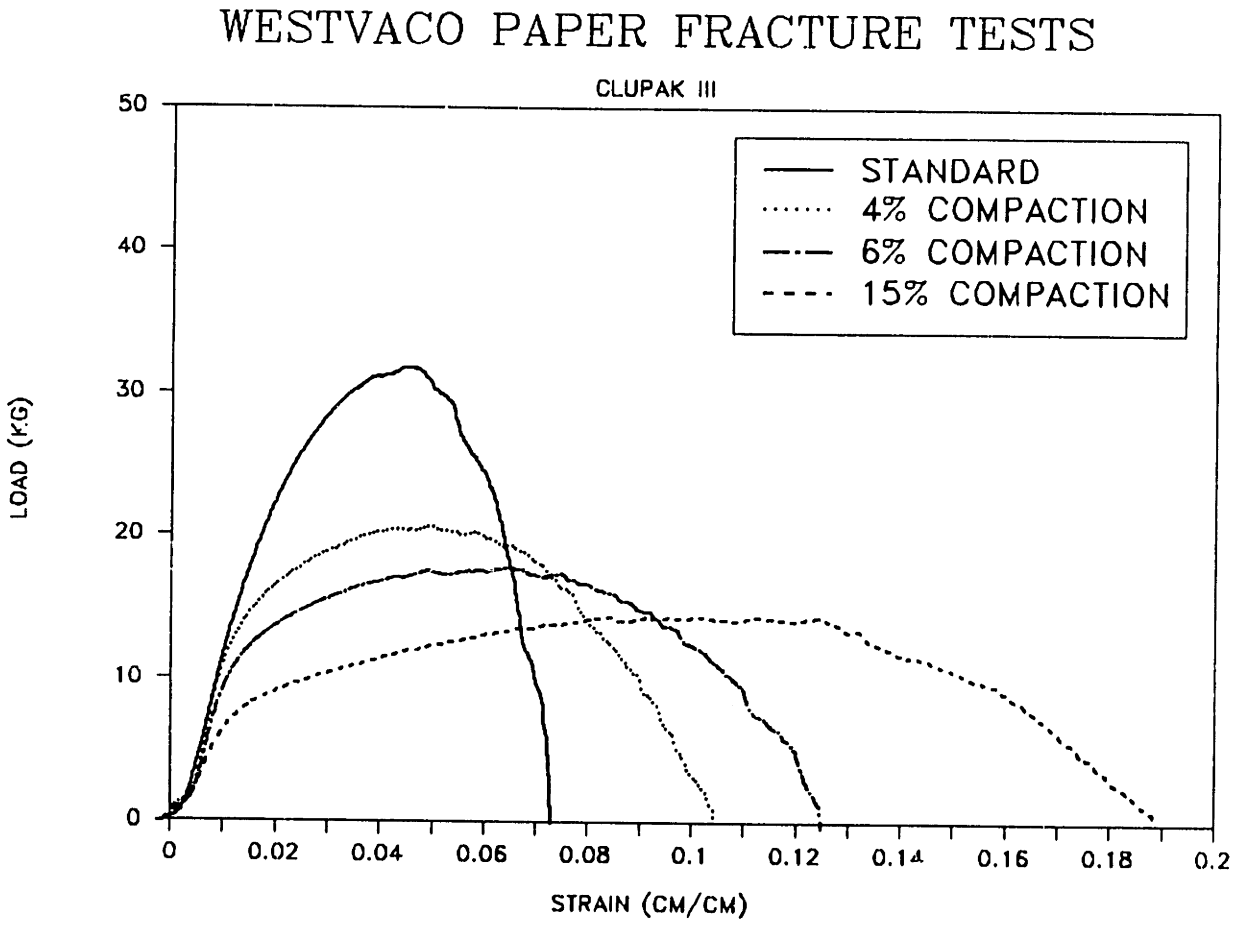

Figure 3.28: Fracture Curve – Clupak Compacted Sheets

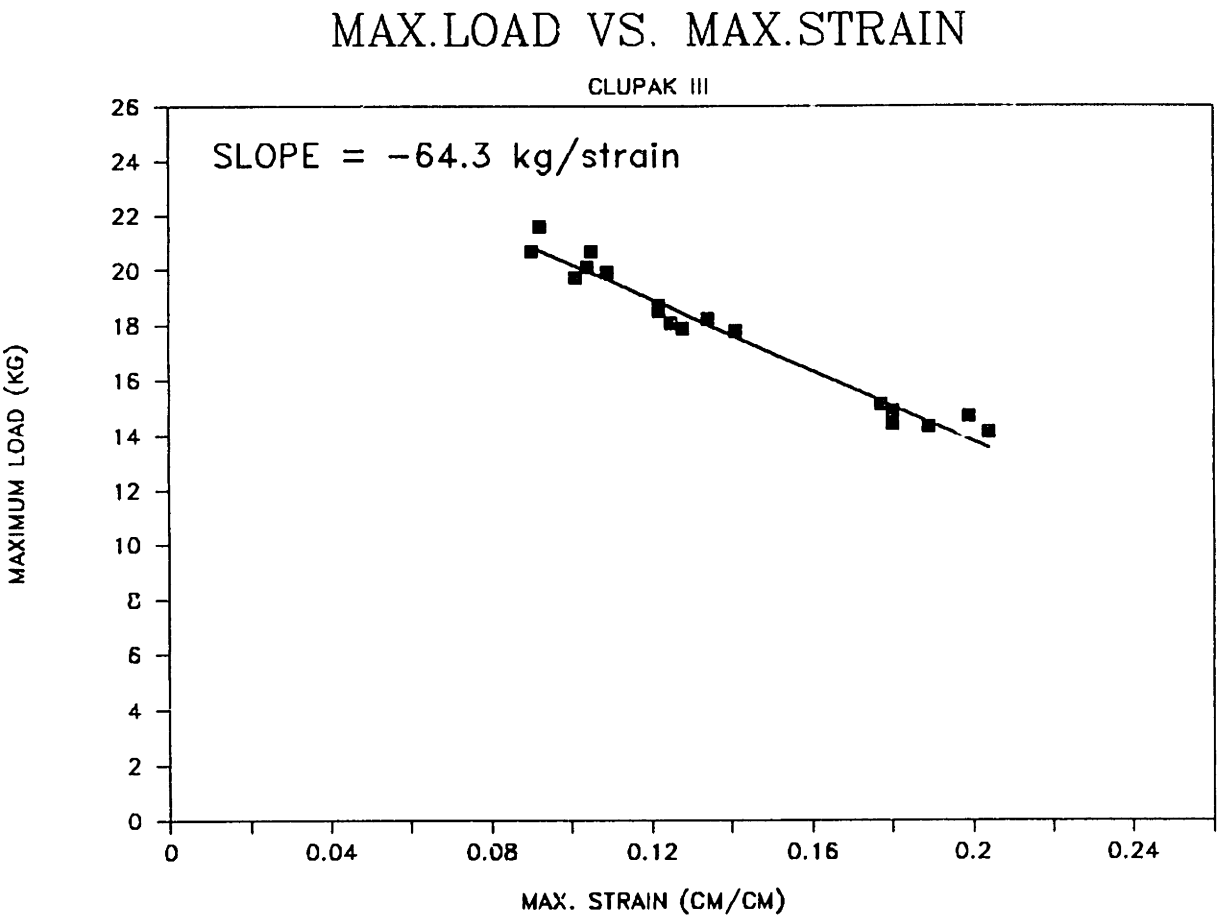

Figure 3.29: Relationship Between Maximum Strain and Maximum Load for Clupak Samples

(Figure 3.30a,b). With respect to the PET fibers, SEM photos of surface PET fibers shows obvious bends in the fibers (Figure 3.31). The bends may act to provide additional mechanical resistance to pullout. The bends do not appear to straighten much during the fracture process. In contrast, some of the cellulose fiber buckles do appear to straighten – i.e., the large ridges tend to flatten out so that the ridge lines are still visible but meld into the rest of the sheet.

Straightening of the cellulose matrix without simultaneous straightening of the PET fibers would indicate that the PET was either being stretched or pulled out. Unfortunately, a look at the fracture curves for these reinforced and compacted samples reveals a slight decrease in the pullout loads (Figure 3.32). Thus, the compaction of the matrix has not increased the mechanical resistance between the reinforcing fibers and the cellulose fibers.

3.6 Effect of Beating

In order to determine whether the increases in fracture energy seen in the compacted samples were a result of bonds being broken and the subsequent "looseness" of the structure, a few samples were produced with fibers which had not been beaten or refined as much. A decrease in beating time reduces the amount of surface area which is available for bonding. The degree of refining is indicated by a Williams slowness test which measures the time it takes for a given amount of water to drain through a given amount of pulp — less refined pulp has faster drainage times. The Williams slowness times for the pulp from each of the three sample series and for the less beaten pulp(LBP) are given in Table 3.5.

SEM photos of the less beaten pulp samples show a slight reduction in degree of bonding between the cellulose fibers (Figure 3.33). The surface is less smooth, and there seem to be more gaps. The fracture curve results indicated that a reduction

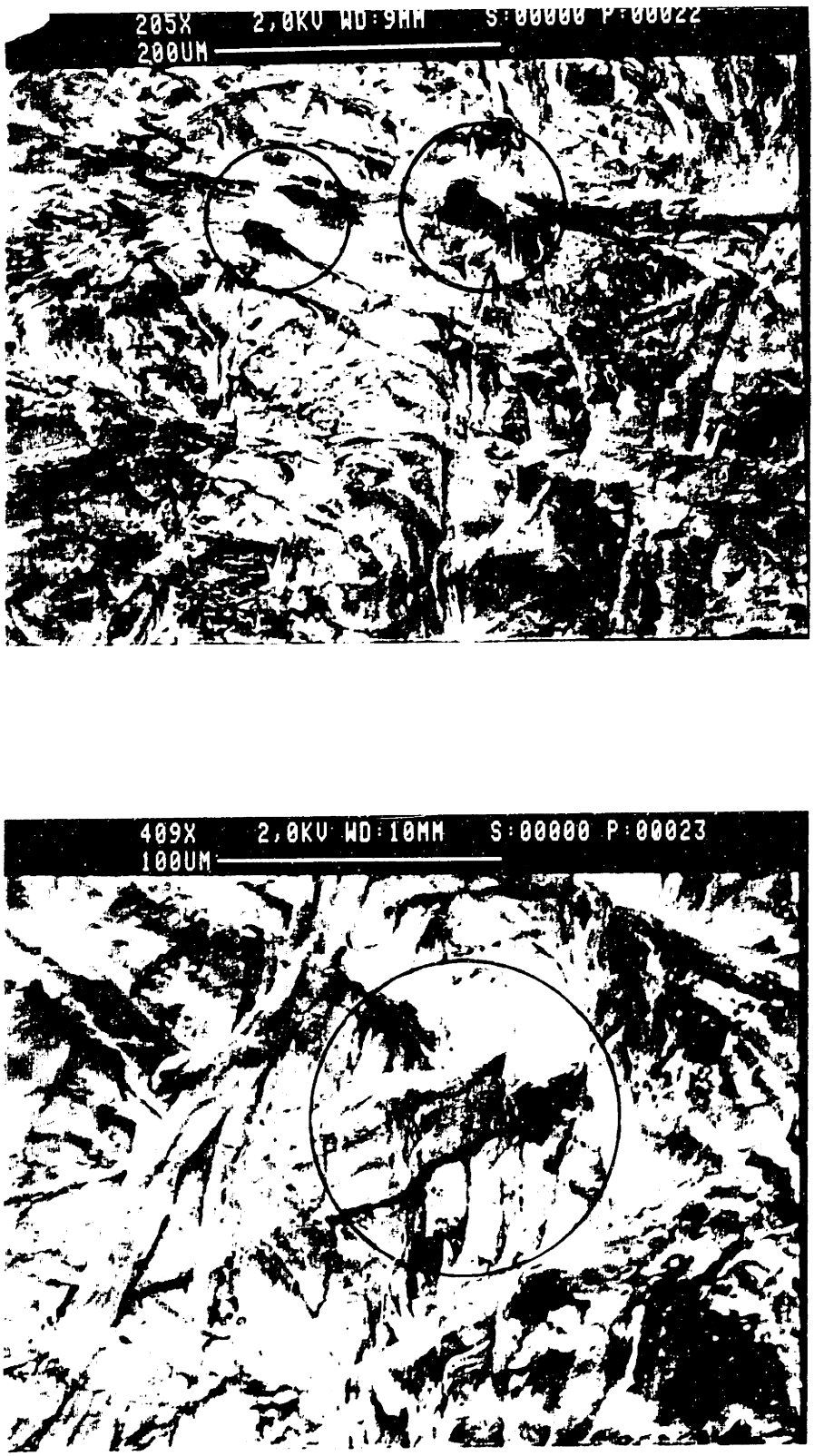

Figure 3.30: SEM photos of Buckled Cellulose Fibers in Clupak Sheets

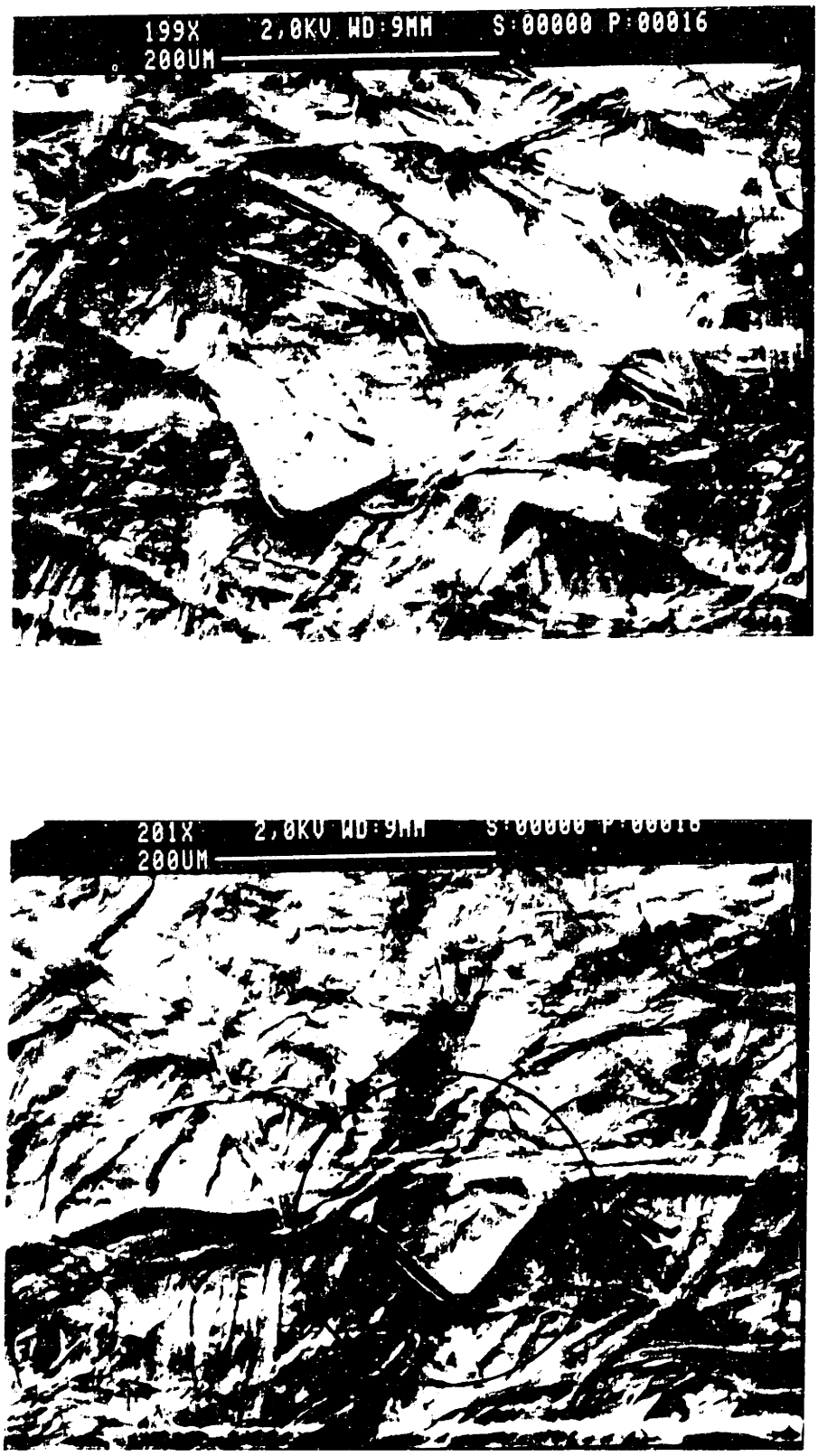

Figure 3.31: SEM photos of Bent PET fibers in Clupak Samples

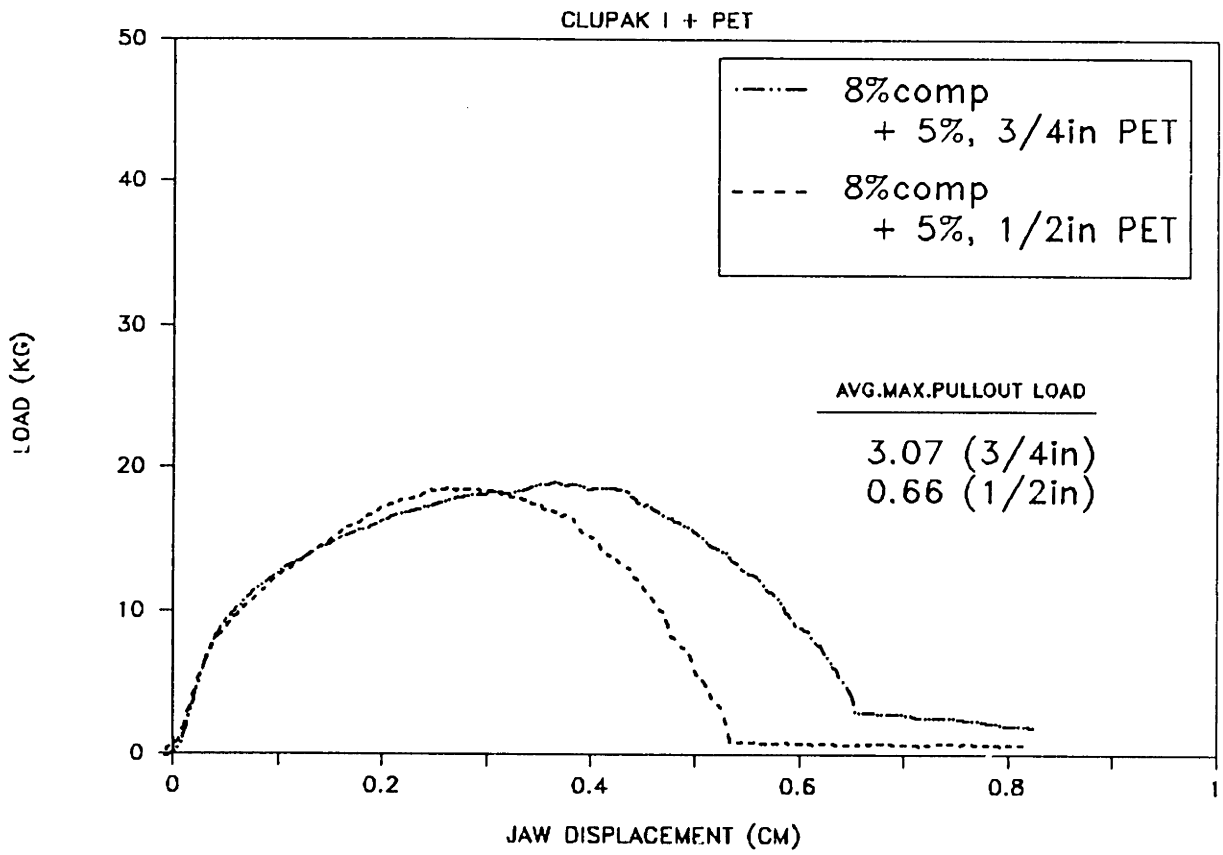

Figure 3.32: Fracture Curve - Clupak + PET

SERIES	WILLIAMS SLOWNESS* (sec)	
	HW†	PINE‡
I	42	14.2
II	40	9.0
II-low	22	9.0
III	40	9.0

* drainage for 3.0 O.D. gms pulp
† HW was beaten in a laboratory Valley beater
‡ Pine was not beaten

Table 3.5: Degree of Refining of Test Samples

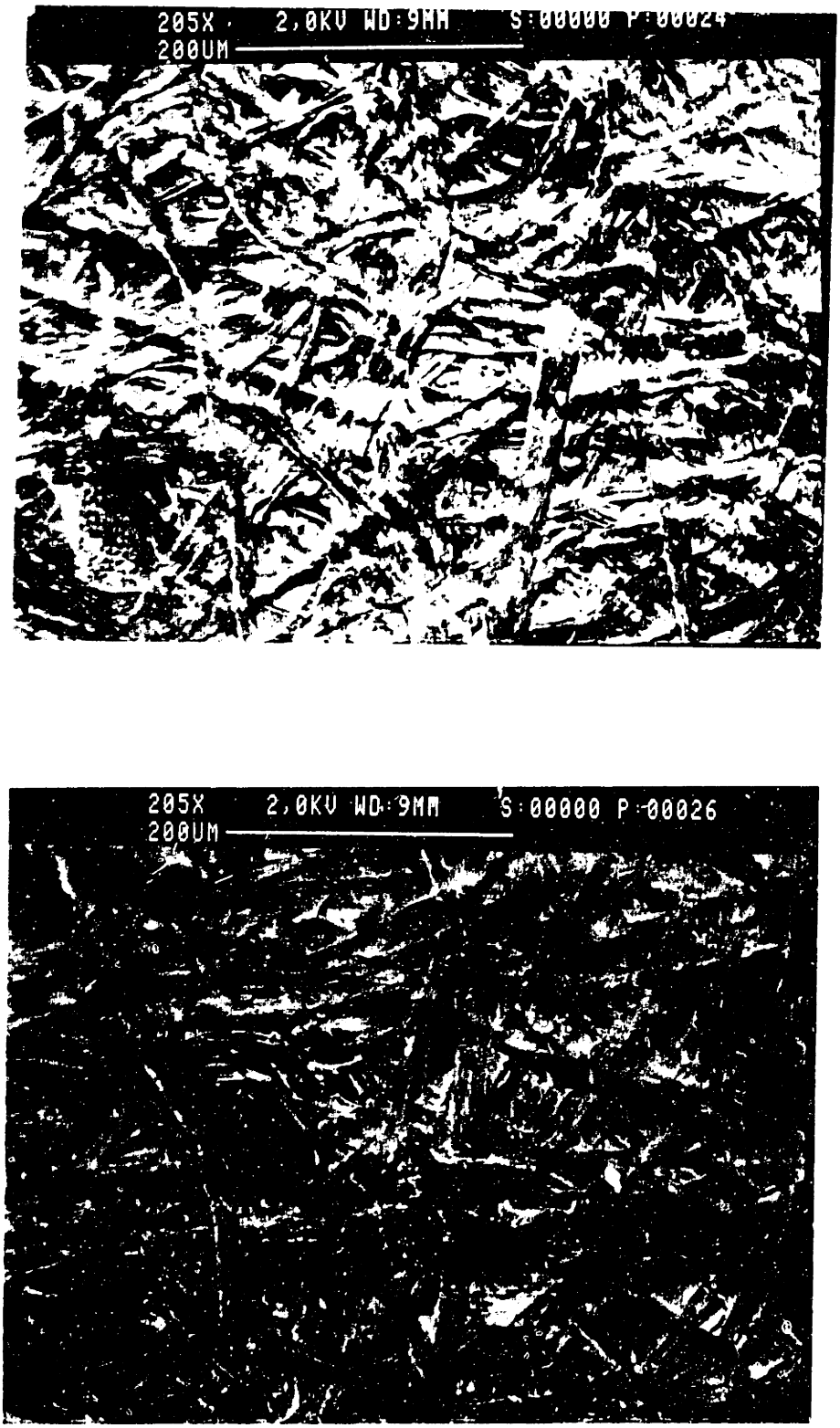

Figure 3.33: SEM photos - Less Beaten Pulp Samples

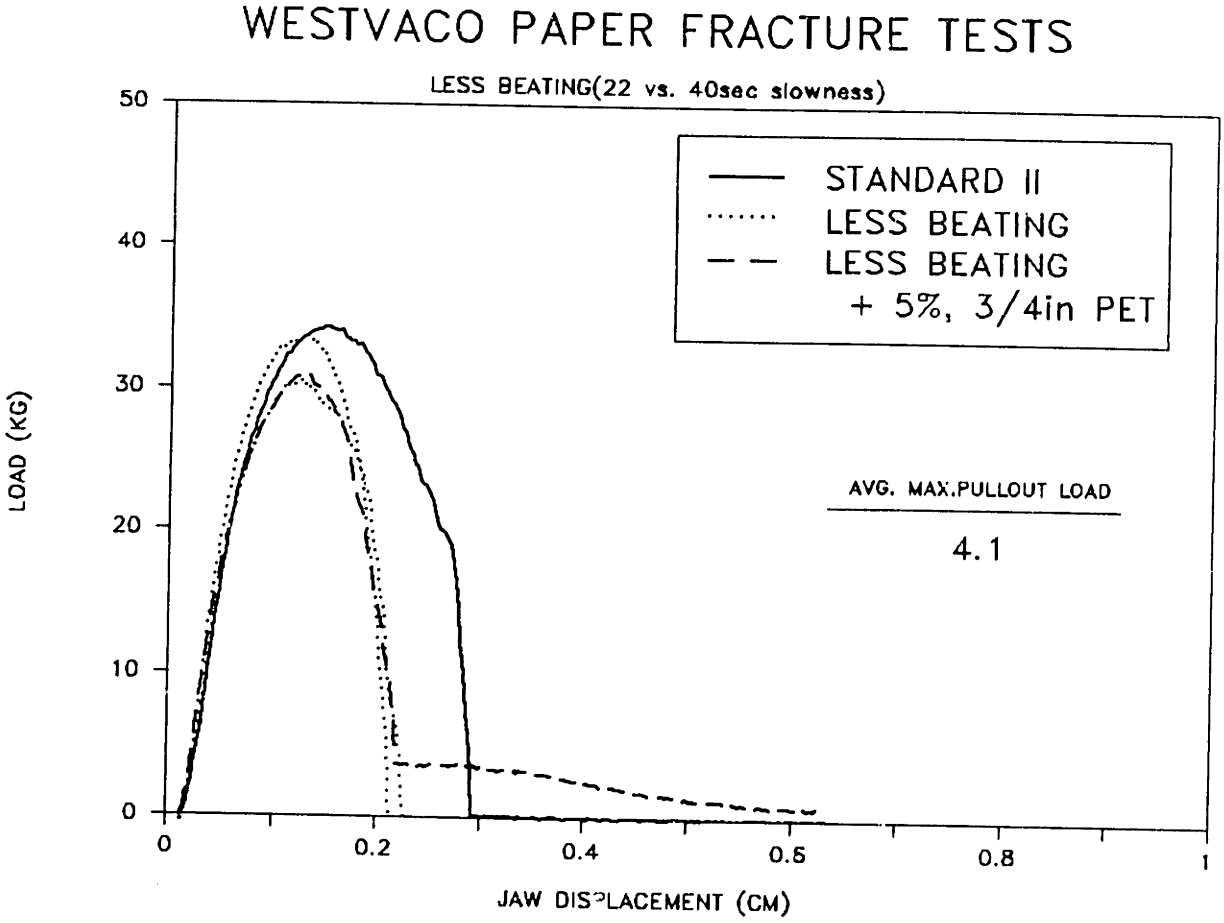

Figure 3.34: Fracture Curve – Less Beaten Pulp Samples

in number of bonds alone was not responsible for the increase in fracture energy values for the compacted samples. The LBP samples had lower crack propagation and pullout loads and lower elongation to break values than the standard sheets (Figure 3.34).

3.7 Conclusion

In terms of this study, the different fracture behaviors exhibited here turned out to be very useful for comparison with the results from the computer model. This will

be discussed in Chapter 6.

From this experimental study, it is obvious that the fracture behavior of paper is affected by a complex combination of factors. We can organize these factors into two main groups — fiber characteristics (e.g., length, %vol, modulus) and bond characteristics (e.g., strength, uniformity) — but within these two groups there are a multitude of variations. Also, these two groups are by no means independent. For example, beating will break down a fiber, reducing its length in some cases, but it will also increase its surface area for bonding.

What we can conclude from this particular set of results is that factors affecting bonding are critical to the fracture behavior. We can significantly change the fracture behavior of any given sheet by applying softer or stiffer binders. If the goal is to improve fracture resistance, a softer binder seems to be the best direction of attack. The optimal bond behavior is resistance just up to but not equal to or exceeding the point of fiber failure.

However, a less intrusive solution appears to be increasing the mechanical bonding in the sheet rather than the chemical bonding. This includes adding longer fibers which can become entangled to some extent with the other fibers. This is seen with the PET fibers that were added. Unfortunately with these longer fibers, dispersion tends to be a problem. Adding a finish to make the fibers hydrophilic definitely improves dispersion, as seen with the Papermaker Staple fibers; even with these fibers, however, positive effects prior to complete matrix failure were limited.

Although problems with dispersion hindered the contributions of the bicomponent and binder fibers, the key to improving fracture resistance without changing the entire nature of the sheet seems to lie in this direction; that is, with improving the interaction between the reinforcing fibers and the cellulose fiber matrix. While these fracture tests have given us a macroscopic composite picture of the factors involved,

we need to go down to a more microscopic level to truly understand what actions are occurring during fracture. The next few chapters will attempt to dissect and inspect some of these details in order to add to our knowledge of how to model and improve this fiber-fiber interaction.

Chapter 4

Material Characterization

Since we are trying to understand how a particular material fractures, it becomes important to characterize the material we are working with – specifically, its tensile behavior and distinctive failure features. In addition, the model is based on knowing certain material parameters, including elastic modulus, plastic modulus, breaking strain, and yield stress. Both of these requirements can be met by a series of basic tensile tests on the different types of paper.

4.1 Fracture Surface Observations

A clue to the differences in fracture behavior discussed in the previous chapter lies in the appearance of the fracture surface of the various materials. SEM photographs of the fracture surfaces of the different paper types failed in tension display a full range from total fiber pullout to total fiber failure.

Most distinctive is the fracture surface of the TR-407 Binder Sheet (Figure 4.1). The edge is very clean, with very few indications of fiber pullout. The TR-407 Binder

sheets behave as if they were not composed of individual fibers. Apparently, the binder was strong enough to prevent the cellulose fibers from separating, and, as a result, the fibers themselves failed. This was also true for many of the PET fibers in the reinforced TR-407 Binder sheets.

In contrast, the fracture surface of the softer binder, TR-934, had a very different appearance (Figure 4.2). There were significant numbers of pulled out fibers, although still not as many as in the Standard samples (Figure 4.3). This agrees with the similarity in fracture curves for these two samples. However, even with the softer binder, there was still more fracturing of fibers than in the Standard samples.

At the other extreme, the Clupak samples exhibited almost entirely fiber pullout for the fracture surface (Figure 4.4). While the difference between the Clupak and Standard fracture surfaces are not drastic - both display mostly fiber pullout - it should be noted that the fibers in the Clupak sample appear to be very independent, while the fibers in the Standard sample appear to be more attached in clumps with some signs of fiber failure.

Interestingly enough, increasing the %compaction to 15% does not result in even more pullout (Figure 4.5). Perhaps, beyond a certain point, the compaction process damages the fibers to the extent that they are severely weakened and fail easily, rather than just crimping the structure.

The next photograph show the fracture surface of the less beaten pulp samples. As expected due to the poorer bonding, the LBP sample has many pulled out fibers (Figure 4.6), and is probably somewhere in between the Standard sample and the Clupak sample in this regard. However, there is a distinctive difference in the fracture surface of the LBP samples; the surface path is much rougher. Rather than having a relatively straight path with fibers extending from that path, the LBP path is strewn with clumps of pulled out and fractured fibers. This is also seen in the bicomponent

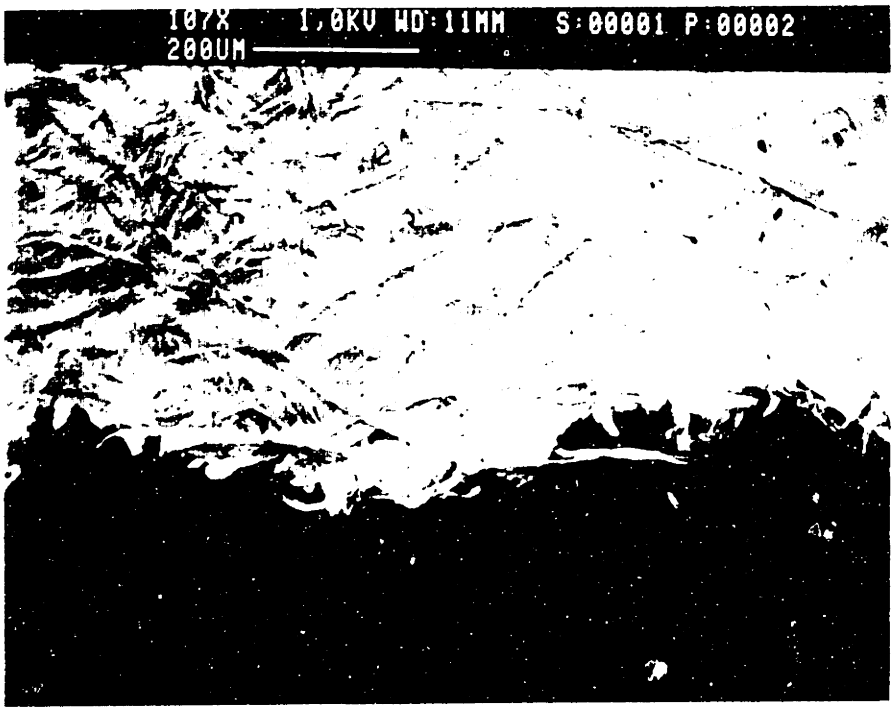

Figure 1.1: SEM photo — TR-107 Binder (Fracture Surface)

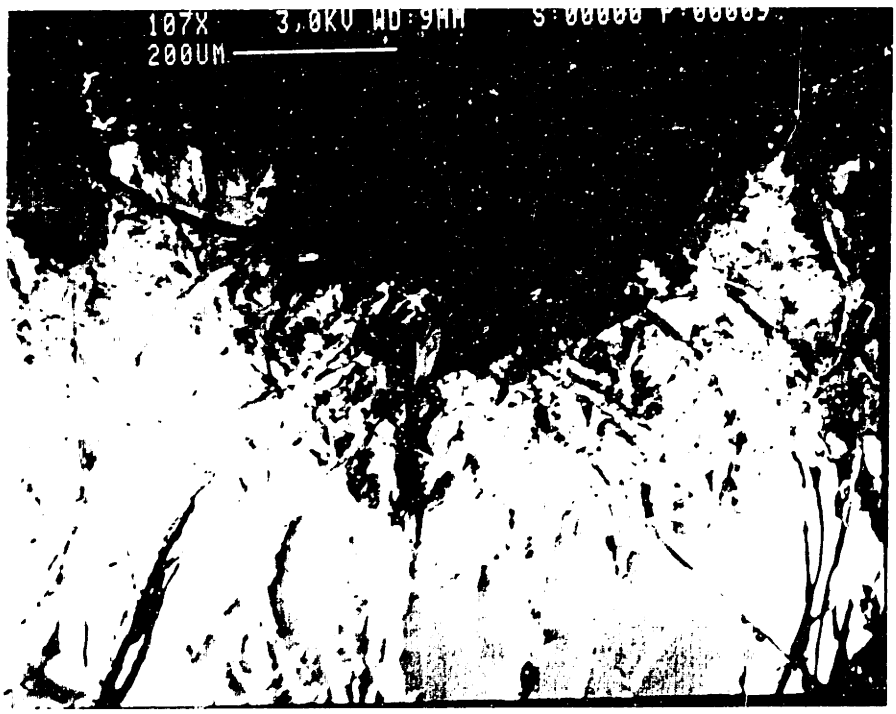

Figure 1.2: SEM photo — TR-934 Binder (Fracture Surface)

Figure 4.3: SEM photo - Standard (Fracture Surface)

Figure 4.4: SEM photo - 8% Clupak (Fracture Surface)

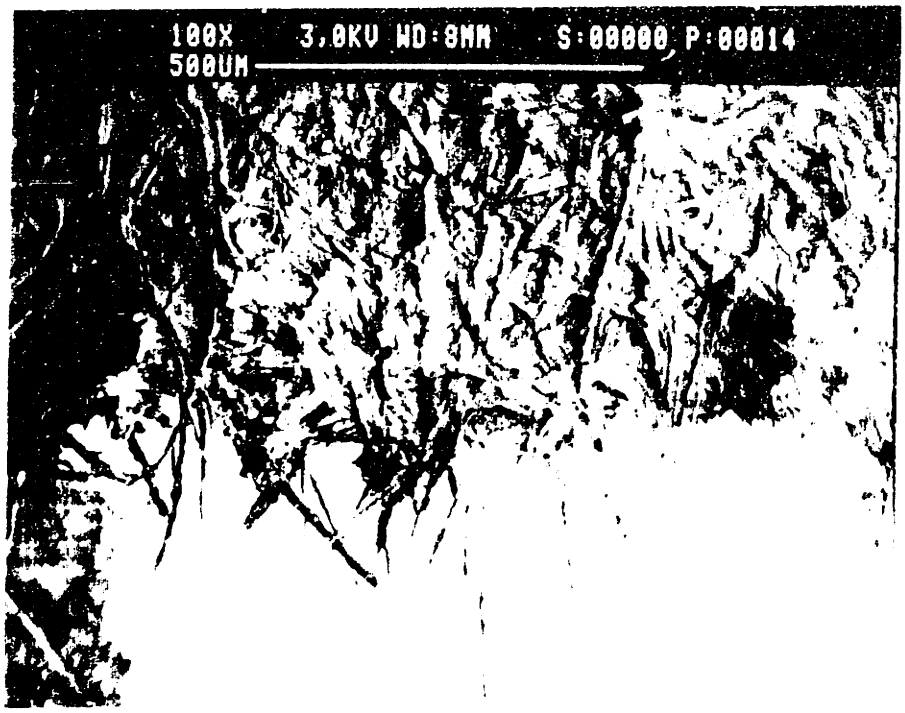

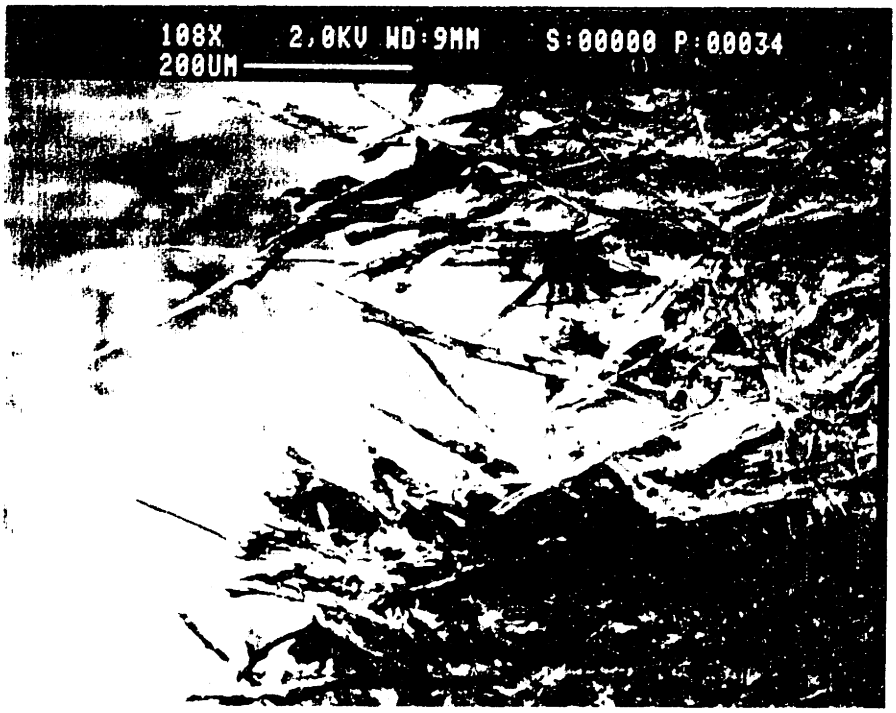

Figure 4.6: SEM photo — Less Beaten Pulp Sample (Fracture Surface)

samples (Figure 4.7), indicating some relationship to the degree of uniformity of the sheet.

The question of an anisotropy effect comes into play with nonrandomly oriented sheets. An examination is made of the fracture surfaces of two mildly anisotropic materials — the Clupak sheets loaded in the direction of compaction and the cross direction and copy paper sheets loaded in the machine direction. Figures 4.8a,b show the fracture surfaces of the 6%Clupak sample in both directions. While the sample is obviously much stiffer when loaded in the cross direction, the fracture surfaces do not appear to differ much.

Similarly, for the copy paper, the fracture surface had a mixture of fiber pullout and fiber fracture, with more fiber fracture than the Standard sheet, but not any great differences when compared to the more isotropic materials (Figure 4.9). The fibers of the copy paper tend to be much more smoothed together, and it is probably reasonable to assume that some type of filler or coating has been applied to the sheet.

In general, we see in the fracture surface observations that stronger bonds lead to fiber fracture and cleaner fracture surfaces. This also leads to a behavior more consistent with continuum fracture mechanics. Thus, we would expect the model to work better with more highly bonded materials. As the bonding becomes looser – in the Clupak and LBP samples, for example – the importance of matrix fiber pullout is augmented, adding another component to the fracture curve.

Figure 4.7: SEM photo – Poorly dispersed bicomponent sheet (Fracture Surface)

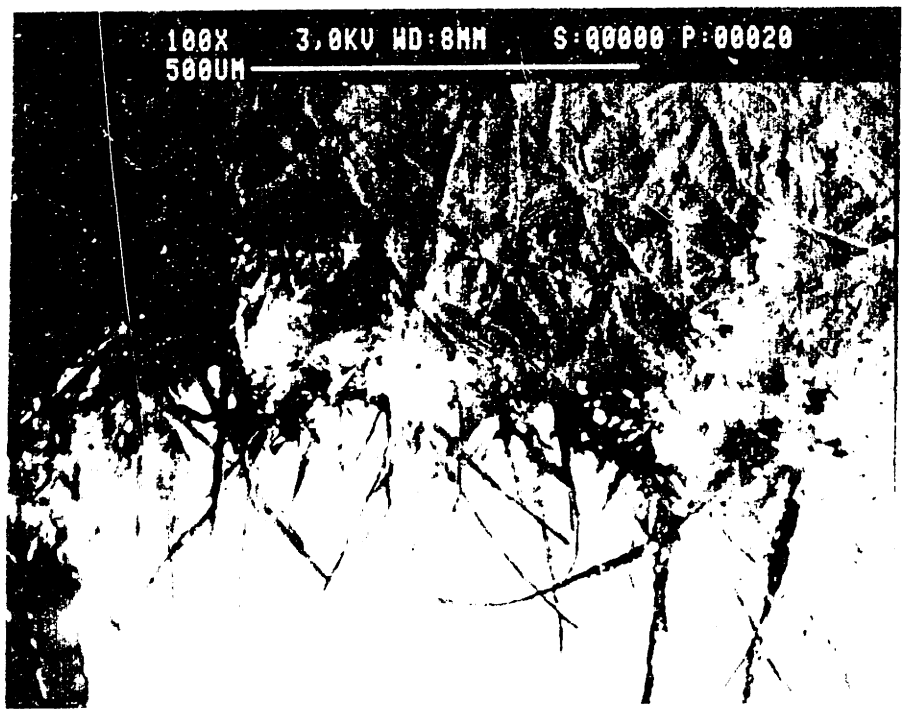

(a)

(b)

Figure 4.8: SEM photo 6% Chipak loaded in (a) direction of compaction and (b) cross direction

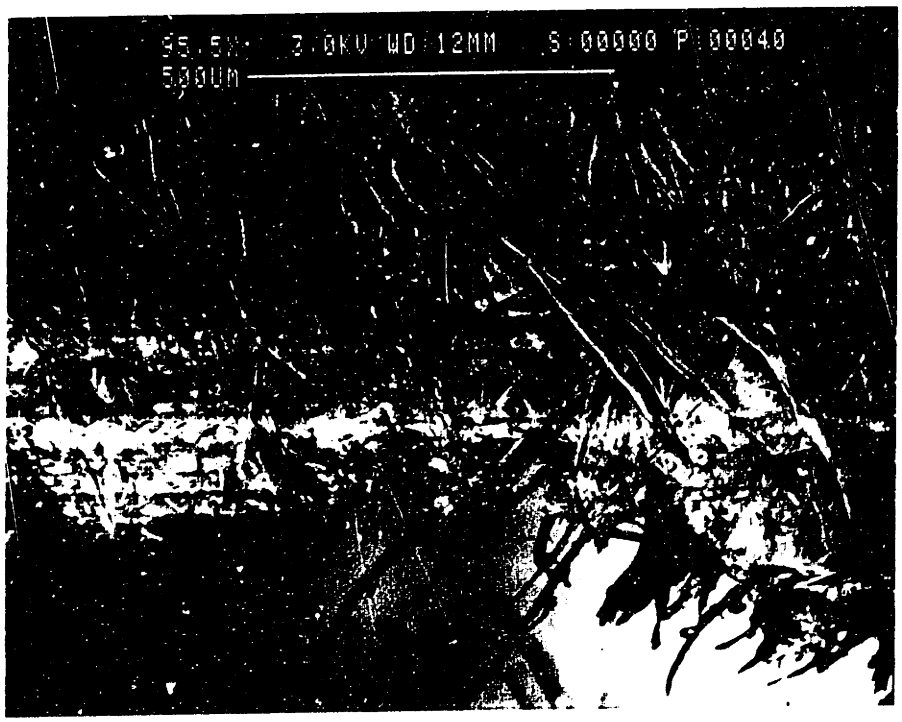

Figure 4.9: SEM photo – Copy Paper (Fracture Surface)

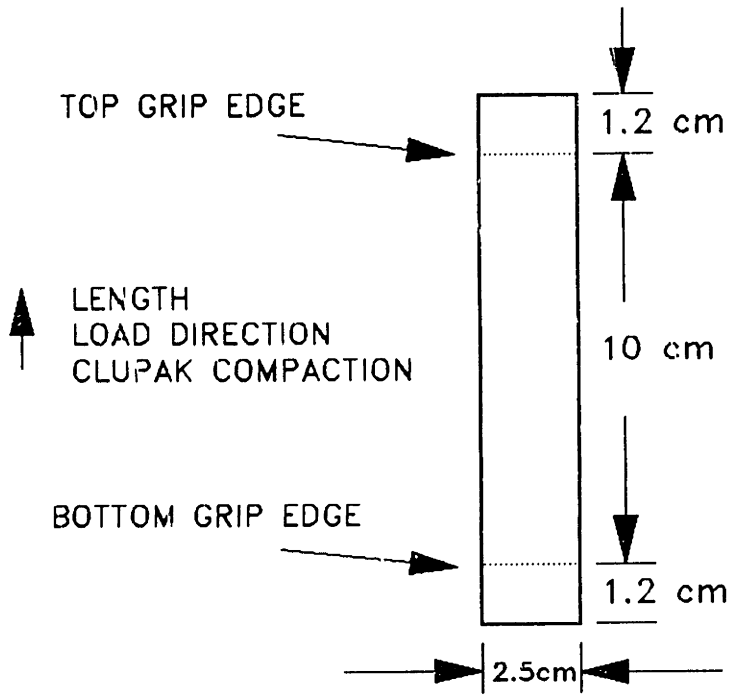

Figure 4.10: Cyclic Test Specimen Dimensions

4.2 Cyclic Behavior

In order to model the fracture behavior of paper, it seemed logical to first identify the tensile behavior of the material, since this has an effect on the behavior prior to crack propagation and in a global sense to the response of the material to tensile loads.

Therefore, cyclic tensile tests were run on 10cm x 2.5cm samples (Figure 4.10). Testing is done at a constant displacement rate of 0.05 in/min. The samples were cut and allowed to condition at $70°C$ and 70%RH for 20 hours prior to testing. This humidity is high, but the results can be qualitatively analyzed, taking into account the expected softening of the material due to the high humidity.

Typical results for each of the four primary paper types are shown (Figures 4.11-4.14). A few samples are run to failure in one cycle in order to get a typical curve for the monotonic loading condition. This curve is displayed as a dotted line. Several samples are then run cyclically. Each sample undergoes about 5-10 cycles prior to failure, with each cycle reaching a slightly higher load than the previous cycle. A

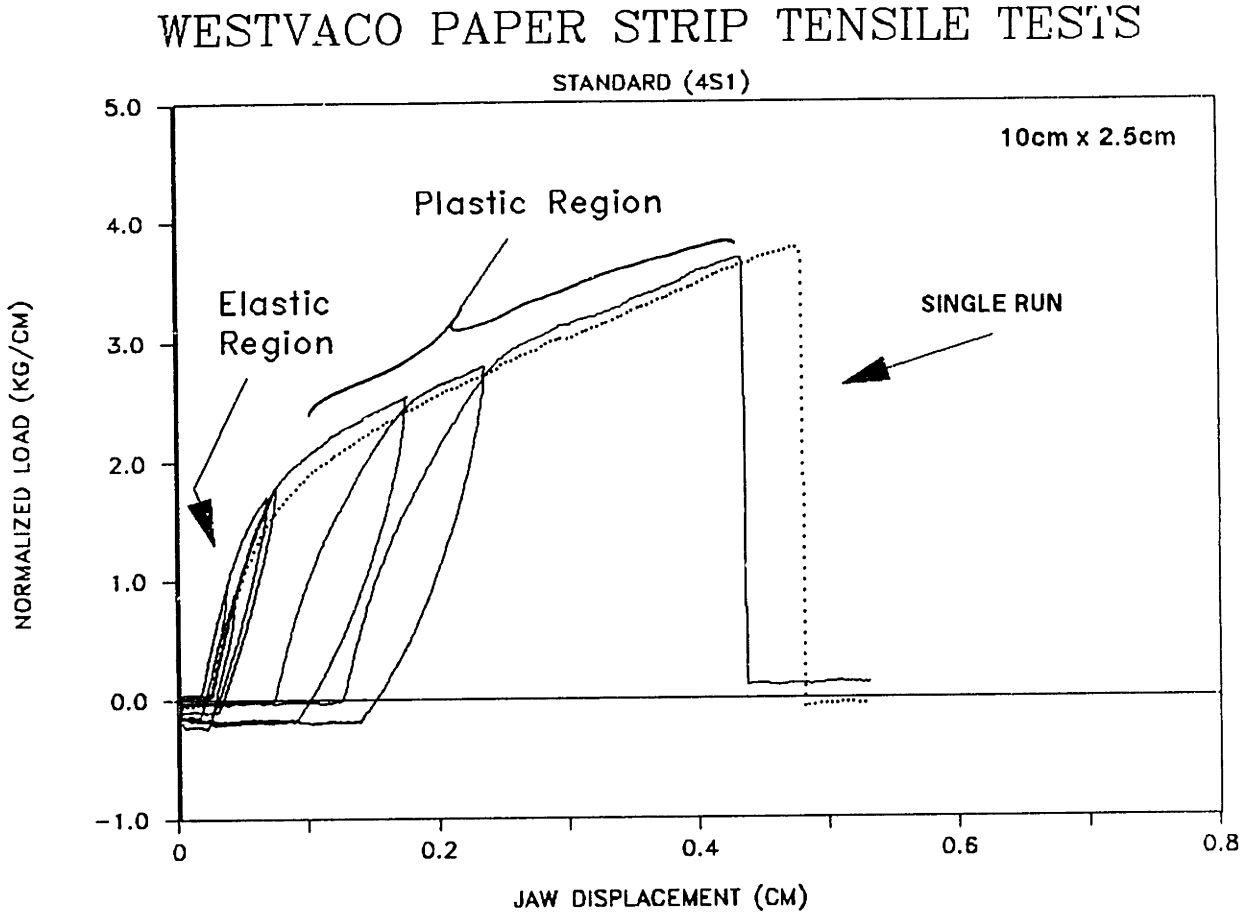

Figure 4.11: Cyclic Test Curves – Standard

typical set of cycles is indicated by the solid line.

Cyclic tests on strips of each of the four different paper types have shown an initial elastic region where the load-displacement curve reversibly follows the same path. Beyond a certain point, typified by a bend in the load-displacement curve, the behavior of the material becomes significantly altered – displaced from the previous load-displacement path but retaining essentially the same initial modulus. Once the maximum load of the previous cycle is reached, the behavior thereafter follows a curve consistent with monotonic loading, much as occurs in elastic-plastic metals. While this plastic region is not perfectly plastic, it is reasonably linear and can be represented by a "plastic modulus".

Note that in the figures, the return of the curve to zero displacement indicates a return to the original gage length. Once plastic deformation occurs, the sample

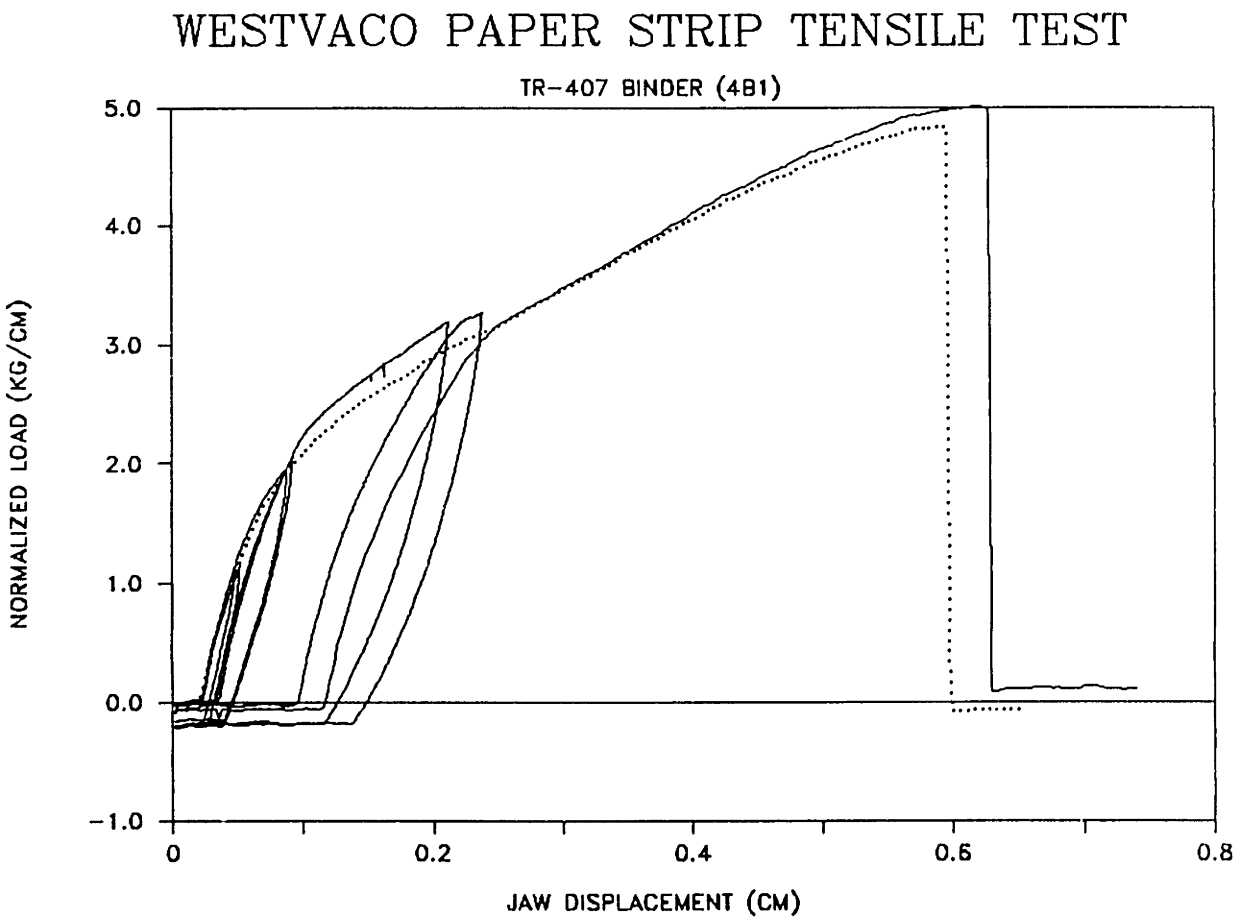

Figure 4.12: Cyclic Test Curves – Binder

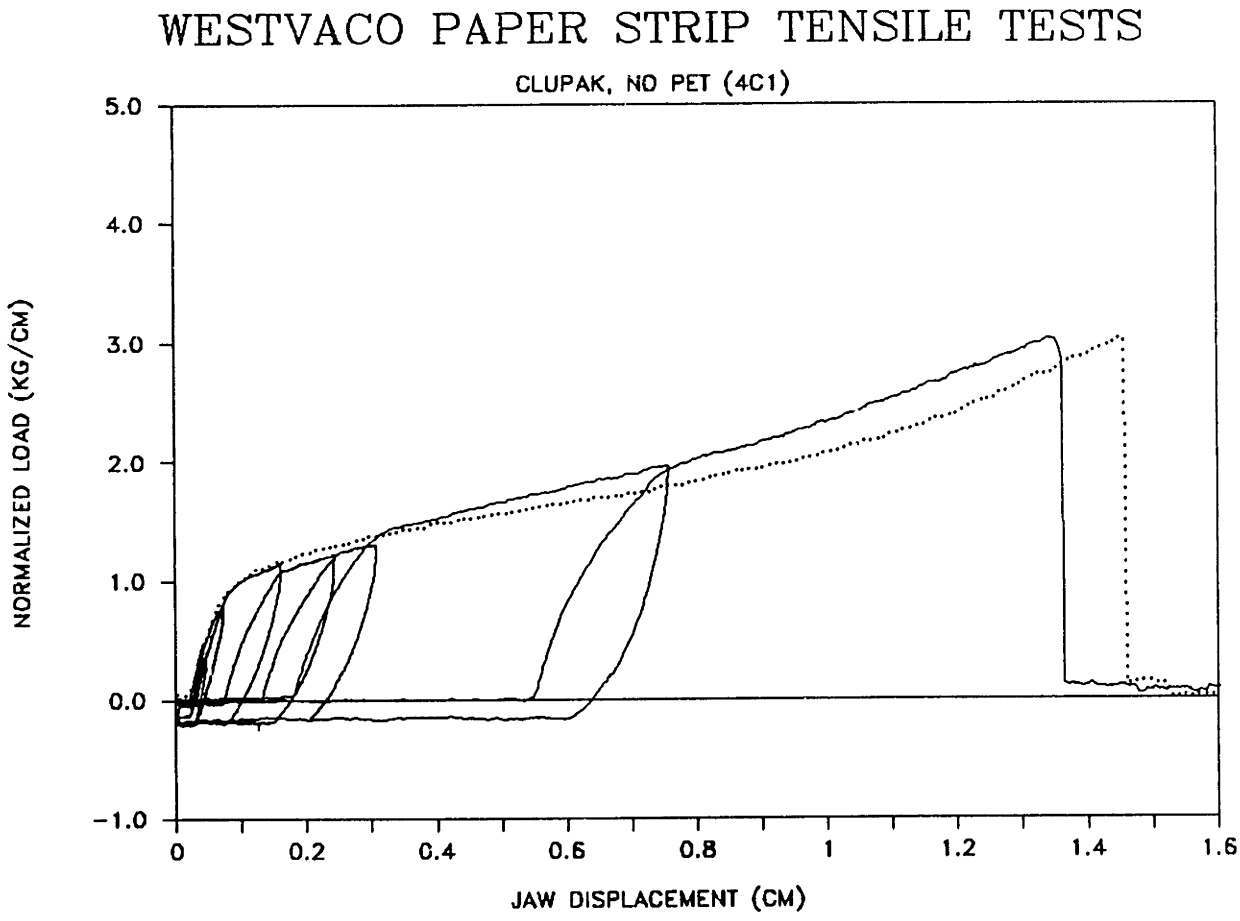

Figure 4.13: Cyclic Test Curves – Clupak

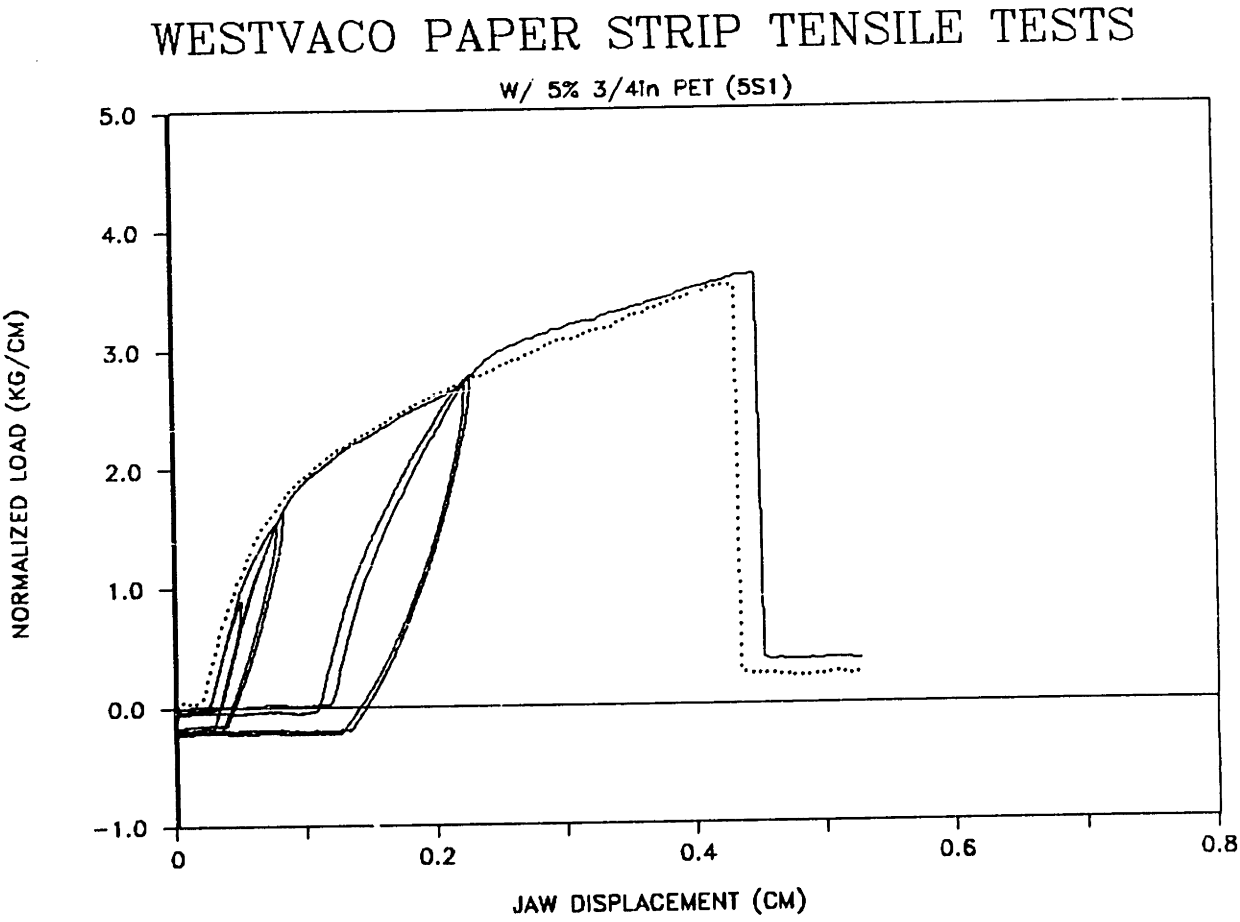

Figure 4.14: Cyclic Test Curves – PET

has elongated irreversibly and thus is actually buckled or in slight compression at the original gage length. This is confirmed visually and accounts for the compression indicated in the cyclic curves.

The plastic deformation is believed to be due almost exclusively to intra-fiber deformation rather than inter-fiber bond breakage. According to reports in the literature [44], the drawing out of microcompressions in the cell wall as a result of shearing in the interfibrillar structure is the main contributor to plastic deformation. This is supported by the observation that changes in bond strength alone only affect the endpoint of the elastic-plastic curve and do not change the shape or magnitudes.

SEM photos comparing the surfaces of a strip subjected to loads in the elastic region only and a strip subjected to loads in the plastic region but prior to failure are shown in Figure 4.15 and Figure 4.16, respectively. There is a sense in the photo of the strip strained in the plastic regime that within the fibers themselves, ligaments of drawn material have formed or fibrils have become exposed. In any case, there is an observable change in the plastically loaded sample, while none exists for the elastically loaded sample.

The elastic-plastic behavior of paper indicates that failure in paper is not generally brittle. That is, there is a damage zone or plastic zone that forms prior to rupture. The formation of a damage zone consumes some of the energy put into the system, thus increasing the fracture resistance of the material. More discussion of this damage zone is given in the next chapter.

When comparing the monotonic tensile test curves (Figure 4.17), unmistakable differences are observed. Most noticeable is the Clupak curve, which has a very short elastic section and a very long plastic section. Thus, we can characterize the material behavior as having a low yield stress, a low plastic modulus, and a high failure strain. Somewhat surprising is the high failure strain of the Binder sample with respect to

Figure 4.15: Standard strip in elastic region

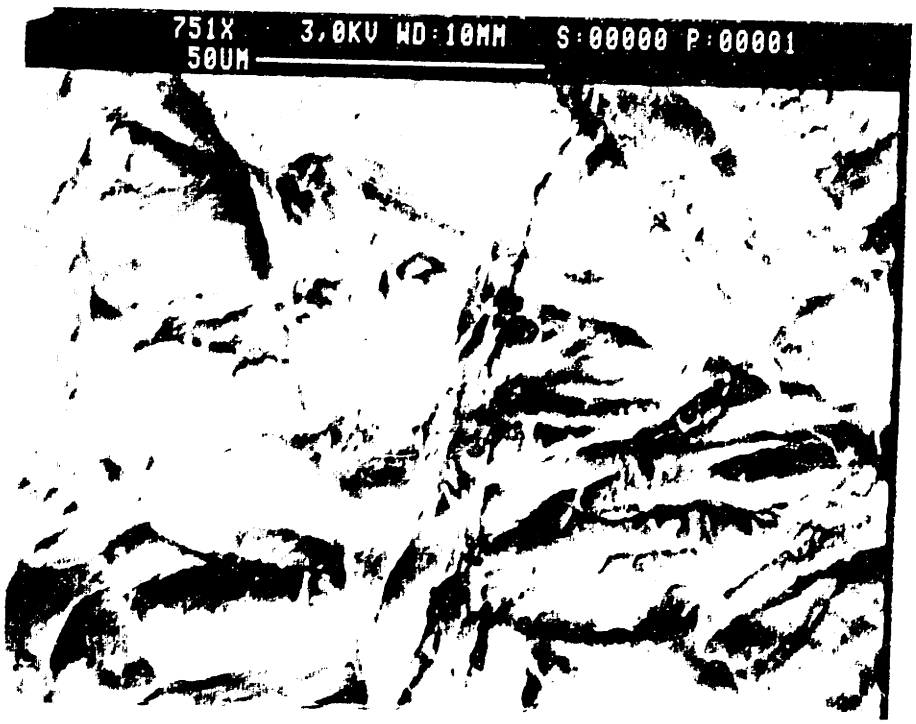

Figure 4.16: Standard strip in plastic region

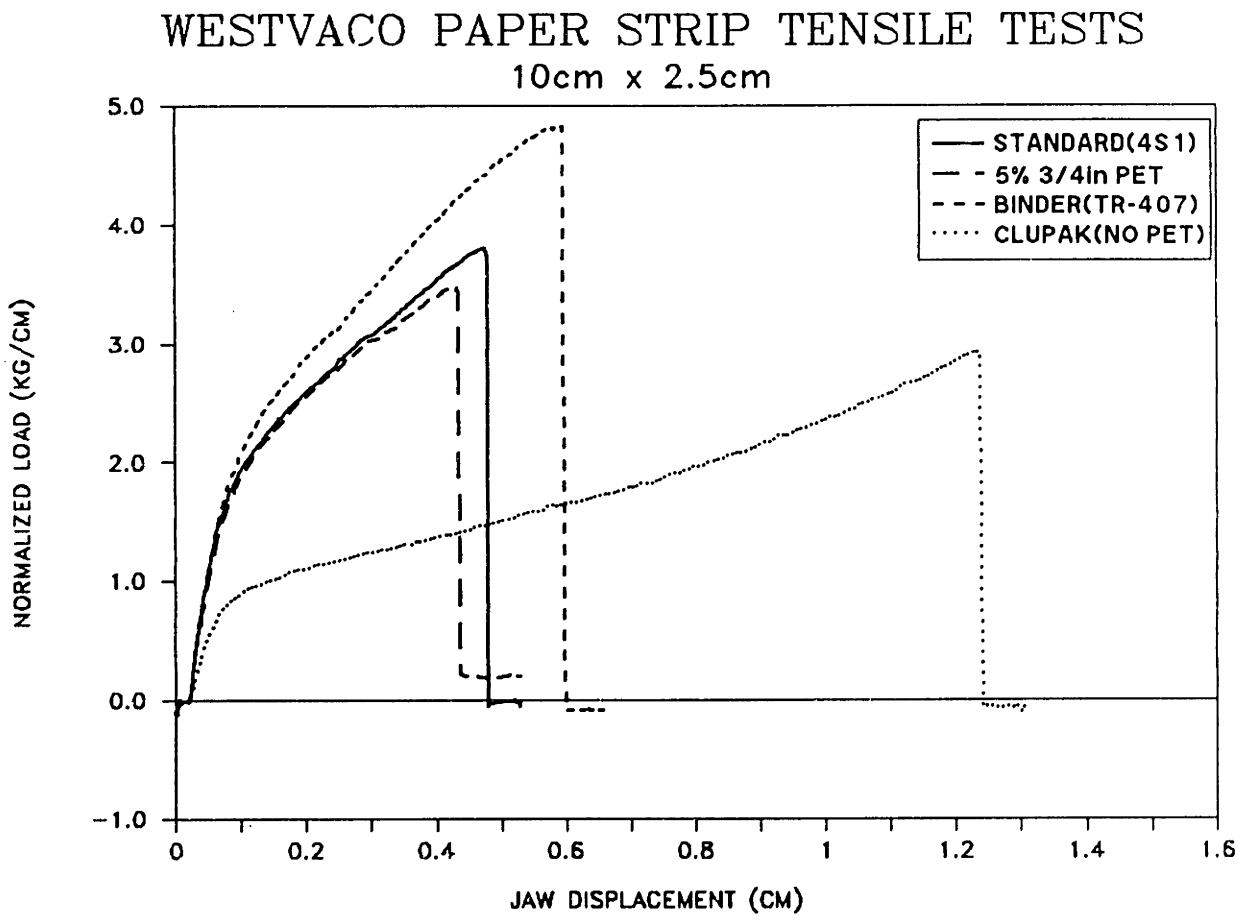

Figure 4.17: Comparison of Tensile Curves

the Standard sample. It seems that the Binder sample withstands loads (and strains) better when they are distributed more evenly over a larger region rather than being concentrated at a crack tip. Not unexpected, however, is the high failure load and stiffer moduli exhibited by the Binder sample. And, as in the fracture tests, the PET curve is slightly below the Standard curve beyond the elastic region.

The reason for not using these test results as input to the model is that they are averaged results over the entire 10cm x 2.5cm strip. We would expect the weakest point in the strip to govern the failure. In long samples, the distribution of these weak point values is generally lower and narrower than for shorter samples. For modeling the fracture of the sheet, however, we have assumed that a crack already exists, and that propagation of the crack is a result of failure of the material directly ahead of the crack tip. Therefore, it is important to know the features of the material inhabiting the crack tip region rather than the average behavior of the entire sheet. This leads us to the statistical tests described in the following section.

4.3 Statistical Behavior

In order to generate the model results, some information about the material is needed. This includes material parameters such as elastic modulus, plastic modulus, breaking strain, and yield stress. To account for the discreteness of the material, these parameters are not represented as single values; rather, they are described by probability density functions, indicating the expected variations from area to area due to factors such as fiber orientation, fiber strength variation, and bond strength variation. In a very uniform sheet, it is expected that the spread of values would be small. However, even in a randomly oriented sheet there may be local nonrandom orientations.

Ideally, these pdf's would come directly from the basic fiber and bonding components. Unfortunately, because it is very difficult to test individual papermaking

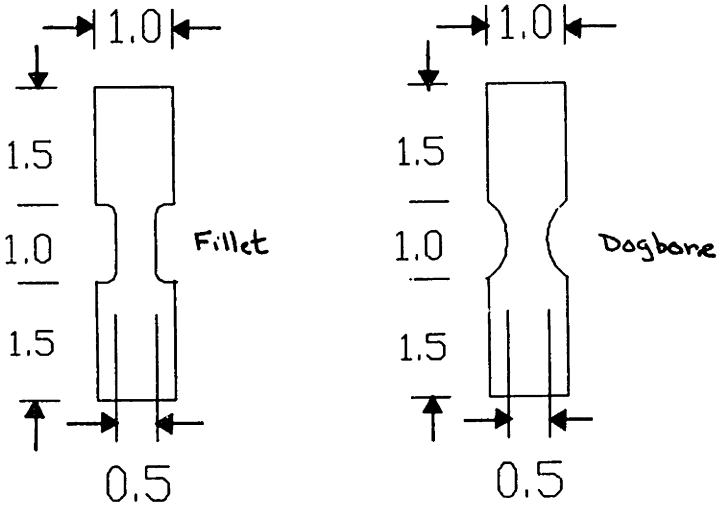

Figure 4.18: Stat Test Specimen Dimensions

fibers which are generally 1-2mm long, we have settled for testing small area samples (SAS's) of the different materials in order to get these pdf's. A combination of fillet tests (uniform cross-section with filleted corners) and dogbone tests (nonuniform cross-section) were used to determine various material parameters (Figure 4.18).

Since these tests are basically tensile tests without a precut (i.e., no stress concentration), some of the current models for predicting paper stress/strain curves to failure from fiber and bond properties would be excellent springboards to eventually eliminating this step. In particular, models by Ramasubramaniam[37], Petterson[34], and Pan[30] come to mind. Of these three, Petterson is the only one who directly addresses the important question of variability of rupture, but all three models contain important features which need to be examined and possibly incorporated.

4.3.1 Specimen Dimensions

As suggested by the name, the SAS's were very small specimens. The goal was to make the specimens as narrow as possible so that the values measured would be representative of only a small area, rather than an average over a large area; the ideal width being close to that of a single fiber. More realistically, a series of tests were run to determine the smallest width at which we could get consistent results. The gage

length was then adjusted to minimize the effects of weakest link over a long sample and the effects of the length/width ratio. In principle, what we arrive at is a section of the paper equivalent to something like a yarn in a fabric – i.e., an intermediate structure larger than the basic fiber but smaller than the whole structure. This analogy can be taken one step further; similar to the effects of twisting and entanglement on fibers in a yarn, the more fixed orientation and bonding in a sheet alters the behavior of the fiber in the SAS with respect to an isolated fiber.

Tests were run on copy paper samples due to the availability and uniformity of this material. Data is given in Appendix B. It is believed that the somewhat oriented structure of this material does not adversely affect the reliability of these tests provided the samples are all cut at the same orientation angle.

Widths of 1cm, 0.5cm, and 0.1cm were tested. While these are all obviously much larger than the typical fiber width, they fell at the low end of feasible values. As it was, the results were not consistent enough at the 0.1cm width, so the 0.5cm width was chosen. The problems at the narrower width could be due to (1) accuracy in cutting such a narrow sample; (2) the increased effect of flaws, nicks, or other damage to the sample; and (3) an impractical length in order to achieve a desired length/width ratio.

In combination with these widths, lengths of 10cm, 5cm, 1cm, and 0.1cm were tested. When the maximum stresses and strains are examined, the minimum acceptable specimen dimensions appear to be 1cm long x 0.5cm wide. These dimensions gave consistent results and were within practical size limits for production and testing of samples. In general, shorter lengths resulted in an unexpected jump in the strains, while much longer lengths resulted in a drop in the maximum strains, as might be expected from weakest link theory.

4.3.2 Specimen Configuration

Because of the small size, however, there was a significant effect of the stress concentration at the jaws. With a regular uniform strip configuration, the sample consistently broke in the grips. If a dogbone specimen is used, the higher stress at the narrower midsection results in consistent breaks at this point, giving an accurate failure stress. However, because of the nonuniform cross-section, the displacement cannot be used as an indication of the strain at the midsection. The strains in the wider sections are less, since the stresses in those sections are less. This causes the overall sample displacement to be less than for the strip configuration at a given strain in the midsection. Thus, a specimen with a constant cross-section is needed to determine the strain component. The problem of jaw failures is mitigated by cutting the specimens with a larger cross-section in the top and bottom for gripping and adding filleted corners between the grip sections and the gage section. Although most of these samples continued to break at the jaw, the load-displacement curves obtained were reliable enough to provide sufficient constitutive data for the model.

In the end, a compromise was struck between the two tests. Peak stress and yield stress values were taken from the dogbone samples; the constitutive relations and the yield stress determined by the fillet samples were then applied to get complete stress-strain curves for these peak stresses. As discussed previously, the assumption is that the constant cross-section fillet test produces an accurate representation of the stress-strain behavior. Due to the tendency to get jaw breaks in these samples, however, it is difficult to get a sufficient number of "good" failure endpoints for analysis. In contrast, the dogbone tests fail in the midsection 90% of the time, providing plenty of usable data. The "good" dogbone tests are thus used to get a peak point for the fillet curves. An example of how this conversion is done is shown in Figure 4.19. Because we assume that the SAS's display a two-segment curve, with the break strain occurring at the peak load, we would expect the break strain values derived from this

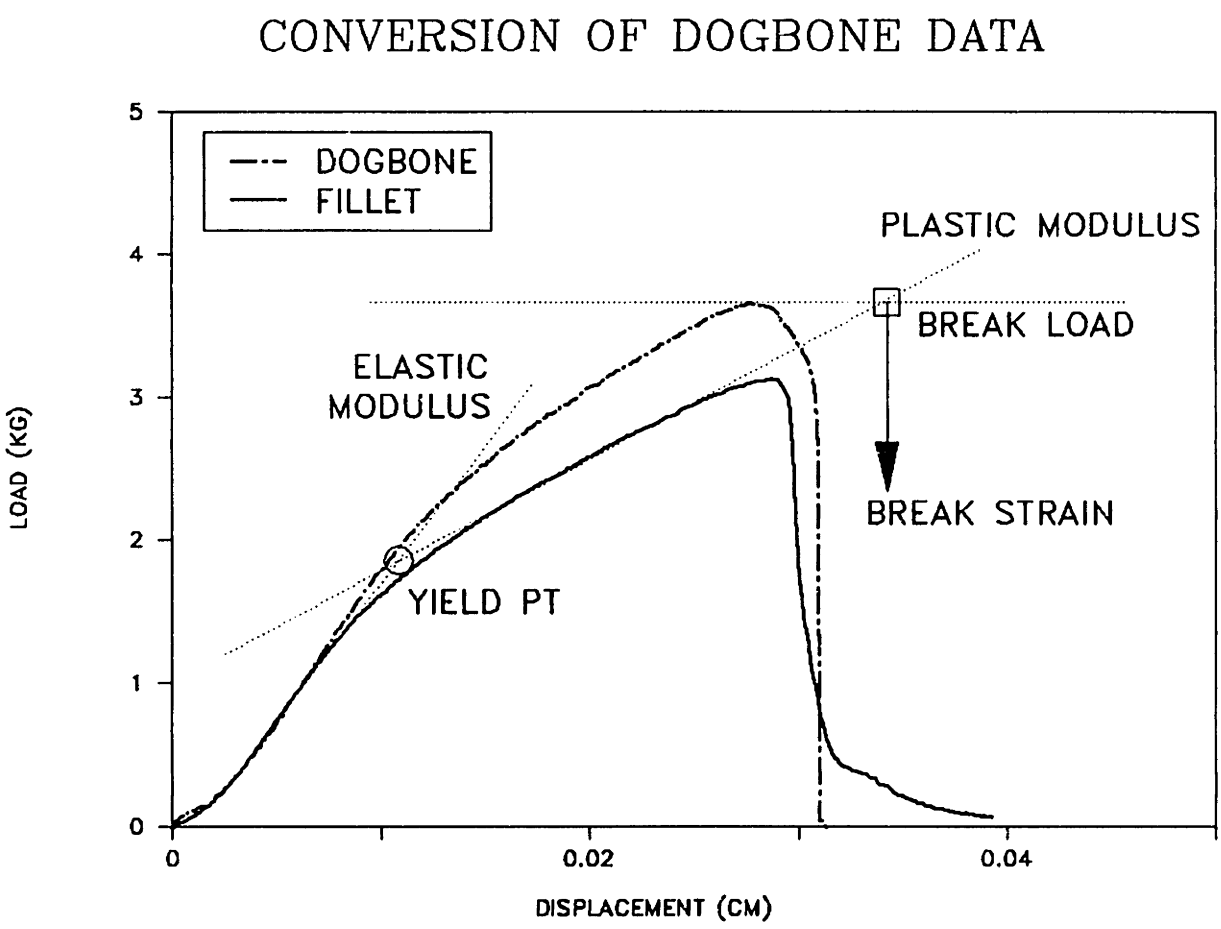

Figure 4.19: Conversion of Dogbone Data Using Fillet Results

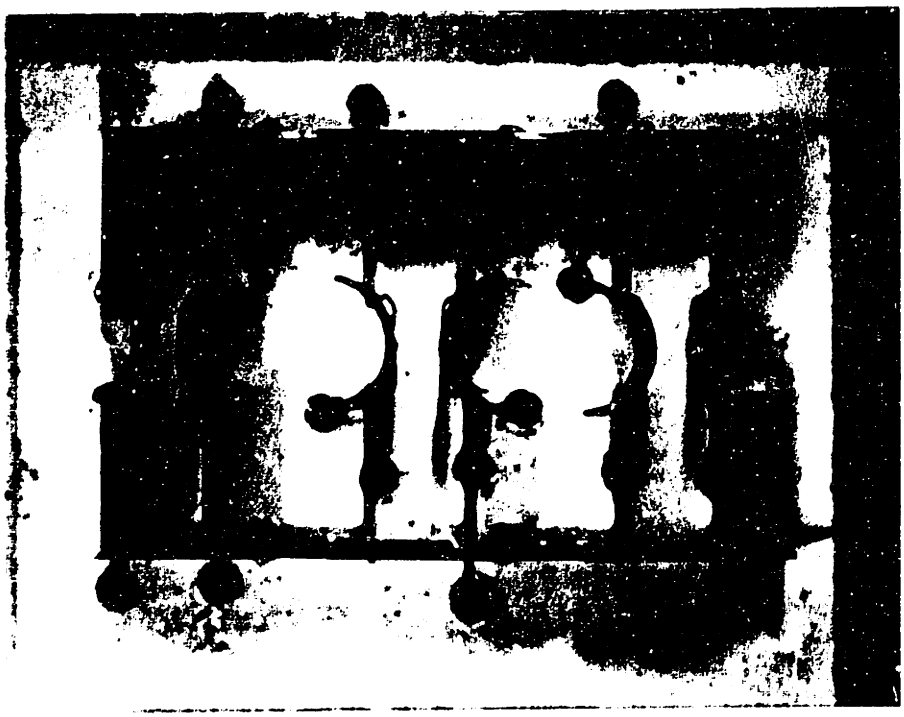

Figure 4.20: Stat Test Specimen Die

method to be on the low side.

Since the samples are so small, they are difficult to make because a nick can create a stress concentration and a slight difference in dimensions can change the critical values. This is compounded by the large number of samples that have to be produced in order to get enough data to accurately determine the pdf's of the material parameters. A special die was made (by Steven Rich of Pearl Bookbinding, South Boston, MA) to punch out the samples with a minimum of damage to the sample (Figure 4.20). With this punch, three samples can quickly be punched out at once – 2 dogbone and 1 fillet. The dimensions of any given sample are then identical to one of the two dogbone samples or to the fillet sample. With over a hundred of each configuration, the results should be fairly consistent.

4.3.3 Procedure

Because of the fragile nature of these SAS's, small air jaws were used to grip the sample. Tests were run at 0.1in/min to minimize grip slippage effects and reduce testing time.

Again, taking advantage of the convenience of copy paper, a short series of tests (see Appendix B) were run to determine the effect of crosshead speed. Two speeds were tested – 0.05in/min and 0.5in/min. The higher speed gave slightly higher stresses and strains with similar deviations, but more jaw breaks. Since the fracture tests are run very slowly, a slower speed of 0.1in/min was chosen for these tests also, rather than going to a much faster speed of say 5in/min.

4.3.4 Analysis

Analysis of the stat test results was done primarily with Vu-Point and Lotus software. From the shape of the stat test curves, it seemed logical to model the SAS behavior as a two linear segment curve. For this model, the break point is defined by the maximum load point L_{max}. A linear curve is fit to the initial part of the curve (before the bend) to determine the elastic modulus, E. The plastic modulus P is calculated by fitting a straight line to the fairly linear section before the break point. The yield stress k is defined by the intersection of the elastic modulus and plastic modulus lines. Breaking strain values were determined directly from the load-displacement curves. For comparison, the breaking strain is also calculated from the other four values (E, P, k, L_{max} as shown in the equation below and previously in Figure 4.19.

$$\epsilon_{brk} = k/E + (L_{max} - k)/P \tag{4.1}$$

The distributions for 4 key material parameters – elastic modulus, plastic modulus, yield stress, and breaking strain (E,P,k,ϵ_{brk}) – were then determined. This meant

taking all values of a given parameter for a given paper type and calculating the mean and standard deviation. Using Microsoft C and some helpful functions from Numerical Recipes[36], a program was written to compile a random (normally distributed) set of values with the same mean and standard deviation; this set was then used as a lookup table by the model.

Calculation of the lookup tables is done by using a random number generator to generate uniform deviates between 0.0 and 1.0. These numbers are each transformed to a Gaussian (normal) deviate with zero mean and unit variance using a Box-Muller transformation[36]. The Gaussian deviate is then converted to a Gaussian deviate with the mean and variance of the given material as determined from the stat test results.

$$f_x(x_0) = \frac{e^{-[x_0 - E(x)]^2/2\sigma_x^2}}{\sqrt{2\pi}\sigma_x} \qquad -\infty < x_0 < \infty \tag{4.2}$$

where

$$\begin{aligned} E(x) &= \text{mean} \\ \sigma_x &= \text{standard deviation} \end{aligned}$$

4.3.5 Results

Table 4.1 summarizes the results of the stat tests. In general, the mean values for the dogbone samples are always higher than for the fillet samples. This is to be expected since the larger average cross-section for the dogbone samples will result in less elongation for a given load (stiffer behavior) and a middle break rather than a grip break (higher failure strains). If we compare breaking strains for the dogbone samples of the different materials, we see the order Clupak >> Binder > Standard. Comparing the Elastic Moduli and the Plastic Moduli, the order is Binder > Standard >> Clupak. The Yield Stress order is similar to that for the moduli.

Material Type	Brk.Strain (cm/cm)			Elas.Mod. (kg/cm)/strain			Plas.Mod. (kg/cm)/strain			Yd.Stress (kg/cm)		
	mean	std	C.V.	mean	std	C.V.	mean	std	C.V.	mean	std	C.V.
STANDARD (DOG)	0.072	0.0073	0.10	228.5	27.3	0.12	89.3	8.37	0.09	4.45	0.366	0.08
STANDARD (FIL)	0.068	0.0093	0.14	177.6	19.1	0.11	71.9	6.88	0.10	3.37	0.279	0.08
BINDER (DOG)	0.090	0.0111	0.12	280.8	23.6	0.08	107.2	13.31	0.12	5.73	0.407	0.07
BINDER (FIL)	0.085	0.0094	0.11	235.1	20.5	0.09	89.0	9.16	0.10	4.41	0.377	0.09
CLUPAK (DOG)	0.243	0.0323	0.13	91.2	18.5	0.20	21.4	2.99	0.14	1.80	0.413	0.23
CLUPAK (FIL)	0.220	0.0349	0.16	76.0	15.1	0.20	20.6	3.40	0.17	1.66	0.151	0.09
PET (DOG)				251.1	33.6	0.13	83.6	13.05	0.16	3.78	0.499	0.13
PET (FIL)				192.8	31.8	0.17	63.0	11.20	0.18	3.74	0.327	0.09

Material Type	Conv.Brk.Strain (cm/cm)		
	mean	std	C.V.
STANDARD	0.073	0.0095	0.13
BINDER	0.074	0.0119	0.16
CLUPAK	0.183	0.0423	0.23
PET	0.056	0.0143	0.25

Table 4.1: Summary of Stat Test Results

Breaking strain values calculated by converting the dogbone and fillet data were close to the directly measured values, but were lower as expected, especially for the Clupak samples. Because the PET samples tended to break less cleanly, there was some difficulty in measuring the breaking strain. We expect that the strain values should be quite similar to the Standard strain values.

Plots of the distributions of these material parameters are given in Appendix B. A few are given here for illustration (Figures 4.21-4.23).

Each of the plots show bars representing the actual values measured from the experiment and the number of samples at each value. The solid line in the plots represents a normal distribution with the same mean and standard deviation as the experimental data. Since a normal curve generally represents an area of 1, the magnitude of the normal curve is adjusted to fit the bar chart by multiplying by the total area of the bars.

Note that for these plots of breaking strain, the mean and standard deviation of the Clupak samples (Figure 4.23) are much higher than that for the Standard or Binder samples (Figures 4.21 and 4.22). The effect on the model of differences in the mean and variance of these parameters for the various materials will be discussed in the parametric study section of Chapter 6.

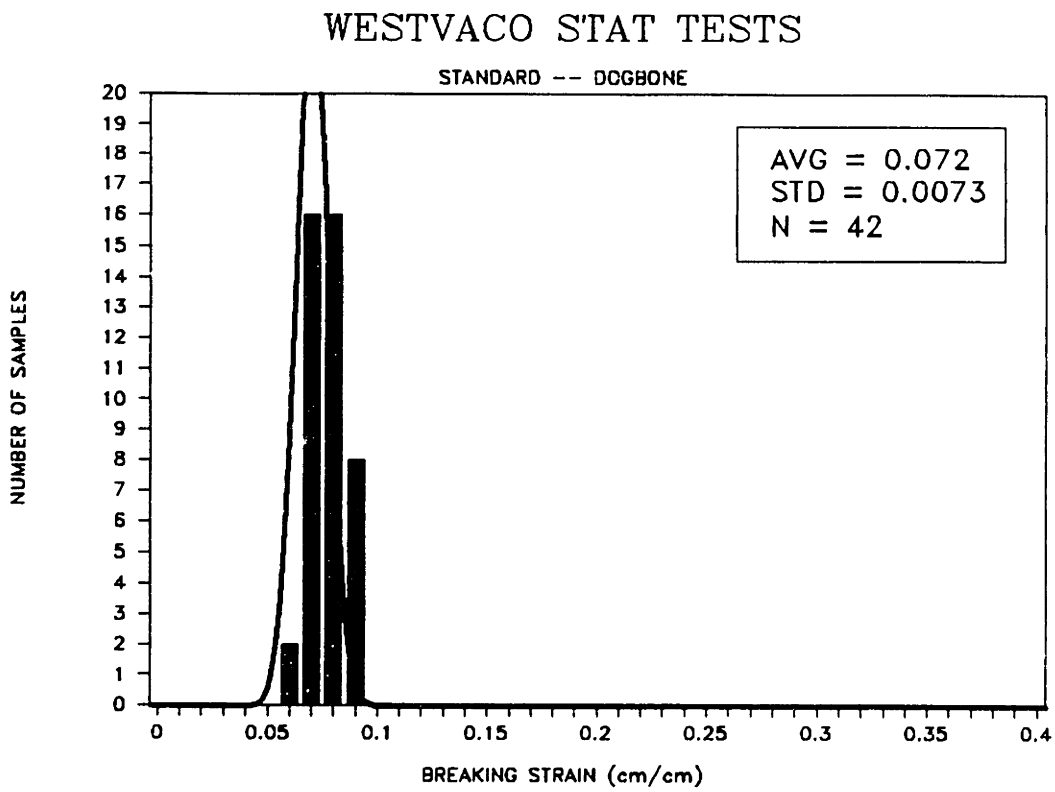

Figure 4.21: Statistical Results of SAS Tests — Breaking Strain of Standard Samples

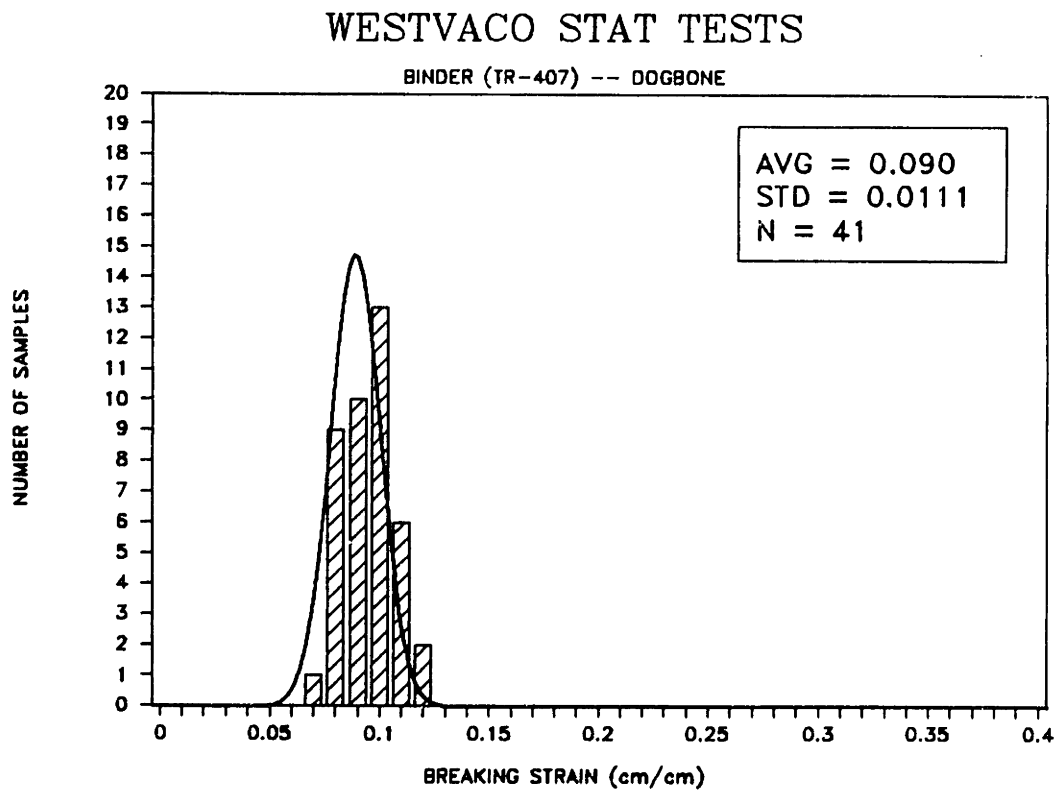

Figure 4.22: Statistical Results of SAS Tests — Breaking Strain of Binder Samples

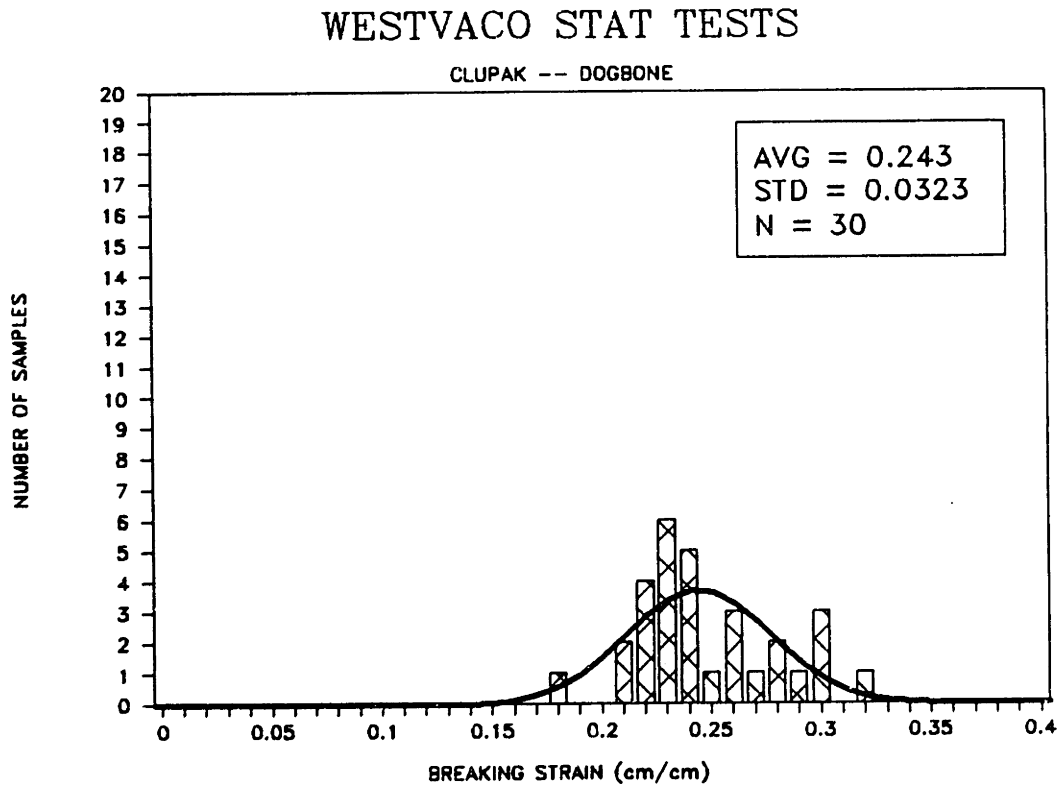

Figure 4.23: Statistical Results of SAS Tests — Breaking Strain of Clupak Samples

Chapter 5

SEM TESTS : Observations of Damage Zone and Determination of Crack-Tip Strain Fields

From the fracture tests we obtained some quantitative comparisons between different structures. But it is often difficult to identify the actual cause of these differences from the numbers alone. Herein lies the usefulness of direct observation. By being able to look at the samples at the fiber level before, during, and after fracture, we gain insight into the mechanics of the process. In the previous chapter, we have already seen how the different materials exhibit varying degrees of fiber pull out and fiber fracture. In this chapter, the development of the damage zone and direct measurements of the strain fields will be presented.

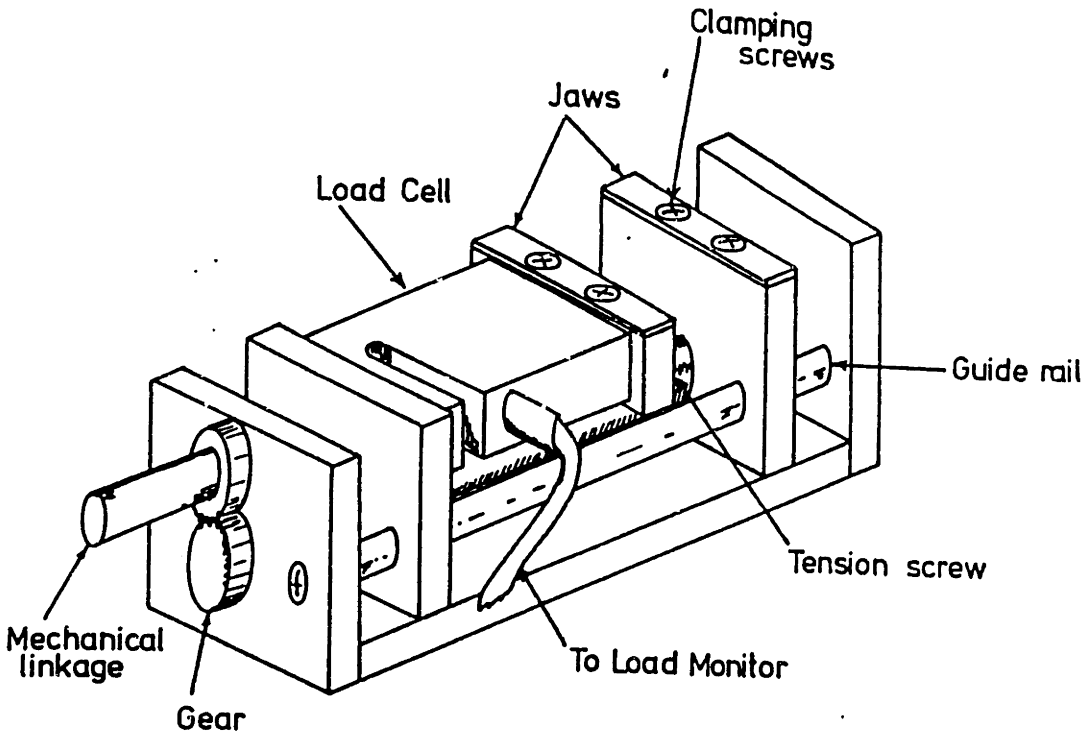

Figure 5.1: Hexland tensile stage schematic

5.1 Scanning Electron Microscope Tests

This direct observation was achieved by using a SEM 20kg tensile stage (Hexland Ltd, Wantage, Oxon, ENGLAND) (see schematic, Figure 5.1) to run fracture tests in a Cambridge Instruments Scanning Electron Microscope (Stereoscan 240) (Figure 5.2). A Hurst motor and motor controller were hooked up to the tensile stage to run constant displacement rate tests – previously, the tensile stage had to be controlled by a hand crank. A video and load cell output enables continuous monitoring of both quantitative and qualitative information. A VHS and super-VHS VCR and the Nicolet oscilloscope were used to store all relevant data.

The specimen dimensions for these tests were 2cm x 2.5cm with a 0.8cm precut, keeping the ratios similar to those of the larger fracture tests but within the limits of the tensile stage. An additional 0.5cm was added to the length on either side for gripping.

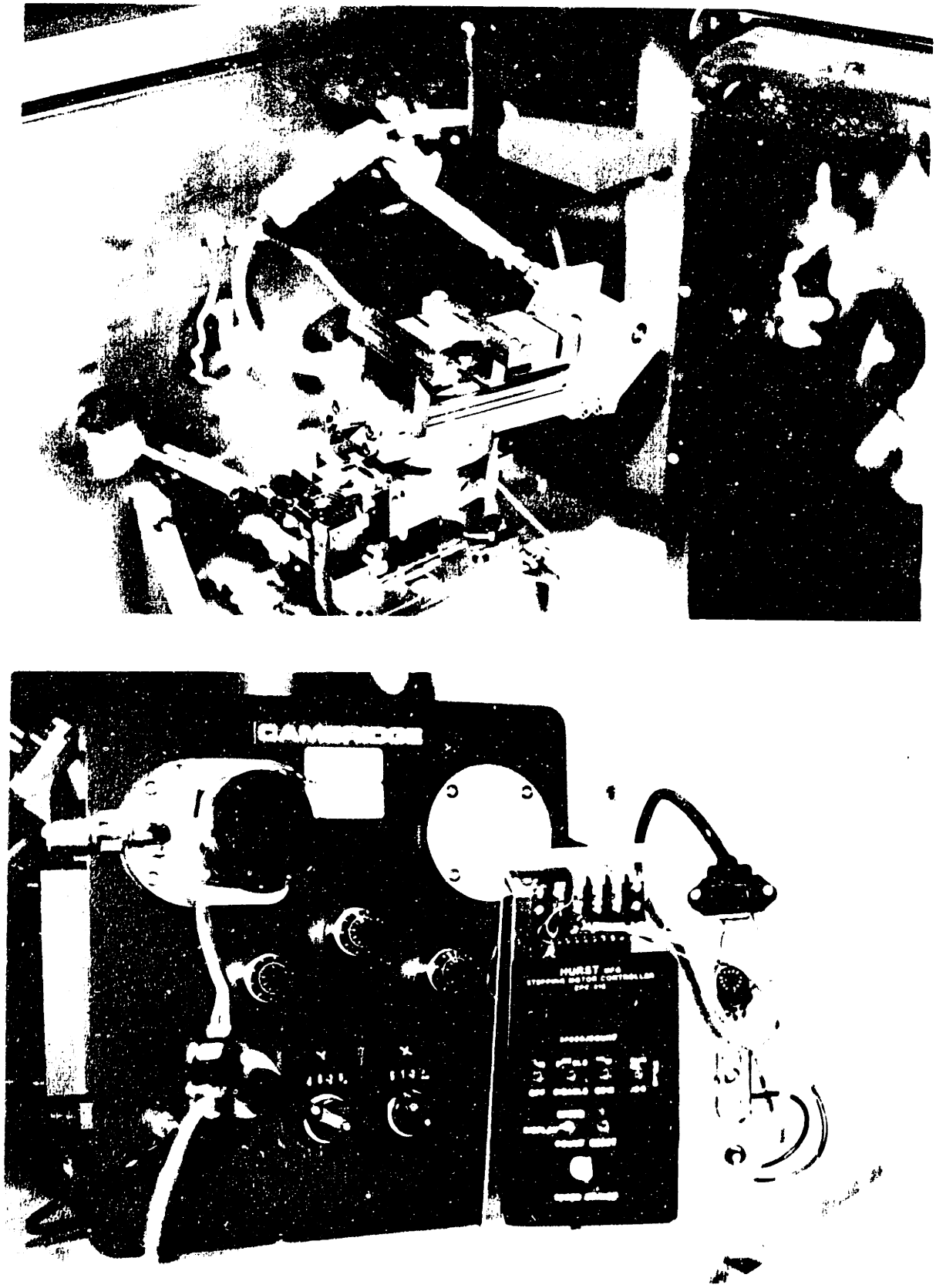

Figure 5.2: SEM tensile stage setup

5.1.1 Calibration

Calibration of the tensile stage setup was achieved for the load cell readings and the displacement rate as follows.

The tensile stage is driven by a worm gear/screw assembly. The screw threads were measured to be 25 threads/inch. The worm gear creates a reduction of 30:1. Thus, the driving shaft requires 750 revolutions per inch of jaw displacement.

The motor controller has a range of 5-400 steps per second (SPS). The motor is set at 0.5 degree/step or 720 steps/revolution. Thus, when the controller is set at **200 SPS**, the motor is turning the driving shaft at 0.28 rev/sec. This translates to **0.022in/min or 0.00094cm/sec.**

In order to calibrate the load cell, a spring was placed in the tensile stage and pulled at a constant displacement rate within the linear region of the spring. The voltage (load) readings from the load cell were collected by the Nicolet. The same spring setup was then placed in the Instron, and a similar test was run. The two results were compared as shown in Figure 5.3. Note that the two sets of curves (SEM load cell and Instron load cell) are offset somewhat to make the graph easier to read. While the SEM setup is a bit noisier, the results were reasonably linear and matched the calibration factor provided by Hexland. This calibration factor turned out to be **1 Volt = 12.5 kg.**

5.1.2 Effect of SEM Conditions – vacuum, gold-coating, and e-beam

A few experiments were run to determine the differences between the results from these SEM tests and the fracture tests described in Chapter 3. These experiments were run on Standard specimens with the same fracture test dimensions of 2cm x

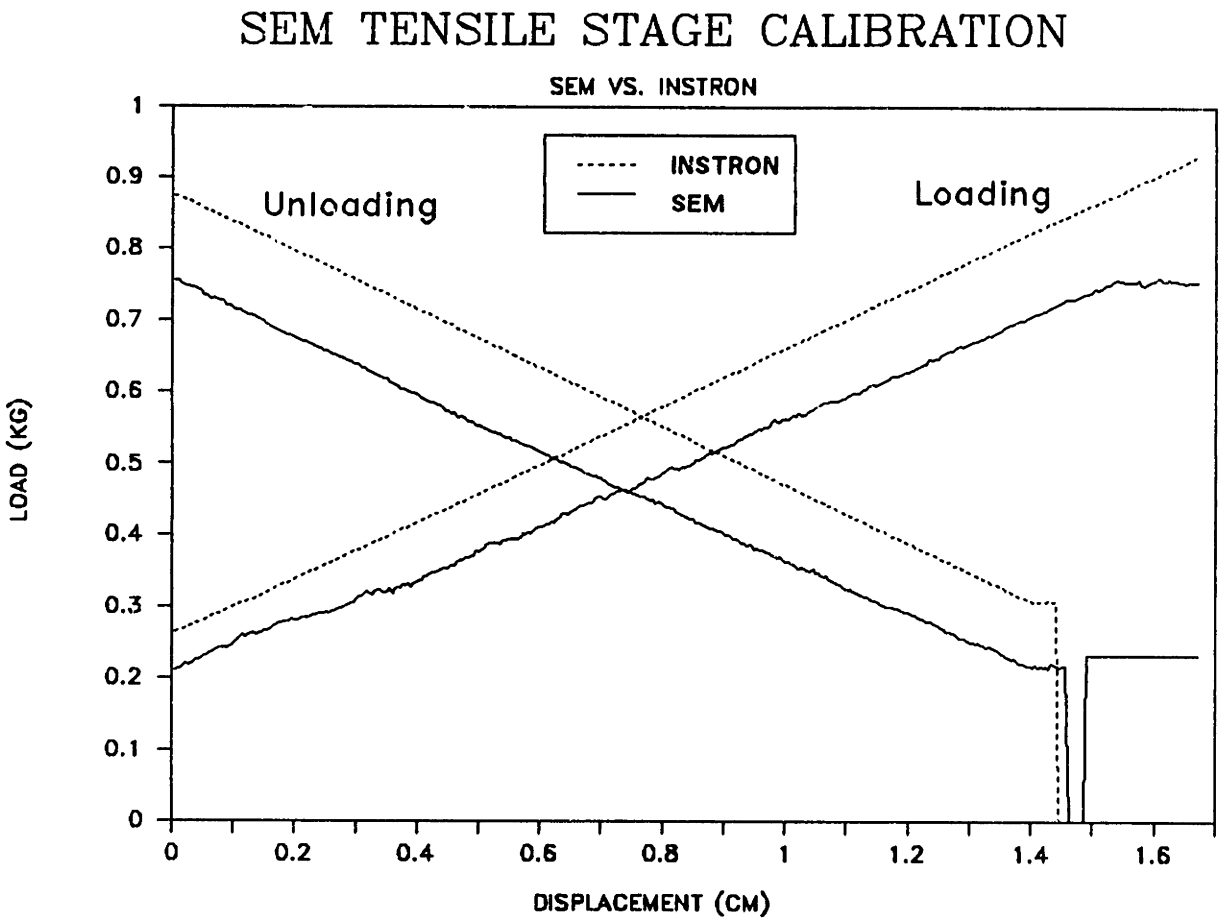

Figure 5.3: SEM Tensile Stage Calibration

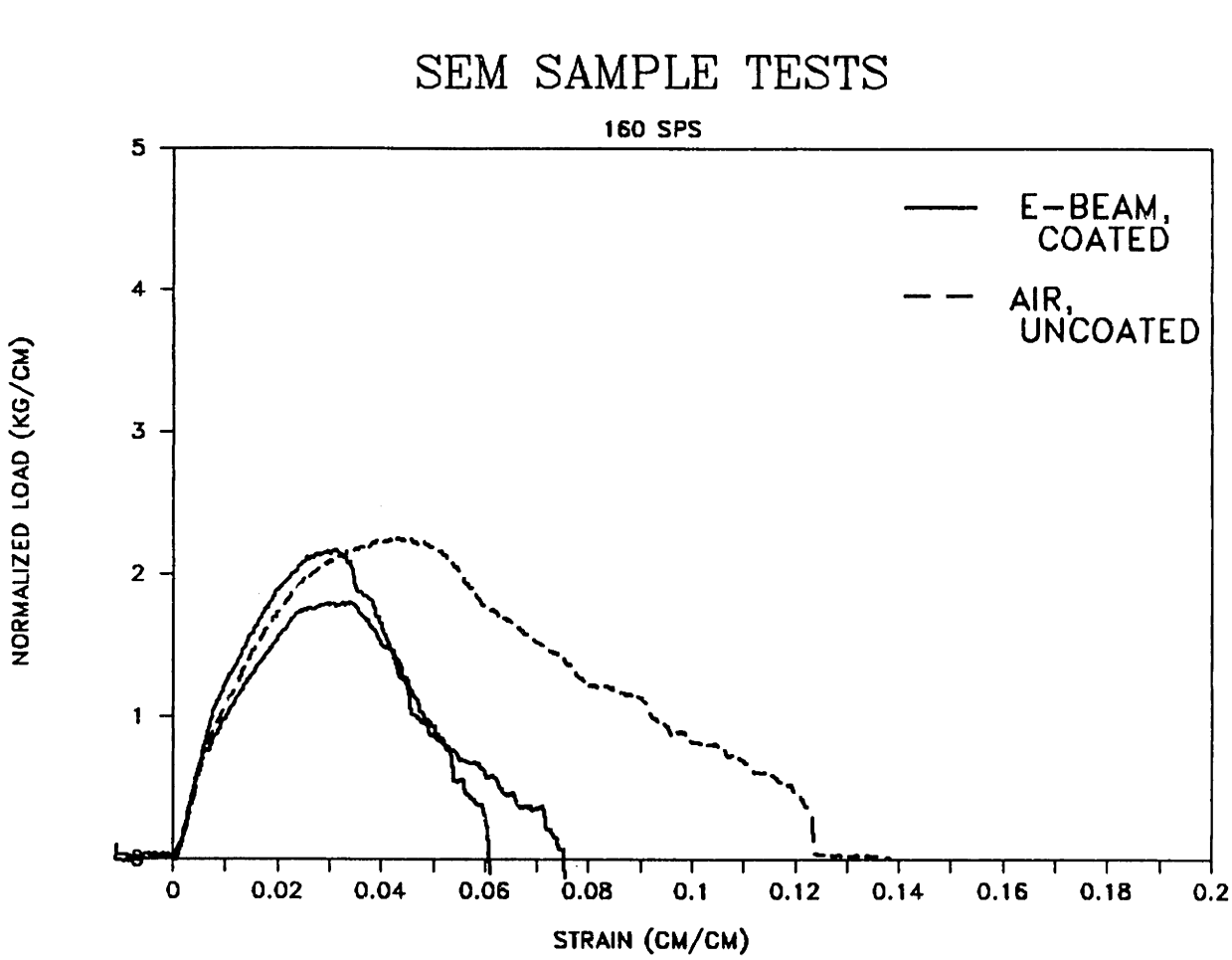

Figure 5.4: General Effect of SEM Test Conditions

2.5cm, 0.8cm precut. Gold-coating, vacuum, and e-beam charging were all examined as possible factors affecting the fracture behavior.

The good news is that none of the factors appeared to affect the initial modulus. Unfortunately, post-peak behavior was significantly affected.

Comparing the fracture curves for the gold-coated samples run in the SEM (vacuum + electron beam) with the uncoated samples run in the Hexland with the SEM chamber open (no vacuum, no e-beam), the peak loads are not drastically different; however, the fracture behavior was more brittle, resulting in failure strains almost half those of the uncoated specimens (Figure 5.4). To elucidate the cause of this embrittlement, several samples were run at 160SPS: (1) Gold-Coated in Air (Hexland tensile stage w/ SEM chamber open); (2) Gold-Coated in Vacuum (Hexland w/ SEM vacuum on, e-beam off); and (3) Gold-Coated w/ E-Beam (Hexland under normal

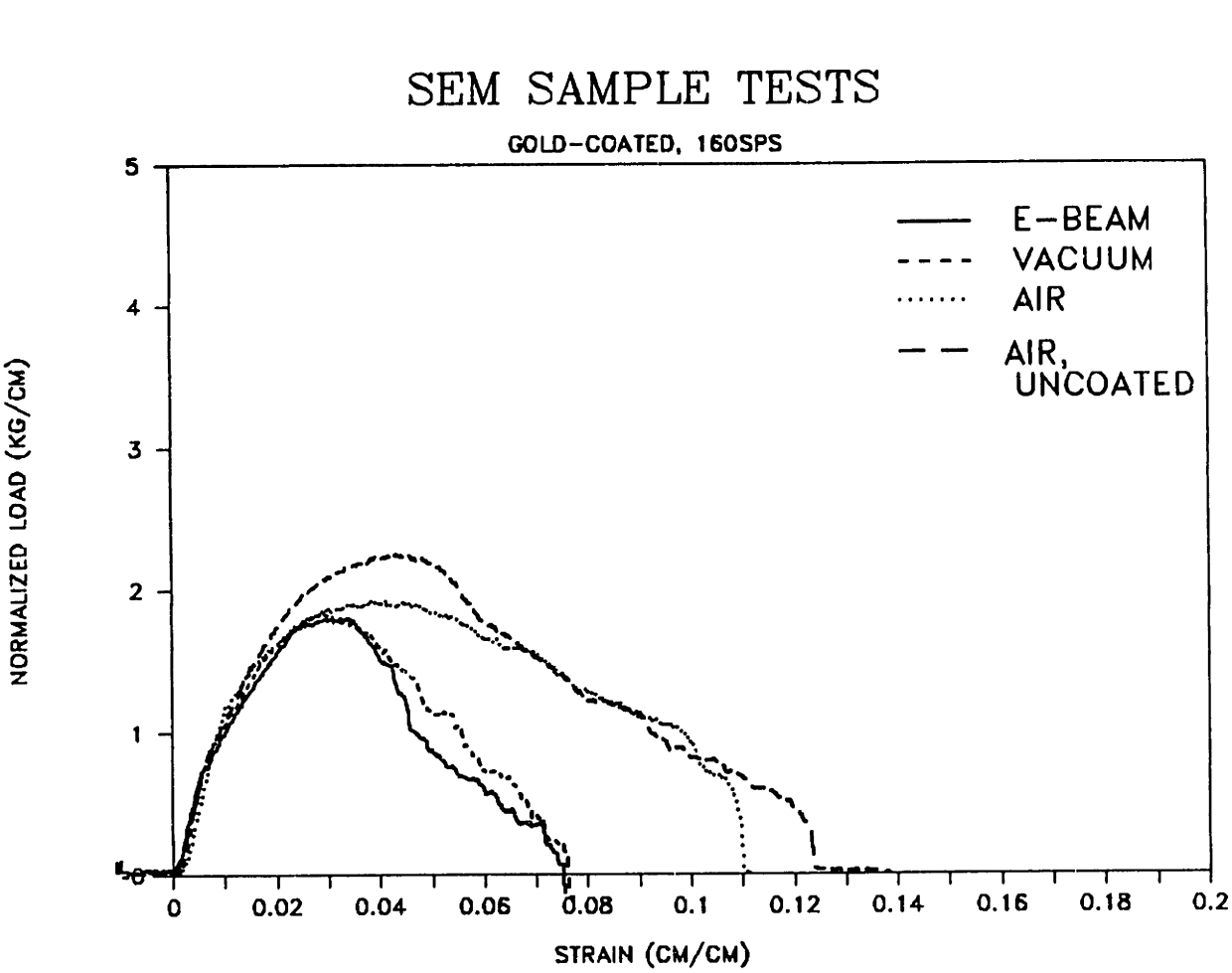

Figure 5.5: Effect of Independent Factors (Gold,Vacuum,E-Beam)

SEM conditions, vacuum on, e-beam on).

The results (Figure 5.5) indicate that the vacuum is the primary culprit. The e-beam and the vacuum samples are quite similar. However, there is a considerable drop in failure strain between the vacuum samples and the "in air" samples. This is not unexpected, as paper is extremely sensitive to changes in humidity. Moisture in paper contributes to its plasticity and ductility. It is suspected that the vacuum removes any unsecured moisture from the sheet, making it more brittle.

Gold-coating seems to affect the fracture behavior slightly, as the peak loads and failure strains decrease by about 10-15%. An attempt was made to run the strain field tests on uncoated samples, but even at 1.0kV the excessive charging resulted in a poor quality picture. Also, for the damage zone tests, the gold-coating made the damaged regions far more obvious and was thus a benefit, as will be discussed later.

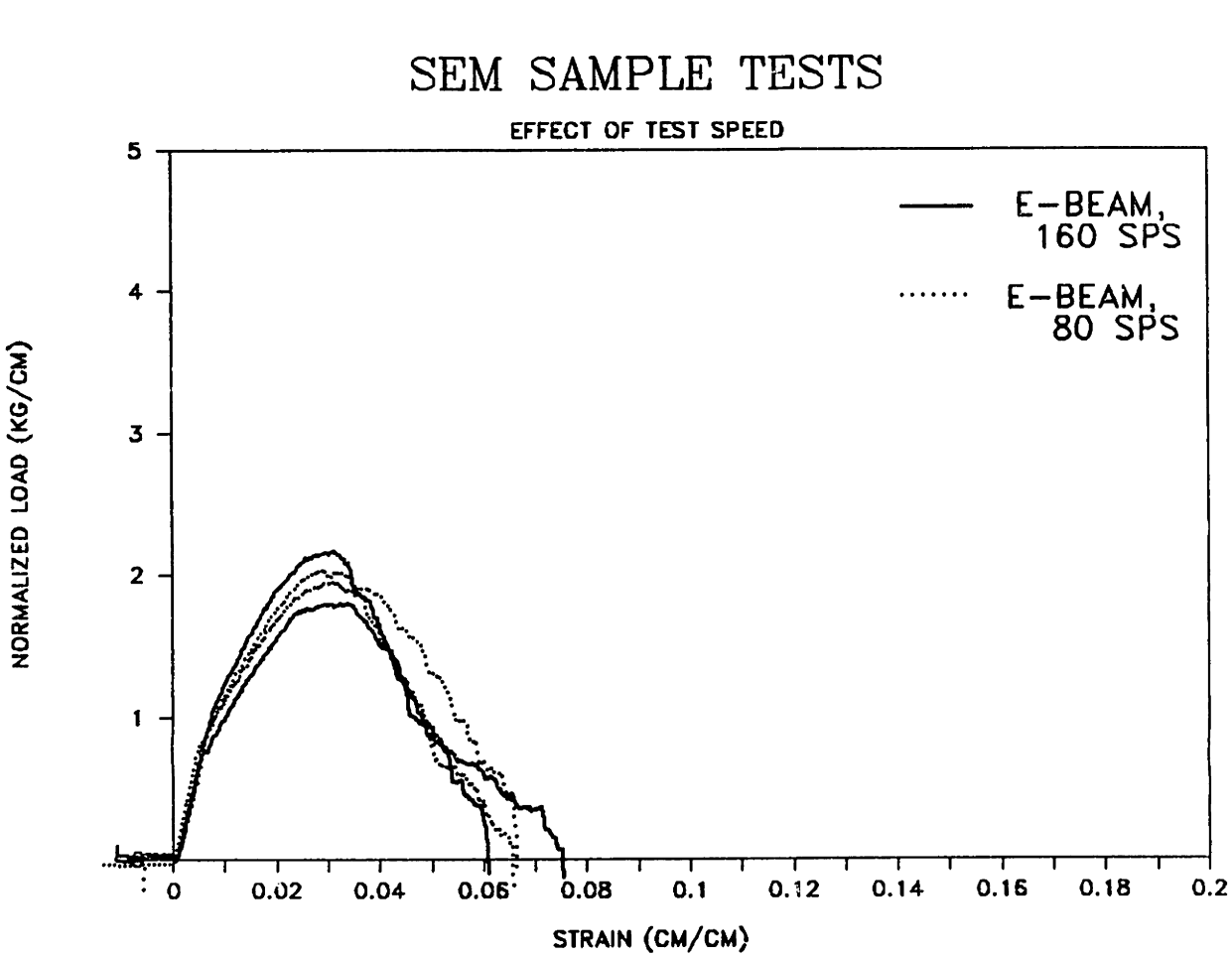

Figure 5.6: Effect of Test Speed

Also noteworthy is the lack of a significant change in the curves from a doubling of the displacement rate for the fracture test (Figure 5.6). Tests at displacement rates of 160 SPS (0.00075 cm/sec) and 80 SPS (0.00037 cm/sec) showed minimal differences. The slower speed was chosen to capture the changes in local strains better on the videotape.

Unfortunately, the effect of the vacuum and, to a lesser extent, the gold-coating, is unavoidable with this method. However, since the shape of the curve is similar, we assume that there is no critical change in the fracture behavior other than the embrittlement of the sample due to the vacuum condition. Similarly, we expect that the general shape of the strain fields will also be representative, although perhaps quantitatively closer to slightly more brittle materials in normal conditions.

5.2 Damage Zone Observations

The degree of damage incurred in each of the samples varied. This became very evident in the gold-coated samples, where due to the strains and subsequent damage, the gold came off the sheet or surface fibers failed, exposing uncoated fibers below. This led to more charging in these areas and was seen as bright regions on the paper surface. Tests were run at 2-5kV.

In these experiments, fracture test samples were strained in the Hexland tensile stage until the crack propagated approximately 2-3mm from the precut. The jaw displacement was halted to prevent further propagation of the crack, and a series of photographs were taken along the crack from the precut to the tip of the damaged region. These photographs were then matched together to give a picture of the entire zone. The magnification was naturally kept the same for each photograph of a given sample. Magnification for each of the different samples was set at approximately 100x.

For the TR-407 Binder samples, the bright region covered a very narrow zone (Figure 5.7). In accord with the fracture surface observations, the zone was also very clean with few if any offshoots. The active region (see Figure 5.7) can be defined as the section of the damage zone displaying damage but still containing loaded fibers (fibers not fractured or completely pulled out). For the TR-407 Binder samples, this active region was very short. Less than 2.5mm from the damage zone tip there are no longer any fibers holding the sheet together.

In contrast, the 8% Clupak sample exhibited a very large damage zone (Figure 5.8), and the zone was not straight like the Binder zone. It meandered and had multiple offshoots, indicating eventual pullout locations. The photographs also suggest a long active region, since the fibers appear to be active from the damage zone tip to the precut tip, a length exceeding 3mm.

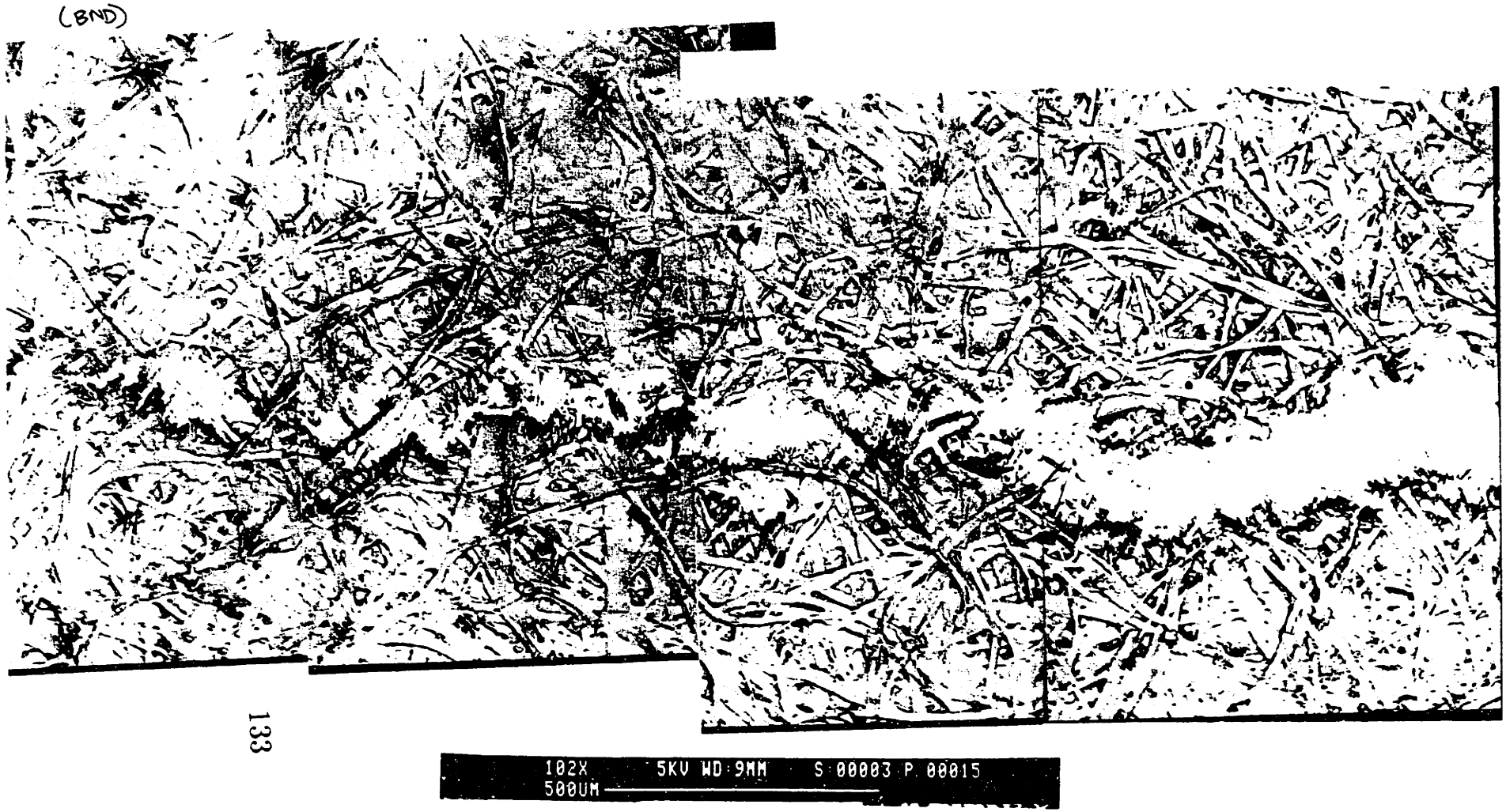

Figure 5.7: SEM Damage Zone – TR-407 Binder

Figure 5.8: SEM Damage Zone – 8% Clupak

The Standard and PET samples fell somewhere in between. With a zone narrower than the Clupak but wider than the Binder, the Standard also exhibited the offshoots related to fiber pullout (Figure 5.9). The PET sample was very similar to the Standard sample, with the addition of evidence of PET debonding and pullout at certain intersections (Figure 5.10).

The next few photographs show damage zones that are slightly shorter than the first four. Comparisons should be made from the damage zone tip back towards the precut, under the assumption that the crack is self-similar.

Comparing the TR-934 Binder sample with the TR-407 Binder sample, the TR-934 sample has a noticeably rougher zone of damage (Figure 5.11). In addition, the width of the zone is larger at an equal distance from the damage zone tip. The damage zone is, however, still fairly contained with only a few long offshoots.

Examining the effect of %compaction on the damage zone, a 15% Clupak sample and a 6% Clupak sample are shown in the next two figures (Figures 5.12 and 5.13). While neither of these samples show quite the same fiber separation and path tortuosity of the 8% Series II sample, we can see by comparing these two Series III samples, that increased compaction to the 15% level does result in a slightly wider damage zone. In conjunction with this, however, the active region seems to be shorter. Apparently, as the %compaction increases, the damage zone becomes more blunted, suggesting an increase in the amount of material undergoing plastic deformation. Nevertheless, because of the compaction, the material is also weaker, so there is a trade-off of increased amount of active material and loss of strength of that material.

Along the same vein, the damage zone of the 6% Clupak sample fractured in the cross-direction, or across the compaction grain, was similar to what might be expected of a material with less than 6%compaction (Figure 5.14). When compared with the 6% Clupak sample fractured in the direction of compaction, the damage zone width is

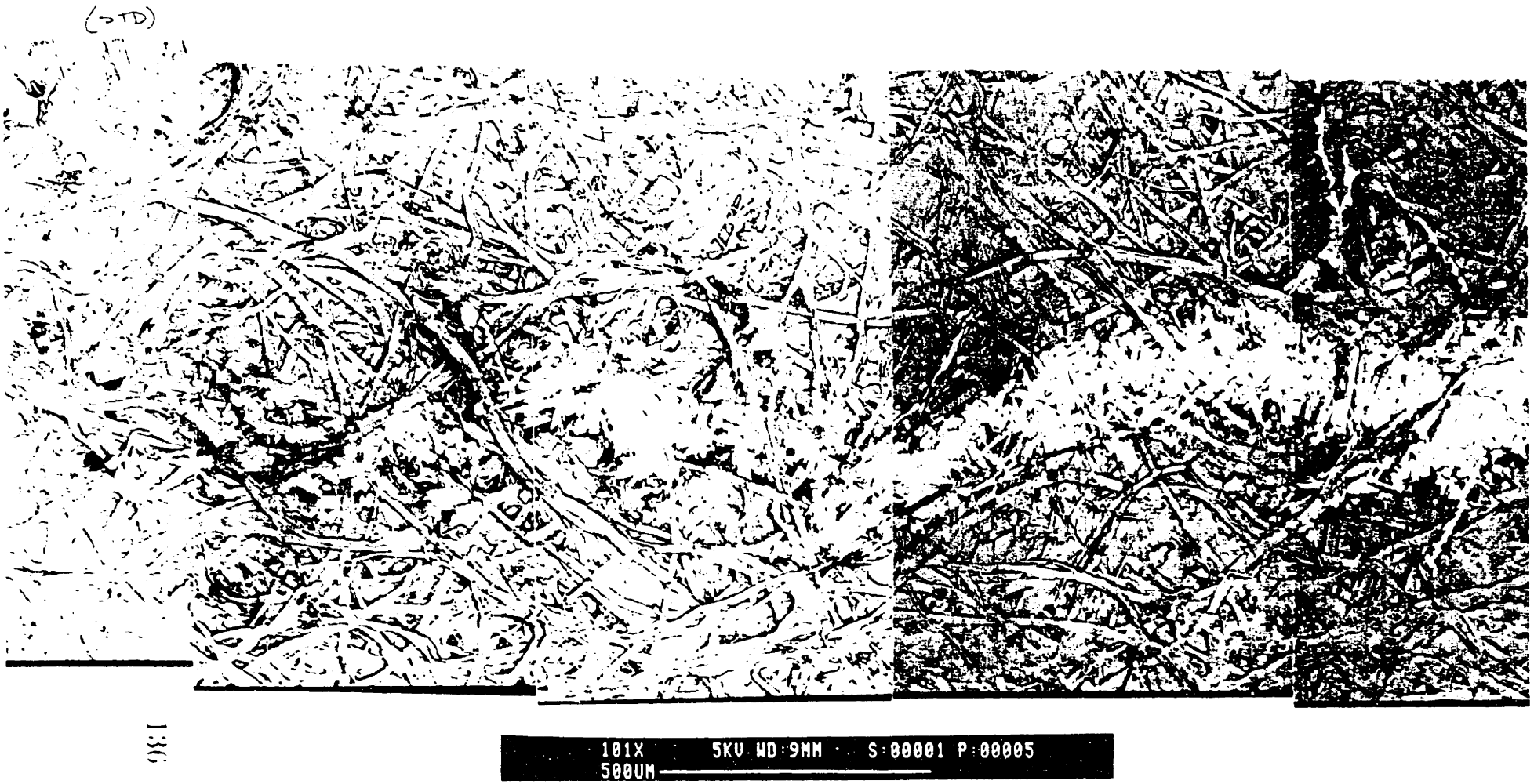

Figure 5.9: SEM Damage Zone - Standard

Figure 5.10: SEM Damage Zone – PET

Figure 5.11: SEM Damage Zone – TR-934 Binder

TR-934

Figure 5.12: SEM Damage Zone - 15% Chupak

Figure 5.13: SEM Damage Zone – 6% Clupak

narrower, especially closer to the damage zone tip, and the active region is longer for the cross-direction sample. This implies that the main effect of anisotropy for these samples is that in the cross direction, the Clupak sample behaves like a more brittle and stiffer material. There is no dramatic difference in the damage zone appearance.

As an additional test, the damage zone of anisotropic copy paper was also examined (Figure 5.15). Commercial copy paper has a machine direction and a cross direction due to the high directional speeds during production. In this case, the photos show the crack propagating in a direction perpendicular to the machine direction. The damage zone appearance is similar to the more brittle isotropic materials (e.g., TR-407 Binder). The major difference is that the path zigzags more and the active region is much longer, indicating that there is less resistance to propagation of the crack. That is, less material has to be pulled apart prior to further growth of the damage zone and the crack. As suggested earlier, it is surmised that the addition of fillers and coatings has produced a smoother sheet closer to that of the Binder sheets than the Standard sheets.

The entire fracture process can be described in fairly simple terms. Prior to crack initiation, the precut starts to widen. At crack initiation, the fibers at the crack tip start to separate. The ensuing crack propagation occurs in a less than smooth manner. The crack seems to be retarded at certain points – e.g., clumps of fibers. Once these points fail or pullout, the crack will tend to jump a little, extending a chunk at a time. That this behavior is due to the presence of weak spots and strong spots rather than a regular buildup to a critical energy level and a dynamic release is suggested by the irregularity of the process.

More brittle materials display a rapid extension of the crack with little signs of damage on either side; most of the material appears untouched. In contrast, tougher or more fracture resistant materials show the development of an extensive damage zone and significant fiber interaction prior to further crack propagation. Unfortu-

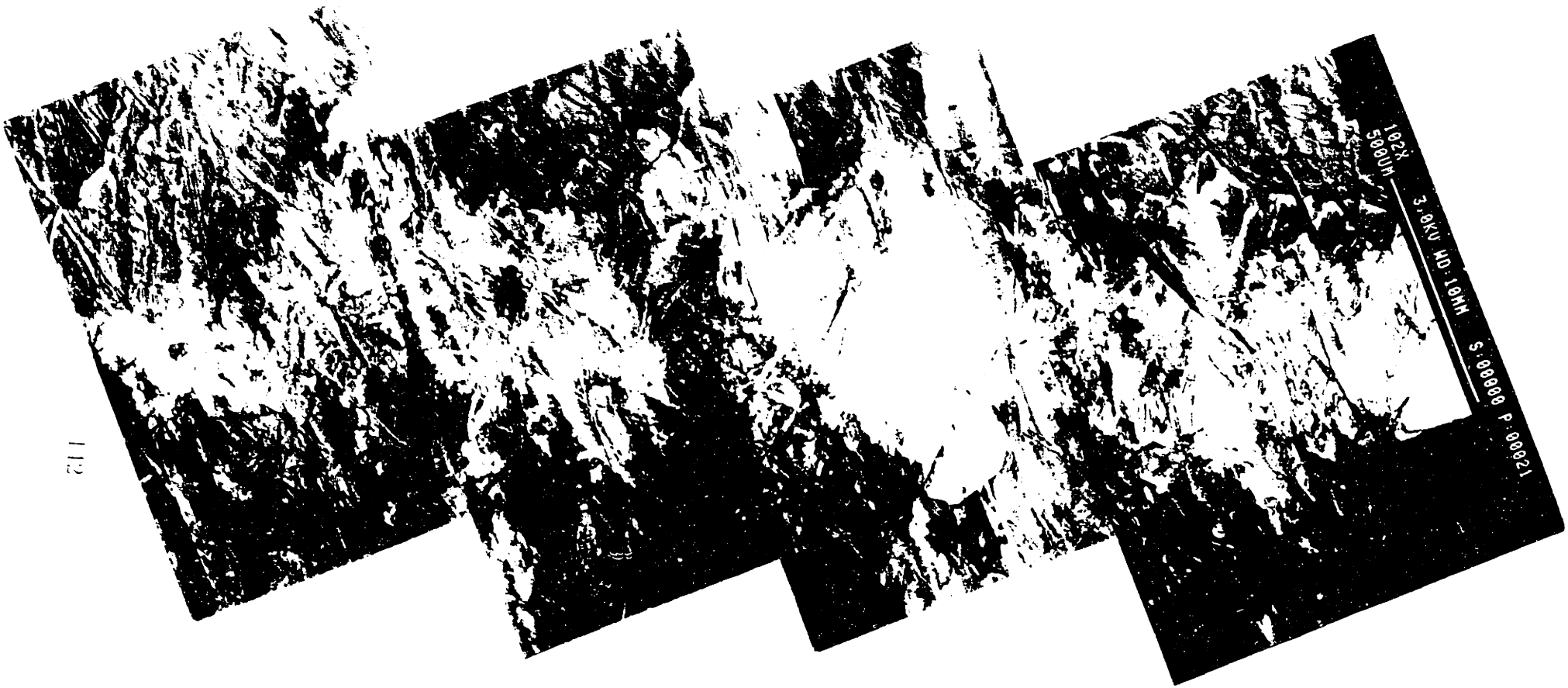

Figure 5.14: SEM Damage Zone — 6% Clupak, Cross-direction

Figure 7.15: SEM Damage Zone - copy paper

nately, the increase in amount of active material may be offset by an coinciding decrease in the average strength of the material. Similarly, the presence of a large flaw may cause the crack to diverge (Figures 5.16a,b), increasing the total crack length, but also tending to lower the resulting loads. Both of these arguments prohibit the proclamation of a blanket statement regarding a direct relationship between the size of the damage zone and fracture resistance.

5.3 Determination of Crack Tip Strain Fields

After searching the relevant literature, we believe that this continuum/statistics method is a new approach to solving the question of fracture in paper. Thus, a large part of the work covered in this thesis deals with supporting the necessary assumptions made in applying the continuum fracture mechanics with statistical variations approach. One set of novel experiments developed during this study involved the *in-situ* measurement of strains at the crack tip at different times during a fracture test. The procedure and the results will be discussed in this section.

5.3.1 Procedure

The fracture process of a region directly in front of the crack tip was videotaped. The test was run at 0.0088in/min (0.00037cm/sec) on a 2cm x 2.5cm, 0.8cm precut gold-coated sample. An acceleration voltage of 1.5kV was used and the magnification was set to 100x so that the entire screen covered an area of approximately $1000\mu m$ x $800\mu m$.

Several frames of the videotape were chosen from the unloaded condition through to various degrees of pre-cracking and crack initiation, ending prior to crack propagation through the viewed region. These frames were transferred to a PC via a

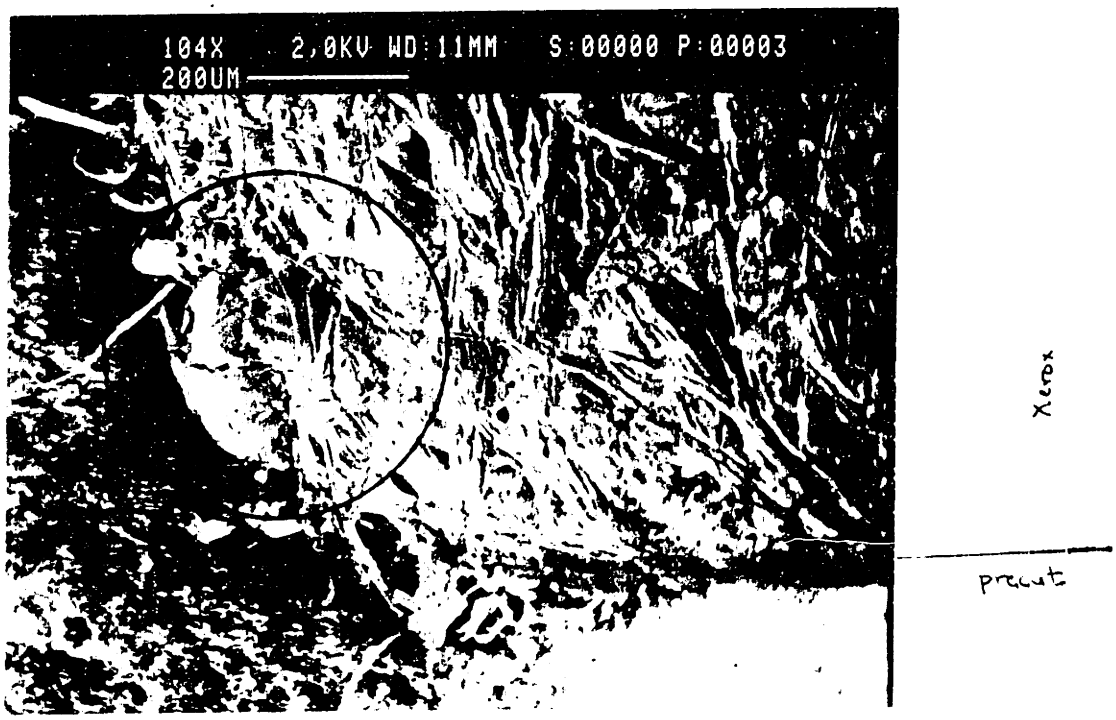

Figure 5.16: Effect of Flow on Crack Path

framegrabber with a resolution of roughly 500 x 400 pixels. Once on the PC, designated points are located on each frame with a trakball and tracked through each successive frame. The relative displacements and local strains with respect to position are calculated for each of these points. The results are then plotted on 3-D and contour plots with a distance weighted least squares 3-D smoothing function using SYGRAPH (SYSTAT, Evanston,IL). Rigid body translation is accounted for by calculating relative displacements. For these tests, only straining in the loading direction was determined.

5.3.2 Strain Fields

From the plots, as expected, higher local strains are present (1) closer to the crack tip, and (2) at higher far-field strains. In these plots, the arrowhead indicates the location of the crack tip (0,0), while the thicker line indicates the eventual crack path.

At the early stages of the fracture test, the far-field strains are low, and the local strains are also low and fairly uniform (Figure 5.17). As the far-field strains increase, we start to see a concentration at the crack tip (Figure 5.18). The local strains start to increase rapidly at this location, while farther away from the crack tip the strains appear to rise gradually and uniformly (Figure 5.19).

Of particular interest is the difference between the Binder, Clupak, and Standard Strain Fields. The Binder sample displays a very high, very concentrated local strain peak at the crack tip, accompanied by a rapid drop-off of strains (Figure 5.20). In contrast, the Clupak sample exhibits much lower maximum local strains despite a higher far-field strain, indicating that the strains are more spread out (Figure 5.21). This correlates well with the damage zone observations we saw in section 5.2. The Clupak samples had a much wider damage zone compared to the narrower, more concentrated zone of the Binder samples.

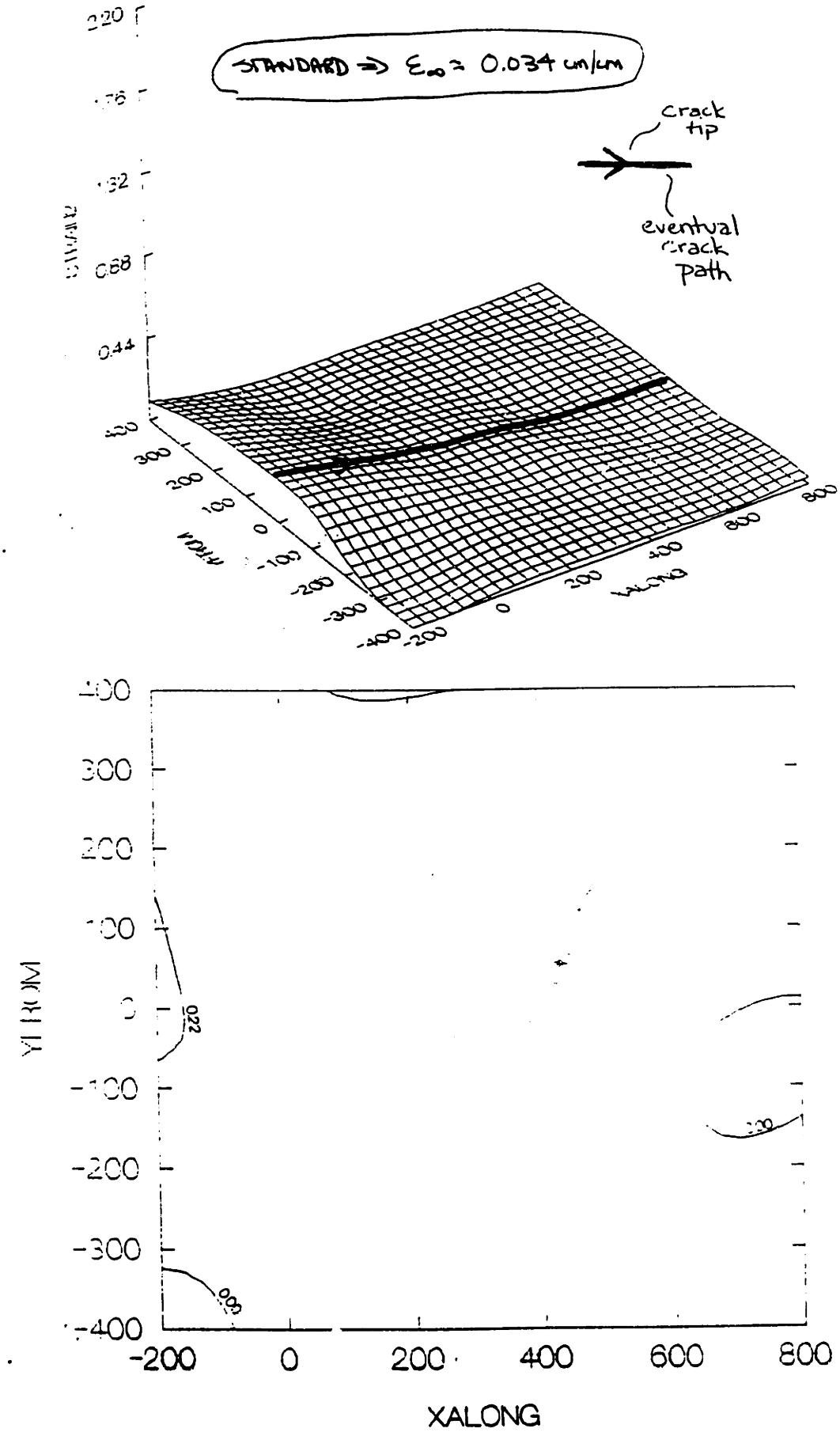

Figure 5.17: Crack-Tip Strain Field: Standard, low strain

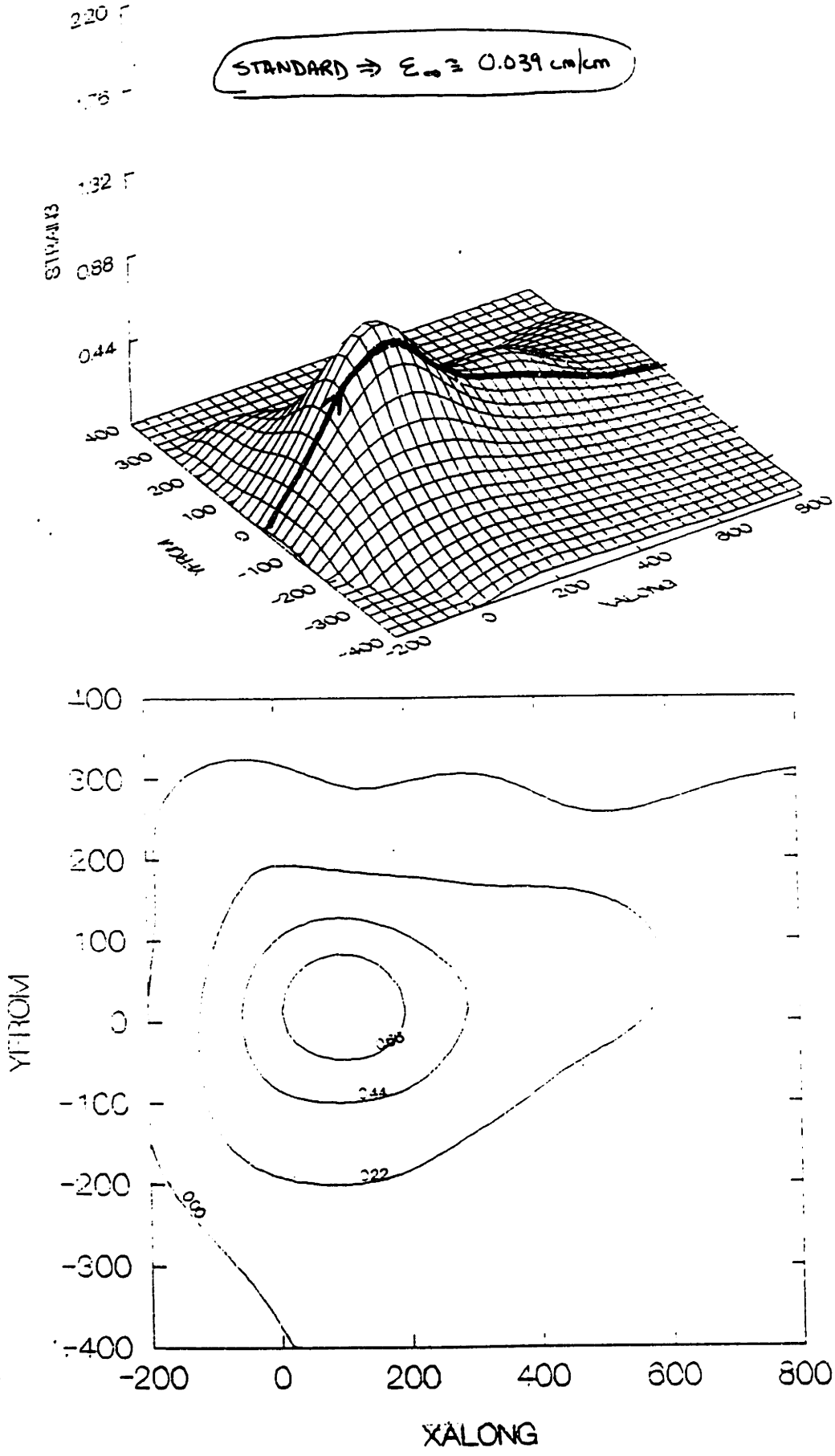

Figure 5.18: Crack-Tip Strain Field: Standard, moderate strain

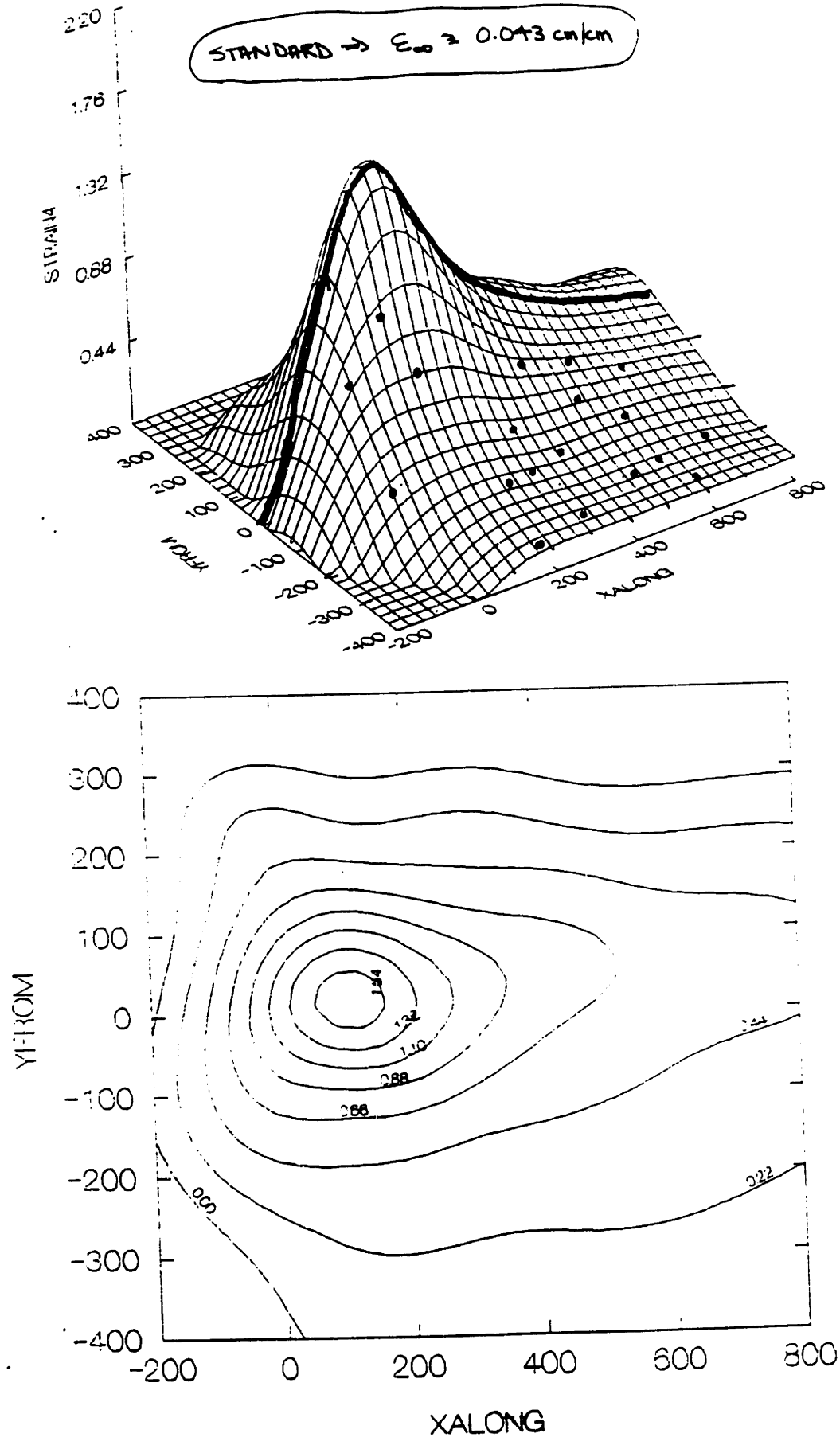

Figure 5.19: Crack-Tip Strain Field: Standard, high strain

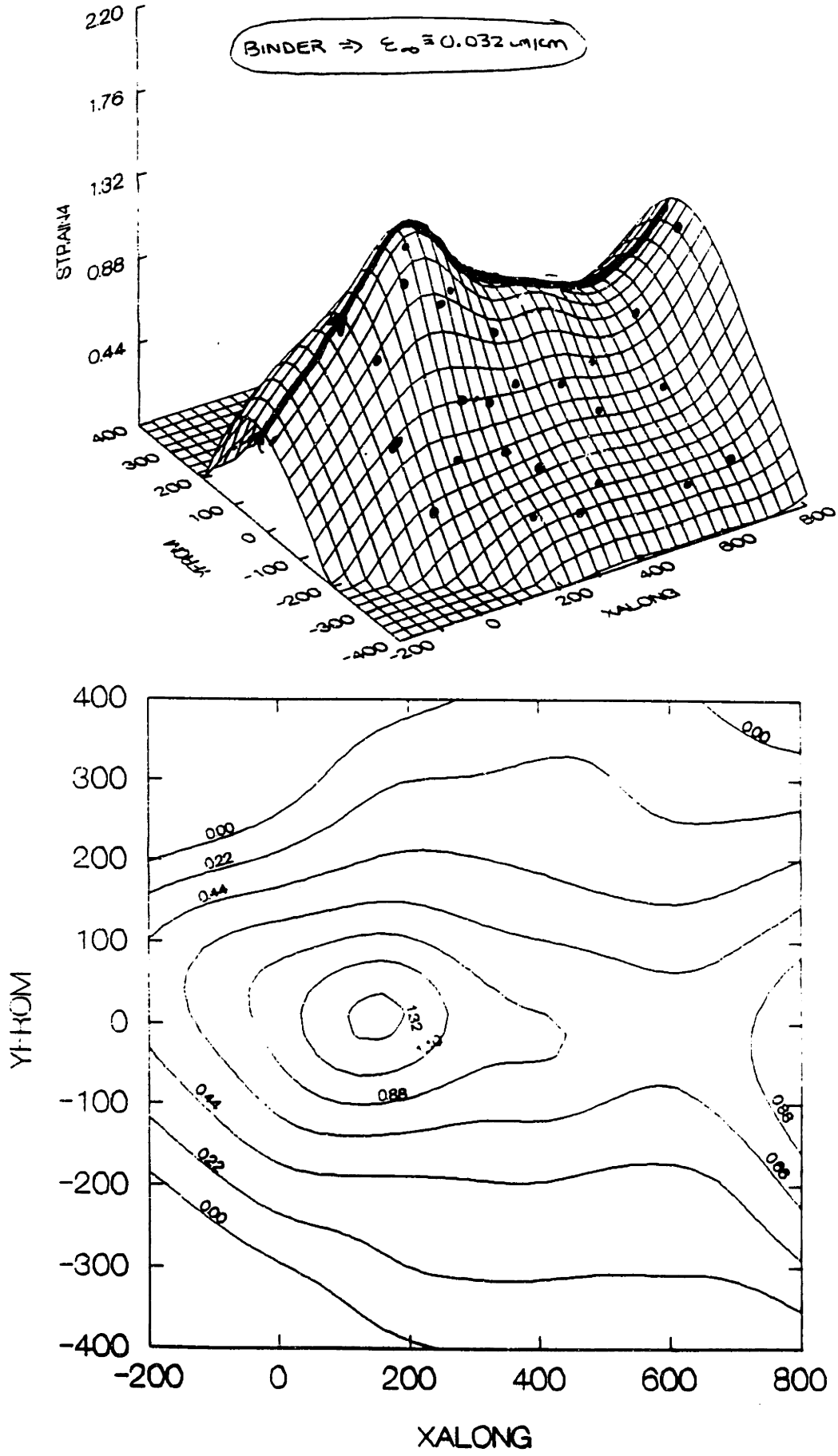

Figure 5.20: Crack-Tip Strain Field: Binder, moderate strain

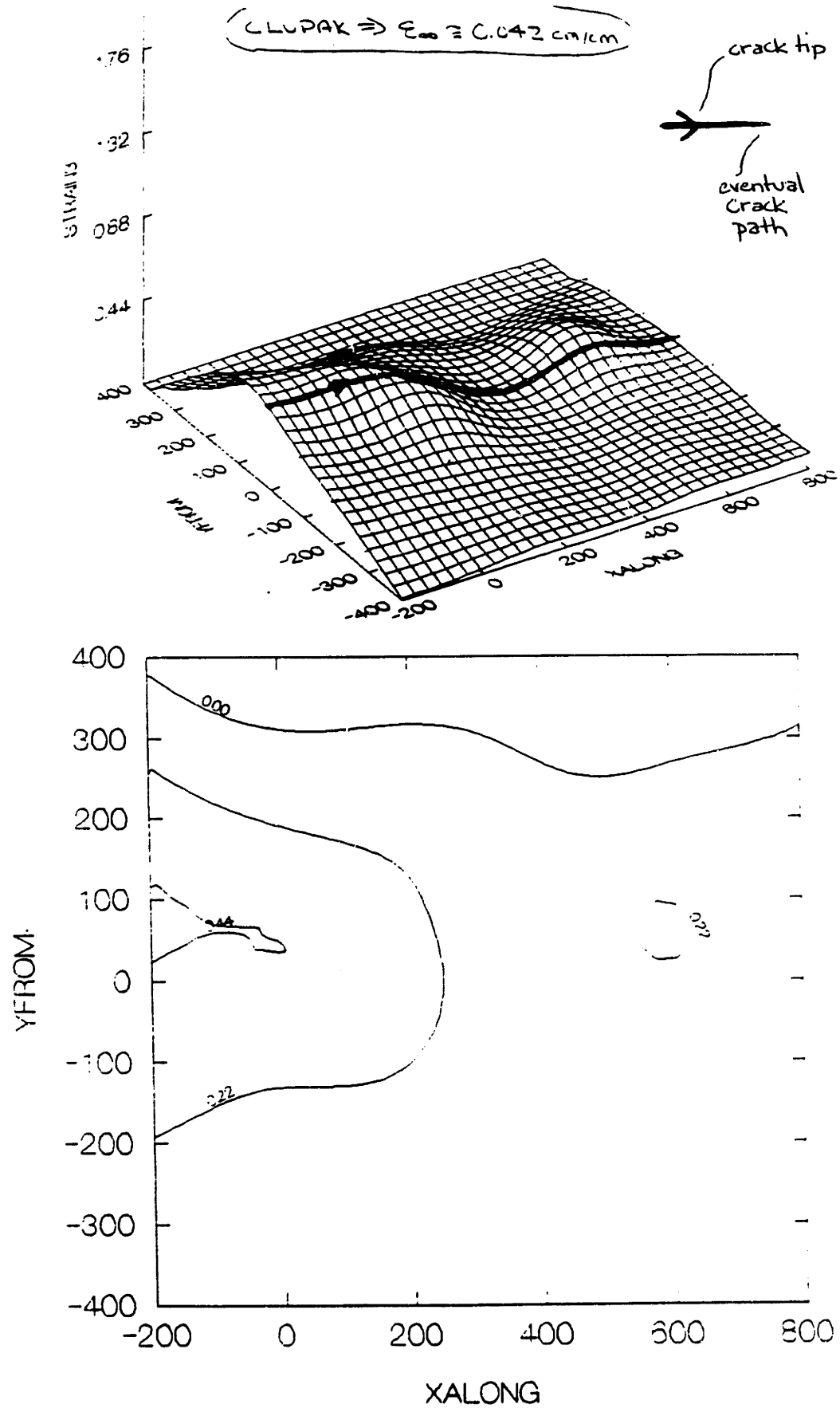

Figure 5.21: Crack-Tip Strain Field: Clupak, moderate strain

As usual, the Standard sample falls somewhere in-between (Figure 5.18).

5.3.3 Comparison with Theory

If the underlying strain field in these papers can be described by a Mode-I type model, the strain fields should generally fit a $1/\sqrt{r}$ relationship. Plotting the local strains versus distance from the crack tip, we see that indeed the points adequately near the crack tip (the filled in points) can be fit successfully to $1/\sqrt{r}$ curves (Figures 5.22, 5.23, 5.24).

Note that the points far away from the crack tip (open points) indicate strains close to the far-field strain values.

The curves fit to the experimental points are of the form

$$\epsilon_{local} = C_0 + C_1 * (\frac{1}{\sqrt{R - C_2}}) \tag{5.1}$$

where R is the distance from the crack tip and the following values for the constants C_0, C_1, and C_2 have been determined for the Standard, Binder, and Clupak samples (Table 5.1).

Table 5.1: Value of Constants for Fit to Mode-I Equation

Material	C_0	C_1	C_2
Standard	-0.096	3.31	16.47
Binder	-0.322	9.13	11.96
Clupak	-0.087	2.91	13.97

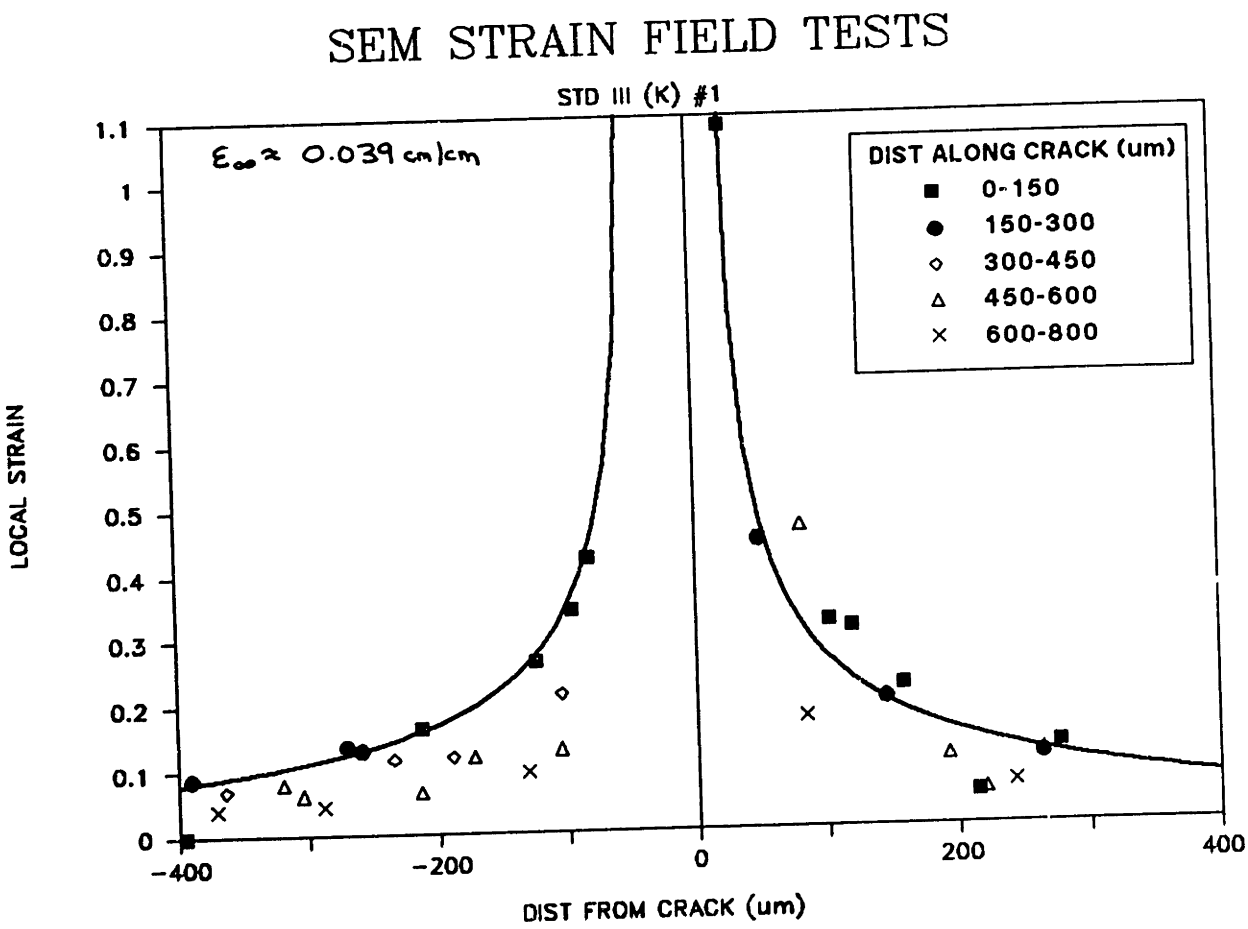

Figure 5.22: Mode-I Curves: Standard

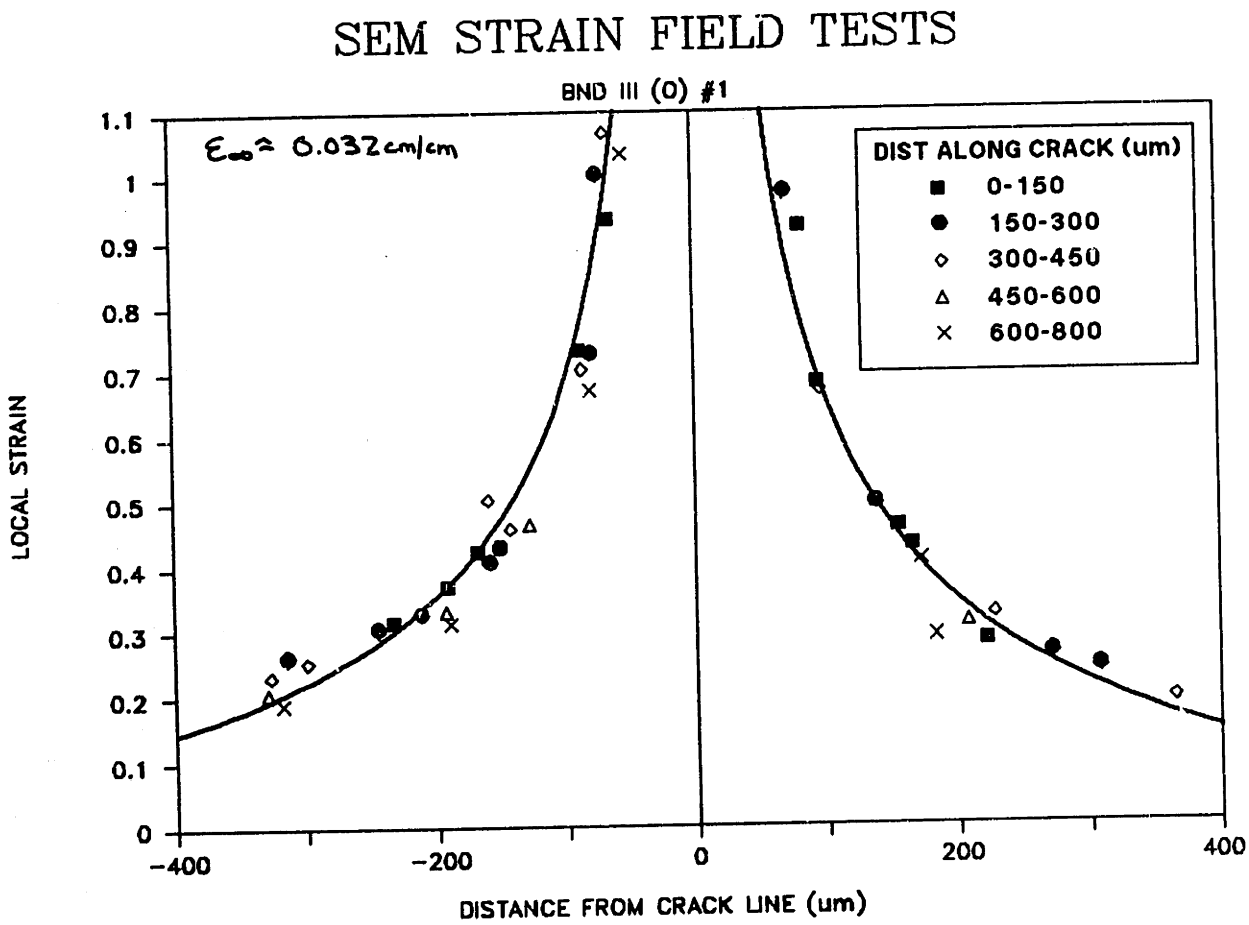

Figure 5.23: Mode-I Curves: Binder

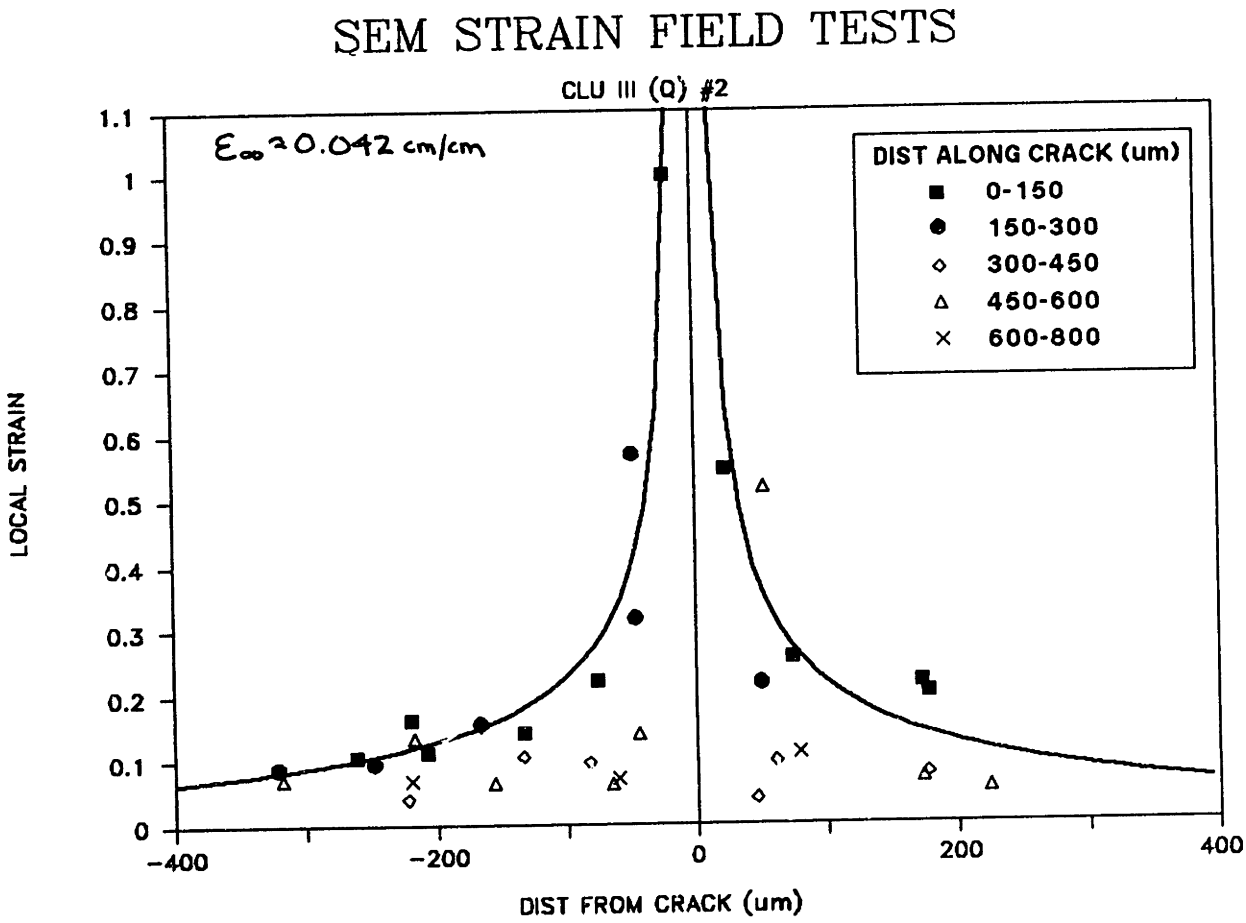

Figure 5.24: Mode-I Curves: Clupak

The reasonably close matches between the measured local strains and the strains expected for a Mode-I elastic field provide strong support for the assumption that the general stress and strain fields near the crack tip can be described in this manner. A more specific derivation of the strains in the plastic zone ahead of the crack tip will be given in the next chapter, along with the complete development of the fracture model.

Chapter 6

The Stochastic-Continuum Model

The specific goal of the model, as stated in Chapter 2, is to predict the fracture behavior of the variety of paper types discussed in this thesis. If successful, this will help to validate the assumptions made in the model. Degrees of success will also help to indicate the strengths and weaknesses of the model and the importance of various factors in controlling or affecting fracture behavior.

In order to clarify the reasoning behind the development of the model, a discussion of the relevant issues and the experimental support for the choices made in the model will be presented in the first section. The second section will cover the fiber pullout analysis. Finally, the last section will present fracture load-displacement curve results from the model for comparison with experimental results. This section will also discuss results of a parametric study of the matrix fracture model and the effect of using probability density functions instead of means for the critical strain values.

6.1 Model Development and Assumptions

How does the fracture of paper occur? We have seen in Chapter 3 that the typical fracture load-displacement curve displays several distinct regions of behavior. These include: (1) an initial, essentially linear, loading region; (2) a crack initiation and incipient crack propagation region prior to reaching a peak stress value; (3) a region of continued, relatively stable crack propagation, eventually leading to complete matrix failure and indicated by a steady load drop; and (4) in the case of the reinforced papers, a fiber pullout region. As also discussed in Chapter 3, for the systems we are dealing with, the fiber reinforcement contribution seems to be primarily independent of the matrix fracture behavior. Therefore, we have chosen as a first approximation to deal with the two subjects – matrix failure and fiber pullout – as additive in terms of modeling the entire fracture load-displacement curve (Figure 6.1). The following section will concentrate on the matrix failure, while section 6.2 will be devoted to the fiber pullout analysis.

As stated previously, the main ingredient of the model is the derivation of the strain field at the crack tip and the application of the critical strain criterion to simulate stable crack propagation behavior. The derivation of the strain, ϵ_y, in the region from the propagating crack tip up to the moving elastic-plastic boundary has been solved by Achenbach and Dunayevsky[1] for steady-state crack propagation in an elastic perfectly-plastic material under plane stress conditions. Portions of their analysis will be presented here; the step-by-step solution can be found in [1]. Interspersed in this condensed form of the strain field solution are relevant results from the experimental work described in the previous chapters and the theoretical basis for the assumptions made. These are provided as evidence supporting the application of Achenbach's strain field solution to the fracture of paper.

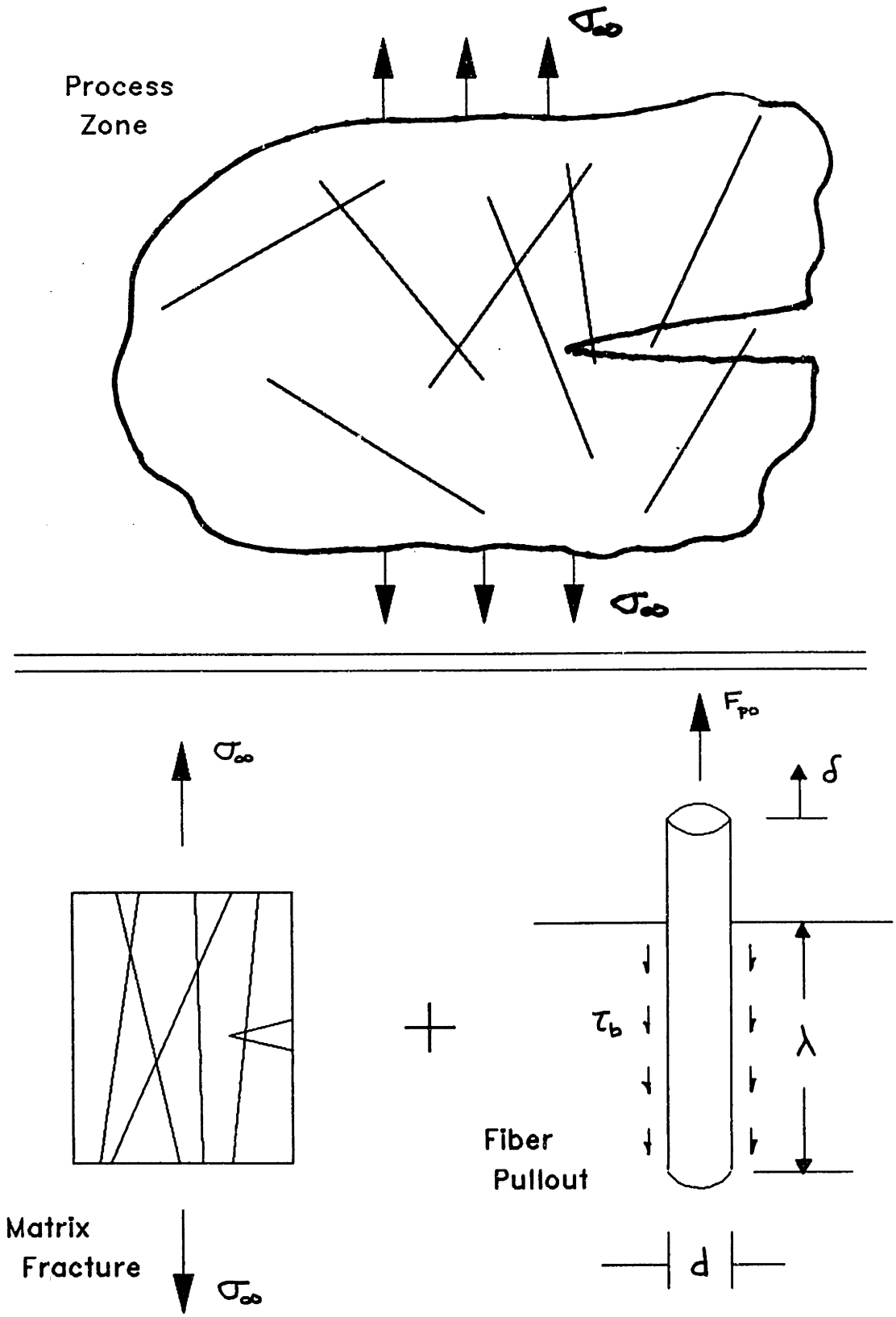

Figure 6.1: Additive Fracture Model Components – Matrix Failure and Fiber Pullout

6.1.1 Plane Stress

Because we are dealing with thin sheets of paper (e.g., $50\mu m$ thick), it is generally accepted that the material is in a state of plane stress. That is, there is no stress in the z-direction ($\sigma_z = 0$), and we can assume that the strains do not vary through the thickness ($\epsilon = \epsilon(x, y)$ only), making the modeling essentially a 2-dimensional problem. The planar structure of paper is due not only to the thinness but also to the fact that in paper the fibers lie primarily in the plane of the sheet.

Analysis of plane stress fracture behavior is not as well defined as that for plane strain. Because of the development of a through the thickness plastic zone and in general, the more significant effect of the plastic zone, one unique characteristic of plane stress fracture is the capacity for stable crack growth. This behavior has been observed in paper and will be discussed more thoroughly in the energy criterion section.

6.1.2 Elastic-Plastic

The basis of Achenbach and Dunayevsky's derivation is the matching of relevant stress components and particle velocities to the dominant terms of appropriate elastic fields at the elastic-plastic boundary. Thus, an obvious condition in our material is the existence of an appropriate elastic zone and plastic zone.

The cyclic test described in Chapter 4 indicated that all the papers we were dealing with did indeed display an elastic-plastic nature. At low loads, uncut samples could be cycled with no significant change in behavior from cycle to cycle. Beyond the apparent yield stress, permanent deformation occurred, as evidenced by the change in the load-deformation behavior (Figures 4.11-4.14) and by the SEM observations of damage in the sample prior to actual failure (Figures 4.15, 4.16).

In the fracture tests, the plastic region is confined to the area directly ahead of the crack tip, as seen in the damage zone observations of Chapter 5 (Figures 5.7-5.15). These observations also satisfied the requirement that there is no net section yielding, which would preclude the assumption of elastic Mode-I fields outside the plastic zone. This is confirmed by the lack of damage observed away from the crack and in the path ahead of the damage zone.

In addition, it should also be noted that effective dimensions of the fibers in the material are reasonably small with respect to the plastic zone size. Fiber diameters are within this limit, and while fiber lengths are greater than this limit, the effective lengths appear to be sufficiently small due to the high degree of bonding between the fibers. This is important in terms of defining the plastic zone behavior in an averaged sense with respect to an array of well-bonded fibers versus the plastic deformation within a single fiber. Of course, the plastic zone behavior is still an aggregate of the intra-fiber deformation within this array of fibers, as discussed briefly in Chapter 4.

From this evidence, we can describe the material behavior during fracture in terms of the behavior within the plastic zone and the elastic behavior outside the plastic zone. For the generalized plane stress case, only the stress components in the x and y directions are relevant. Thus, the Huber-Mises yield criterion describing the material just entering the plastic regime for work hardening materials — or for the entire plastic zone for perfectly plastic materials — can be written as

$$\sigma_x^2 + \sigma_y^2 - \sigma_x\sigma_y + 3\sigma_{xy}^2 = 3k^2 \tag{6.1}$$

A solution which satisfies both Eqn(6.1) and $\sigma_{ij,j} = 0$ (equilibrium) is

$$\sigma_x = k\cos^3\theta \tag{6.2}$$

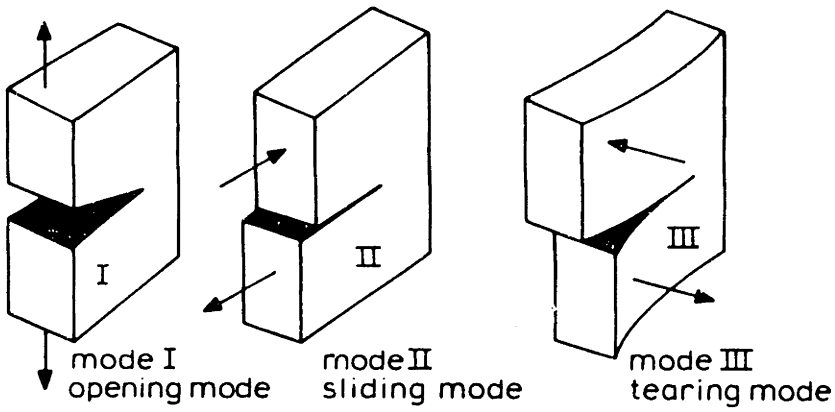

Figure 6.2: Mode-I loading

$$\sigma_y = k(2\cos^3\theta + 3\sin^2\theta\cos\theta) \tag{6.3}$$

$$\sigma_{xy} = -k\sin^3\theta \tag{6.4}$$

It should be noted that this analysis assumes a constant k or perfectly plastic condition, while the experimental results indicate an essentially linear, nonzero plastic modulus. For our model, we have chosen to use the initial yield stress as the constant value for k and have partially accounted for the nonzero plastic modulus by the addition of the alpha factor (see Eqn.6.70, Figure 6.15) to describe the expected load contribution of the plastic zone..

6.1.3 Elastic Mode-I Fields and the Stress Intensity Factor

While we have observed the existence of a plastic zone, the assumption is that outside this plastic zone, the strain and the stress fields behave in a manner consistent with Elastic Mode-I behavior (in-plane loading – Figure 6.2).

For an elastic Mode-I stress field, the in-plane stresses can be expressed as a function of location in polar coordinates (r, θ) with respect to the "crack tip". This expression is of the form

$$\sigma_{ij} = \frac{K_I}{\sqrt{2\pi r}} f_{ij}(\theta) \tag{6.5}$$

where K_I, the stress intensity factor, describes the stress field near the crack tip. For the Mode-I plane stress condition, the stress field is characterized by K_I and the specimen thickness, regardless of the other specimen dimensions and the shape.

Evidence supporting the assumption that elastic Mode-I stress fields could be used to describe the material behavior outside the plastic zone was given by the crack tip strain field measurements presented in Chapter 5. As shown by these measurements, the strain fields exhibit the $1/\sqrt{r}$ form given above (Figures 5.22-5.24).

The Mode-I stress fields chosen by Achenbach and Dunayevsky were developed by Creager and Paris[13] for a notch with a radius of curvature at its tip of ρ. As shown in Figure 6.3, the notch is located at a distance of $\frac{1}{2}\rho$ from E, the center of the elastic field. This configuration was selected because it satisfies the conditions of both yield and continuity of σ_x at the elastic-plastic boundary.

The Mode-I stress fields for this notch configuration near the notch are

$$\sigma_x = (\frac{1}{2\pi R})^{\frac{1}{2}} K_I \{\cos\frac{\psi}{2}[1 - \sin\frac{\psi}{2}\sin\frac{3\psi}{2}] - \frac{\rho}{2R}\cos\frac{3\psi}{2}\} \tag{6.6}$$

$$\sigma_y = (\frac{1}{2\pi R})^{\frac{1}{2}} K_I \{\cos\frac{\psi}{2}[1 + \sin\frac{\psi}{2}\sin\frac{3\psi}{2}] + \frac{\rho}{2R}\cos\frac{3\psi}{2}\} \tag{6.7}$$

$$\sigma_{xy} = (\frac{1}{2\pi R})^{\frac{1}{2}} K_I \{\sin\frac{\psi}{2}\cos\frac{\psi}{2}\cos\frac{3\psi}{2} - \frac{\rho}{2R}\sin\frac{3\psi}{2}\} \tag{6.8}$$

For generalized plane stress, the displacements in the x and y directions corresponding to the above stresses are

$$u = (\frac{R}{2\pi})^{\frac{1}{2}} \frac{1}{2\mu} K_I \{\cos\frac{\psi}{2}[\kappa - 1 + 2\sin^2\frac{\psi}{2}] + \frac{\rho}{R}\cos\frac{\psi}{2}\} \tag{6.9}$$

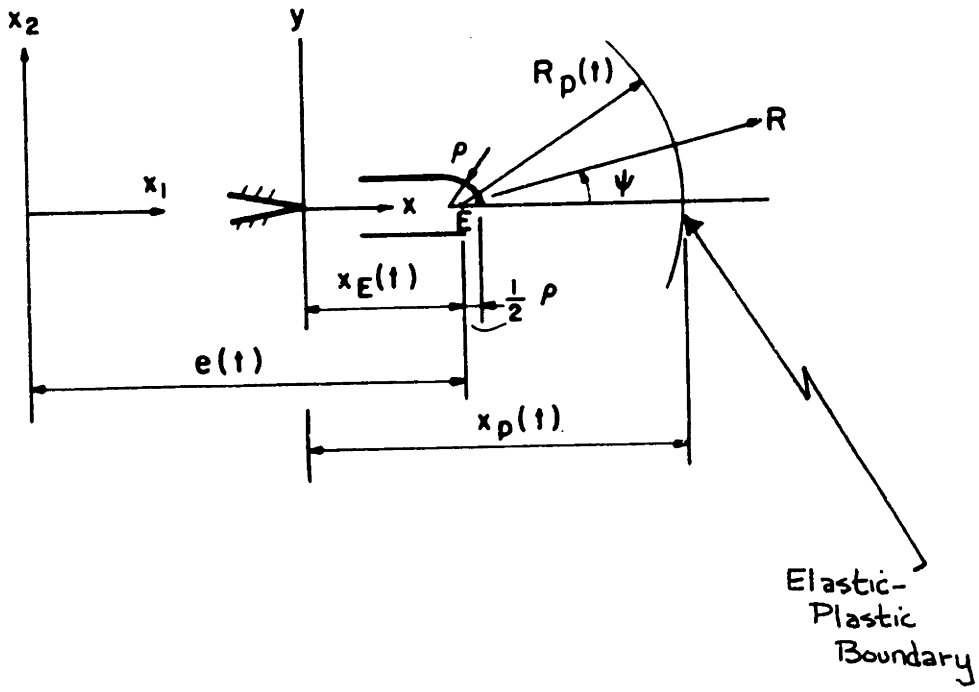

Figure 6.3: Mode-I Elastic Field – Notch Configuration

$$v = (\frac{R}{2\pi})^{\frac{1}{2}} \frac{1}{2\mu} K_I \{\sin\frac{\psi}{2}[\kappa + 1 - 2\cos^2\frac{\psi}{2}] + \frac{\rho}{R}\sin\frac{\psi}{2}\} \tag{6.10}$$

where

$$\kappa = (3-\nu)/(1+\nu)$$

6.1.4 The Plastic Zone and the Elastic-Plastic Boundary

Since the elastic field should just reach the yield condition at the elastic-plastic boundary, we can substitute Eqns(6.6-6.8) into the yield criterion (Eqn.6.1), for $R = R_p$ and small values of y.

$$[(\frac{1}{2\pi R_p})^{\frac{1}{2}} K_I]^2 [1 + 3(\frac{\rho}{2R_p})^2] = 3k^2 \tag{6.11}$$

For the second condition, σ_x should be continuous at the elastic-plastic boundary on y=0. Therefore, we can set the elastic field value for σ_x (Eqn.6.6), at $R = R_p$ equal to the value for σ_x in the plastic yield zone (Eqn.6.2). For y=0, $\theta = 0$ and $\psi = 0$, and the resulting equation is

$$k = (\frac{1}{2\pi R_p})^{\frac{1}{2}} K_I (1 - \frac{\rho}{2R_p}) \tag{6.12}$$

From Eqn(6.11) and Eqn(6.12),

$$\frac{\rho}{R_p} = \frac{2}{3} \tag{6.13}$$

And Eqn(6.12) simplifies to

$$R_p = \frac{1}{2\pi}(\frac{K_I}{\frac{3}{2}k})^2 \tag{6.14}$$

In addition, from matching other stress components,

$$x_E = (1-\gamma)x_p, \quad \textit{and thus} \quad x_p = \frac{1}{\gamma} R_p \tag{6.15}$$

6.1.5 Strain Rates and Strains

The rate of deformation or strain rates are defined below

$$D_{ij} = D^e_{ij} + D^p_{ij} \tag{6.16}$$

$$D^e_{ij} = \frac{1}{E}[(1+\nu)\dot{\sigma}_{ij} - \nu\delta_{ij}\dot{\sigma}_{kk}] \tag{6.17}$$

$$D^p_{ij} = \dot{\Lambda} s_{ij} \tag{6.18}$$

$$s_{ij} = \sigma_{ij} - \frac{1}{3}\sigma_{kk}\delta_{ij} \tag{6.19}$$

Using the small angle representation ($\tan\theta \Rightarrow \theta \Rightarrow y/x << 1$) and a Taylor expansion for the trigonometric functions ($\sin\theta, \cos\theta$) of Eqns. 6.2-6.4, the stress-strain relations above yield the following expressions for the rates of deformation.

$$D_x = -\dot{a}(t)\frac{k}{E}\frac{3}{x}(\frac{y}{x})^2 - \dot{\Lambda}k(\frac{y}{x})^2 + O(\frac{y}{x})^4 \tag{6.20}$$

$$D_y = \dot{a}(t)\frac{k\nu}{E}\frac{3}{x}(\frac{y}{x})^2 + \dot{\Lambda}k[1 + \frac{1}{2}(\frac{y}{x})^2] + O(\frac{y}{x})^4 \tag{6.21}$$

$$D_{xy} = -\dot{a}(t)\frac{(1+\nu)k}{E}\frac{3}{x}(\frac{y}{x})^3 - \dot{\Lambda}k(\frac{y}{x})^3 + O(\frac{y}{x})^5 \tag{6.22}$$

If we expand the strains $\dot{u}, \dot{v}$, and $\dot{\Lambda}$ in terms of powers of y

$$\dot{u}(x,y,t) = \dot{u}_0(x,t) + \dot{u}_2(x,t)y^2 + O(y^4) \tag{6.23}$$

$$\dot{v}(x,y,t) = \dot{v}_1(x,t)y + O(y^3) \tag{6.24}$$

$$\dot{\Lambda}(x,y,t) = \dot{\Lambda}_0(x,t) + \dot{\Lambda}_2(x,t)y^2 + O(y^4) \tag{6.25}$$

The rates of deformation can be expressed in terms of these strains as

$$D_x = \frac{\partial \dot{u}_0}{\partial x} + \frac{\partial \dot{u}_2}{\partial x}y^2 \tag{6.26}$$

$$D_y = \dot{v}_1 \tag{6.27}$$

$$D_{xy} = \frac{1}{2}(2\dot{u}_2 + \frac{\partial \dot{v}_1}{\partial x})y \tag{6.28}$$

where

$$\frac{\partial \dot{u}_0}{\partial x} = 0, \quad \frac{\partial \dot{u}_2}{\partial x} = -3\frac{k}{E}\frac{\dot{a}}{x^3} - \frac{1}{x^2}\dot{\Lambda}_0 k \tag{6.29}$$

$$\dot{v}_1 = \dot{\Lambda}_0 k \tag{6.30}$$

$$2\dot{u}_2 + \frac{\partial \dot{v}_1}{\partial x} = 0 \tag{6.31}$$

By combining Eqns(6.29-6.31), we obtain

$$\frac{1}{2}\frac{\partial^2 \dot{v}_1}{\partial x^2} - \frac{\dot{v}_1}{x^2} = 3\frac{k}{E}\frac{\dot{a}}{x^3} \tag{6.32}$$

The general solution to Eqn(6.32) is

$$\dot{v}_1 = \frac{k}{E}\{-2\frac{\dot{a}}{x}ln(\frac{x}{x_p}) + \frac{B(t)}{x} + C(t)x^2\} \tag{6.33}$$

where

$$B(t) = B_1\dot{a}(t) + B_2\dot{x_p}(t) \tag{6.34}$$

$$C(t) = [C_1\dot{a}(t) + C_2\dot{x_p}(t)]/[x_p(t)]^3 \tag{6.35}$$

Note that in the plane of the crack, $\epsilon_y = v_1$.

6.1.6 Steady-State Crack Propagation

For the steady-state case, we assume that all fields are time-invariant to an observer traveling with the crack tip. That is, ϵ_y depends on $x + x_1 - a(t)$ only. Thus, we have $\dot{a} = constant = c_F$, $\dot{x}_p = 0$, *and* $(\dot{}) = -c_F\partial_x$. Equation 6.33 becomes

$$\frac{dv_1}{dx} = \frac{k}{E}\{\frac{2}{x}ln(\frac{x}{x_p}) - \frac{B_1}{x} - \frac{C_1x^2}{x_p^3}\} \tag{6.36}$$

where x_p = constant. The above equation can then be integrated to yield

$$\epsilon_y(x) = (\epsilon_y)_{PB} + \frac{k}{E}\{[ln(\frac{x}{x_p})]^2 - B_1ln(\frac{x}{x_p}) - \frac{1}{3}C_1[(\frac{x}{x_p})^3 - 1]\} \tag{6.37}$$

where

$$B_1 = \frac{1}{32}\frac{1}{\gamma^2}[\kappa + 5 + 4\gamma(\kappa+1)](E/\mu) - \frac{2}{3} \quad (6.38)$$

$$C_1 = \frac{1}{32}\frac{1}{\gamma^2}[-(\kappa+5) + 2\gamma(\kappa+1)](E/\mu) + \frac{2}{3} \quad (6.39)$$

$$(6.40)$$

Thus for a given external load, the plastic zone x_p, and subsequently the strain at a given x along the crack plane and within the plastic zone, can be determined. This strain can be compared to the critical strain required for matrix failure at that location.

6.1.7 Energy Criterion

For general reference, see Broek[6]

From Griffith-Irwin, one requirement for crack propagation is that the elastic energy in the system available for release (G) must be equal or greater than the resistance to crack propagation (R). G is the elastic energy release rate and can be calculated from

$$G = \frac{\pi\sigma^2 a}{E} \quad (6.41)$$

where

$$\sigma = \text{far} - \text{field stress}$$

$$a = \text{crack length}$$

G can also be represented in terms of the stress intensity factor K_I

$$G = K_I^2/E \qquad \text{for plane stress} \quad (6.42)$$

For brittle materials, the crack resistance (R) or the energy required for crack growth is simply the surface energy required to create the two new surfaces of the crack. This was the original discovery made by Griffith for glass in the 1920's. In the aftermath of the fracture studies initiated during World War II, Irwin and Orowan discovered that the energy requirement for more ductile materials was actually much higher and was related to the energy utilized in formation of the plastic zone. If this plastic zone and the energy expended is identical for each unit of crack extension, we would expect R to be constant. This is generally true for plane strain conditions. However, for plane stress, R has been shown to vary with amount of crack growth.

R versus crack size exhibits a concave shape, increasing with some crack growth and then leveling off, often eventually resulting in a critical crack length leading to fracture instability ($G > R$). In general, for materials in a condition of plane stress, this increase in crack resistance results in stable crack growth. At a certain stress level, the crack will start to propagate. Since the crack resistance then increases, propagation will cease unless the stress level is increased. In the fracture tests described in Chapter 3, the crack growth was stable up until the last centimeter or so of crack propagation. In the model we have assumed stable crack propagation for the entire test. Thus, we have only the following possible conditions

$$G < R \qquad \text{(no crack propagation)} \tag{6.43}$$

$$or \quad G = R \qquad \text{(stable crack propagation)} \tag{6.44}$$

An analytical expression for R is needed in order to use the model as a predictive tool. Unfortunately, a satisfactory expression has not yet been derived. However, Achenbach and Li[2] have derived a relationship between a dimensionless crack length and the ratio of crack resistance K_R to the critical stress intensity factor K_{IC}. Since the ratio of critical failure strain ϵ_y^f to strain at the elastic-plastic boundary ϵ_{PB}

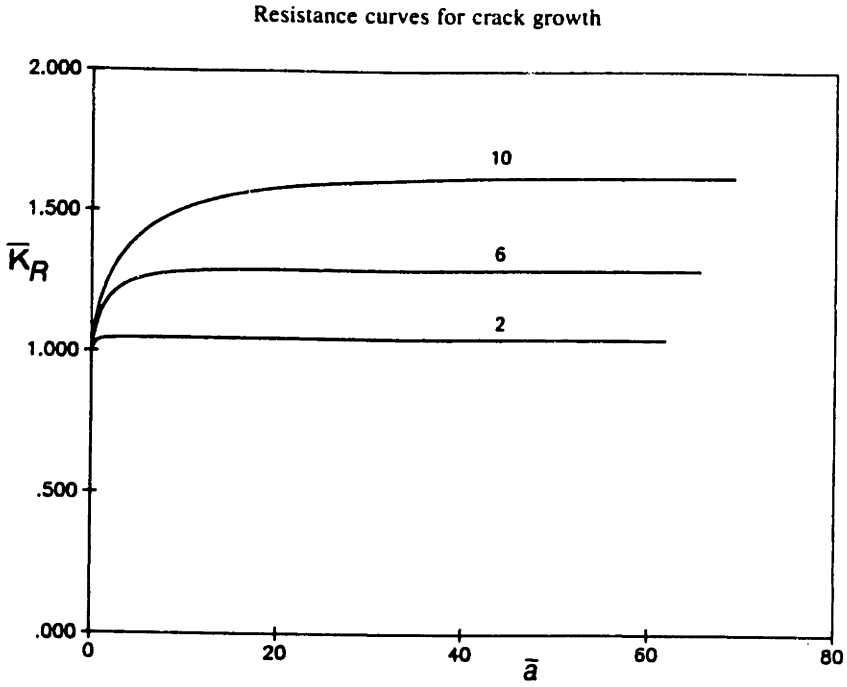

Fig. 2. Resistance curves for values of $\epsilon_v^f \equiv \epsilon_v^{Pf}/(\epsilon_v)_{PB} = 2$, 6 and 10; $\overline{K}_R(\bar{a}) = K_R(\bar{a})/K_{IC}$; $\bar{a} = a(t)/x_f$.

Figure 6.4: Crack Resistance/KIC ratio

for our materials is close to 2, we see from Figure 6.4 [2] that the crack resistance does not change significantly with crack length and is very close to K_{IC}. Thus, in the computer implementation of this model, the energy criterion for stable crack propagation is manifested in the requirement

$$K_I < K_{IC} \qquad \text{(no crack propagation)} \tag{6.45}$$

$$or \quad K_I = K_{IC} \qquad \text{(stable crack propagation)} \tag{6.46}$$

6.1.8 Strain Criterion

As stated by Broek and others, the energy criterion is necessary *but not sufficient* for crack propagation. In addition to satisfying the energy criterion, the material

at the crack tip must be ready to fail, i.e., the local strain must reach the critical breaking strain level. This strain criterion is tested by comparing the local strains from the elastic-plastic strain field analysis with the expected breaking strains of the local material.

An additional criterion proposed by McClintock and Irwin[23] requires that the strain at a fixed microstructural distance x_f ahead of the crack tip exceed the critical failure strain. Using either the elastic-plastic strain field or the elastic mode-I strain field, the strains at the crack tip approach infinity as $r \rightarrow 0$. Since this would result in immediate crack initiation, there must be a minimum characteristic distance from the crack tip where the strain field analysis can be applied. The choice of x_f is rather arbitrary at this time. However, since x_f should be related to the material structure in some way, we have chosen x_f to be approximately equal to the diameter of the wood fibers or $10\mu m$. As it turns out, at this value, the strain criterion was satisfied when the energy criterion was satisfied for all the cases that were run.

Note that we have chosen to use a strain criterion. This is because failure is occurring within the plastic zone where the stress gradient is quite low in comparison to the strain gradient. Using strain thus gives us a much more sensitive criterion. In this stochastic model of fracture, the critical strains are actually represented by a probability density function (normally distributed) rather than an average constant value.

6.1.9 Summary

In summary, the entire fracture sequence can be described as follows. As the material is initially loaded, a plastic zone begins to form at the crack tip, but the majority of the material is still in the elastic state. In order for fracture to occur, two requirements must be satisfied. First, there must be enough energy in the body to overcome the

resistance to crack growth. This resistance is primarily the energy it takes to form the plastic zone. Second, if the energy criterion is satisfied, the material in the plastic zone must be strained to its critical strain level so that it is ready to fail. If both these conditions exist, then the crack will propagate.

6.2 Fiber Pullout Analysis

Once the crack has propagated through a section of the matrix, the reinforcing fibers bridging the gap will begin to pull out. The force required for this pullout can be added to the fracture load-displacement curve. We treat this pullout contribution as an additive factor which is independent from the matrix fracture component except for the effect of the distance of the crack propagation. A theoretical analysis of this pullout force is given in this section.

In a fracture test, the fibers are actually in a double-sided pullout configuration. That is, they are embedded in the material on both sides of the crack. Pullout, however, can only occur from one side at any given instant. Hein[16] has shown (Figure 3.16) that rather than constantly alternating, pullout occurs primarily from one side only – the side with the weakest resistance due to either a shorter embedment length or weaker bonding. Thus, we have chosen to model the pullout as a summation of the one-sided pullout force contribution from each fiber active in the pullout region.

For one-sided pullout, the force for a single fiber inclined to the crack plane at an angle ϕ (Figure 6.5) is [50]

$$F_{sf} = e^{f\phi} F_{sf(\phi=0)} = e^{f\phi} \tau_b \pi d \lambda \tag{6.47}$$

where

f = friction coefficient

ϕ = angle of inclination

τ_b = bond strength (frictional)

d = fiber diameter

λ = remaining embedded length

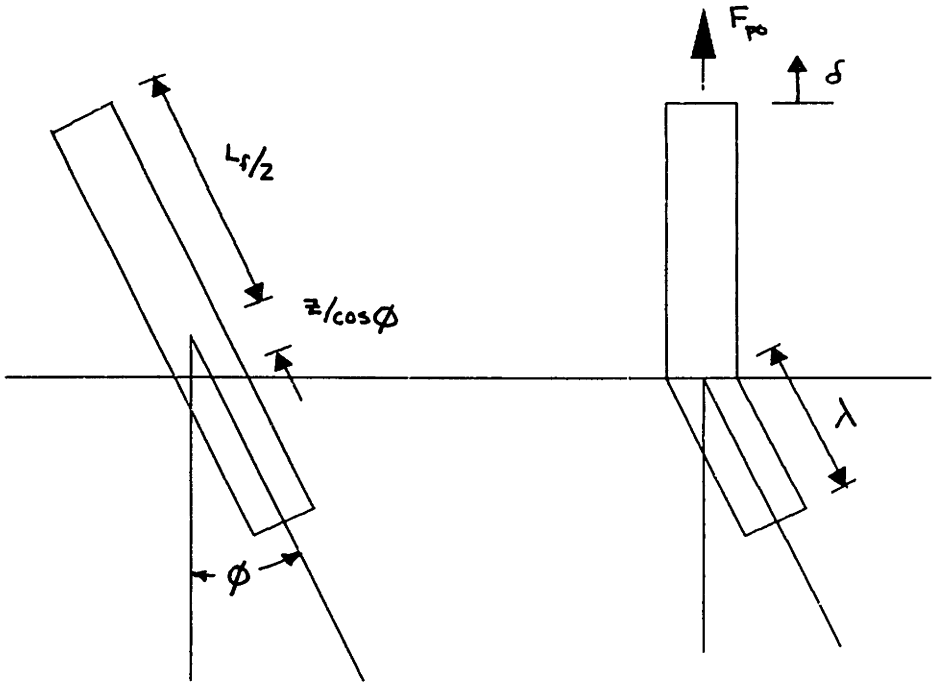

Figure 6.5: One-sided single fiber pullout

$$\lambda = \frac{L_f}{2} - \frac{z}{\cos\phi} - \delta \tag{6.48}$$

Since the crack propagates from one side of the sample to the other, there is a slight angle to the crack tip opening prior to complete specimen failure. As a result, fibers are pulled out to different degrees depending on their proximity to the crack tip. Fibers at the crack tip have just started to pull out, while fibers at locations where the crack tip has already passed through have experienced more pullout. If we assume that the pullout length, δ, is a linear function of the location of the fiber with respect to the current location of the crack tip (Figure 6.6), the following expression can be used to relate pullout length and crack tip opening displacement or crack propagation length.

$$\delta = \frac{y_o(x_o - x)}{x_o} = y_o - 2x\tan\alpha \tag{6.49}$$

$$x_o = y_o/2\tan\alpha \tag{6.50}$$

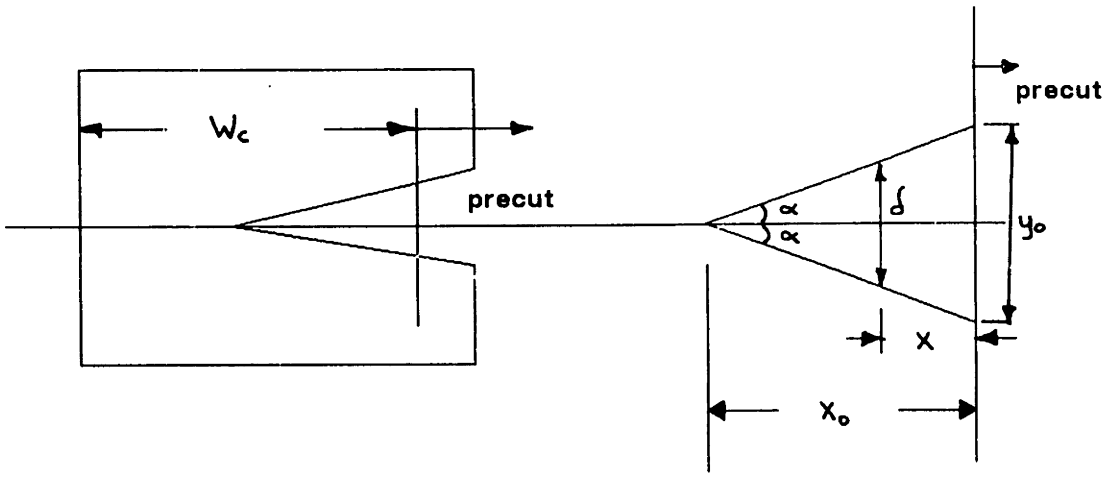

Figure 6.6: Pullout Length as a Function of Fiber Location Along Crack

where

y_o = crack opening displacement at original crack initiation point

x_o = crack propagation length for a given y_o

x = fiber location along crack

δ = pulled – out length at x

α = misalignment angle

So, at the instant when $y = y_o$,

$$F_{po}(allfibers) = N_a \int_{x_1}^{x_2} p(x)dx \int_0^{\frac{L_f}{2}} p(z)dz \int_0^{\arccos(\frac{2z}{L_f})} p(\phi)d\phi F_{sf} \tag{6.51}$$

where from Eqns (6.45) and (6.46)

$$F_{sf} = e^{f\phi}\tau_b \pi d(\frac{L_f}{2} - \frac{z}{\cos\phi} - \delta) \tag{6.52}$$

x_2, x_1 = range of active pull – out

N_a = number of active bridging fibers

v_f = fiber volume fraction

n_{lay} = number of fiber layers in sheet

$$N_a = \frac{(x_2 - x_1)v_f n_{lay}}{d} \tag{6.53}$$

If we assume that the reinforcing fibers are randomly distributed throughout the sheet, then the probability density functions for their expected orientation with respect to the crack (ϕ), the initial embedment length (z), and the location along the eventual crack (x) are

$$p(\phi) = 1/\pi \qquad ,0 \leq \phi < \pi \tag{6.54}$$

$$p(z) = 2/L_f \qquad ,0 \leq z \leq L_f/2 \tag{6.55}$$

$$p(x) = 1/(x_2 - x_1) \qquad ,x_1 \leq x \leq x_2 \tag{6.56}$$

If we take $\tau_b, d, f, y_o, \alpha, n_{lay}$, and L_f to be constants, the total pullout force contribution for the sheet is

$$F_{po} = \tau_b dN_a \int_{x_1}^{x_2} \frac{1}{x_2 - x_1} dx \int_0^{\frac{L_f}{2}} \frac{2}{L_f} dz \int_0^{\arccos(\frac{2z}{L_f})} \frac{1}{\pi} d\phi e^{f\phi} \pi (\frac{L_f}{2} - \delta - \frac{z}{\cos\phi}) \tag{6.57}$$

In order to simplify the integration of this expression, we break it down into two parts

$$let\ A = \tau_b dN_a \int_{x_1}^{x_2} \frac{1}{x_2 - x_1} dx \int_0^{\frac{L_f}{2}} \frac{2}{L_f} dz \int_0^{\arccos(\frac{2z}{L_f})} \frac{1}{\pi} d\phi e^{f\phi} \pi (\frac{L_f}{2} - \delta) \tag{6.58}$$

$$let\ \ B = \tau_b dN_a \int_{x_1}^{x_2} \frac{1}{x_2 - x_1} dx \int_0^{\frac{L_f}{2}} \frac{2}{L_f} dz \int_0^{\arccos(\frac{2z}{L_f})} \frac{1}{\pi} d\phi e^{f\phi} \pi (\frac{z}{\cos\phi}) \tag{6.59}$$

such that $F_{po} = A - B$

Integrating A by substitution and B by using a Taylor Series Expansion for the trigonometric and exponential functions (see Appendix C), we get

$$A = \tau_b dN_a[\frac{e^{\frac{f\pi}{2}} - f}{f^2+1}]\int_{x_1}^{x_2} \frac{1}{x_2 - x_1}(\frac{L_f}{2} - \delta)dx \tag{6.60}$$

$$B = \tau_b dN_a[(\frac{f\pi^2}{32} - \frac{f}{8}) + (\frac{f^2+1}{6})(\frac{\pi^3 - 6\pi}{32})]\int_{x_1}^{x_2} \frac{1}{x_2 - x_1}(\frac{L_f}{2})dx \tag{6.61}$$

During fracture of the sheet, there are three distinct regimes of fiber pullout, In the first regime, as the crack initiates and begins to propagate through the sheet, more and more reinforcing fibers are being added to the active pullout region. In the second regime, a steady state case is reached where as fibers are being added through the exposure of new crack surfaces, fibers on the other end have just completely pulled out. The average number of active fibers and their relative remaining pullout lengths remain constant, simply shifting over as the crack progresses. In the third and final regime, the sheet has completely failed, and no more new reinforcing fibers are being added. This regime consists of the pullout of the remaining fibers.

The transition points between these three regimes are

$$0 < \ y_o \ \leq \frac{L_f}{2} - Z \qquad \text{(initial crack propagation)} \tag{6.62}$$

$$\frac{L_f}{2} - Z < \ y_o \ \leq 2W_c \tan\alpha \qquad \text{(crack propagation plateau)} \tag{6.63}$$

$$2W_c \tan\alpha < \ y_o \ \leq 2W_c \tan\alpha + \frac{L_f}{2} - Z \qquad \text{(post matrix failure)} \tag{6.64}$$

Now, integrating the force (Eqn.6.54) over the region of active pull-out

where

$$Z = \text{effect of term B} = L_f \frac{K_B}{K_A}$$

$$W_c = \text{initial uncracked sheet width}$$

$$m = \text{value of x where average embedded length just equals 0}$$
$$= \frac{y_o - \frac{L_f}{2} + Z}{2\tan\alpha}$$

and

$$K_A = \frac{e^{\frac{f\pi}{2}} - f}{f^2 + 1} \tag{6.65}$$

$$K_B = (\frac{f\pi^2}{32} - \frac{f}{8}) + (\frac{\pi^3 - 6\pi}{32})(\frac{f^2 + 1}{6}) \tag{6.66}$$

We get for the three regimes:

Initial Crack Propagation

For $0 < y_o \leq \frac{L_f}{2} - Z$,

$$x_2 - x_1 = x_o = y_o/2\tan\alpha$$

$$F_{po} = K_A\tau_b d\frac{v_f}{d}[(\frac{L_f}{2} - y_o)(y_o/2\tan\alpha) + (y_o^2/4\tan\alpha)]$$
$$-K_B\tau_b d\frac{v_f}{d}[y_o/2\tan\alpha](\frac{L_f}{2})$$

$$= \tau_b v_f[y_o/2\tan\alpha][K_A(\frac{L_f}{2} - \frac{y_o}{2}) - K_B(\frac{L_f}{2})] \tag{6.67}$$

Crack Propagation Plateau

For $\frac{L_f}{2} - Z < y_o \leq 2W_c\tan\alpha$,

$$x_2 - x_1 = x_o - m = (\frac{L_f}{2} - Z)/2\tan\alpha$$

$$F_{po} = K_A\tau_b d\frac{v_f}{d}[(\frac{L_f}{2}-y_o)((\frac{L_f}{2}-Z)/2\tan\alpha)+((\frac{L_f}{2}-Z)(2y_o-(\frac{L_f}{2}-Z))/4\tan\alpha)]$$
$$-K_B\tau_b d\frac{v_f}{d}[(\frac{L_f}{2}-Z)/2\tan\alpha](\frac{L_f}{2})$$

$$= \tau_b v_f[\frac{\frac{L_f}{2}-Z}{2\tan\alpha}][K_A(\frac{L_f}{4}+\frac{Z}{2})-K_B(\frac{L_f}{2})] \quad (6.68)$$

Post Matrix Failure

And, for $2W_c\tan\alpha < y_o \leq 2W_c\tan\alpha + \frac{L_f}{2} - Z$,

$$x_2 - x_1 = W_c - m = W_c - (y_o - (\frac{L_f}{2}-Z))/2\tan\alpha$$

$$F_{po} = K_A\tau_b d\frac{v_f}{d}[(\frac{L_f}{2}-y_o)(W_c-(y_o-(\frac{L_f}{2}-Z))/2\tan\alpha)$$
$$+(W_c^2\tan\alpha-(y_o-(\frac{L_f}{2}-Z))^2/4\tan\alpha)]$$
$$-K_B\tau_b d\frac{v_f}{d}[W_c-(y_o-(\frac{L_f}{2}-Z))/2\tan\alpha](\frac{L_f}{2})$$

$$= \tau_b v_f[W_c-\frac{y_o-(\frac{L_f}{2}-Z)}{2\tan\alpha}][K_A(\frac{L_f}{4}-\frac{y_o}{2}+W_c\tan\alpha+\frac{z}{2})-K_B(\frac{L_f}{2}) \quad (6.69)$$

Figure 6.7 shows a typical result of this analysis. The three distinct regions discussed above and in the fiber reinforcement section of Chapter 3 can be seen clearly in this figure. The first region involves ever increasing numbers of active fibers. However, the load per fiber drops as the crack propagates due to the drop in the average pullout length per fiber. This gives the first part of the curve its concave shape. In the second part, a load plateau is reached as the addition of fibers bridging the newly formed crack surfaces is offset by an equal number of fibers which have been

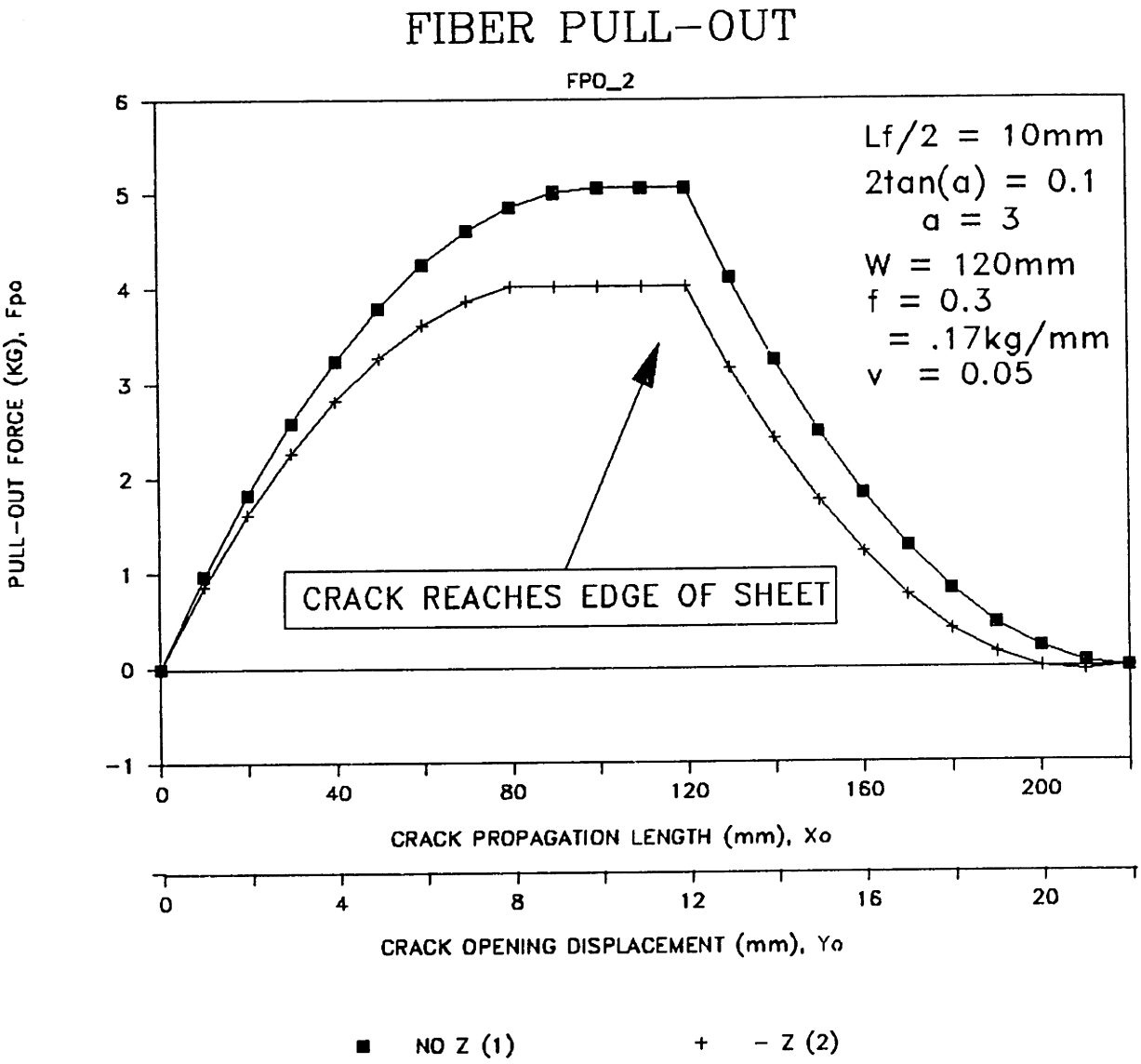

Figure 6.7: Typical Fiber Pullout Results

completely pulled out. In the third and final part, the matrix has failed completely, and the contribution from the remaining bridging fibers continues to drop until all the fibers have been pulled out.

A study of the effect of various parameters – e.g., fiber length, fiber %vol, uncracked sheet width – was presented in Chapter 3.

6.3 Parametric Study and Model Results

6.3.1 Computer Model Results

In order to check this model, a computer implementation based on the model has been written to produce results for comparison with experimental results. A flowchart for the computer model is shown in Figure 6.8.

The computer model involves the incremental displacement of a computer generated sheet. The material properties of the sheet determined from the statistical experiments discussed in Chapter 4 and the geometric parameters are inputs to the computer model. The sheet is then displaced incrementally until failure – i.e., until the crack has propagated completely through the sheet and any reinforcing fibers have ceased to contribute.

After each increment the energy criterion is checked. If the energy criterion is satisfied, the strains at the crack tip are calculated to determine if the strain criterion is satisfied. These strains are compared with the local critical strain value picked from a table of possible values. The values in this table represent the probability density function for the critical strain; the values are generated from the experimentally determined mean and standard deviation of the material breaking strain.

In the results described here, only the critical strain was represented by a pdf;

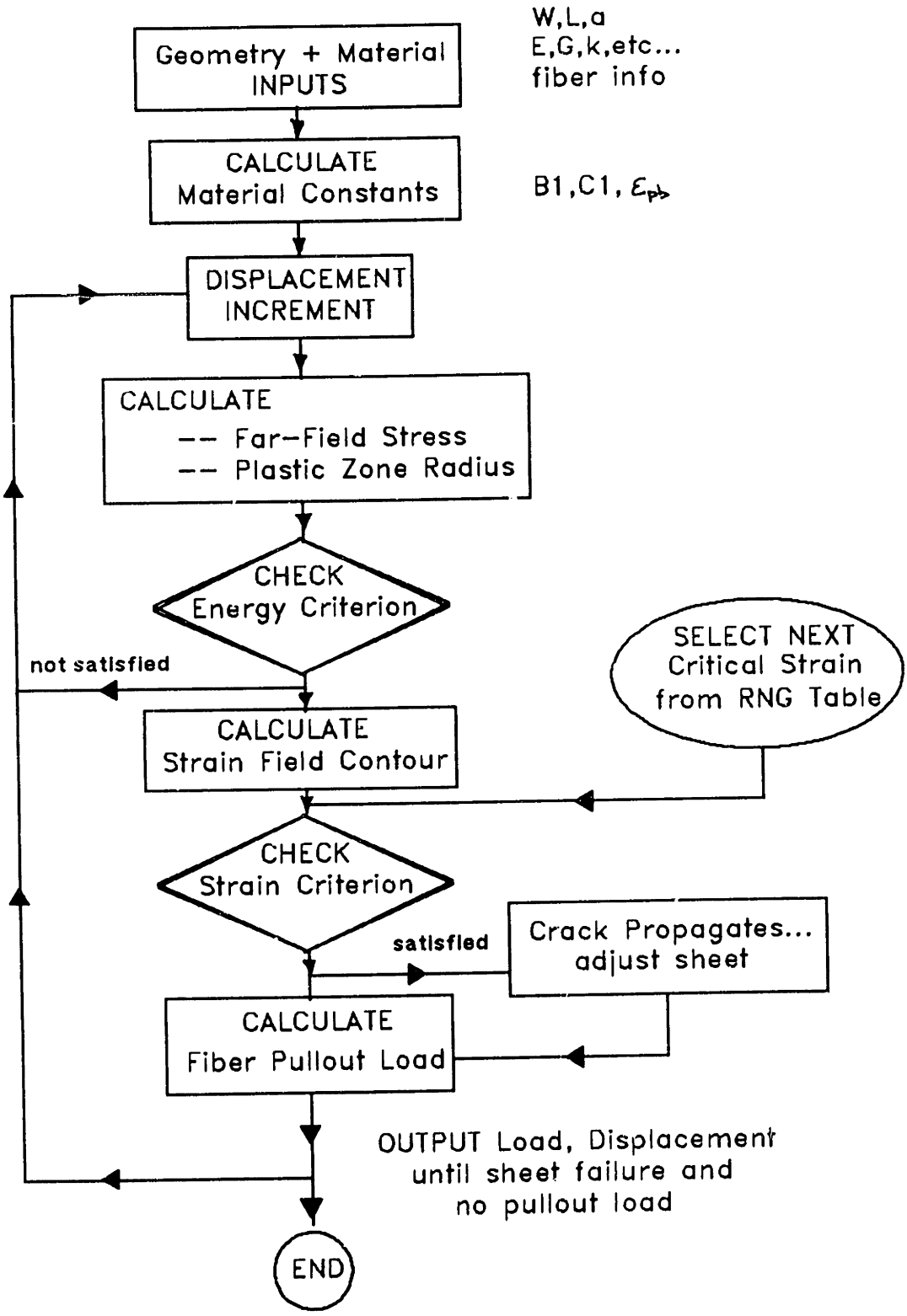

Figure 6.8: Flowchart for Computer Fracture Model

Parameter	STD	BND	CLU	PET
E (kg/cm)	230	280	90	250
G (kg/cm)	80	110	35	100
k (kg/cm)	4.5	5.7	1.8	3.8
Brk.Strn.	0.08	0.08	0.24	0.07
Alpha	0.61	0.62	0.77	0.67
R	11.0	15.0	6.0	11.0

Table 6.1: Mean Material Parameter Values - Model Input

mean values were used for all other material parameters. However, more extensive results could be attained by also accounting for variations in these other parameters. In particular, the variation in local yield stress should have a considerable influence on the plastic zone and thus the fracture behavior. On the other hand, parameters such as the elastic modulus and the plastic modulus are more relevant in terms of macroscopic sheet behavior. Rather than changing these values for every segment along the crack path, it seems to be more logical to modify these values from run to run (i.e., sheet to sheet).

Table 6.1 shows the mean material values used as inputs to the computer model. The values are in general close to those obtained from the SAS statistical tests covered in Chapter 4. In general, it was found that the dogbone values produced better fracture curve predictions; the fillet values tended to be on the low side. The shear modulus, G, is taken to be approximately $E/(2(1+\nu))$ where $\nu = 0.3$. Alpha represents the relationship between the elastic and plastic moduli, indicating in some sense the loss in strength of the plastic zone.

$$Alpha = 1 - P/E \tag{6.70}$$

Unfortunately, the energy criterion R is determined somewhat arbitrarily. We know that it should be close to K_{IC}, but an analytical solution is not to our knowledge currently available. This is an important task for further development of this model.

Parameter	Value
PET Length (cm)	1.8
PET Diameter (cm)	0.001
Bond Strength, τ_b (Shear, kg/cm^2)	1.4
Volume Fraction, v_f	0.05
Sheet Width (initial uncracked region, cm)	8.0
Coefficient of Friction	0.3
2tan α	0.03

Table 6.2: Fiber Pullout Parameters

For the fiber pullout contribution, the following fiber and geometric parameters were used (Table 6.2)

From these parameters, we can generate average curves for the 4 main paper types — Standard, Binder, Clupak, and PET. The experimental and computer model curves are shown in Figures 6.9 and 6.10, respectively. Although the curves do not match exactly, the shapes and magnitudes are close enough to suggest that this method has merit. It should be noted that the Clupak sample, which is probably the least continuous of the four, also yields the poorest correlation. Perhaps even more useful is a parametric study; this enables us to identify the effect on fracture behavior of changing certain material parameters.

6.3.2 Parametric Study of Matrix Fracture Model

In the parametric study, we are interested in delineating the effect of the various material parameters on the fracture behavior. By varying one parameter at a time while holding the others constant, we can see how each parameter changes the shape and magnitude of the fracture curve.

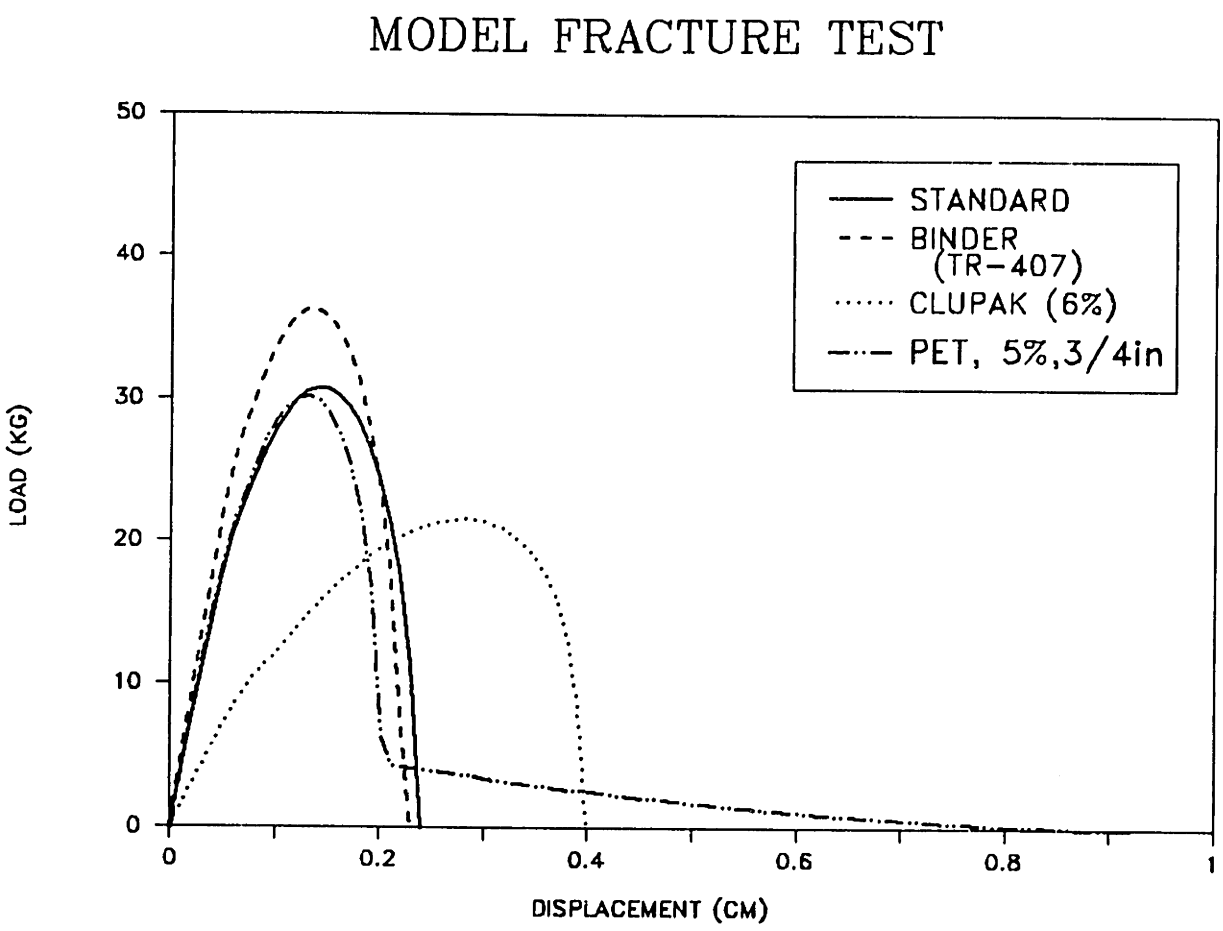

Figure 6.9: Computer Model Results – Average Curves

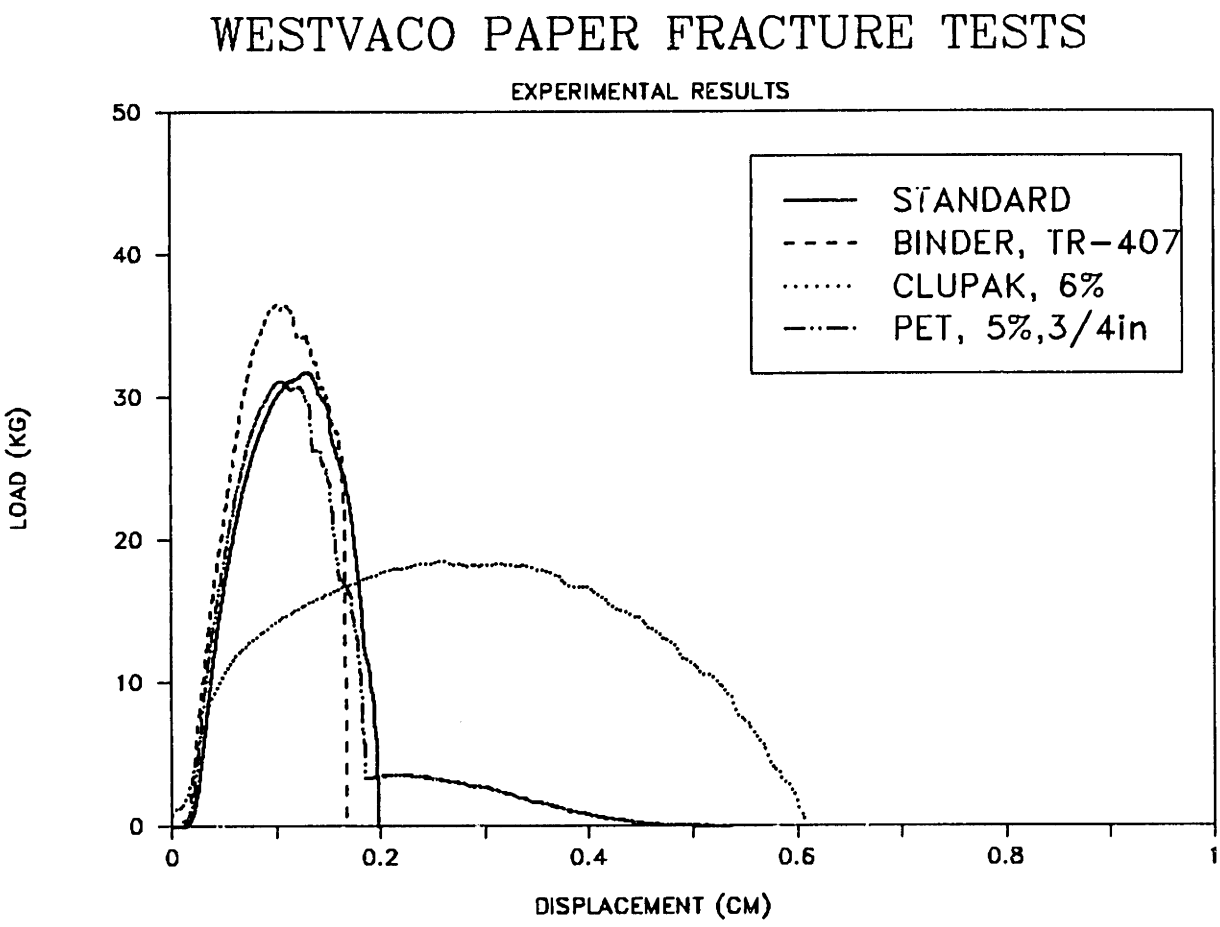

Figure 6.10: Experimental Results – Typical Curves

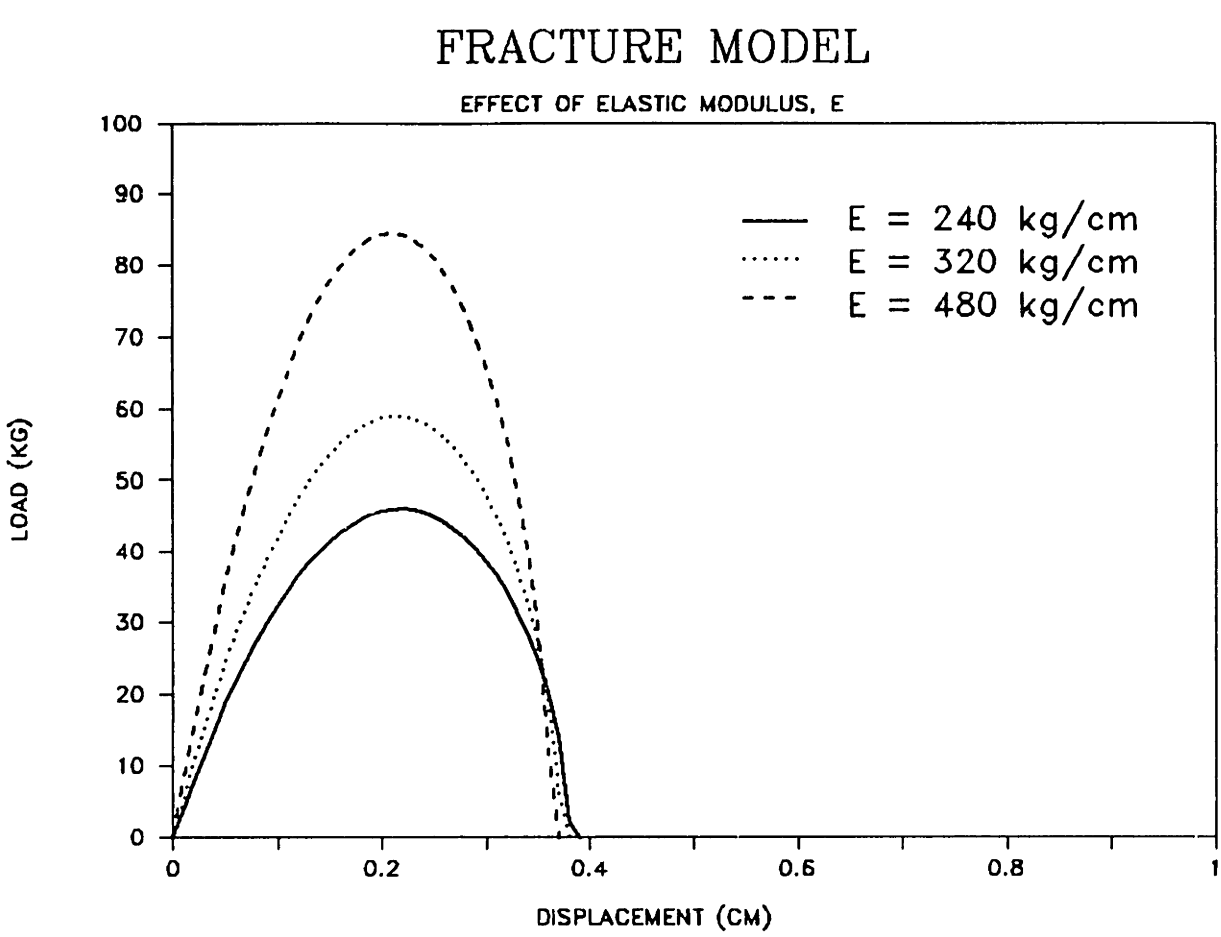

Figure 6.11: Effect of Elastic Modulus

In the first figure, the effect of elastic modulus is shown (Figure 6.11). As expected, with increasing modulus, the initial part of the curve becomes stiffer. It is interesting to note that the peak load increases, but the failure displacement is similar for all three cases. This seems to be the result of the two main controlling mechanisms — the plastic zone size and the strain contour. The former is a function of E while the latter is a function of 1/E, apparently cancelling each out to a considerable extent in terms of crack propagation rate. These two competing effects will be seen in more detail later in this section.

The shear modulus has a very different effect. In figure 6.12, an increase in shear modulus significantly increases both the failure displacement and the peak load.

As expected, independently increasing the failure strain and the yield stress has a similar effect (Figures 6.13 and 6.14). Both the failure displacements and the peak

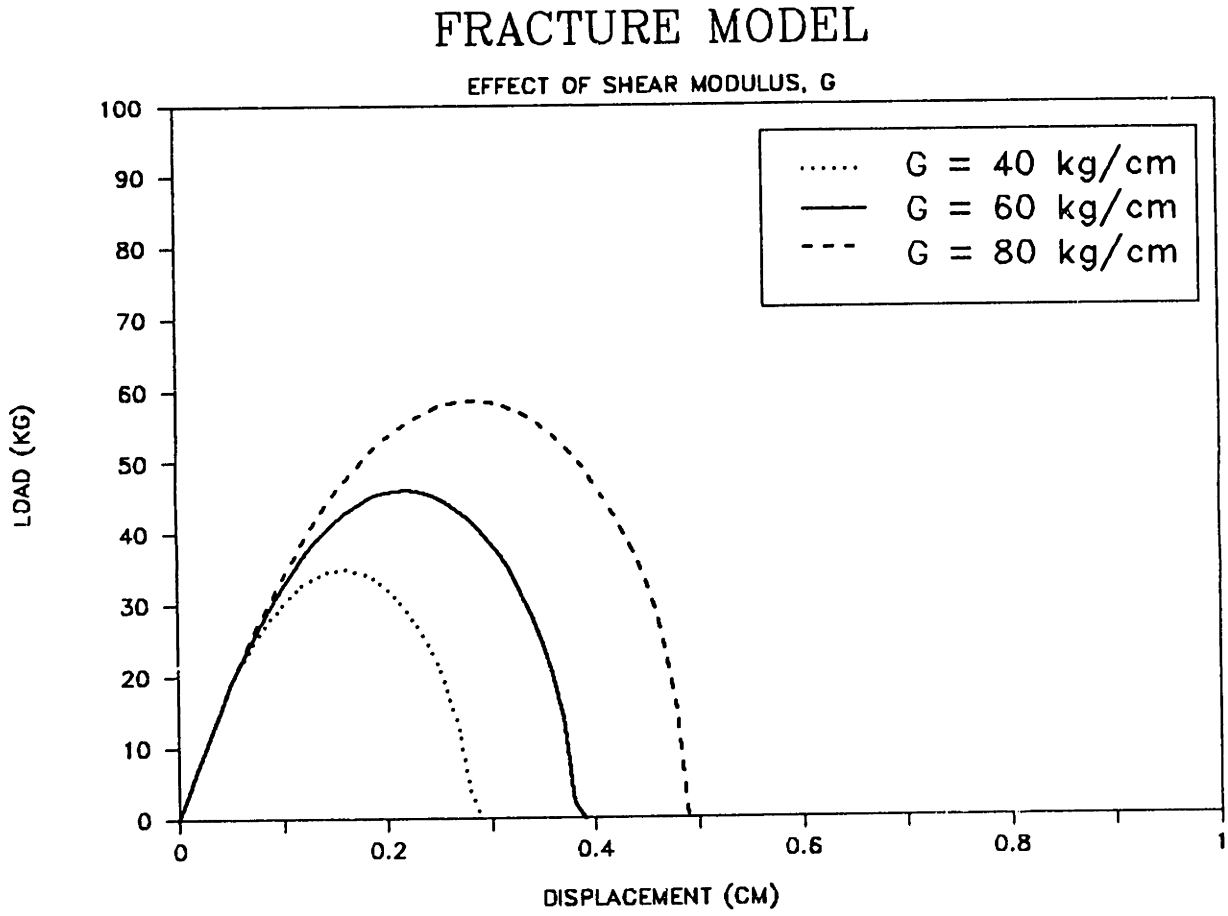

Figure 6.12: Effect of Shear Modulus

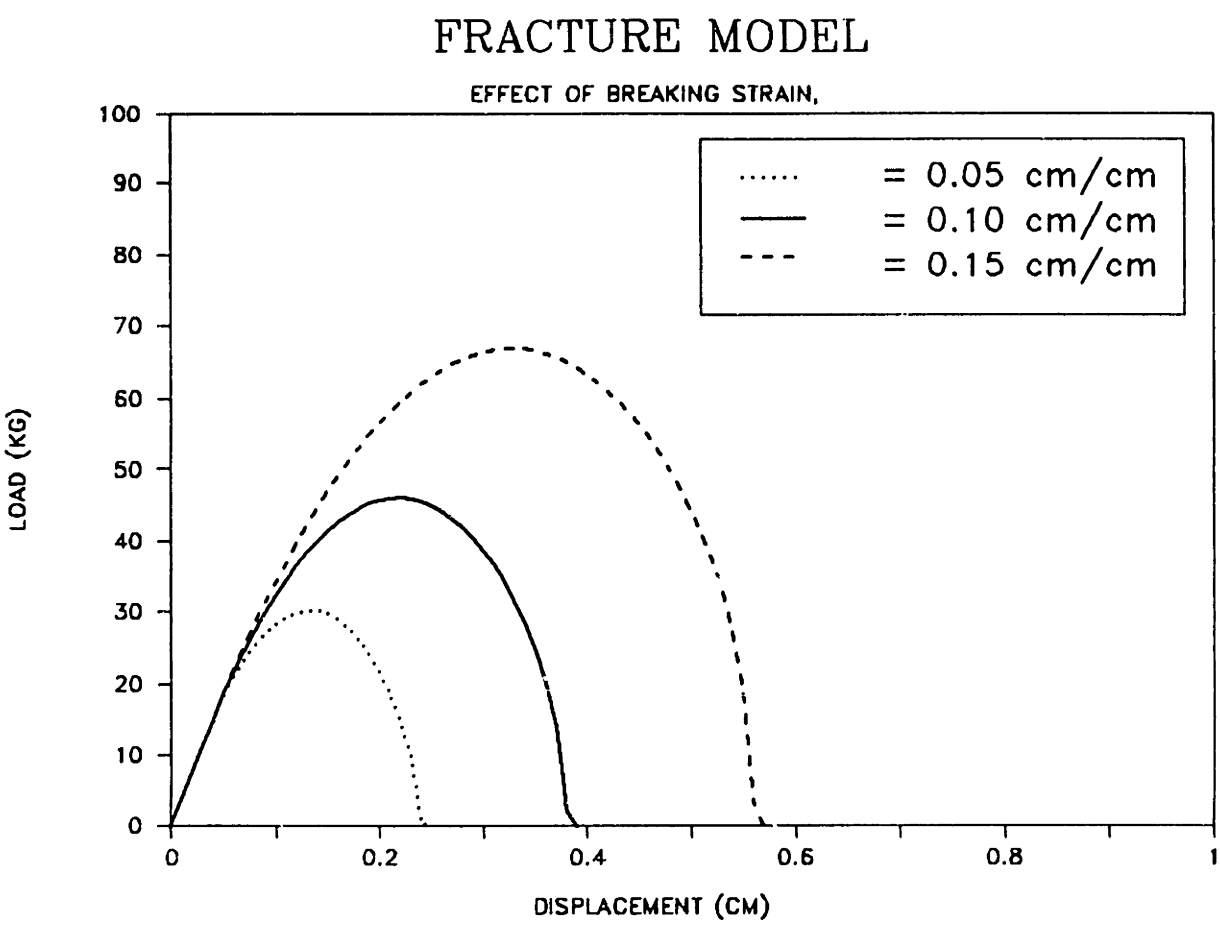

Figure 6.13: Effect of Failure Strain

loads increase.

Alpha has a much less substantial effect on the fracture behavior (Figure 6.15). It does, however, indicate that a perfectly plastic material (Alpha = 1) would tend to have less resistance to fracture than a hardening material.

What are the specific causes of these trends? Since crack propagation is governed to a great extent by two factors — the strain field given in Equation 6.33 and the plastic zone size in Equation 6.14 — we shall take a closer look at these equations.

Effect of k/E ratio

From Figure 6.16, increasing the ratio k/E clearly affects the strain contour. All of these curves are for a ratio of E/G equal to 3. Higher values of k/E result in much

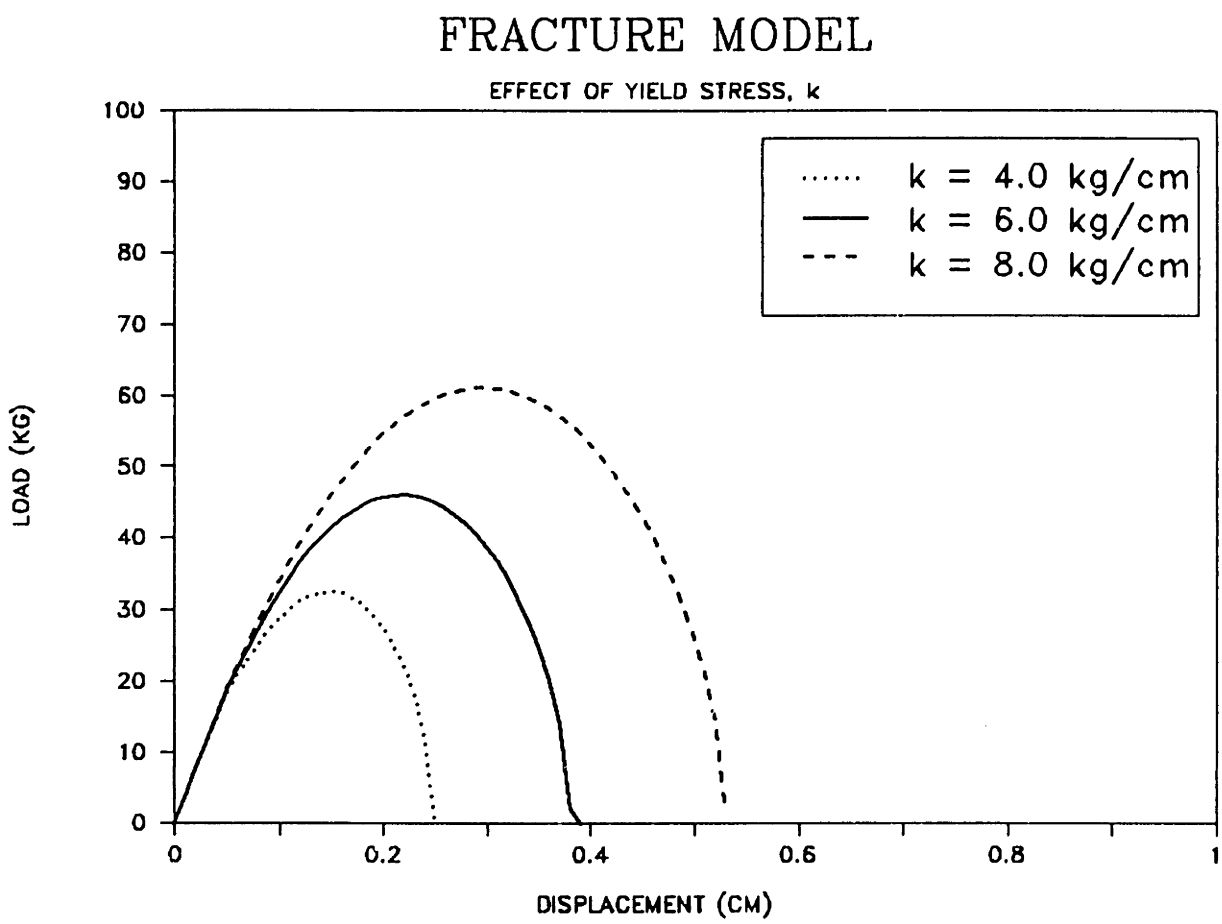

Figure 6.14: Effect of Yield Stress

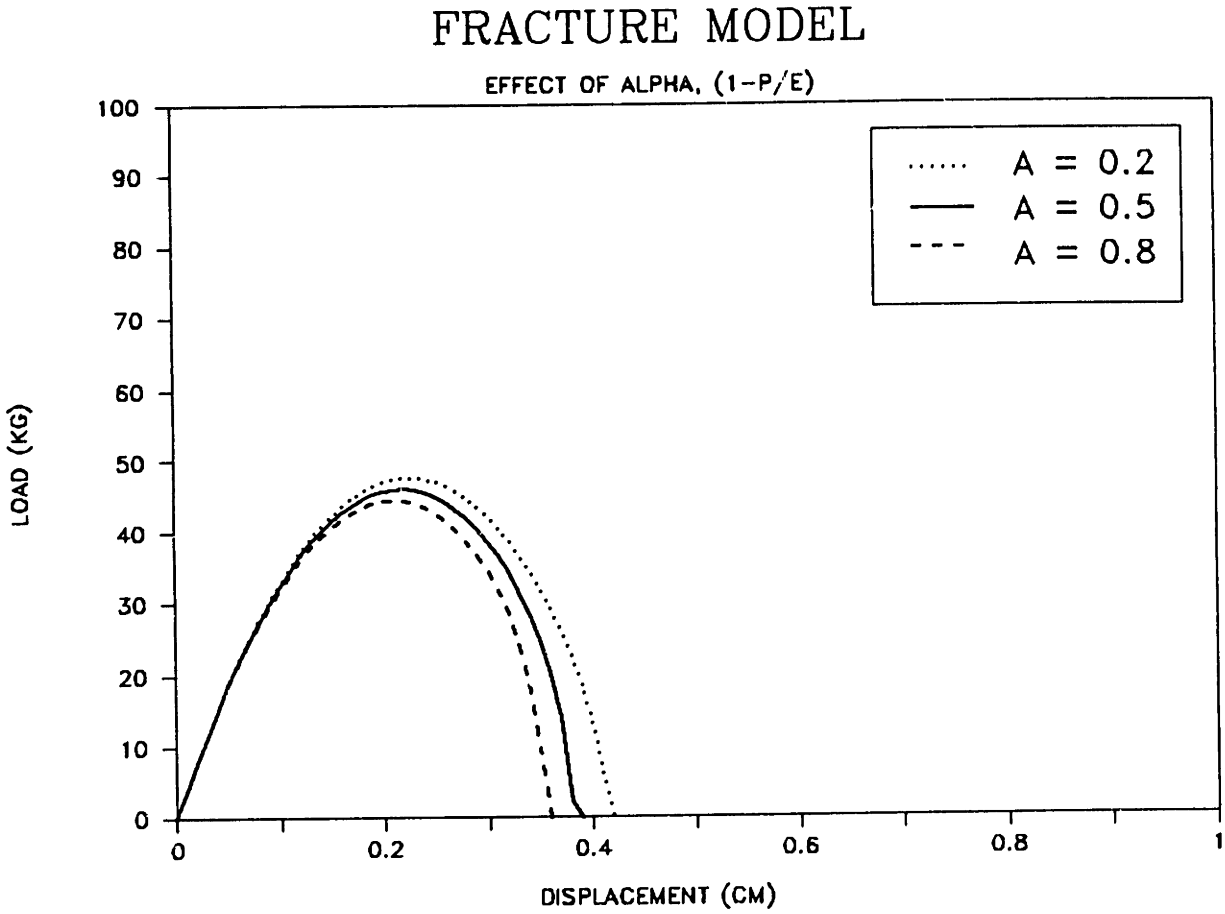

Figure 6.15: Effect of Alpha

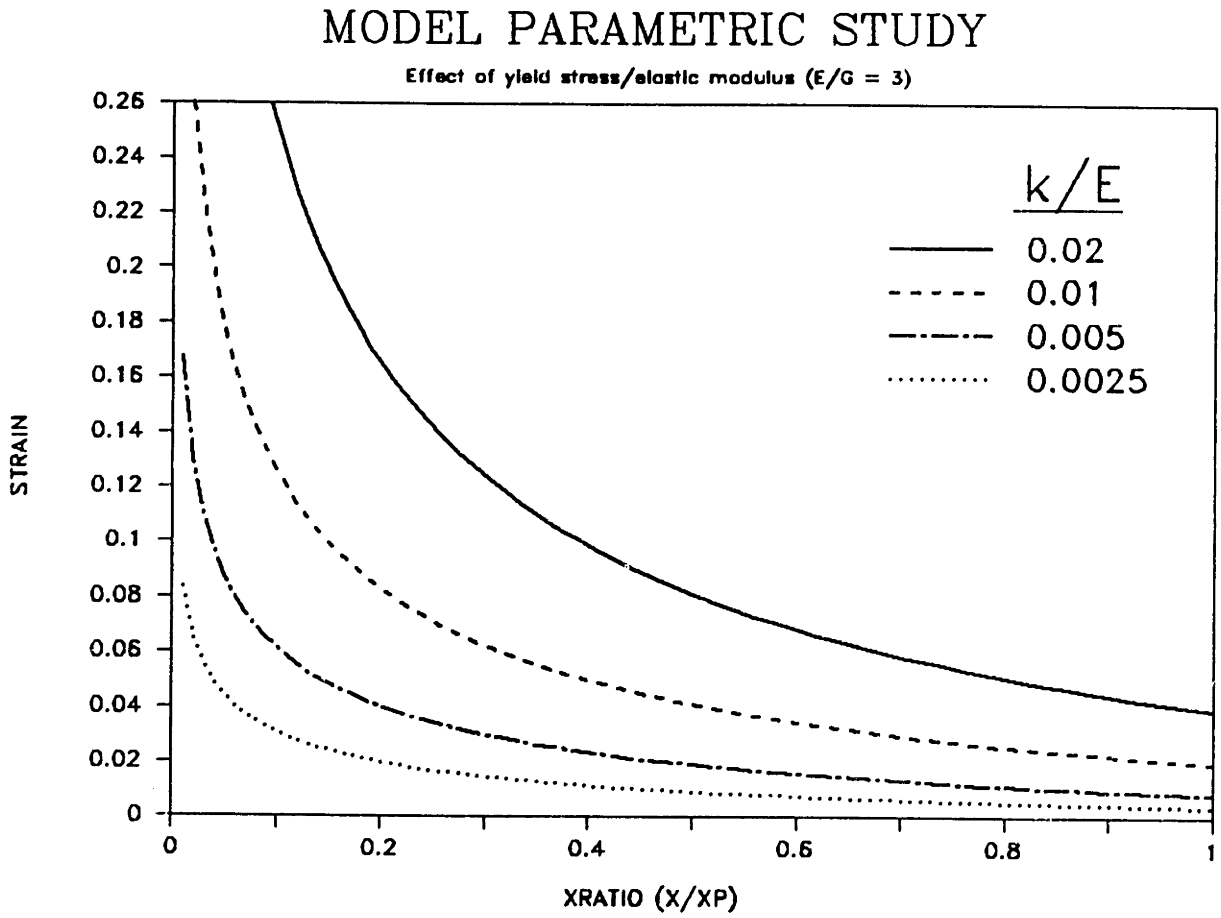

Figure 6.16: Effect of Yield Stress/Elastic Modulus Ratio

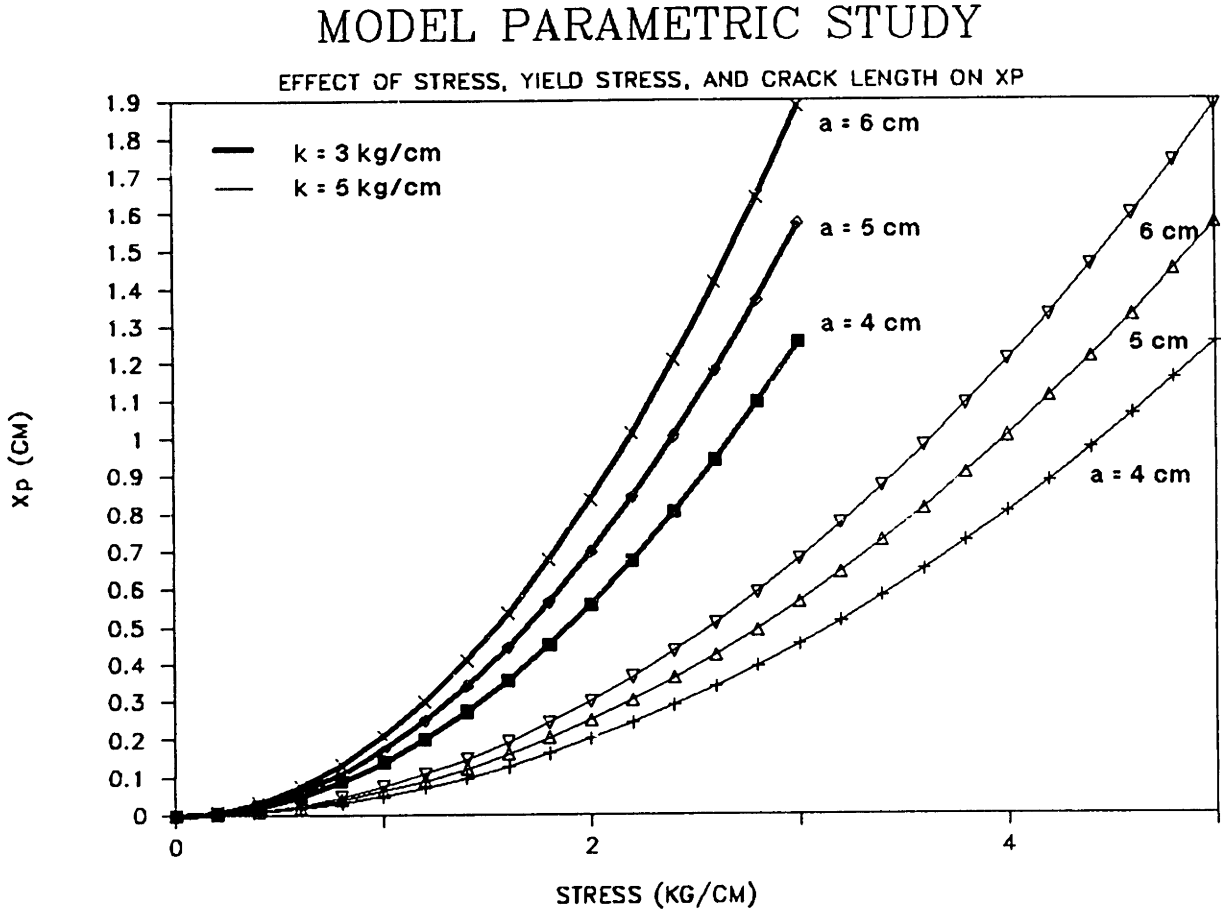

Figure 6.17: Effect of Stress, Yield Stress, and Crack Length on Xp

higher strains for a given distance within the plastic zone (x/x_p). Thus, increasing the k/E ratio should decrease the fracture resistance. From Figures 6.11 and 6.14, however, this is not in good agreement with the respective elastic modulus and yield modulus results. The reason lies in the competing plastic zone effect.

From equation 6.14, the radius of the plastic zone is inversely proportional to the yield stress. This is seen clearly in Figure 6.17. So, while decreasing the k/E ratio by decreasing k will reduce the local strains, it will also increase the plastic zone size. From Figure 6.14, the plastic zone size effect seems to be dominant, since decreasing k reduces the fracture resistance.

Also noteworthy is that at k/E ratios much below 0.005, the strain exhibits a very steep drop close to the crack tip and then is very flat beyond $x/x_p = 0.1$. This would tend to decrease the amount of propagation, since the critical strain would only be

exceeded very close to the crack tip. If this distance is less than the critical distance, then no crack propagation would be expected.

The flatness of the strain contour also suggests the potential for failures occurring in a nonconsecutive manner. That is, the critical strain at a point farther away from the crack tip may be lower than for a point close to the crack tip; if this lower critical strain is below the local strain value at that location, a failure should occur. This would cause the crack to jump. While an interesting theory, this subject is beyond the scope of this study, but should be examined in further work.

Effect of E/G

Increasing the elastic modulus/shear modulus ratio also increases the crack tip strains, but affects the curve shape less than changing the k/E ratio (Figure 6.18). For lower k/E ratios, the effect of E/G is diminished even further. In general, increasing E/G will increase the local strains and decrease the fracture resistance. There is agreement with the model results for G (decreasing G results in less fracture resistance).

Effect of k, Stress, a on Rp

Apparently, the effects of E, G, and k on the strain field cannot be used independently to predict fracture behavior. There is a competing effect of the plastic zone size. The actual crack propagation distance is determined by the local strains as a function of a critical x/x_p times the plastic zone size (x_p). In addition to the effect of yield stress which was discussed earlier in this section, the effects of far-field stress and crack length on the plastic zone size are also shown in Figure 6.17.

The convex shape of the curves in Figure 6.17 is a result of a sharp increase in plastic zone size at far-field stresses close to the yield stress. As expected, the size

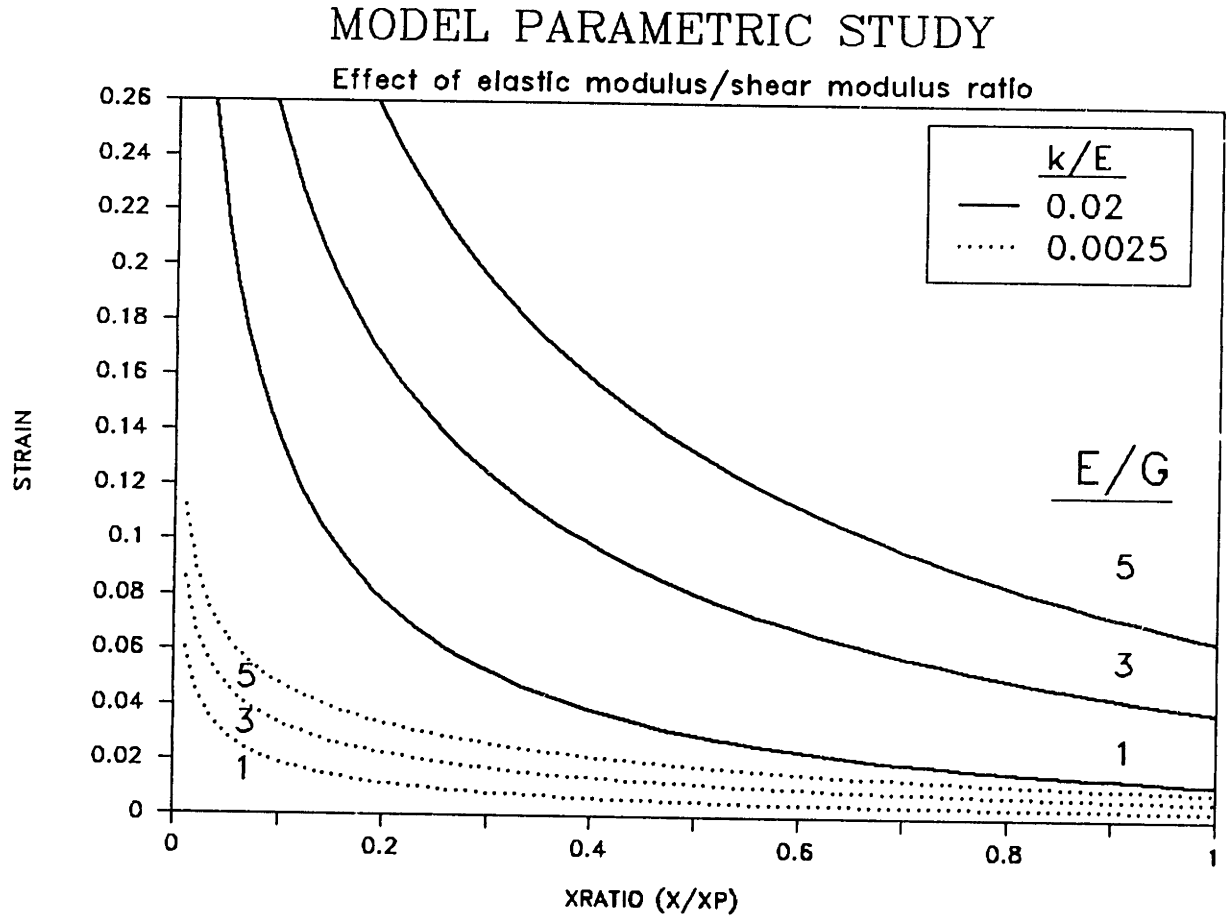

Figure 6.18: Effect of Elastic Modulus/Shear Modulus Ratio

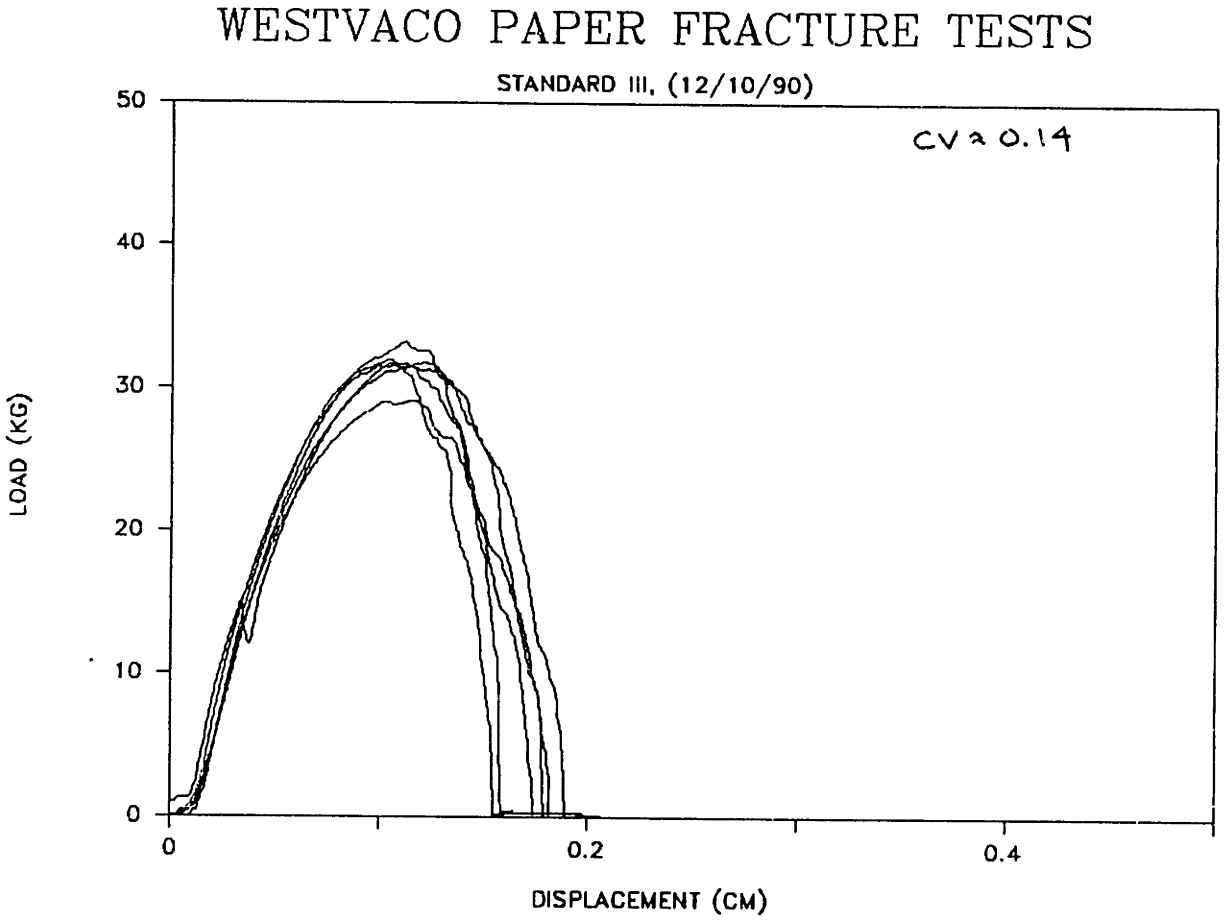

Figure 6.19: Variation in Experimental Fracture Curves

of the plastic zone increases with increasing far-field stresses. A longer crack length tends to soften the material, also producing a larger plastic zone for a given far-field stress.

6.3.3 Effect of Variation of Critical Strain Values

A key part to simulating the discrete nature of the material involves the use of probability density functions to represent material values rather than mean values. A plot of several experimental fracture curves for a Standard sheet (Figure 6.19, CV=0.14) reflects the irregular nature of fracture. Crack propagation obviously occurs at different far-field loads and strains within a sheet and between sheets.

The next three figures (Figures 6.20-22) show how the variation about a mean

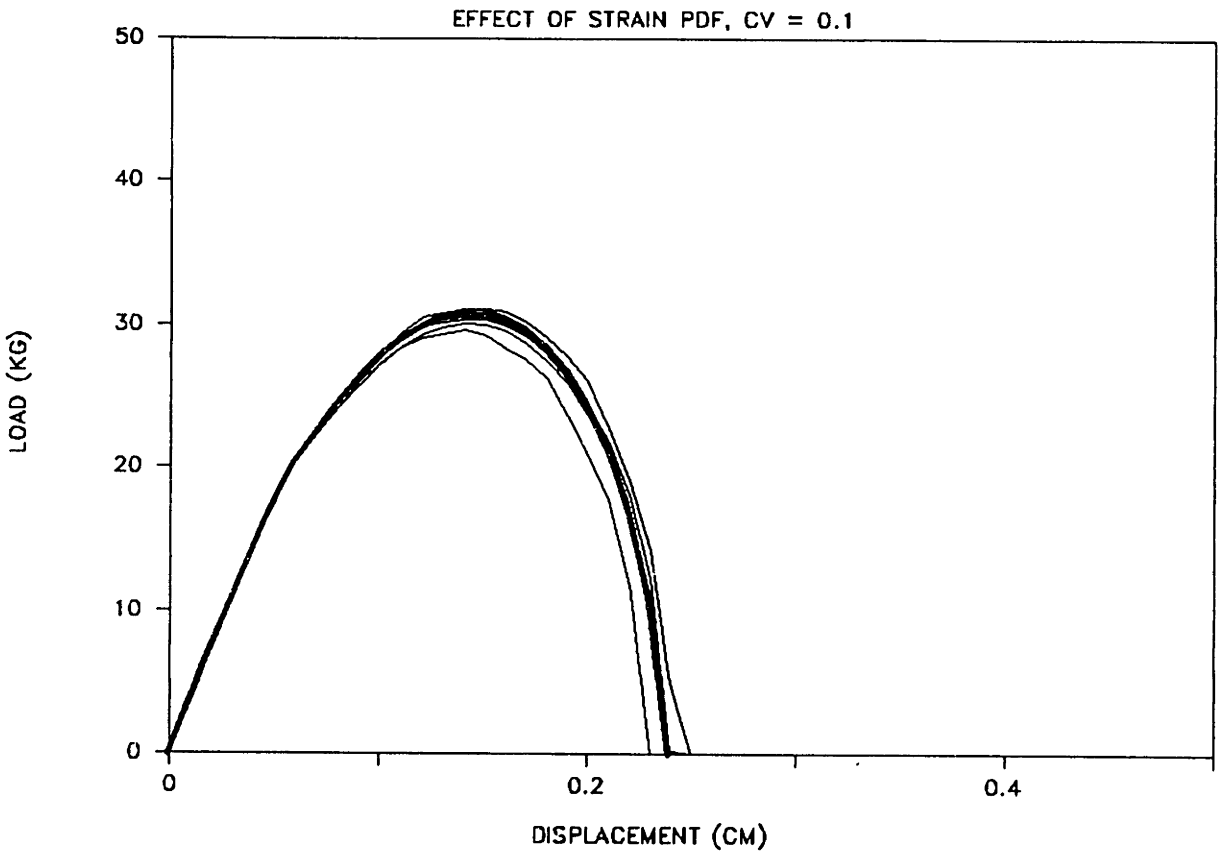

Figure 6.20: Effect of Critical Strain Variation, CV = 0.1

can significantly affect the fracture behavior, producing deviations similar to those seen in the experimental curves. Mean material parameters for the model curves were close to those for the Standard sheet but were not specifically chosen to match the Standard sheet values.

In each figure, the thicker line represents the curve attained by using the mean value only. Figure 6.20 shows six additional curves generated from a table of critical strain values with the same mean but with a coefficient of variation of 0.1 (CV = standard deviation/mean). Similarly, Figures 6.21 and 6.22 show curves generated from tables with the same mean and CV's equal to 0.2 and 0.4, respectively. The experimental SAS results for the Standard, Binder, Clupak, and PET samples generally had coefficient of variation values between 0.1 and 0.2.

With a CV equal to 0.1, the difference in the fracture curves is not substantial.

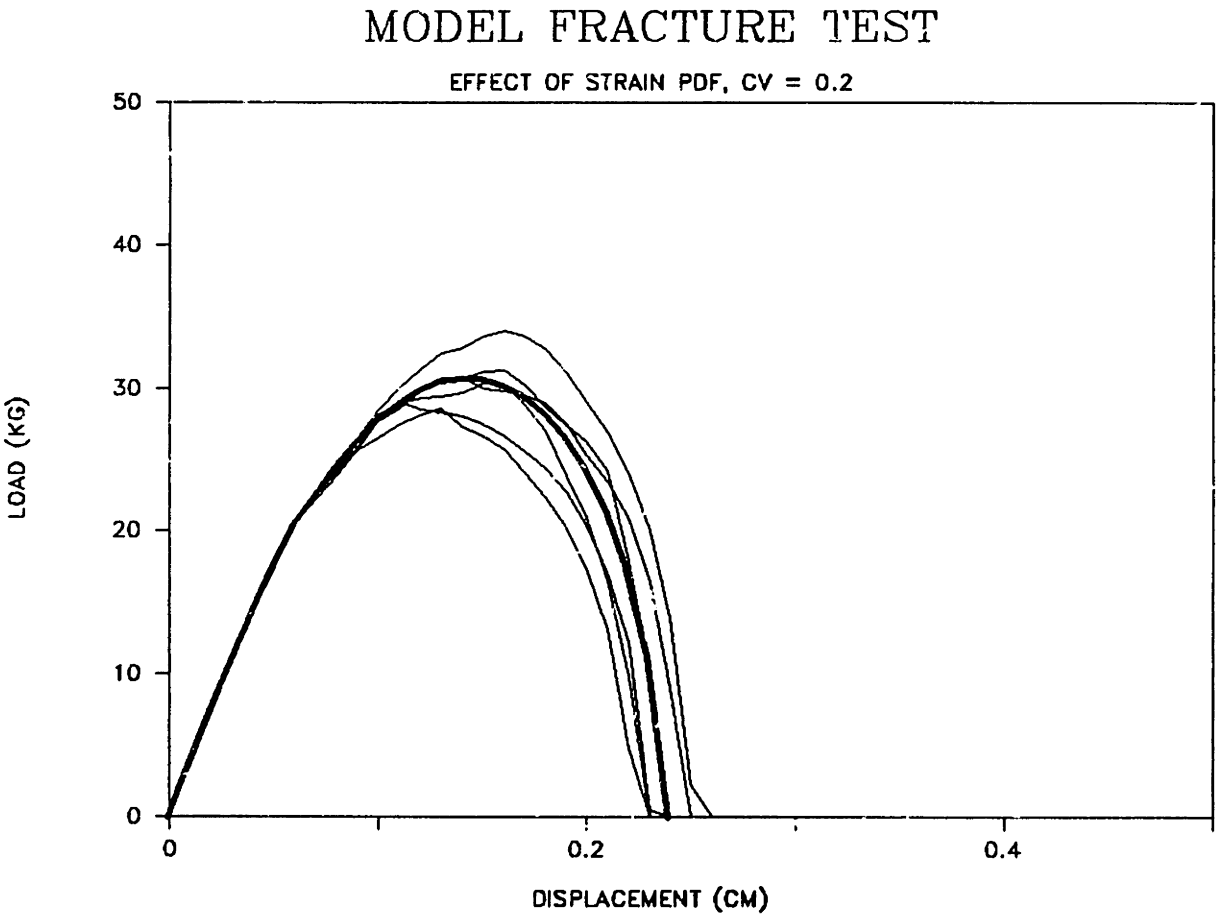

Figure 6.21: Effect of Critical Strain Variation, CV = 0.2

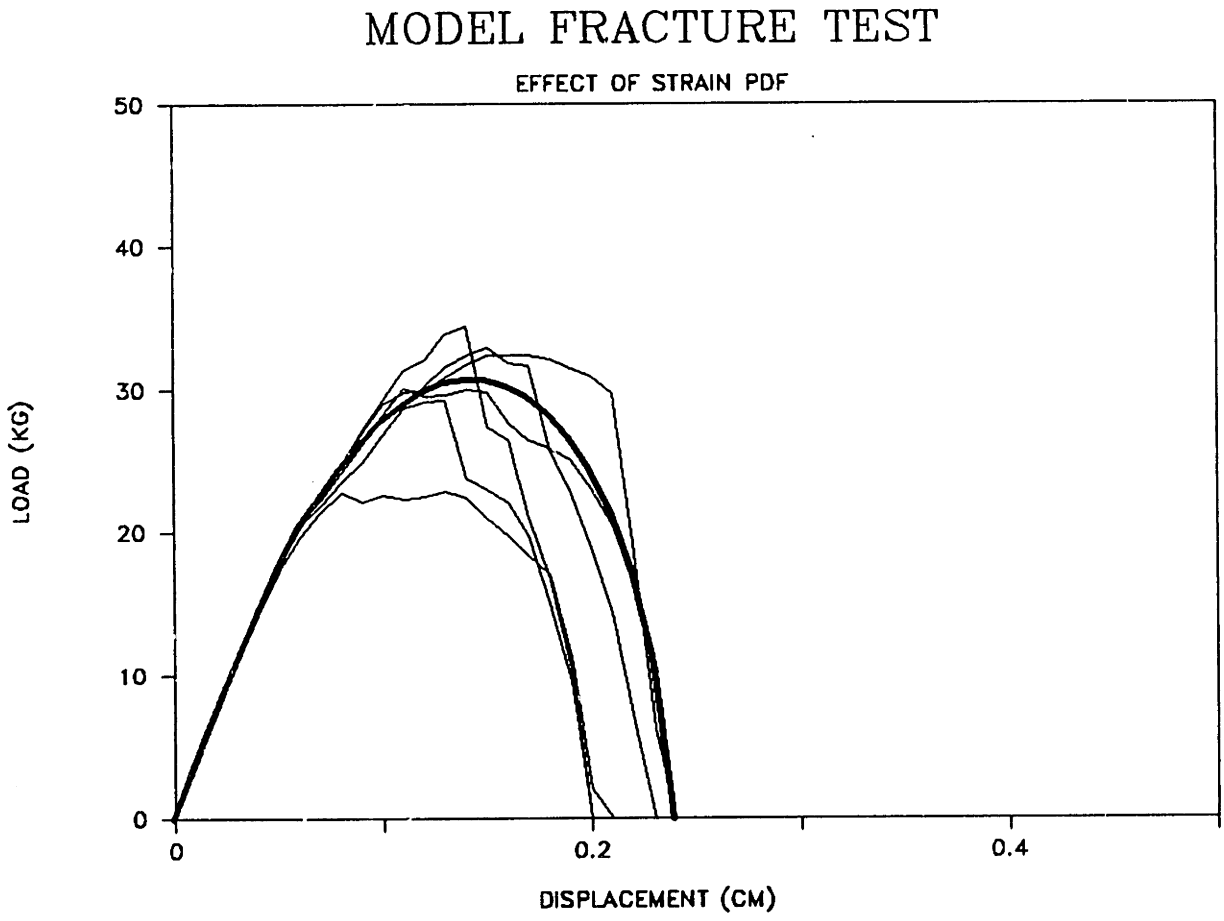

Figure 6.22: Effect of Critical Strain Variation, CV = 0.4

However, when the coefficient of variation for the critical strain values is equal to 0.2, the curves start to exhibit different peak loads and post peak behavior. The curves still remain relatively smooth. At an extreme value of 0.4 for the CV, the curves now display a very erratic behavior. A low peak load is caused by several weak sections in the computer sheet, while a stronger curve is generated as a results of several consecutive strong sections. Sharp drops in load also occur as a result of a large drop in critical strain from section to section. This suggests that if the reinforcing fibers are bonded well enough to increase the local critical strain without also creating weak spots, then an increase in the fracture resistance will also result.

Despite having the same mean critical strain value, a large variation within the sheet and between sheets from the same population results in severe fluctuations in fracture behavior. This correlates well with the erratic fracture behavior seen in the fracture tests in chapter 3 for poorly dispersed materials. It is expected that poorly dispersed materials such as the bicomponent samples would have larger variations in properties from area to area, and this would therefore be one major cause of the observed erratic behavior. The ability of the model to predict this variability is an important part of its usefulness and applicability.

Chapter 7

Conclusions and Recommendations

As stated in the introduction, the goal of this thesis was not to answer all the questions relating to fracture of quasi-continuous materials. Rather, this study was undertaken to determine if a new method of analysis could be applied to these types of problems. In this light, the following conclusions can be made.

7.1 Conclusions

- *In-situ* measurements can be made of the local crack-tip strains during fracture using a tensile stage in a scanning electron microscope (Section 5.3).
- These local strain measurements supported the existence of Mode-I type behavior at the crack tip (Figures 5.22-24).
- The paper used in this study exhibited an elastic-plastic behavior in cyclic tensile loading (Figures 4.11-14).

- SEM photographs of the fracture surface and the damage zone ahead of the crack tip indicated that the plastic behavior of different materials was related to its fracture behavior. This differing plastic behavior included (1) area of damage; (2) degree of fiber pullout; and (3) tortuosity of the path.

    1. Stiffer materials (e.g., TR-407 Binder Samples) exhibited an extremely narrow damage zone (Fig.5.**7**), while softer materials (e.g., Clupak Samples) exhibited a much wider damage zone (Fig.5.**8**). The blunted or wider damage zones usually translated to higher fracture resistances, since more material had to be plastically deformed before the crack propagated further. However, sometimes a wider zone was offset by the weakness of the material within the plastic zone (i.e., the ease of deformation).
    2. Materials which were more highly bonded (i.e., more continuous) displayed primarily fiber fracture at the crack surface (TR-407 Binder, Fig.4.1). The less bonded, less continuous materials had different proportions of fiber pullout and fiber fracture. In general, large amount of fiber fracture results in a more brittle, less fracture resistant material.
    3. Tortuosity of the damage zone and eventual crack path was governed mainly by material uniformity. Aggregates of reinforcing fibers and large variations in bonding usually resulted in very uneven crack propagation rate and direction. This was also seen in the erratic shape of the fracture curves.

- Based on Achenbach's [1] analysis for plane stress elastic-plastic steady state crack propagation and a probabilistic fiber pullout analysis, model results can be generated which are similar in shape and magnitude to the experimental results.

- Of particular interest is the effect of variation of critical strain values on the model fracture curves. Because fracture is so dependent on concentrations and

weak points, the model's ability to account for the effects of means and variations is critical to the prediction of fracture behavior.

- Greater variations result in more erratic fracture behavior. Erratic behavior is not always a negative, however, as this behavior showed how a series of stronger sections can increase the fracture resistance of a material. This suggests that if the bonding between the reinforcing fibers and the cellulose fibers can be improved such that the local critical strains are increased, then an increase in fracture resistance will result. Thus, the most promising route for improving the fracture resistance of these cellulose fiber sheets without totally changing the nature of the sheet (e.g., using saturants) is further development of the bicomponent fiber method. Dispersion and uneven melting seem to be the primary obstacles at this point.

7.2 Recommendations

Obviously, since this is a relatively new concept, several points beyond the scope of this work remain to be addressed.

- While the results from this study were very encouraging, the theory needs to be tested against some very different materials to determine the limits of its application.

- Specifically, one question that needs to be answered is whether simply deriving different crack-tip strain field equations for different types of materials can make the method universal.

- A method must be established for determining the material parameters from the basic components (fiber and bonding) rather than a macroelement (the SAS

samples). One suggestion for this is the extension of the models developed by Perkins, Petterson, et al.

- A satisfactory expression for the energy criterion needs to be developed. Further advancement of work done by Broek and Achenbach on the R curve seems worth pursuing.

- With the development of new technology such as higher resolution optical microscopes and environmental scanning electron microscopes which do not require gold-coating or a vacuum, the technique of directly measuring local crack-tip strains can be further refined and applied to other fracture problems. The technique can also be used to measure non-fracture type deformations.

Bibliography

[1] Achenbach,J.D., and Dunayevsky,V., "Crack Growth Under Plane Stress Conditions in an Elastic Perfectly-Plastic Material", *J.Mech.Phys.Solids*, v32, n2, pp.89-100, **1984**.

[2] Achenbach,J.D., and Li,Z.L., "Resistance Curves for Crack Growth Under Plane-Stress Conditions in an Elastic Perfectly-Plastic Material", *Engineering Fracture Mechanics*, v22, n6, pp.1073-1078, **1985**.

[3] Argon, A.S., "Statistical Aspects of Fracture", in Fracture and Fatigue, vol.5, ed.by L.J.Broutman, Academic Press, New York, **1974**, pp.153-190.

[4] Baum, G.A., Habeger,C.C., and Fleischman,E.H., "Measurement of the Orthotropic Elastic Constants of Paper", in The Role of Fundamental Research in Papermaking, Transactions, Cambridge: Sept 1981, ed. J.Brander, Mechanical Engineering Publications, London, **1983**, pp.453-477,pp.594-597.

[5] Britton, P.N., and Sampson,A.J., et al., "Computer Simulation of the Mechanical Properites of Nonwoven Fabrics", *Textile Research Journal*, v53, **June 1983**, pp.363-368; v54, **Jan 1984**, pp.1-5; v54, **July 1984**, pp.425-428.

[6] Broek,D. Elementary Engineering Fracture Mechanics, Martinus Nijhoff Publishers, Dordrecht, **1986**.

[7] Brouard, D., "On a Theory of Progressive Fatigue and Fracture for Random Arrangements in Fibrous Textiles", in Nonwovens and Disposables: New Technical/ Marketing Developments, ed. V.M.Bhatnagar, Technomic Publishing, **1978**, pp.5-16; also, Part 6 *Bulletin Scientifique ITF*, v7,n28, **Nov 1978**, pp.455-484.

[8] Casey, J.P., Pulp and Paper: Chemistry and Chemical Technology, 2vols., Interscience Publishers, New York, **1952**.

[9] Chen, J., "The Effect of Synthetic Fibers on the Failure Resistance of Wet-laid Cellulose Papers", M.I.T. Fibers and Polymers Lab Report, **July 1989**.

[10] Chen, J., "The Effect of Synthetic Fibers on the Failure Resistance of Wet-laid Cellulose Papers, Part II", M.I.T. Fibers and Polymers Lab Report, **April 1990**.

[11] Cox, H.L., "The Elasticity and Strength of Paper and Other Fibrous Materials", *British Journal of Applied Physics*, v3, **March 1952**, pp.72-79.

[12] Collier's Encyclopaedia, "Paper"

[13] Creager,M. and Paris,P.C., "Elastic Field Equations for Blunt Cracks with Reference to Stress Corrosion Cracking", *Int. J. Fract. Mech.*, v3, pp.247-252, **1967**.

[14] Hansen, S.M., "Modeling of Nonwoven Fabric Properties", in 1987 Nonwoven Conference: TAPPI Proceedings, pp.75-85.

[15] Heckers, W., Hart,D., and Gottsching,L., "Bruchmechanische Untersuchungen an Papier", *Das Papier*, v34,n3, **1980**, pp.85-94; v34,n7, **1980**, pp.255-265; v34,n10, **1980**, pp.421-427; v35,n7, **1981**, pp.265-274.

[16] Hein, T.L., "Isolating the Effect that Embedded Fibers Have Upon the Strength of Paper During Fractures", poster presentation, INDA-TEC '91, The International Nonwovens Technical Conference, *Orlando, FL* , **April 9-12, 1991** and M.I.T. Fibers and Polymers Lab Report, **May, 1991**.

[17] Ihrman, C.B. and Ohm, O.E., "Extensible Paper by the Double-Roll Compacting Process", in Consolidation of the Paper Web, Transactions, Cambridge, Sept.1965, ed. F. Bolam, Technical Section of the British Paper and Board Makers' Association, London, **1966**.

[18] Jayne, B.A., "Some Mechanical Properties of Wood Fibers in Tension", *Forest Products Journal*, **June 1961**, pp.316-322.

[19] Kallmes, O., and Corte,H., "The Structure of Paper: I. The Statistical Geometry of an Ideal Two Dimensional Fiber Network", *TAPPI Journal*, v43,n9, **Sept 1960**, pp.737-752.

[20] Kanninen, M.F. and Popelar, C.H., Advanced Fracture Mechanics, Oxford University Press, New York, **1985**.

[21] Long, P., and Levering, R., Paper - Art & Technology, based on the International Paper Conference, San Francisco, March 1978; World Print Council, San Francisco, 1979.

[22] Mark,R.E., Handbook of Physical and Mechanical Testing of Paper and Paperboard, 2vols., Marcel Dekker, New York, **1983**.

[23] McClintock, F.A., and Irwin,G.R., "Plasticity Aspects of Fracture Mechanics", in Fracture Toughness Testing and its Applications, ASTM STP 381, American Society of Testing Materials, Philadelphia, PA, **1965**.

[24] Nissan, A.H., Boyd,V.L., Batten,G.L.,Jr., and Ogden,R.W., "Paper as an H-bond Dominated Solid in the Elastic and Plastic Regime", *TAPPI Journal*, v68,n9, **Sept 1985**, pp.118-124.

[25] Nissan, A.H. and Batten, G.L.,Jr., "On the Primacy of the Hydrogen Bond in Paper Mechanics", *TAPPI Journal*, **Feb 1990**, pp.159-164.

[26] Ott, E., Cellulose and Cellulose Derivatives, Interscience Publishers, New York, **1943**.

[27] Page, D.H., El-Hosseiny, F., Winkler, K., and Lancaster, A.P.S., "Elastic Modulus of Single Wood Pulp Fibers", *Tappi Journal*, v60, n4, **April 1977**, pp.114-117.

[28] Page, D.H. and Schulgasser, K., "Evidence for a Laminate Model for Paper", in Mechanics of Cellulosic and Polymeric Materials, Proceedings of the Third Joint ASCE/ASME Mechanics Conference, AMD-99/MD-13, ed. R.W.Perkins, **July 1989**, pp.35-39.

[29] Page, D.H. and Seth, R.S., "The elastic modulus of paper : I. The controlling mechanisms; II. The importance of fiber modulus, bonding, and fiber length; III. The effects of dislocations, microcompressions, curl, crimps, and kinks.", *TAPPI Journal*, v62,n9, **Sept 1979**, pp.99-102; v63,n6, **June 1980** pp.113-116; v63,n10, **Oct 1980**, pp.99-102.

[30] Pan, N., *personal communication*, University of California, Davis, **1991**.

[31] Perkins, R.W. and Mark, R.E., "Some New Concepts of the Relation Between Fibre Orientation, Fibre Geometry, and Mechanical Properties", in The Role of Fundamental Research in Papermaking, Transactions, Cambridge: Sept 1981, ed. J.Brander, Mechanical Engineering Publications, London, **1983**, pp.479-525.

[32] Perkins, R.W. and Ramasubramanian, M.K., "Concerning Micromechanics Models for the Elastic Behavior of Paper", in Mechanics of Cellulosic and Polymeric Materials, Proceedings of the Third Joint ASCE/ASME Mechanics Conference, AMD-99/MD-13, ed. R.W.Perkins, **July 1989**, pp.23-33.

[33] Petterson, D.R. and Backer, S. "Relationships between the Structural Geometry of a Fabric and its Physical Properties. Part VII: Mechanics of Nonwovens: Orthotropic Behavior", *Textile Research Journal*, **Oct 1963**, pp.809-816.

[34] Petterson, D.R., "On the Mechanics of Non-Woven Fabrics", Sc.D. Thesis, Dept. of Mechanical Engineering, M.I.T., **August 1958**.

[35] Pouyet, J., Volozinskis,X., Poustis,J., and Lataillade,J.C., "Investigation of the Fracture Toughness of Paper", in Mechanics of Cellulosic and Polymeric Materials, Proceedings of the Third Joint ASCE/ASME Mechanics Conference, AMD-99/MD-13, ed. R.W.Perkins, **July 1989**, pp.133-140.

[36] Press,W.H., Flannery,B.P., Teukolsky,S.A., Vetterling,W.T., Numerical Recipes in C, Cambridge University Press, Cambridge, **1988**.

[37] Ramasubramanian, M.K. and Perkins,R.W., "Computer Simulation of the Uniaxial Elastic-Plastic Behavior of Paper", *J. of Engineering Materials and Technology: Transactions of the ASME*, v110, **April 1988**, pp.117-123.

[38] Rigdahl, M., Andersson,H., Westerlind,B., and Hollmark,H., "Elastic Behaviour of Low Density Paper Described by Network Mechanics", *Fibre Science and Technology*, v19, **1983**, pp.127-144.

[39] Roisum, D.R., "Runnability of Paper: Part 1 Predicting runnability", *TAPPI Journal*, **Jan 1990**, pp.97-101.

[40] Schulgasser, K., "On the In-Plane Elastic Constants of Paper", *Fibre Science and Technology*, v15, **1981**, pp.257-270.

[41] Schulgasser, K., "The In-Plane Poisson Ratio of Paper", *Fibre Science and Technology*, v19, **1983**, pp.297-309.

[42] Schulgasser, K. and Page,D.H., "The Influence of Transverse Fibre Properties on the In-Plane Elastic Behaviour of Paper", *Composites Science and Technology*, v32, **1988**, pp.279-292.

[43] Seth, R.S. and Page,D.H., "Fiber Properties and Tearing Resistance", *TAPPI Journal*, **Feb 1988**, pp.103-107.

[44] Seth, R.S. and Page,D.H., "The Stress-Strain Curve of Paper", in The Role of Fundamental Research in Papermaking, Transactions, Cambridge: Sept 1981, ed. J.Brander, Mechanical Engineering Publications, London, **1983**, pp.421-452, pp.585-593.

[45] Seth, R.S., "Measurement of Fracture Resistance of Paper", *TAPPI Journal*, v62,n7, **July 1979**, pp.92-95.

[46] Seth, R.S. and Page,D.H., "Fracture Resistance: a failure criterion for paper", *TAPPI Journal*, v58,n9, **Sept 1975**, pp.112-117.

[47] U.S. Bureau of the Census, Statistical Abstract of the United States, 1990, 110th edition, Washington, DC, 1990.

[48] Van Den Akker, J.A., "Instrumentation Studies LXXXIX, Tearing Strength of Paper: III. Tearing Resistance by the In-Plane Mode of Tear", *TAPPI Journal*, v50,n9, **Sept 1967**, pp.466-470.

[49] Van Issum, B.E., *personal communication*, E.I.DuPont, **1989**.

[50] Wang, Y.J., "Mechanics of Fiber Reinforced Cementitious Composites", Ph.D. Thesis, M.I.T. Mechanical Eng. Dept., **May 1989**.

[51] Welsh, H.S. "Fundamental Properties of High Stretch Paper", in Consolidation of the Paper Web, Transactions, Cambridge, Sept.1965, ed. F. Bolam, Technical Section of the British Paper and Board Makers' Association, London, **1966**.

[52] Westvaco Corporation, "Panorama of Papermaking Today", **1982**.

[53] Weyerhaeuser Paper Company Annual Report **1989**.

[54] Wilkinson, N.B., Papermaking in America, Eleutherian Mills–Hagley Foundation, Inc., The Hagley Muscum, Greenville, Delaware, 1975.

Appendix A

Fracture Tests

- Specimen Dimensions
  - Fracture Toughness vs. Length
  - Fracture Toughness vs. Width
  - Fracture Toughness vs. a/W
- Westvaco Paper Fracture Results
  - Fracture Energy
  - Comparison w/o PET
  - Comparison w/ PET
  - Fracture Toughness
  - Fracture Resistance
  - Series I Table
  - Series II Table

Fracture Toughness vs. Length

Xerox paper, 75g/m

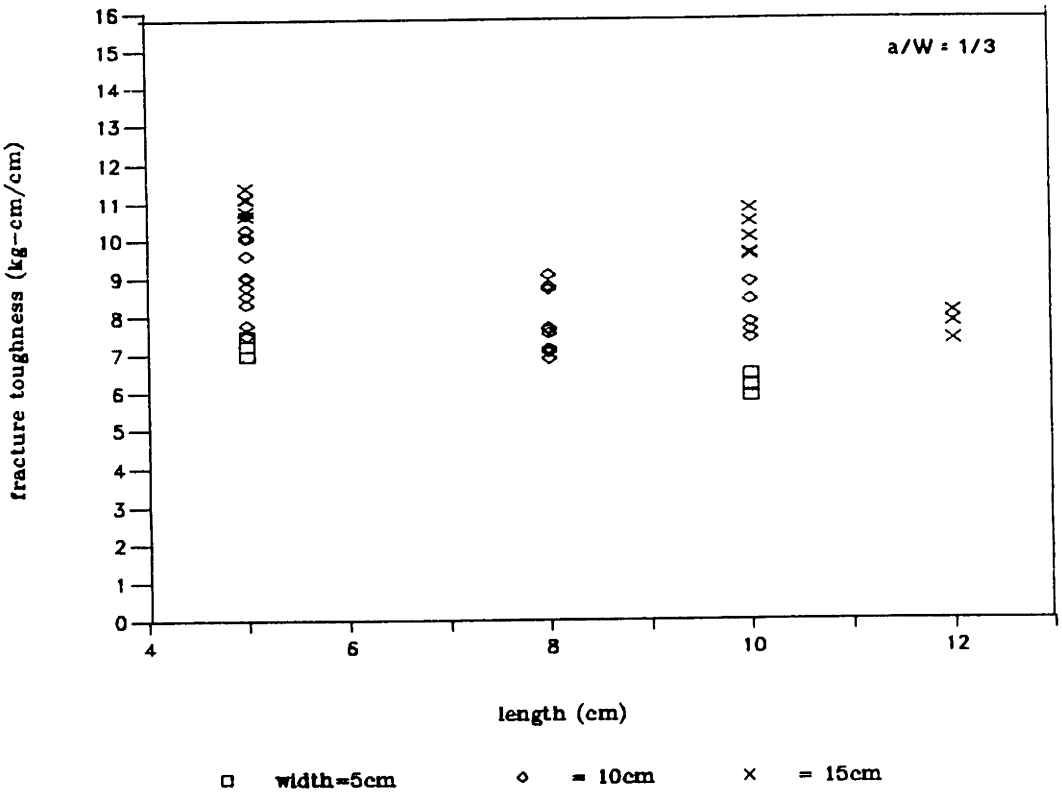

Fracture Toughness vs. Width

Xerox paper, 75g/m^2

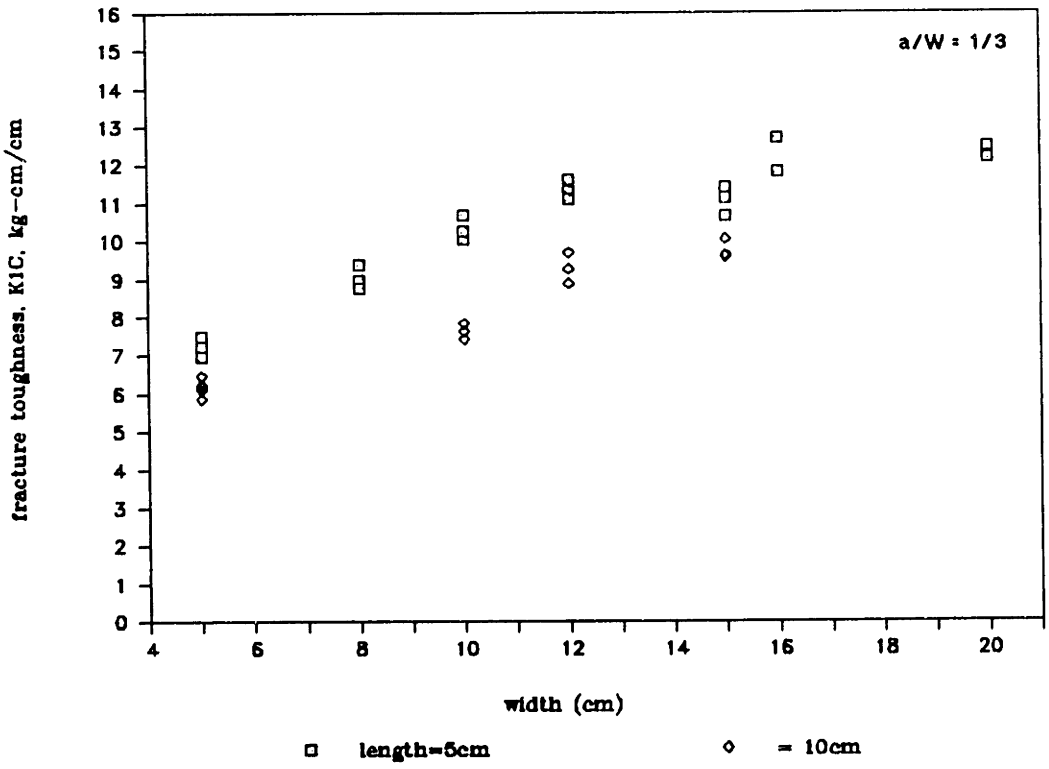

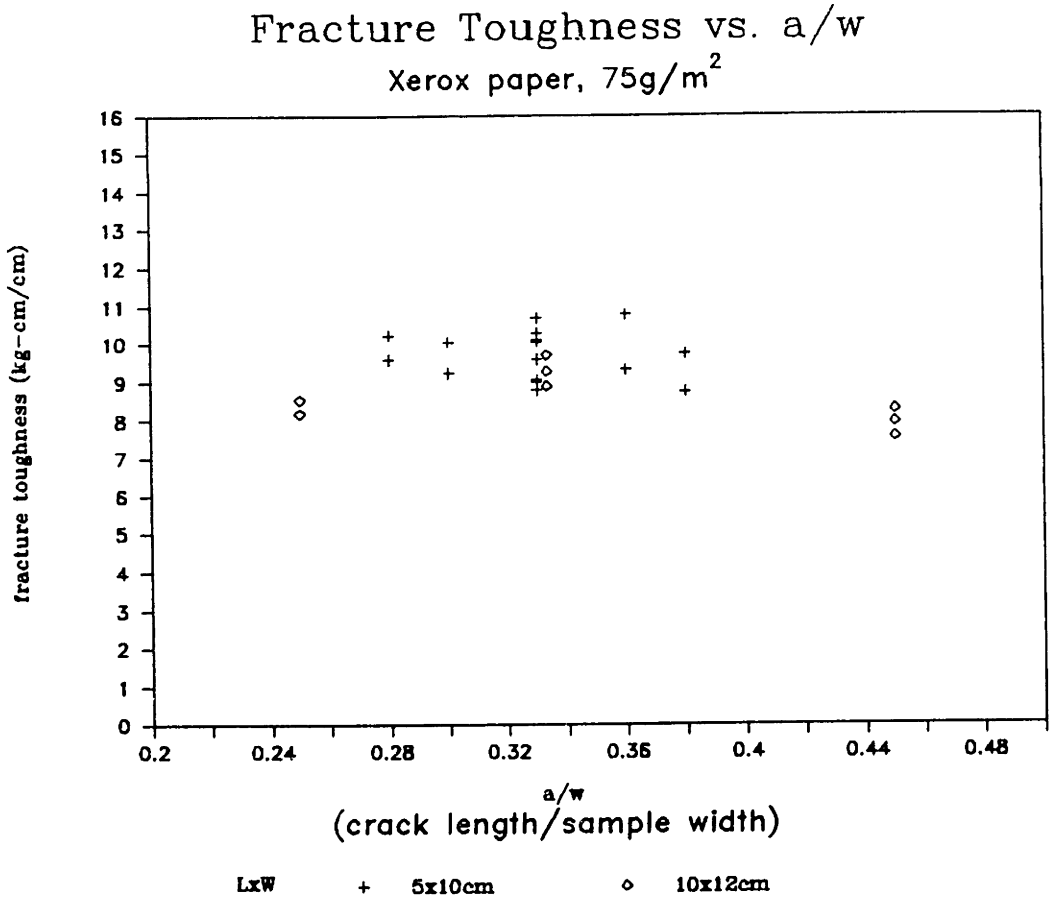
Fracture Toughness vs. a/w
Xerox paper, 75g/m2
fracture toughness (kg-cm/cm)
16
15
14
13
12
11
10
9
8
7
6
5
4
3
2
1
0
0.2
0.24
0.28
0.32
0.36
0.4
0.44
0.48
a/w
(crack length/sample width)
LxW
+ 5x10cm
◇ 10x12cm

WESTVACO PAPER FRACTURE TEST

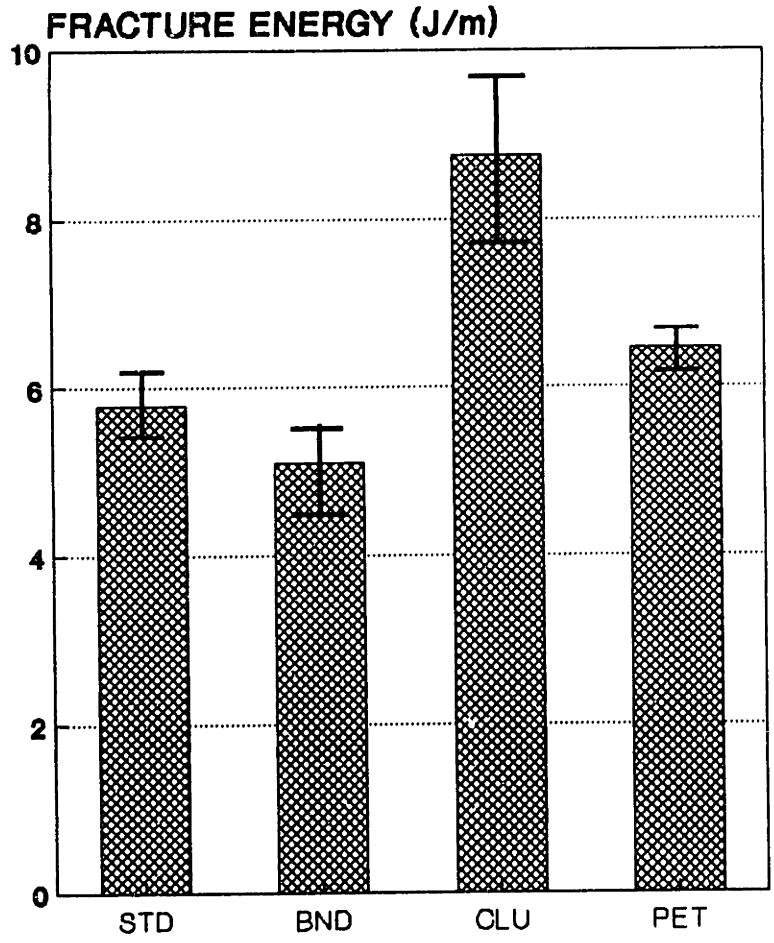

WESTVACO PAPER TESTS
ENERGY VALUES

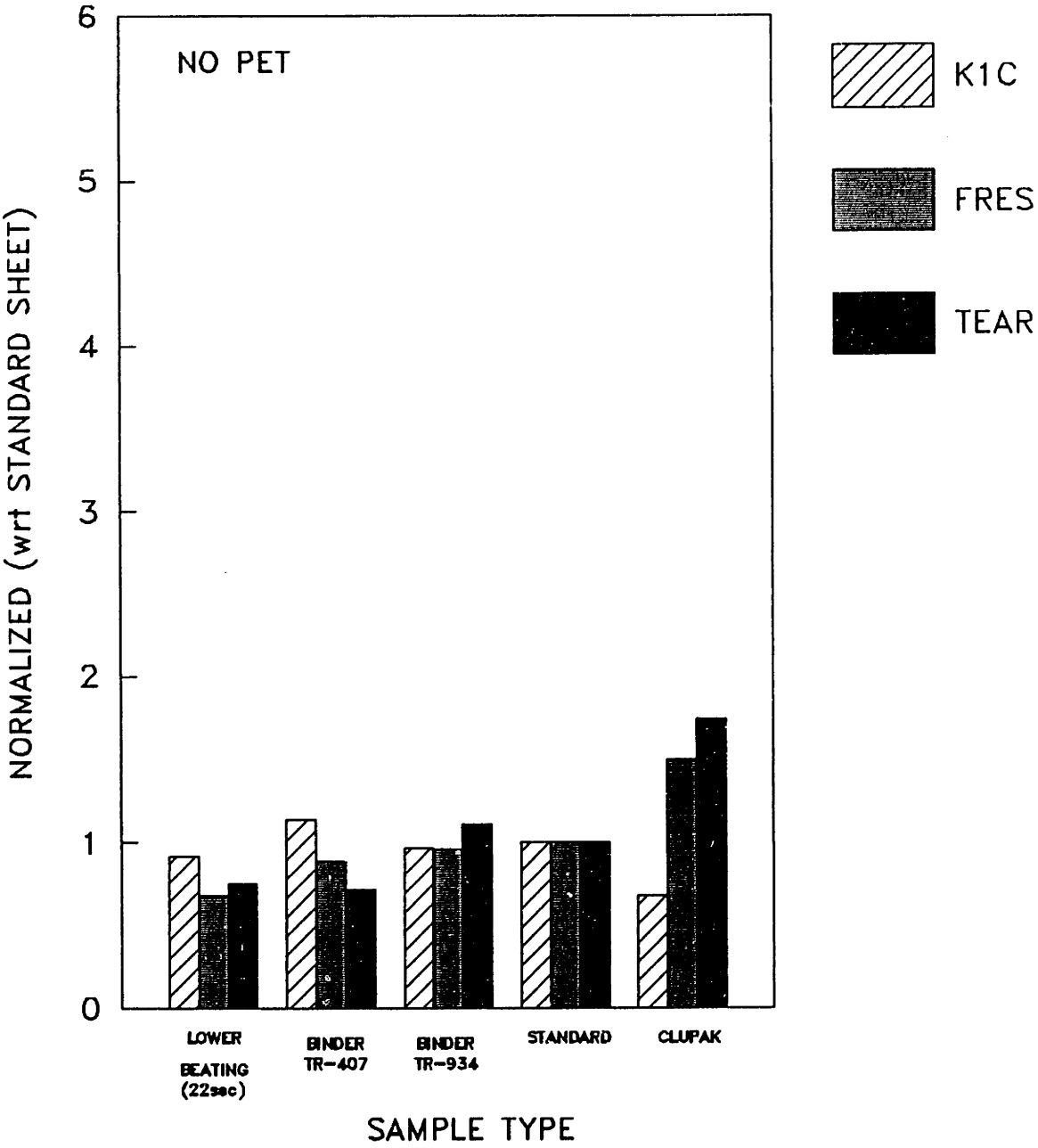

WESTVACO PAPER TESTS
ENERGY VALUES

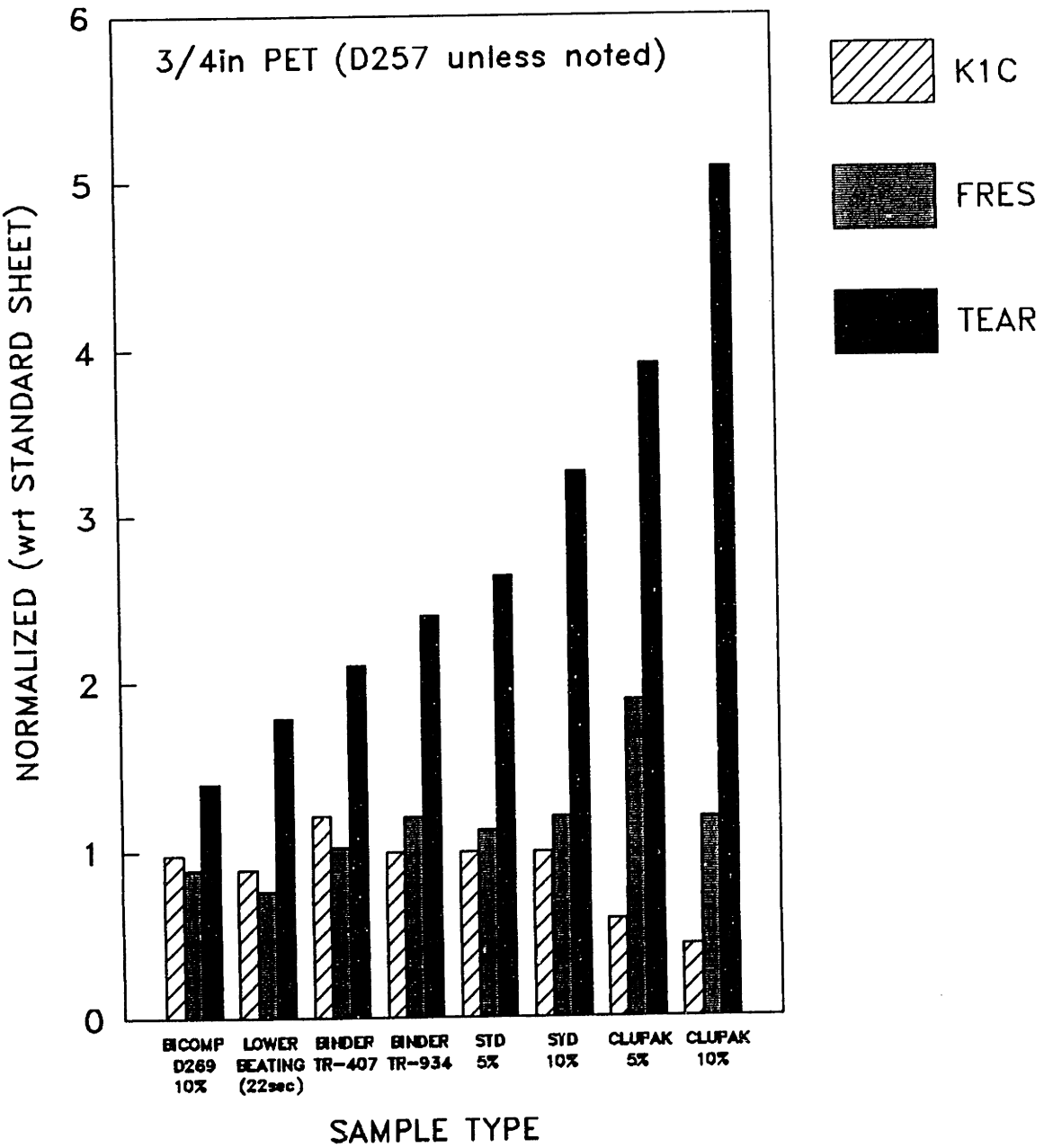

WESTVACO PAPER FRACTURE TESTS
FRACTURE TOUGHNESS
SERIES 2

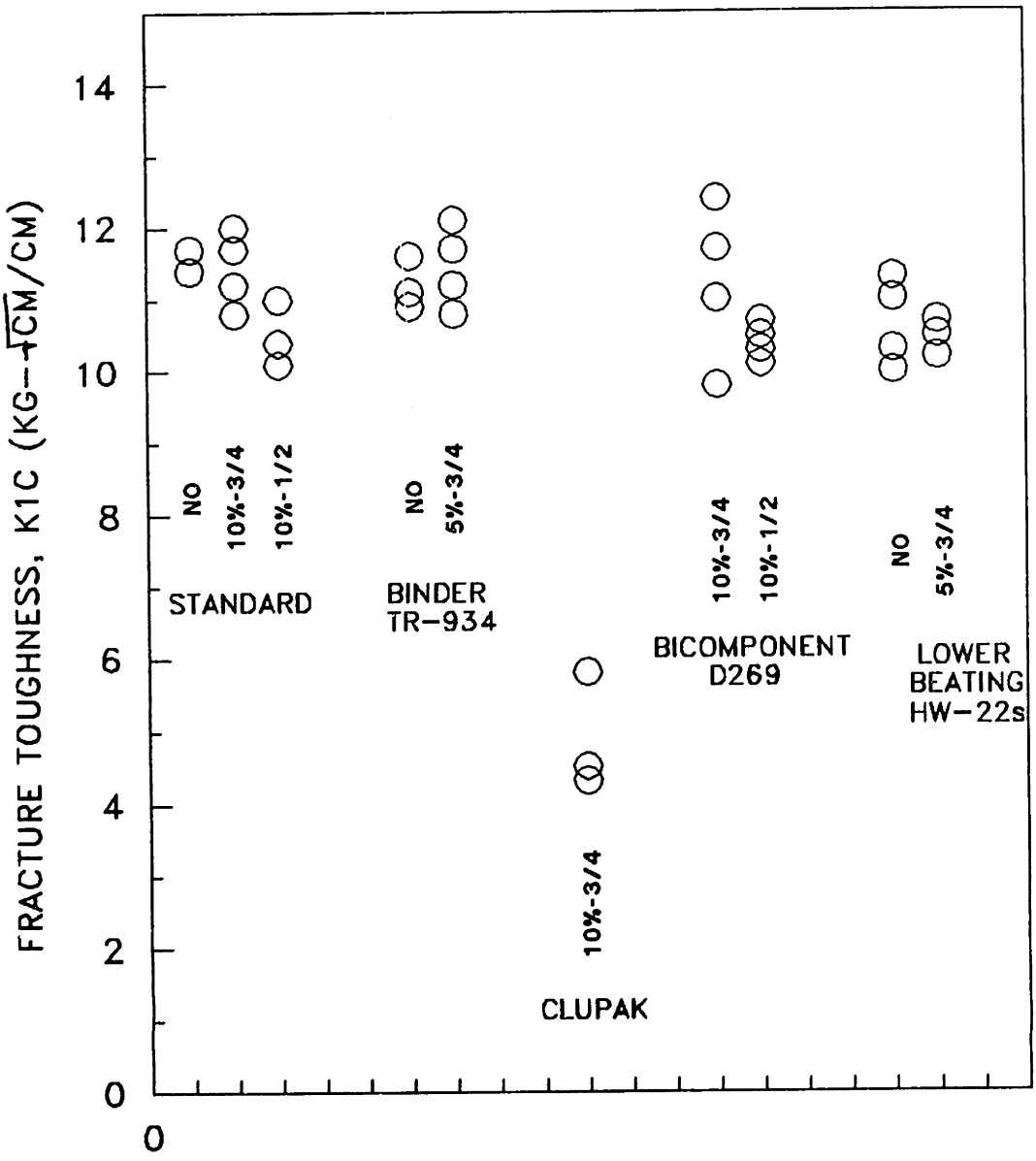

WESTVACO PAPER FRACTURE TESTS
FRACTURE RESISTANCE
SERIES 2

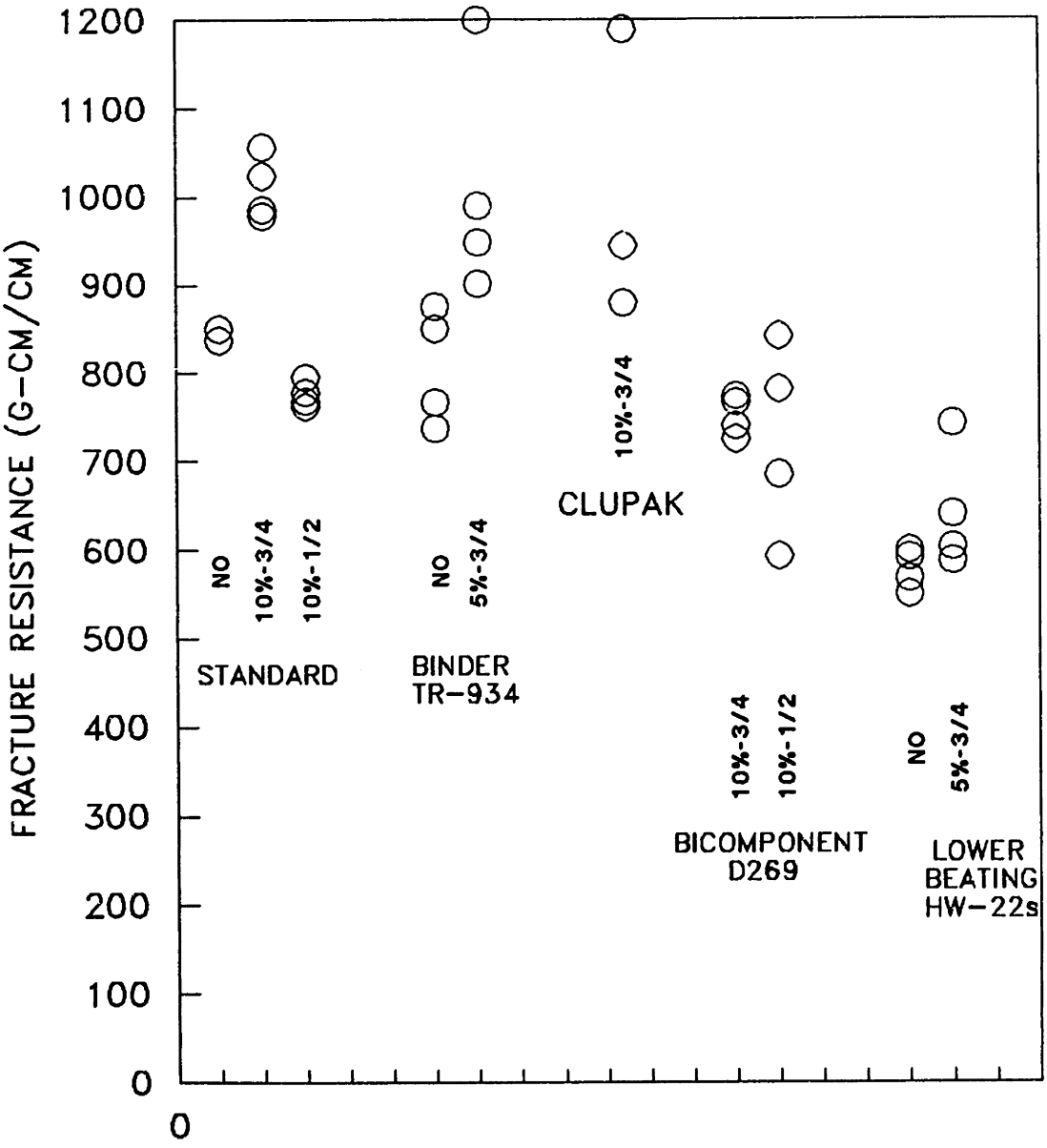

	A	B	C	D	E	F	G	H	I	J
1	WESTVACO PAPER FRACTURE AND TEAR TESTS						SERIES I			
2		4S	5S	6S	4B	5B	6B	4C	5C	6C
3		no	3/4in-5%	1/4in-5%	no	3/4in-5%	1/4in-5%	no	3/4in-5%	1/4in-5%
4		STD	D257	D257	TR-407	TR-407	TR-407	Clupak	Clupak	Clupak
5										
6	FRACTURE TOUGHNESS, K1C (KG-CM/CM)									
7		10.7	11.2	11.3	12.1	13.2	12.3	7.1	6.1	6.0
8		11.4	11.2		11.8	12.5	12.5	7.4	6.4	6.2
9		10.9						7.2	6.3	6.0
10		10.7	10.0	10.4	12.2	12.7	12.9	7.1	7.1	5.9
11		10.6	9.9	10.6	11.8	13.1	12.4	7.5	6.3	5.8
12		9.7	10.7	10.3	12.7	13.1	12.1	7.4	5.4	5.7
13										
14	AVG	10.7	10.6	10.7	12.1	12.9	12.4	7.3	6.2	5.9
15	'=/STD	1.00	0.99	1.00	1.14	1.21	0.43	0.68	0.59	0.56
16	STDEVP	0.48834471	0.54079941	0.40449815						
17										
18	FRACTURE RESISTANCE (G-CM/CM)									
19		600	676	440	583	660	684		1064	868
20		558	697		544	638	692	1058	1031	865
21		552						862	1199	851
22		662	628	388	502	524	472	848	1102	871
23		570	606	403	552	596	487	782	1184	812
24		592	647	359	402	523	457	779	973	823
25										
26	AVG	579	651	398	517	588	688	866	1092	848
27	'=/STD	1.00	1.12	0.69	0.89	1.02	1.19	1.50	1.89	1.47
28	STDEVP	36.855574	32.5907962	29.1933212						
29										
30	TEAR ENERGY (G-CM/CM)									
31		123	297	146	86	276	172	196	468	306
32		124	351	133	88	243	171	205	490	285
33		111	300	150	87	245	167	214	461	300
34		107	313	159	95	243	172	205	495	298
35		119	346	124	93	242	169	205	463	252
36		118	279	153	81	229	192	207	396	269
37		126	317	132	60	279	171			
38		118	296	139	90	227	171			
39										
40	AVG	118	312	142	85	248	173	205	462	285
41	'=/STD	1.00	2.64	1.20	0.72	2.10	1.46	1.74	3.91	2.41

	A	B	C	D	E	F	G	H	I	J	K
1	WESTVACO PAPER FRACTURE AND TEAR TESTS										
2		4S2	5S2	7S2	4B2	5B2	5C2	5D2	7D2	4F2	5F2
3		no	3/4in-10%	1/2in-10%	no	3/4in-5%	3/4in-10%	3/4in-10%	1/2in-10%	no	3/4in-5%
4		STD	D257	D257	TR-934	TR-934	Clupak	D269(bic)	D269(bic)	HW-22s	HW-22s
5											
6	FRACTURE TOUGHNESS, K1C (KG-CM/CM)										
7		11.7	11.7	10.1	10.9	11.2	4.5	11.0	10.5	11.0	10.7
8		11.4	10.8	10.4	11.6	12.1	4.3	9.8	10.3	10.0	10.2
9			12.0	11.0	11.1	11.7	5.8	12.4	10.1	11.3	10.5
10			11.2	11.0		10.8		11.7	10.7	10.3	9.7
11											
12	AVG	11.5	11.4	10.6	11.2	11.4	4.9	11.2	10.4	10.6	10.3
13	'=/STD	1.00	0.99	0.92	0.97	0.99	0.43	0.98	0.90	0.92	0.89
14	STDEVP	0.14	0.48	0.41	0.30	0.49	0.66	0.94	0.24	0.53	0.38
15											
16	FRACTURE RESISTANCE (G-CM/CM)										
17		838	1024	778	876	949	945	767	685	550	743
18		851	1056	796	851	1200	880	740	782	592	641
19			979	768	737	902	1189	725	593	600	588
20			986	762	767	990		774	842	568	604
21											
22	AVG	844	1011	776	808	1010	1005	752	726	577	644
23	'=/STD	1.00	1.20	0.92	0.96	1.20	1.19	0.89	0.86	0.68	0.76
24	STDEVP	6.60	30.82	12.71	57.49	113.77	133.02	19.85	95.05	19.88	60.29
25											
26	TEAR ENERGY (G-CM/CM)										
27		157	573	474	233	430	879	165	286	121	286
28		176	525	435	213	448	922	201	320	122	317
29		168	584	520	176	392	1002	269	175	132	338
30		158	541	510	178	437	1128	199	175	124	326
31		206	568	467	203	380	726	332	216	158	310
32		212	725	455	197	506	845	356	236	153	321
33		196	589	444	189	479	916	277	273	148	335
34		185	652	451	223	434	984	242	240	134	375
35											
36	AVG	182	595	470	202	438	925	255	240	137	326
37	'=/STD	1.00	3.26	2.58	1.11	2.40	5.08	1.40	1.32	0.75	1.79

Appendix B

Stat Tests

- Test Dimensions and Conditions
  - Specimen Dimensions and Max. Strain
  - Specimen Dimensions and Max. Stress
  - Effect of Crosshead Speed
- Barcharts and Normal Curves
  - Elastic Modulus — Dogbone
  - Elastic Modulus — Fillet
  - Plastic Modulus — Dogbone
  - Plastic Modulus — Fillet
  - Yield Stress — Dogbone
  - Yield Stress — Fillet
  - Breaking Strain — Dogbone
  - Breaking Strain — Fillet

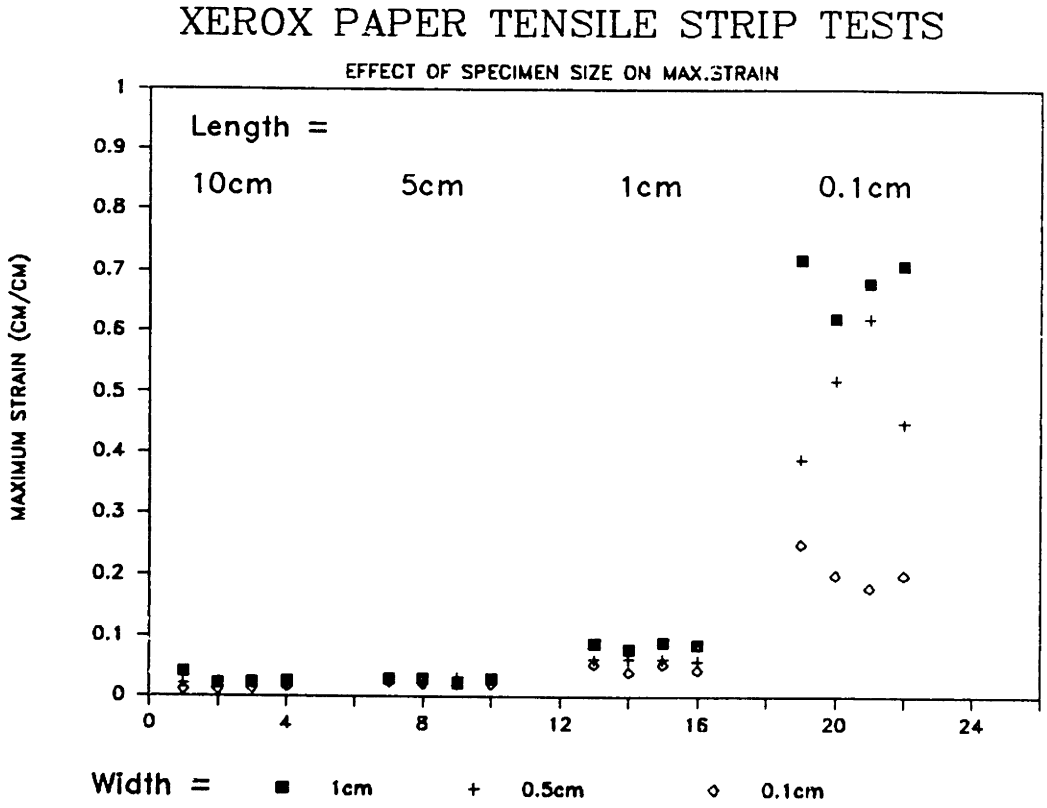
XEROX PAPER TENSILE STRIP TESTS
EFFECT OF SPECIMEN SIZE ON MAX.STRAIN
MAXIMUM STRAIN (CM/CM)
Length =
10cm
5cm
1cm
0.1cm
0
0.1
0.2
0.3
0.4
0.5
0.6
0.7
0.8
0.9
1
0
4
8
12
16
20
24
Width =
1cm
0.5cm
0.1cm

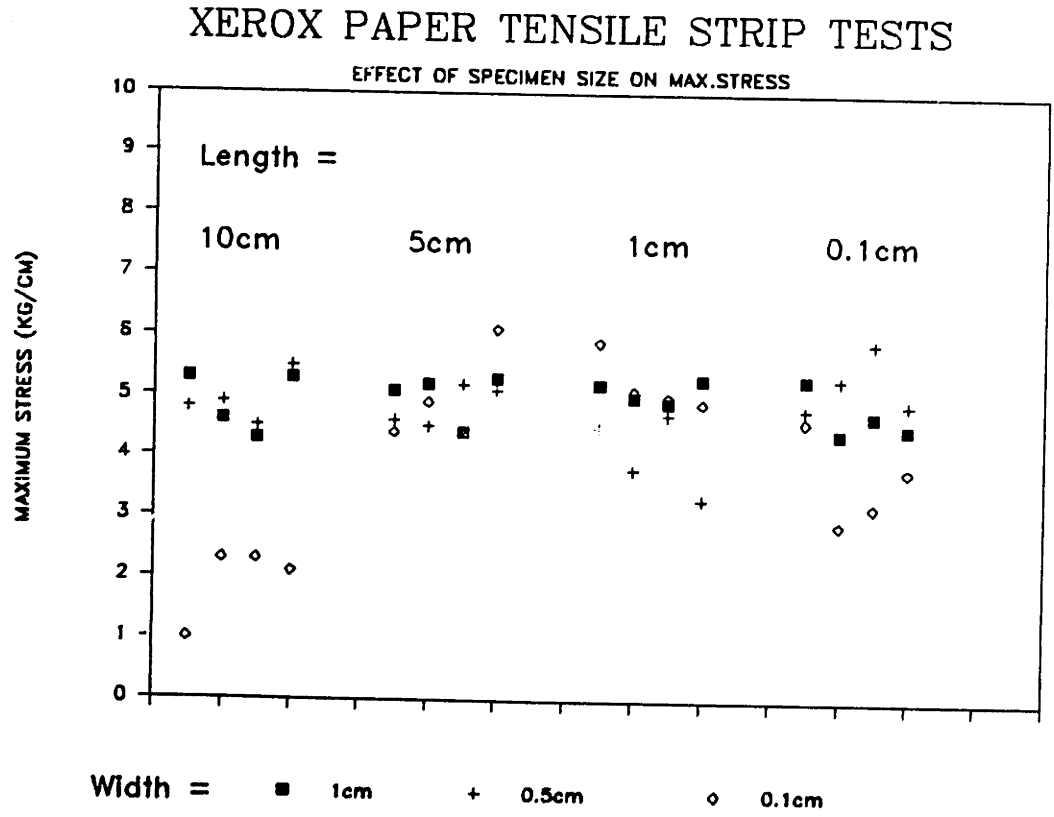
XEROX PAPER TENSILE STRIP TESTS
EFFECT OF SPECIMEN SIZE ON MAX.STRESS
MAXIMUM STRESS (KG/CM)
Length =
10cm
5cm
1cm
0.1cm
0
1
2
3
4
5
6
7
8
9
10
Width =
1cm
0.5cm
0.1cm

XEROX PAPER TENSILE STRIP TESTS

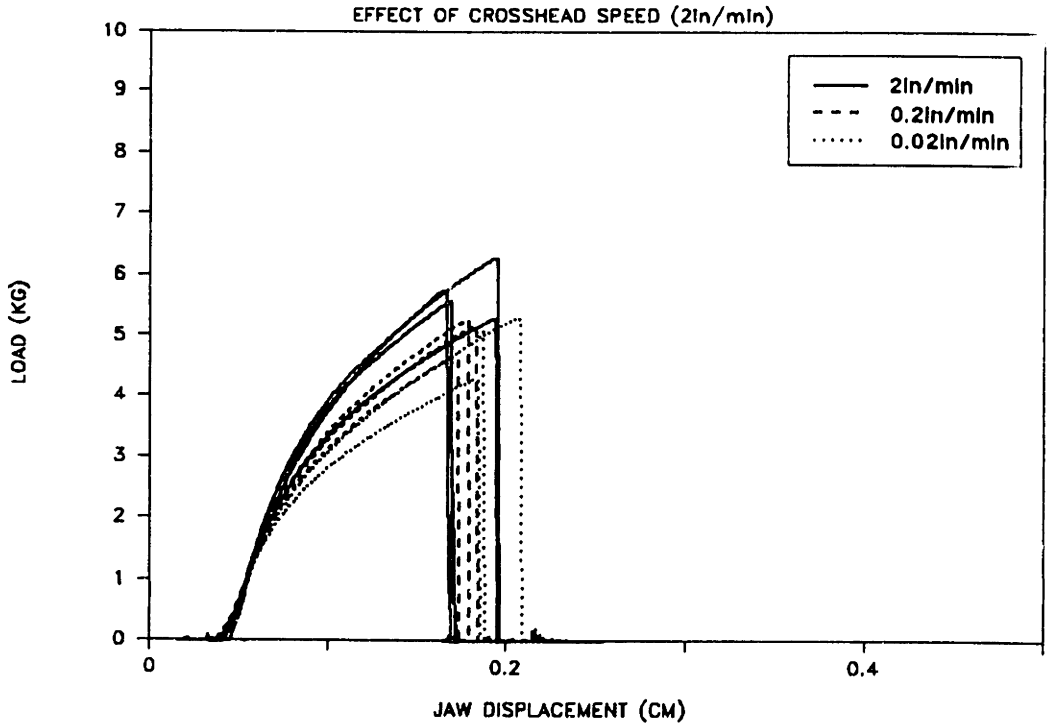

XEROX PAPER TENSILE STRIP TESTS

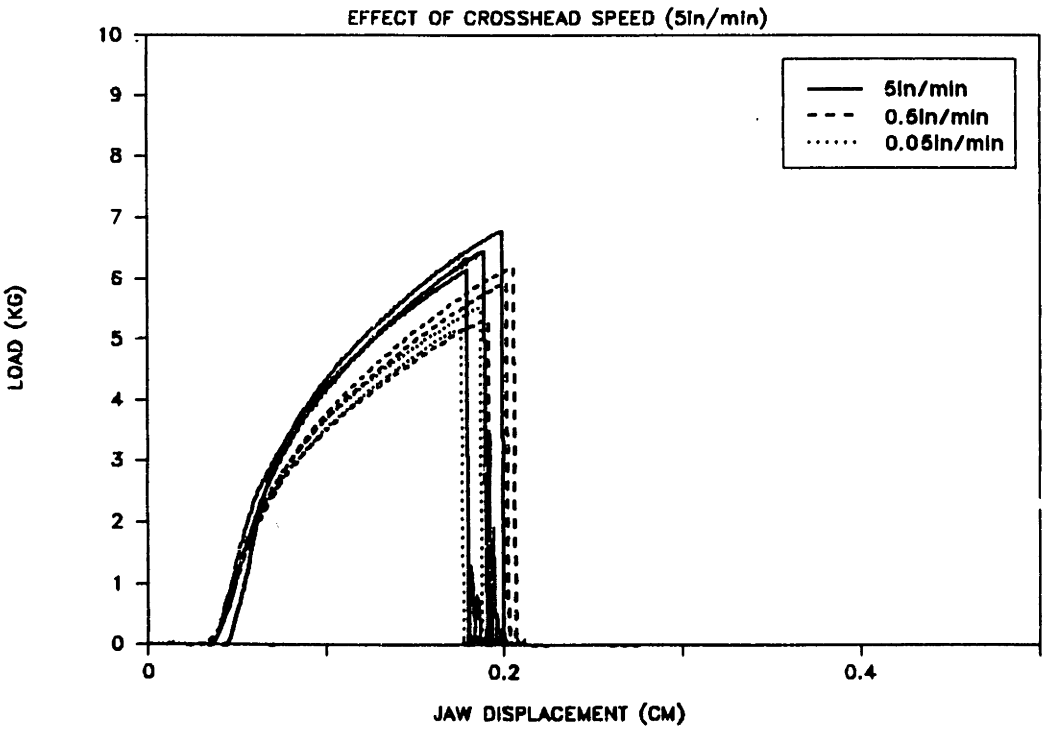

WESTVACO STAT TESTS

STANDARD -- DOGBONE

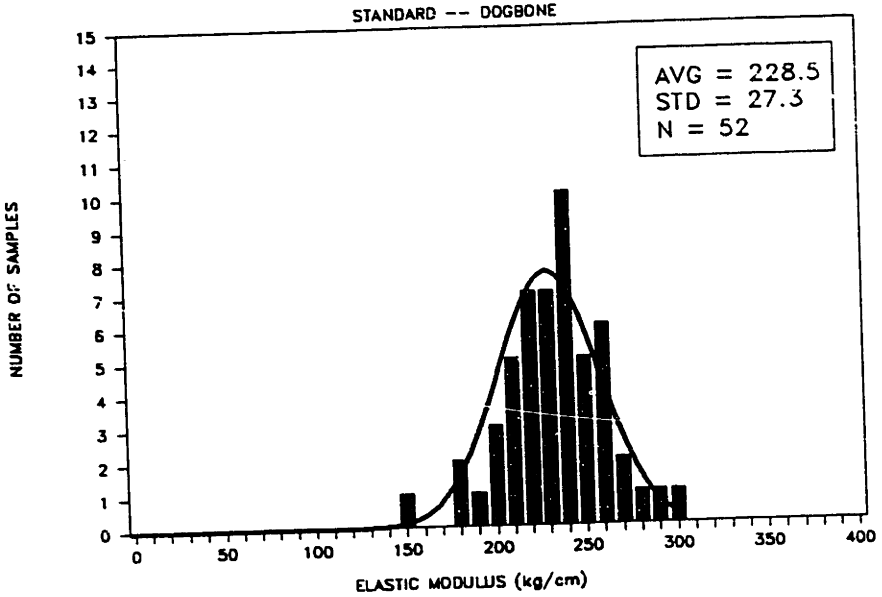

WESTVACO STAT TESTS

BINDER (TR-407) -- DOGBONE

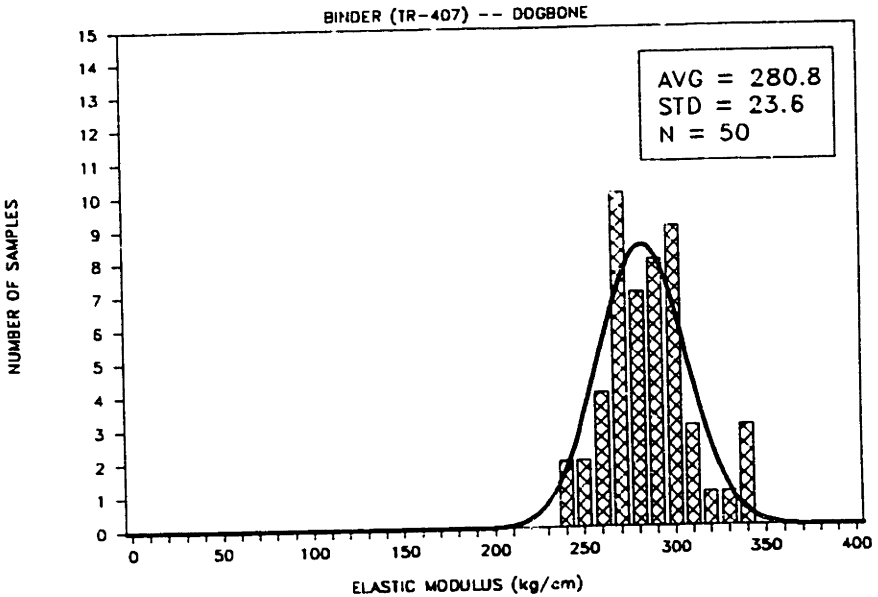

WESTVACO STAT TESTS

CLUPAK (6%) -- DOGBONE

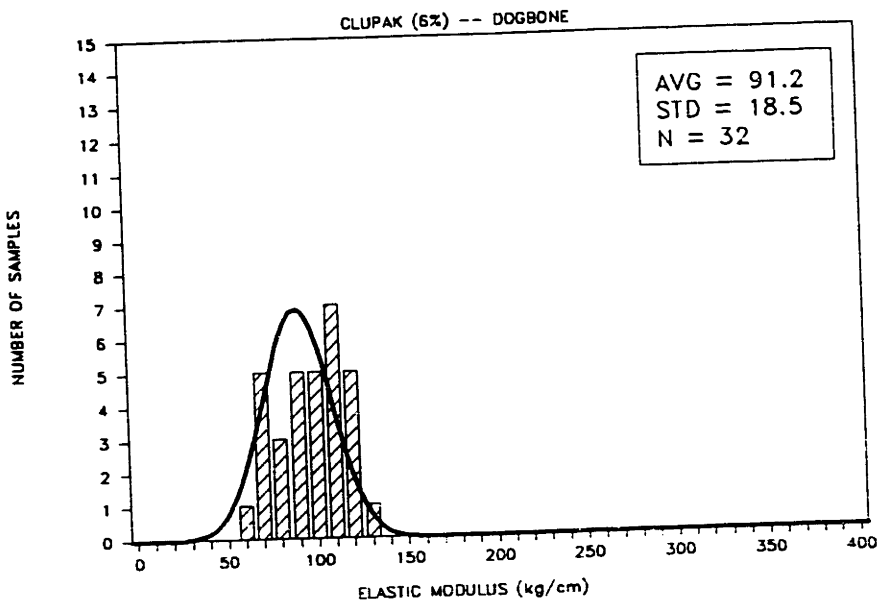

WESTVACO STAT TESTS

PET (5%,3/4in) -- DOGBONE

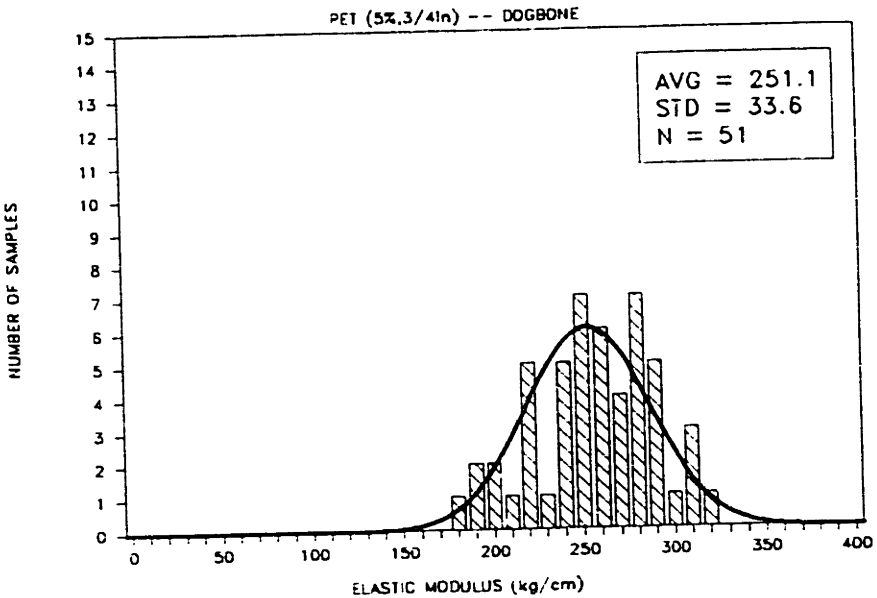

WESTVACO STAT TESTS

STANDARD -- FILLET

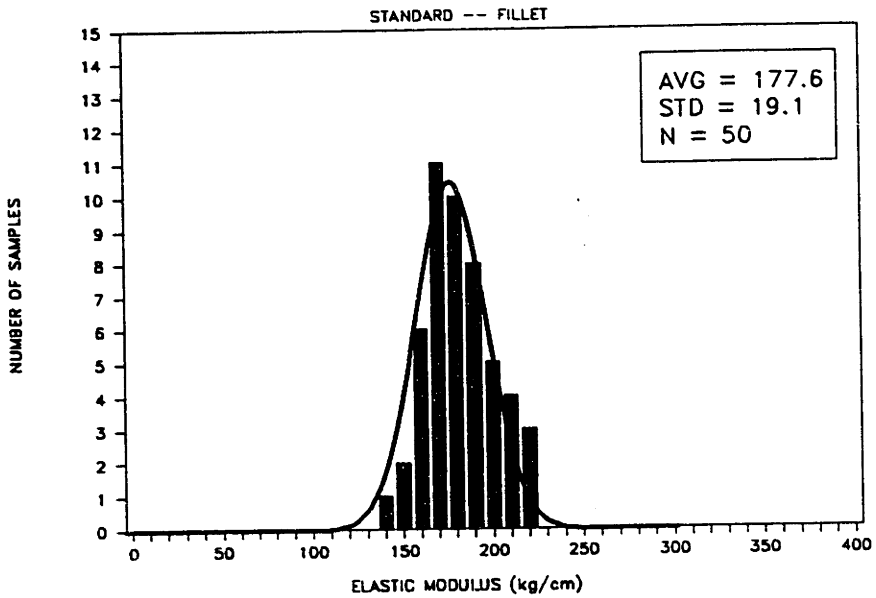

WESTVACO STAT TESTS

BINDER (TR-407) -- FILLET

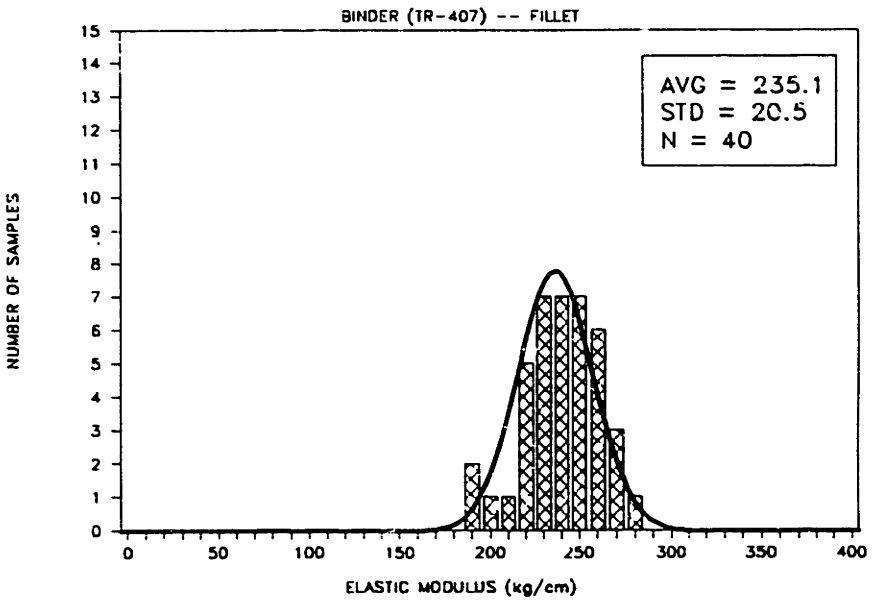

WESTVACO STAT TESTS

CLUPAK (6%) -- FILLET

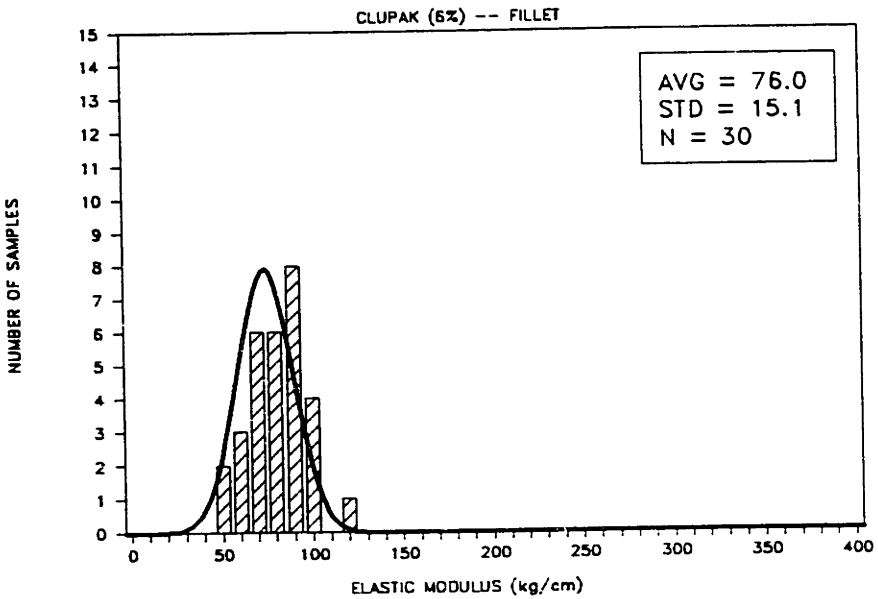

WESTVACO STAT TESTS

PET (5%,3/4in) -- FILLET

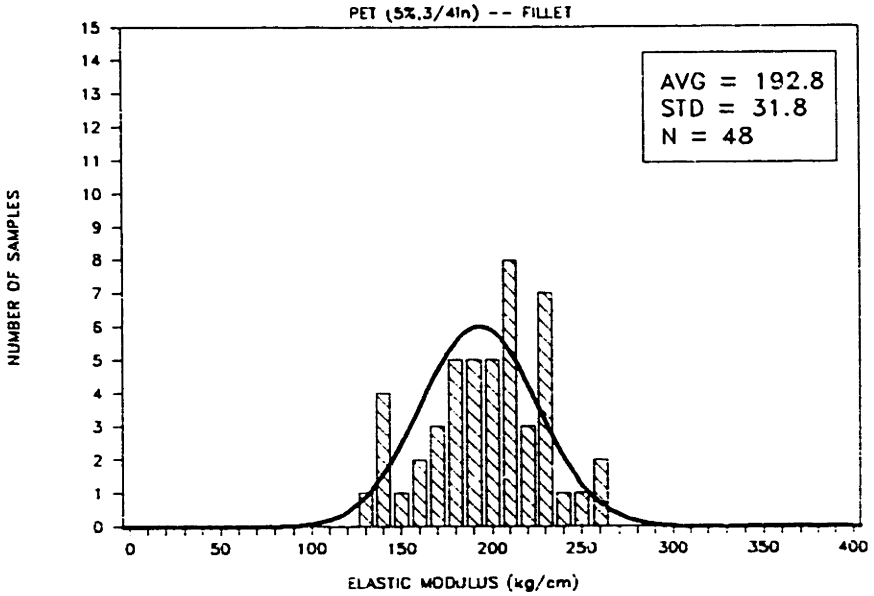

WESTVACO STAT TESTS

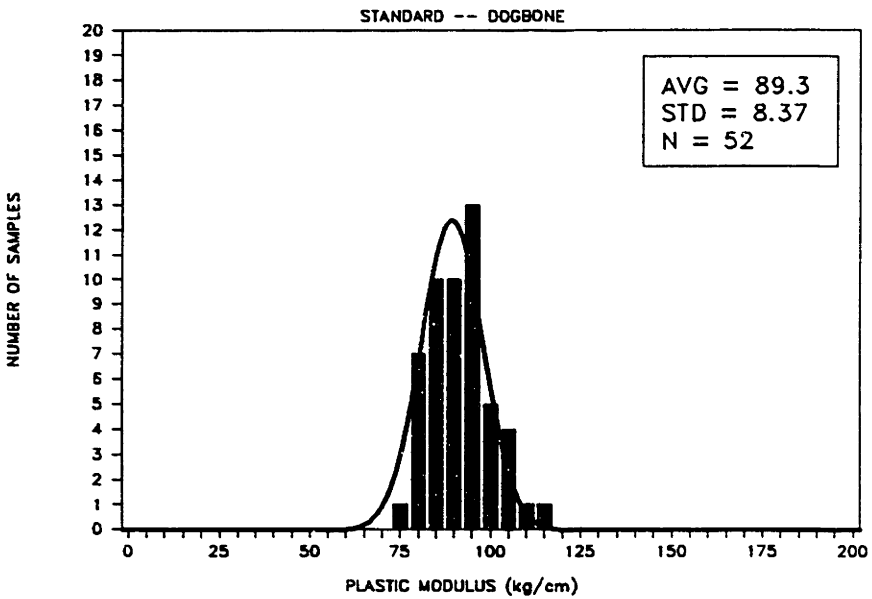

WESTVACO STAT TESTS

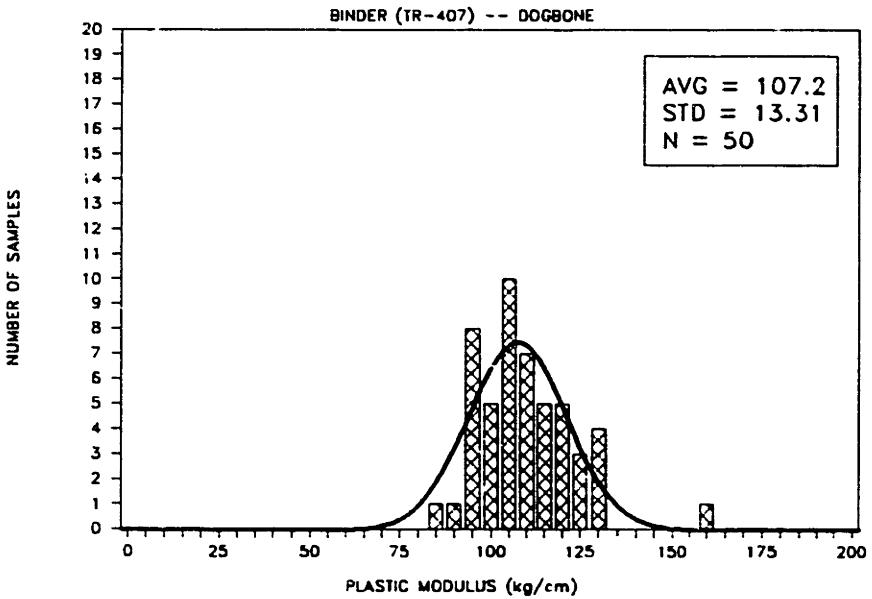

WESTVACO STAT TESTS

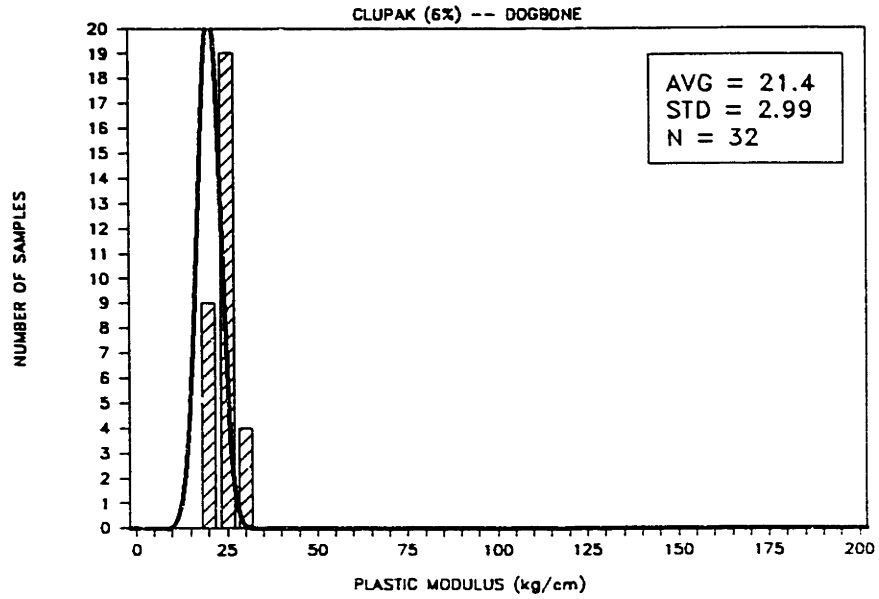

WESTVACO STAT TESTS

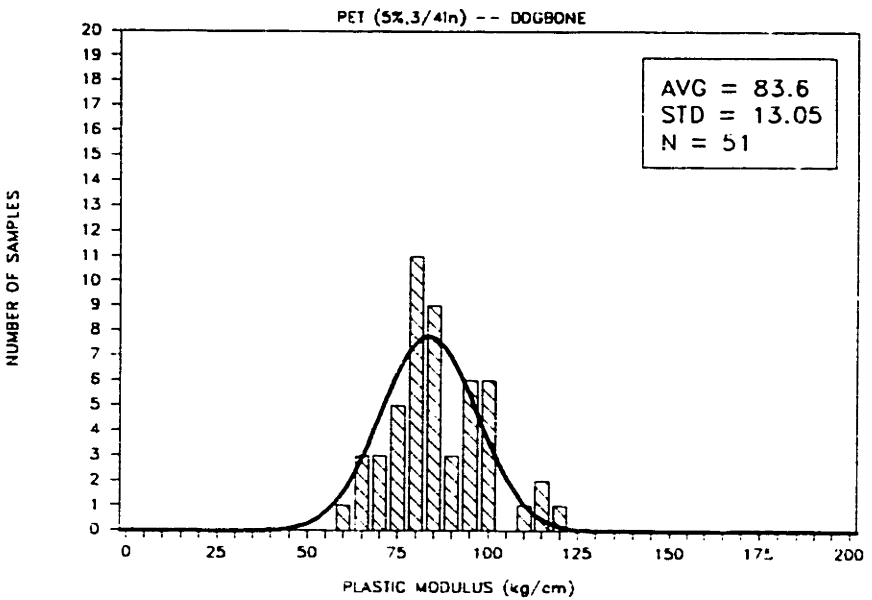

WESTVACO STAT TESTS

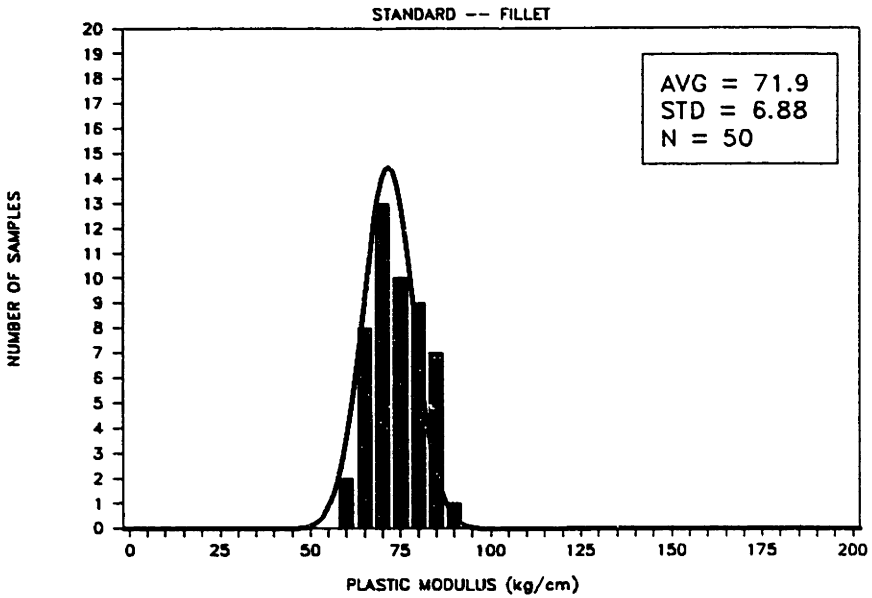

WESTVACO STAT TESTS

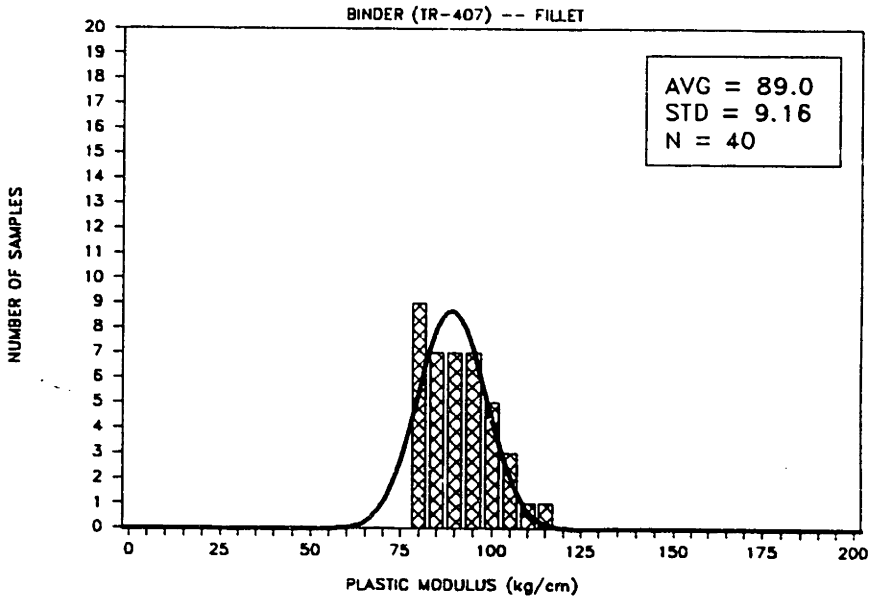

WESTVACO STAT TESTS

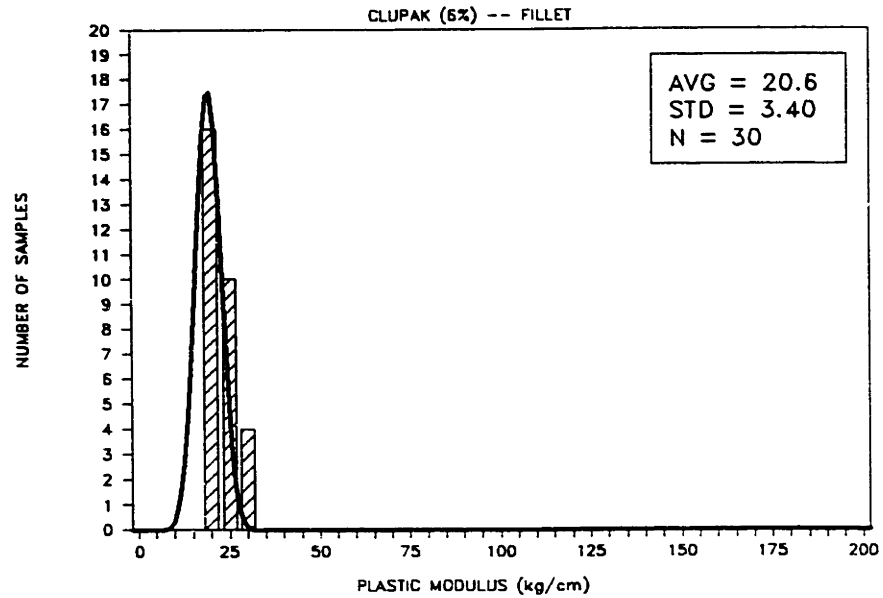

WESTVACO STAT TESTS

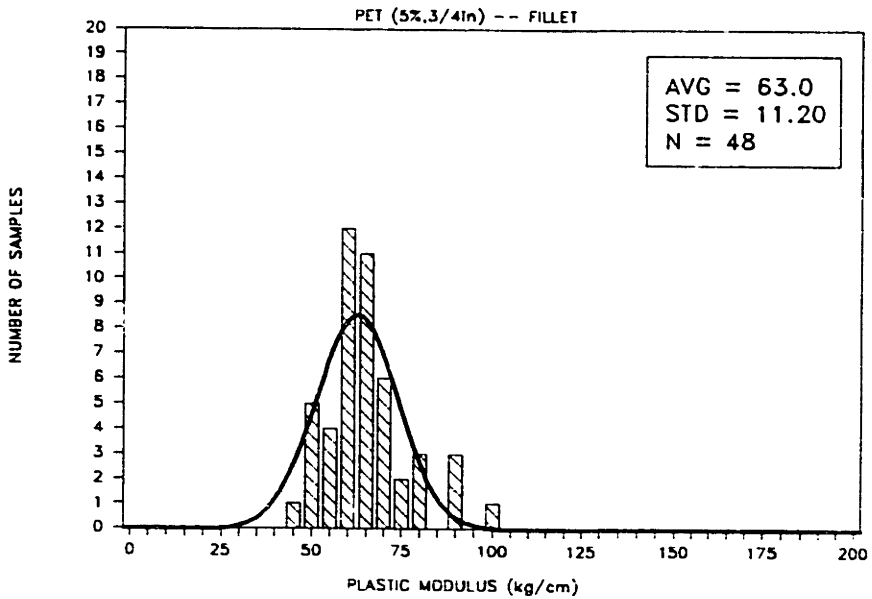

WESTVACO STAT TESTS

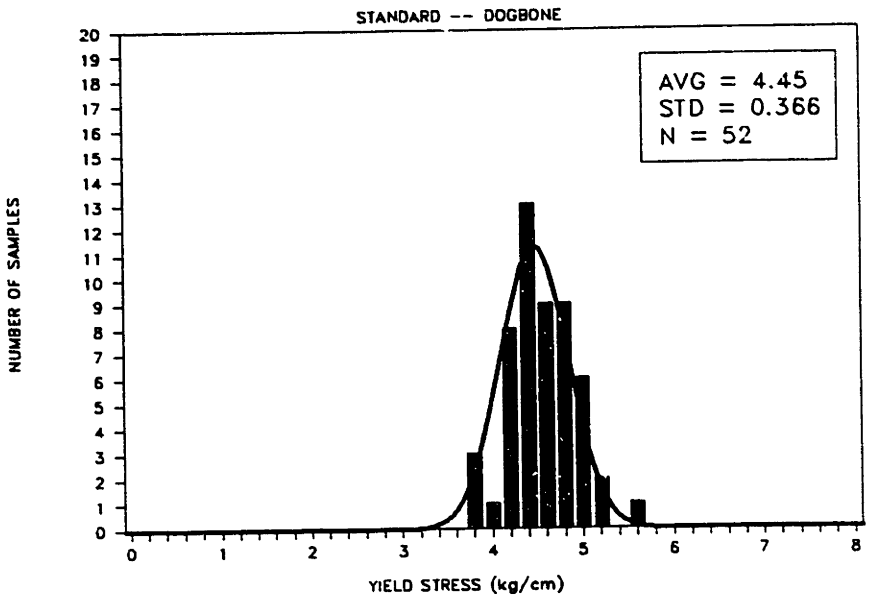

WESTVACO STAT TESTS

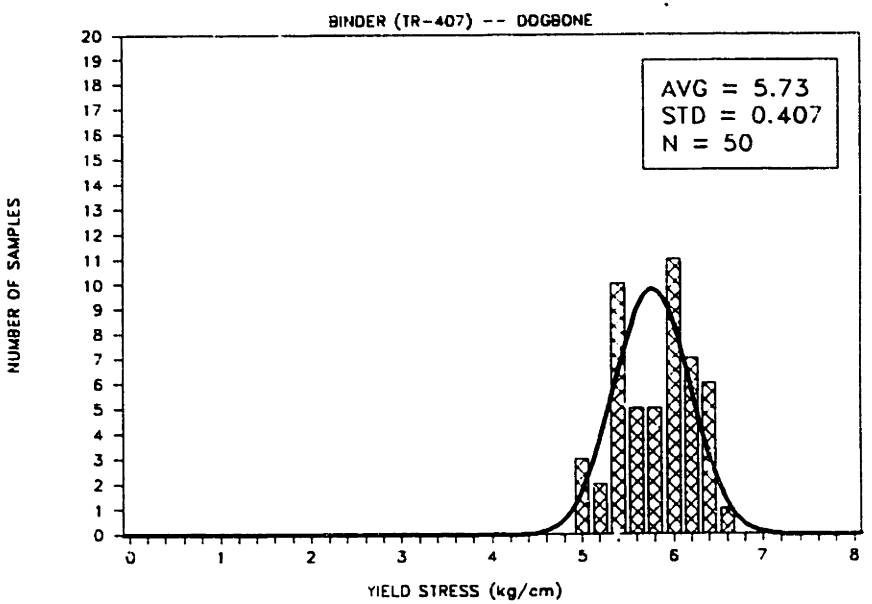

WESTVACO STAT TESTS

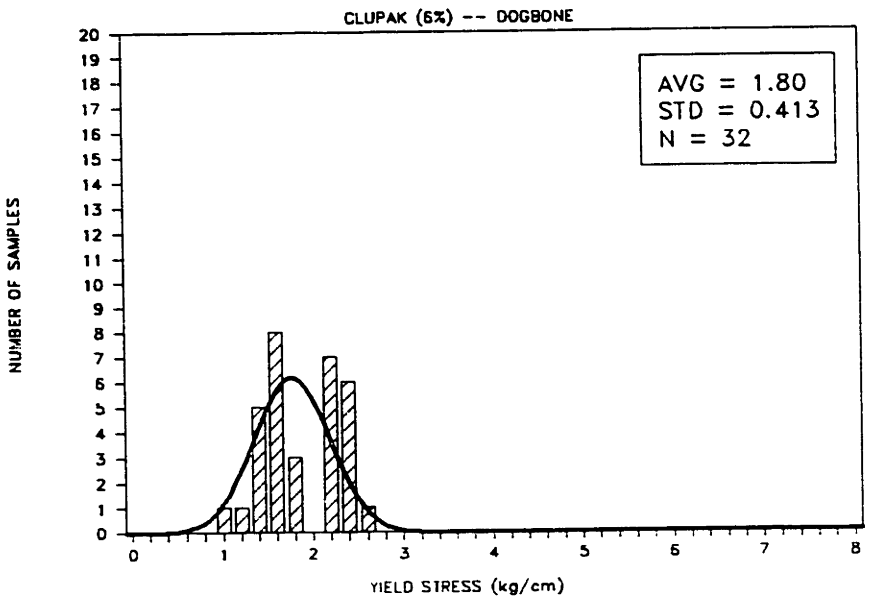

WESTVACO STAT TESTS

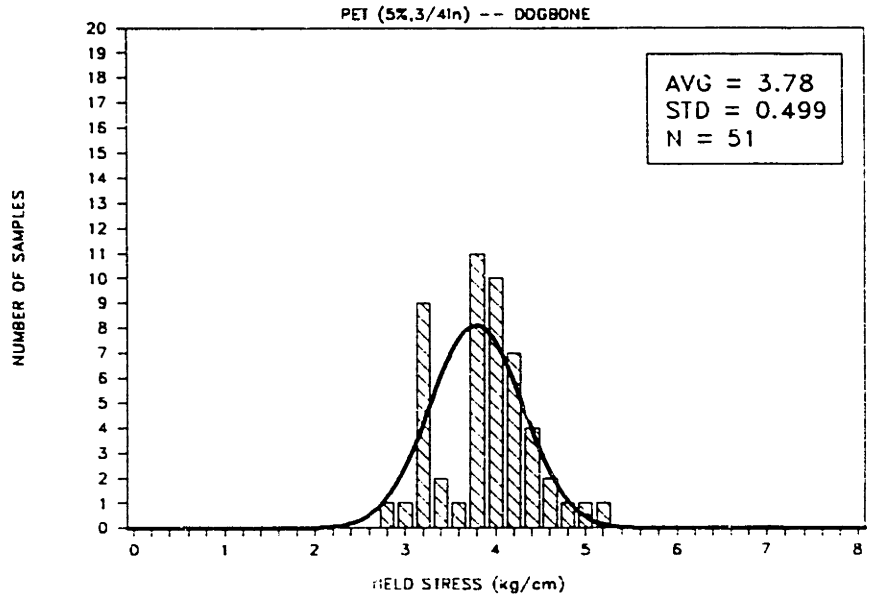

WESTVACO STAT TESTS

STANDARD -- FILLET

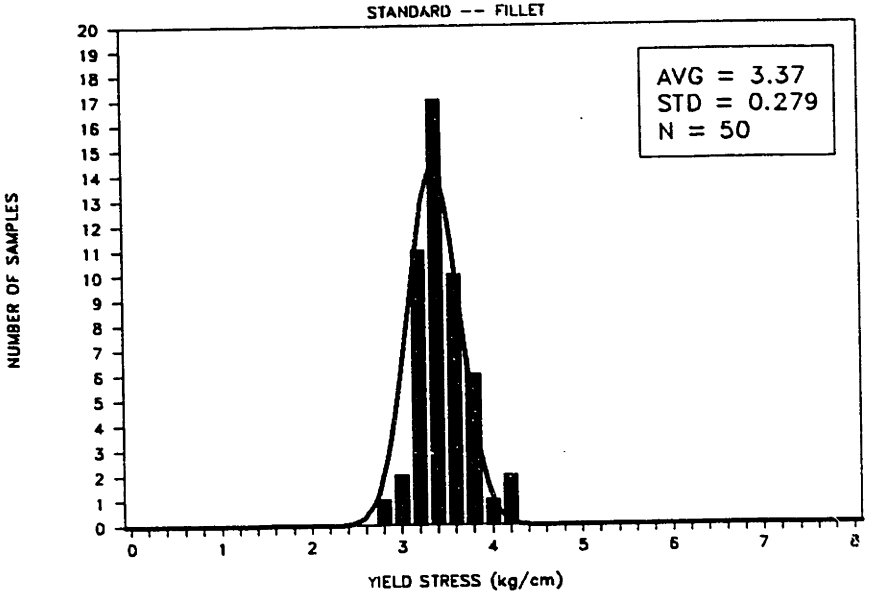

WESTVACO STAT TESTS

BINDER (TR-407) -- FILLET

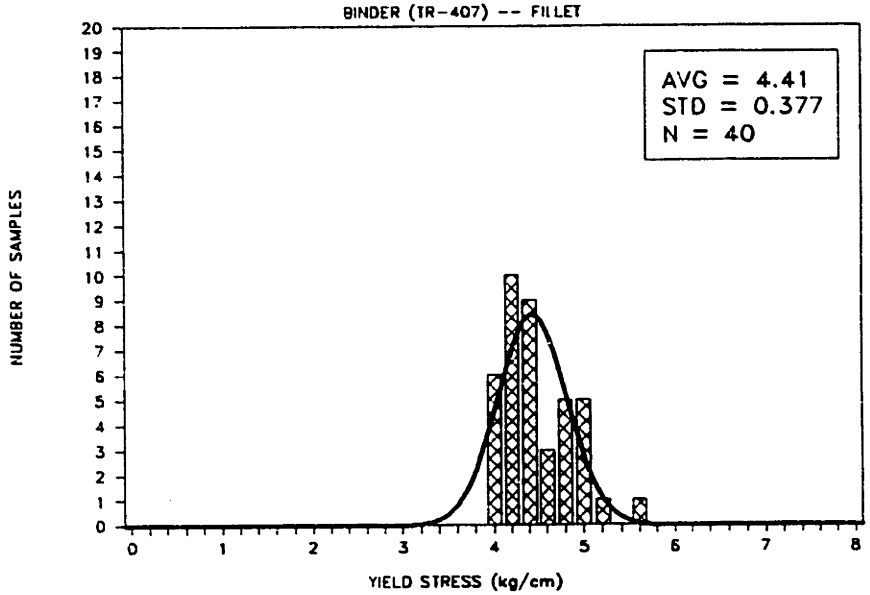

WESTVACO STAT TESTS

CLUPAK (6%) -- FILLET

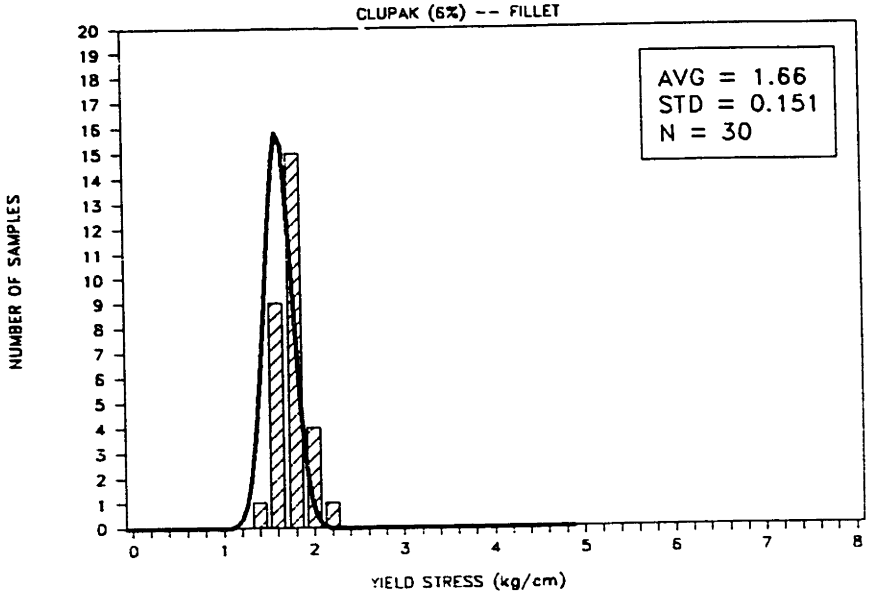

WESTVACO STAT TESTS

PET (5%,3/4in) -- FILLET

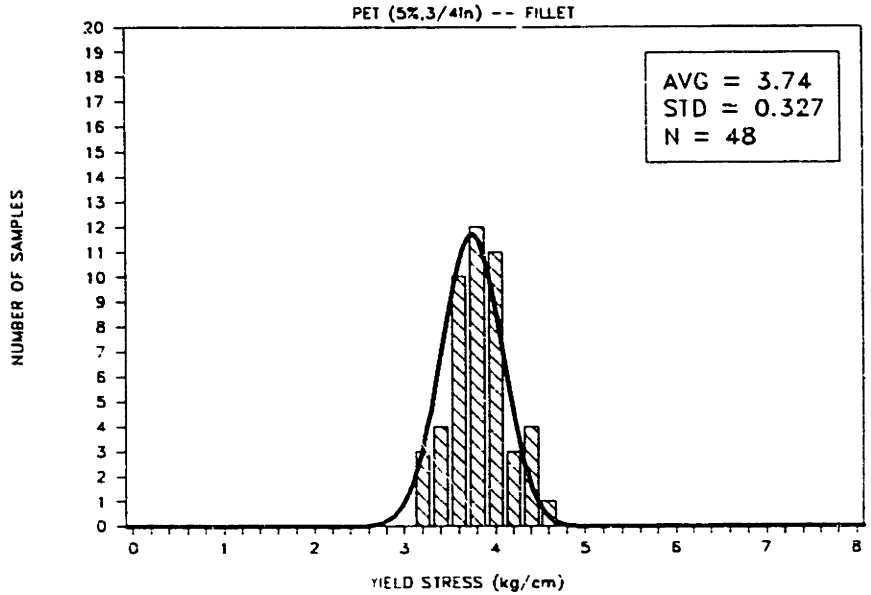

WESTVACO STAT TESTS

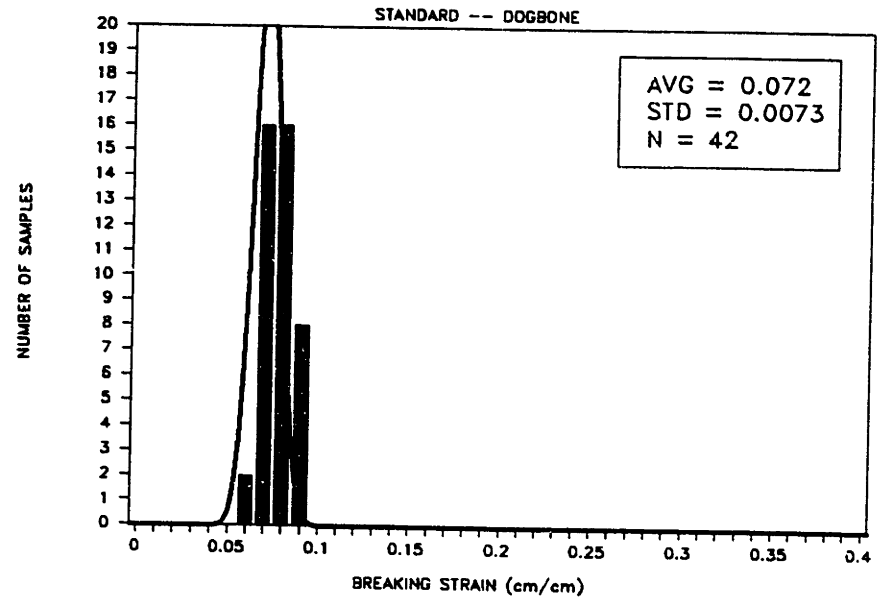

WESTVACO STAT TESTS

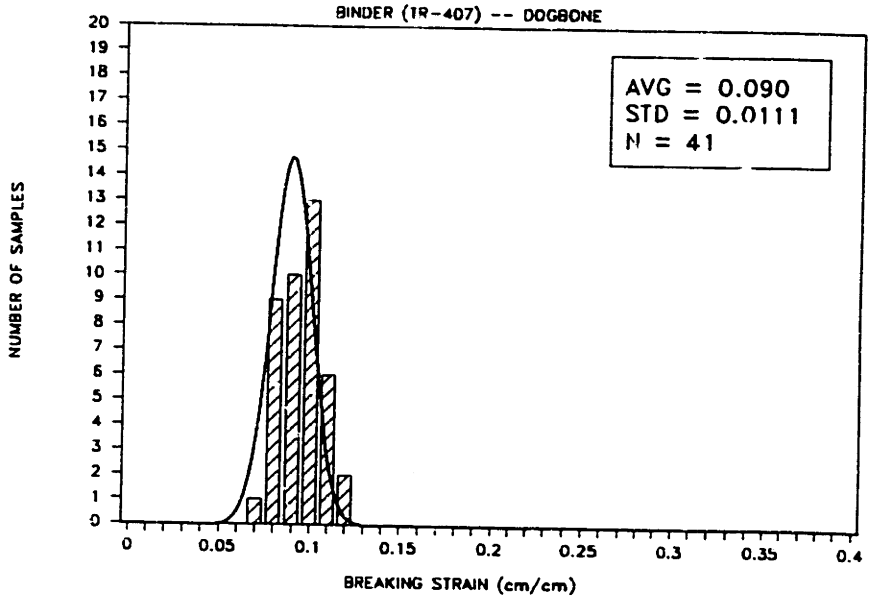

WESTVACO STAT TESTS

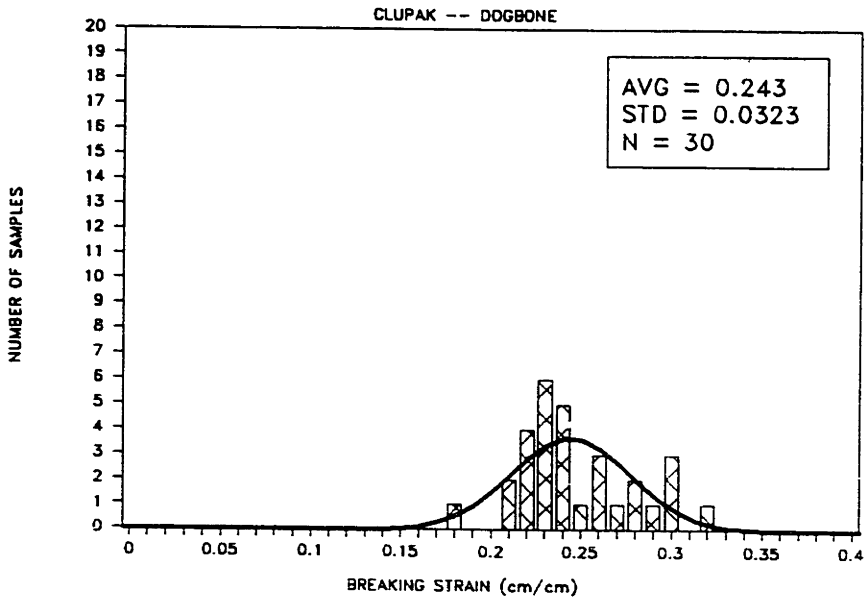

WESTVACO STAT TESTS

STANDARD -- FILLET

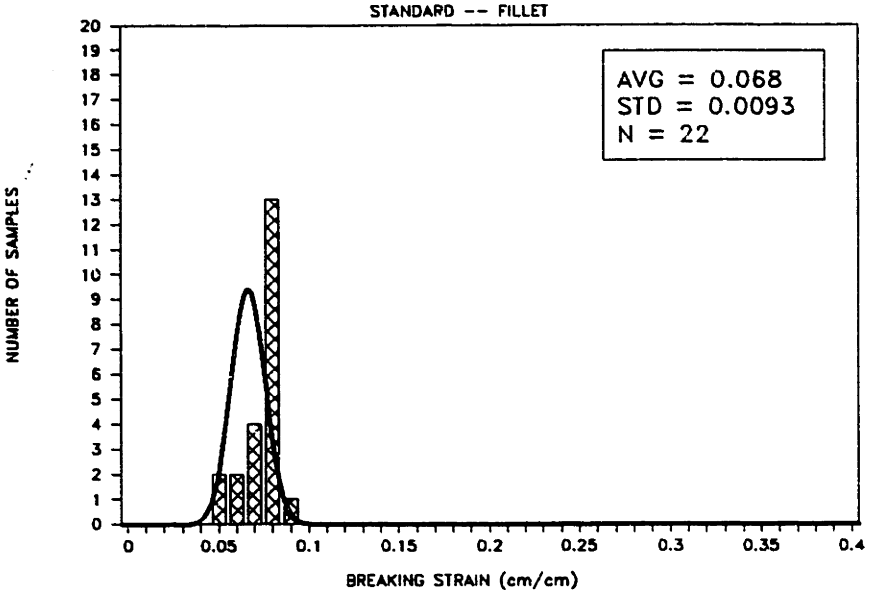

WESTVACO STAT TESTS

BINDER (TR-407) -- FILLET

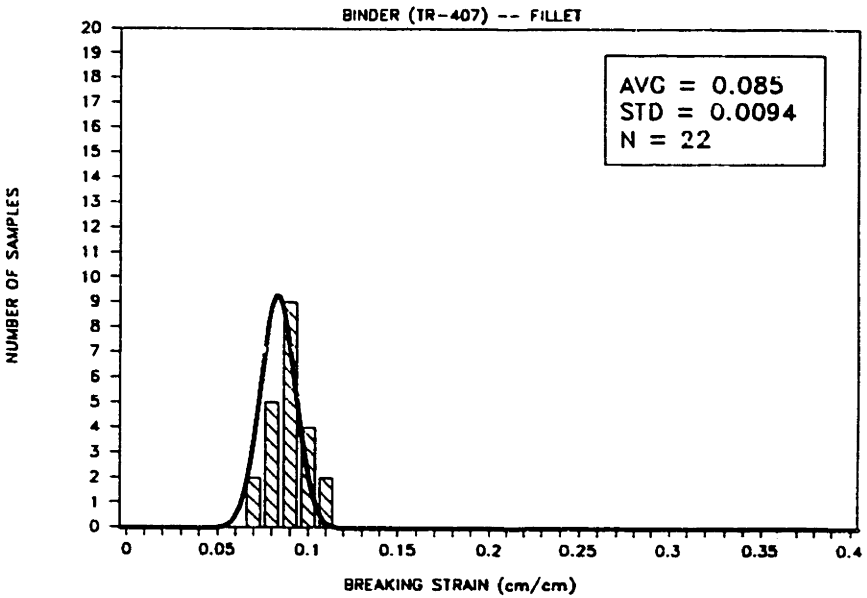

WESTVACO STAT TESTS

CLUPAK -- FILLET

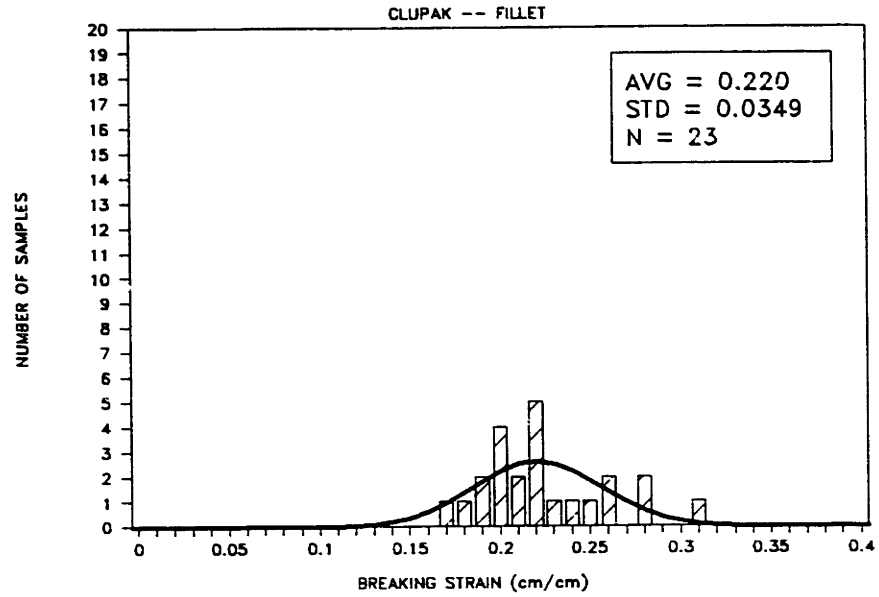

Appendix C

Fiber Pullout Analysis

FIBER PULL-OUT ANALYSIS

One-Sided Pull-Out: (see Figure 6.5)

$$Single\ Fiber\ Force\ = F_{sf} = e^{f\phi} F_{sf(\phi=0)} = e^{f\phi} \tau_b \pi d\lambda \tag{1}$$

where

f = friction coefficient
ϕ = angle of inclination
τ_b = bond strength (frictional)
d = fiber diamter
λ = remaining embedded length

$$\lambda = \frac{L_f}{2} - \frac{z}{\cos\phi} - \delta \tag{2}$$

Relationship of δ with crack tip opening displacement (one-sided pull-out only) :
(see Figure 6.6)

$$\delta = \frac{y_o(x_o - x)}{x_o} = y_o - 2\tan\alpha(x) \tag{3}$$

$$x_o = y_o / 2\tan\alpha \tag{4}$$

where

y_o = crack opening displacement at original crack initiation point
x_o = crack propagation length for a given y_o
x = fiber location along crack
δ = pulled-out length at x
α = misalignment angle

at instant when $y = y_o$,

$$F_{po}(allfibers) = N_a \int_{x_1}^{x_2} p(x)dx \int_0^{\frac{L_f}{2}} p(z)dz \int_0^{\arccos(\frac{2z}{L_f})} p(\phi)d\phi F_{sf} \tag{5}$$

where from eqns (1) and (2)

$$F_{sf} = e^{f\phi}\tau_b \pi d(\frac{L_f}{2} - \frac{z}{\cos\phi} - \delta) \tag{6}$$

x_2, x_1 = range of active pull-out
N_a = number of active bridging fibers
Constants: $\tau_b, d, f, y_o, \alpha, L_f$
Probability Functions:

$$\begin{aligned} p(\phi) &= 1/\pi & ,0 \le \phi < \pi \\ p(z) &= 2/L_f & ,0 \le z \le L_f/2 \\ p(x) &= 1/(x_2 - x_1) & ,x_1 \le x \le x_2 \end{aligned}$$

So,

$$F_{po} = \tau_b dN_a \int_{x_1}^{x_2} \frac{1}{x_2 - x_1}dx \int_0^{\frac{L_f}{2}} \frac{2}{L_f}dz \int_0^{\arccos(\frac{2z}{L_f})} \frac{1}{\pi}d\phi e^{f\phi}(\frac{L_f}{2} - \delta - \frac{z}{\cos\phi})\pi \tag{7}$$

$$let\ A = \tau_b dN_a \int_{x_1}^{x_2} \frac{1}{x_2 - x_1}dx \int_0^{\frac{L_f}{2}} \frac{2}{L_f}dz \int_0^{\arccos(\frac{2z}{L_f})} \frac{1}{\pi}d\phi e^{f\phi}(\frac{L_f}{2} - \delta)\pi \tag{8}$$

$$let\ \ B = \tau_b dN_a \int_{x_1}^{x_2} \frac{1}{x_2 - x_1}dx \int_0^{\frac{L_f}{2}} \frac{2}{L_f}dz \int_0^{\arccos(\frac{2z}{L_f})} \frac{1}{\pi}d\phi e^{f\phi}(\frac{z}{\cos\phi})\pi \tag{9}$$

i.e., $F_{po} = A - B$

$$\text{let } w = \arccos(2z/L_f)$$
$$\text{then } z = \tfrac{L_f}{2}\cos w$$
$$\text{and } dz = -\tfrac{L_f}{2}\sin w\, dw$$
$$\text{limits: } z = 0, w = \pi/2 \ \leftrightarrow\ z = L_f/2, w = 0$$

$$A = \tau_b dN_a \int_{x_1}^{x_2} \frac{1}{x_2 - x_1}dx \int_0^{\frac{L_f}{2}} \frac{2}{L_f}dz \int_0^{w} e^{f\phi}(\frac{L_f}{2} - \delta)d\phi \tag{10}$$

$$\begin{aligned} let\ \ A1 &= \int_0^w e^{f\phi}(\frac{L_f}{2} - \delta)d\phi \\ &= (\frac{L_f}{2} - \delta)[\frac{1}{f}e^{f\phi}]_0^w \\ &= (\frac{L_f}{2} - \delta)\frac{1}{f}(e^{fw} - 1) \end{aligned} \tag{11}$$

$$
\begin{aligned}
let\ \ A2 &= \int_0^{\frac{L_f}{2}} \frac{2}{L_f} dz(A1) \\
&= \int_0^{\frac{L_f}{2}} \frac{2}{L_f} dz(\frac{L_f}{2} - \delta)\frac{1}{f}(e^{fw} - 1) \\
&= (\frac{2}{L_f}(\frac{L_f}{2} - \delta)\frac{1}{f})(A2.1 - A2.2) \qquad (12)
\end{aligned}
$$

$$
\begin{aligned}
where\ \ A2.1 &= \int_0^{\frac{L_f}{2}} e^{fw} dz \\
&= \int_{\frac{\pi}{2}}^{0} [e^{fw}(-\frac{L_f}{2}\sin w)dw] \\
&= \frac{e^{fw}}{f^2+1}(f\sin w - \cos w)]_{\frac{\pi}{2}}^{0}(-\frac{L_f}{2}) \\
&= \frac{L_f}{2}[\frac{1 + fe^{\frac{f\pi}{2}}}{f^2+1}] \qquad (13)
\end{aligned}
$$

note: $\int e^{ax}\sin bx dx = \frac{e^{ax}}{a^2+b^2}(a\sin bx - b\cos bx) + C$

$$
\begin{aligned}
and\ \ A2.2 &= \int_0^{\frac{L_f}{2}} dz \\
&= \frac{L_f}{2} \qquad (14)
\end{aligned}
$$

$$
\begin{aligned}
So\ \ A2 &= \frac{1}{f}(\frac{L_f}{2} - \delta)[\frac{1 + fe^{\frac{f\pi}{2}}}{f^2+1} - 1] \\
&= \frac{1}{f}(\frac{L_f}{2} - \delta)[\frac{fe^{\frac{f\pi}{2}} - f^2}{f^2+1}] \\
&= (\frac{L_f}{2} - \delta)[\frac{e^{\frac{f\pi}{2}} - f}{f^2+1}] \qquad (15)
\end{aligned}
$$

$$
\begin{aligned}
Thus\ \ A &= \tau_b dN_a \int_{x_1}^{x_2} \frac{1}{x_2 - x_1} dx(A2) \\
&= \tau_b dN_a [\frac{e^{\frac{f\pi}{2}} - f}{f^2+1}] \int_{x_1}^{x_2} \frac{1}{x_2 - x_1}(\frac{L_f}{2} - \delta)dx \qquad (16)
\end{aligned}
$$

Taylor Series Expansion (to solve B)

$$e^{f\phi} = 1 + (f\phi) + \frac{(f\phi)^2}{2} + \frac{(f\phi)^3}{3!} + \frac{(f\phi)^4}{4!} + ... \quad (17)$$

$$\cos\phi = 1 - \frac{\phi^2}{2} + \frac{\phi^4}{4!} - \frac{\phi^6}{6!} + \frac{\phi^8}{8!} - ... \quad (18)$$

Taking the first 3 terms:

$$\begin{aligned}\frac{e^{f\phi}}{\cos\phi} &= \frac{1 + f\phi + \frac{f^2\phi^2}{2}}{1 - \frac{\phi^2}{2} + \frac{\phi^4}{24}} \\ &= \frac{24 + 24f\phi + 12f^2\phi^2}{24 - 12\phi^2 + \phi^4} \\ &= 1 + f\phi + \frac{1}{2}(f^2+1)\phi^2 + \frac{12f\phi^3 + (6f^2+5)\phi^4 - f\phi^5 - \frac{1}{2}(f^2+1)\phi^6}{24 - 12\phi^2 + \phi^4} \quad (19)\end{aligned}$$

$$\begin{aligned}let\ \ B1 &= \int_0^{\arccos(\frac{2z}{L_f})} \frac{ze^{f\phi}}{\cos\phi} d\phi \\ &= \int_0^w z[1 + f\phi + \frac{1}{2}(f^2+1)\phi^2]d\phi \\ &= z[1 + \frac{f}{2}\phi^2 + \frac{1}{6}(f^2+1)\phi^3]_0^w \\ &= (\frac{L_f}{2}\cos w)\frac{f}{2}w^2 + (\frac{L_f}{2}\cos w)\frac{1}{6}(f^2+1)w^3 \quad (20)\end{aligned}$$

$$\begin{aligned}let\ \ B2 &= \int_0^{\frac{L_f}{2}} \frac{2}{L_f} dz(B1) \\ &= \int_{\frac{\pi}{2}}^0 \frac{f}{2}\cos w(w^2)(-\frac{L_f}{2}\sin w)dw + \int_{\frac{\pi}{2}}^0 \frac{1}{6}(f^2+1)\cos w(w^3)(-\frac{L_f}{2}\sin w)dw \\ &= (-\frac{fL_f}{4})B2.1 + (-\frac{L_f}{12}(f^2+1))B2.2 \quad (21)\end{aligned}$$

$$\begin{aligned}where\ \ B2.1 &= \int_{\frac{\pi}{2}}^0 w^2\cos w\sin w dw \\ &= \frac{1}{2}w^2\sin^2 w]_{\frac{\pi}{2}}^0 - \int_{\frac{\pi}{2}}^0 w\sin^2 w dw\end{aligned}$$

$$= -\frac{\pi^2}{8} - (\frac{w^2}{2} - \frac{w\sin 2w}{4}]_{\frac{\pi}{2}}^{0}) + (\int_{\frac{\pi}{2}}^{0}(\frac{w}{2} - \frac{\sin 2w}{4})dw)$$
$$= -\frac{\pi^2}{8} + \frac{\pi^2}{8} + [\frac{w^2}{4} + \frac{\cos 2w}{8}]_{\frac{\pi}{2}}^{0}$$
$$= \frac{1}{8} - \frac{\pi^2}{16} + \frac{1}{8}$$
$$= \frac{1}{4} - \frac{\pi^2}{16} \qquad (22)$$

note: $\int \sin^2 x dx = \frac{x}{2} - \frac{\sin 2x}{4} + C$

$$\textit{and}\ \ B2.2 = \int_{\frac{\pi}{2}}^{0} w^3 \cos w \sin w dw$$
$$= \frac{1}{2}w^3 \sin^2 w]_{\frac{\pi}{2}}^{0} - \int_{\frac{\pi}{2}}^{0} \frac{3}{2}w^2 \sin^2 w dw$$
$$= -\frac{\pi^3}{16} - (\frac{3w^3}{4} - \frac{3w^2 \sin 2w}{8}]_{\frac{\pi}{2}}^{0}) + (\int_{\frac{\pi}{2}}^{0}(\frac{3w^2}{2} - \frac{3w\sin 2w}{4})dw)$$
$$= -\frac{\pi^3}{16} + \frac{3\pi^3}{32} + [\frac{3w^3}{6}]_{\frac{\pi}{2}}^{0} + (\frac{3}{8}w\cos 2w]_{\frac{\pi}{2}}^{0}) - (\int_{\frac{\pi}{2}}^{0}\frac{3}{8}\cos 2w dw)$$
$$= \frac{\pi^3}{32} - \frac{3\pi^3}{48} + \frac{3\pi}{16} - [\frac{3}{16}\sin 2w]_{\frac{\pi}{2}}^{0}$$
$$= \frac{6\pi - \pi^3}{32} \qquad (23)$$

$$\textit{So}\ \ B2 = \frac{fL_f}{4}(\frac{\pi^2}{16} - \frac{1}{4}) + \frac{L_f}{12}(f^2+1)(\frac{\pi^3 - 6\pi}{32})$$
$$= \frac{L_f}{2}[(\frac{f\pi^2}{32} - \frac{f}{8}) + (\frac{f^2+1}{6})(\frac{\pi^3 - 6\pi}{32})] \qquad (24)$$

$$\textit{Thus}\ \ B = \tau_b dN_a \int_{x_1}^{x_2} \frac{1}{x_2 - x_1} dx(B2)$$
$$= \tau_b dN_a[(\frac{f\pi^2}{32} - \frac{f}{8}) + (\frac{f^2+1}{6})(\frac{\pi^3 - 6\pi}{32})] \int_{x_1}^{x_2} \frac{1}{x_2 - x_1}(\frac{L_f}{2})dx \qquad (25)$$

Now, integration of the force over the region of pull-out :

$$\begin{aligned}\frac{F_{po}}{K\tau_b d} &= H(y_o)(\frac{v_f}{d})\int_0^{x_o}(R+2Sx)dx - H(y_o-\frac{L_f}{2}+Z)(\frac{v_f}{d})\int_0^{x_o}(R+2Sx)dx \\ &+ H(y_o-\frac{L_f}{2}+Z)(\frac{v_f}{d})\int_m^{x_o}(R+2Sx)dx - H(y_o-2W_c\tan\alpha)(\frac{v_f}{d})\int_m^{x_o}(R+2Sx)dx \\ &+ H(y_o-2W_c\tan\alpha)(\frac{v_f}{d})\int_m^{W_c}(R+2Sx)dx \\ &- H(y_o-2W_c\tan\alpha-\frac{L_f}{2}+Z)(\frac{v_f}{d})\int_m^{W_c}(R+2Sx)dx \qquad (26)\end{aligned}$$

where

$H(y_o - Y) \Rightarrow$ Heaviside step function

Z = effect of term B = $L_f\frac{K_B}{K_A}$

y_o = crack opening displacement at original crack initiation point

x_o = crack propagation length

W_c = original uncracked sheet width

$N_a = \frac{(x_2-x_1)v_f}{d}$ = number of active fibers

m = value of x where average embedded length just equals 0 = $\frac{y_o-\frac{L_f}{2}+Z}{2\tan\alpha}$

for A	*for B*
$R = \frac{L_f}{2} - y_o$	$R = \frac{L_f}{2}$
$2S = 2\tan\alpha$	$2S = 0$
$K_A = \frac{e^{\frac{f\pi}{2}}-f}{f^2+1}$	$K_B = (\frac{f\pi^2}{32}-\frac{f}{8})+(\frac{\pi^3-6\pi}{32})(\frac{f^2+1}{6})$

---

for a numerical estimate,

$\tau_b = 0.17 kg/mm$ $\qquad$ $v_f = 0.05$

$W = 120mm$ $\qquad$ $L_f/2 = 10mm$

$2\tan\alpha = 0.1 \Rightarrow \alpha \approx 3^o$

$f = 0.3 \Rightarrow K_A = 1.19 \qquad K_B = 0.124$

$$\int_{x_1}^{x_2}(R+2Sx)dx = R(x_2-x_1)+S(x_2^2-x_1^2) \qquad (27)$$

So, for $0 < y_o \leq \frac{L_f}{2} - Z$

$$\begin{aligned} x_2 - x_1 &= x_o = y_o/2\tan\alpha \\ x_2^2 - x_1^2 &= x_o^2 = y_o^2/4\tan^2\alpha \end{aligned}$$

$$\begin{aligned} F_{po} &= K_A\tau_b d\frac{v_f}{d}[(\frac{L_f}{2} - y_o)(y_o/2\tan\alpha) + (y_o^2/4\tan\alpha)] \\ &\quad -K_B\tau_b d\frac{v_f}{d}[y_o/2\tan\alpha](\frac{L_f}{2}) \\ &= \tau_b v_f[y_o/2\tan\alpha][K_A(\frac{L_f}{2} - \frac{y_o}{2}) - K_B(\frac{L_f}{2})] \end{aligned} \tag{28}$$

For $\frac{L_f}{2} - Z < y_o \leq 2W_c\tan\alpha$

$$\begin{aligned} x_2 - x_1 &= x_o - m = (\frac{L_f}{2} - Z)/2\tan\alpha \\ x_2^2 - x_1^2 &= x_o^2 - m^2 = (\frac{L_f}{2} - Z)(2y_o - (\frac{L_f}{2} - Z))/4\tan^2\alpha \end{aligned}$$

$$\begin{aligned} F_{po} &= K_A\tau_b d\frac{v_f}{d}[(\frac{L_f}{2} - y_o)((\frac{L_f}{2} - Z)/2\tan\alpha) + ((\frac{L_f}{2} - Z)(2y_o - (\frac{L_f}{2} - Z))/4\tan\alpha)] \\ &\quad -K_B\tau_b d\frac{v_f}{d}[(\frac{L_f}{2} - Z)/2\tan\alpha](\frac{L_f}{2}) \\ &= \tau_b v_f[\frac{\frac{L_f}{2} - Z}{2\tan\alpha}][K_A(\frac{L_f}{4} + \frac{Z}{2}) - K_B(\frac{L_f}{2})] \end{aligned} \tag{29}$$

And, for $2W_c\tan\alpha < y_o \leq 2W_c\tan\alpha + \frac{L_f}{2} - Z$

$$\begin{aligned} x_2 - x_1 &= W_c - m = W_c - (y_o - (\frac{L_f}{2} - Z))/2\tan\alpha \\ x_2^2 - x_1^2 &= W_c^2 - m^2 = W_c^2 - (y_o - (\frac{L_f}{2} - Z))^2/4\tan^2\alpha \end{aligned}$$

$$\begin{aligned} F_{po} &= K_A\tau_b d\frac{v_f}{d}[(\frac{L_f}{2} - y_o)(W_c - (y_o - (\frac{L_f}{2} - Z))/2\tan\alpha) \\ &\quad +(W_c^2\tan\alpha - (y_o - (\frac{L_f}{2} - Z))^2/4\tan\alpha)] \\ &\quad -K_B\tau_b d\frac{v_f}{d}[W_c - (y_o - (\frac{L_f}{2} - Z))/2\tan\alpha](\frac{L_f}{2}) \\ &= \tau_b v_f[W_c - \frac{y_o - (\frac{L_f}{2} - Z)}{2\tan\alpha}][K_A(\frac{L_f}{4} - \frac{y_o}{2} + W_c\tan\alpha + \frac{z}{2}) - K_B(\frac{L_f}{2})] \end{aligned} \tag{30}$$

Appendix D

Computer Programs

- PRAN.C (generate random numbers)
- PROB.C (generate normally distributed values with given mean and standard deviation)
- PCRACK.C (fracture model)

```
/* ------------------------------------------- */
/*   Prob1.C --- Program to Generate Lookup    */
/*               Table of Values with Designated */
/*               Mean and Standard Deviation   */
/*               (Normally Distributed)        */
/*                                             */
/*   program written at M.I.T., Spring, 1991   */
/*   by Julie Chen, Fibers and Polymers Lab    */
/*   (parts taken from Numerical Recipes)      */
/* ------------------------------------------- */

#include <stdio.h>
#include <ctype.h>
#include <stdlib.h>
#include <math.h>

float gasdev(int *idum);

main()
{
  FILE *fopen(), *fp_out;
  char fn_out[12];

  int idum=(-13),j;
  float rannum[1010];
  float sig,xmean;

  /* ------- setup I/O files ---------------------- */
  printf ("enter name of output file:  ");
  scanf ("%s", fn_out);
  fp_out = fopen (fn_out, "w");

  printf ("input idum, sig, xmean\n");
  scanf ("%d %f %f", &idum, &sig, &xmean);
  printf ("the number is %d\n", idum);

  for (j=1;j<=1000;j++)
   {
     rannum[j] = sig*gasdev(&idum) + xmean;
     fprintf (fp_out,"%f\n", rannum[j]);
   }

  /* ----------- close -------------------------- */
  printf ("output in file: %s\n", fn_out);
  fclose (fp_out);
  exit(0);

}

/* random number function */

#include <math.h>

float gasdev(idum)
int *idum;
{
  static int iset=0;
  static float gset;
  float fac,r,v1,v2;
  float ran1();
```

```
/*  printf("you have entered gasdev\n");    */
  if (iset == 0)
  {
   do {
        v1 = 2.0*ran1(idum)-1.0;
        v2 = 2.0*ran1(idum)-1.0;
        r  = v1*v1 + v2*v2;

/*        printf("v1 = %f\t v2 = %f\t r = %f\n",v1,v2,r); */

   } while (r >=1.0);


   fac = sqrt(-2.0*log(r)/r);
   gset = v1*fac;
   iset = 1;

/*   printf("v2fac = %f\n", v2*fac);     */

   return v2*fac;
  }
  else
  {
   iset=0;
   return gset;
  }
}
```

```
/* ------------------------------------------- */
/*    PRAN1.C --- Function linked to PROB1.C   */
/*                to generate uniform random   */
/*                deviates between 0.0 and 1.0 */
/*                (improved random number      */
/*                    generator)               */
/*                                             */
/*    program taken from Numerical Recipes in C */
/* ------------------------------------------- */


#define M1 259200
#define IA1 7141
#define IC1 54773
#define RM1 (1.0/M1)
#define M2 134456
#define IA2 8121
#define IC2 28411
#define RM2 (1.0/M2)
#define M3 243000
#define IA3 4561
#define IC3 51349

float ran1(idum)
int *idum;
{
  static long ix1,ix2,ix3;
  static float r[98];
  float temp;
  static int iff=0;
  int j;
/*  void nrerror();   */

  if (*idum < 0 || iff == 0)
   {
     iff=1;
     ix1=(IC1-(*idum)) % M1;
     ix1=(IA1*ix1+IC1) % M1;
     ix2=ix1 % M2;
     ix1=(IA1*ix1+IC1) % M1;
     ix3=ix1 % M3;
     for (j=1;j<=97;j++)
      {
        ix1=(IA1*ix1+IC1) % M1;
        ix2=(IA2*ix2+IC2) % M2;
        r[j]=(ix1+ix2*RM2)*RM1;
      }
      *idum=1;
   }
   ix1=(IA1*ix1+IC1) % M1;
   ix2=(IA2*ix2+IC2) % M2;
   ix3=(IA3*ix3+IC3) % M3;
   j=1 + ((97*ix3)/M3);
/*   if (j > 97 || j < 1) nrerror("RAN1: This cannot happen."); */
   temp=r[j];
   r[j]=(ix1+ix2*RM2)*RM1;
   return temp;
}
```

```
/* ------------------------------------------------- */
/*   PROGRAM (PCRACK.C) --- Critical Strain/         */
/*                          Crack propagation        */
/*                          Fracture Model w/Pullout */
/*                                                   */
/*   program written at M.I.T., Spring, 1991         */
/*   by Julie Chen, Fibers and Polymers Lab          */
/* ------------------------------------------------- */

#include <stdlib.h>
#include <math.h>
#include <stdio.h>

#define PI 3.141592
#define E 250.0   /* elast mod (kg/cm/strain) */
#define MU 100.0  /* shear mod (kg/cm/strain)  */
#define KYIELD 3.8   /* yield stress (kg/cm)  */
/* #define STR_BK 0.07 */  /* failure strain (cm/cm) */
#define KIC 11.0     /* critical KI (kg-cm/cm) */

#define DELINC 0.01  /* jaw displ increment */
#define GAMMA 0.707  /* theta/psi ratio */
#define NU 0.3      /* poisson's ratio */
#define SWID 8.0   /* uncut sheet width (cm)  */
#define SLEN 5.0    /* sheet length (cm) */
#define ALPHA 0.67   /* loss in strength of process zone */

#define XR_LOW 0.01
#define XR_HI 1.0

#define TAUB 1.4   /* bond strength (kg/cm2) */
#define FDIA 0.001  /* fiber dia (cm) */
#define FLEN 1.8       /* fiber length (cm) */
#define LAY 5
#define KA  1.19
#define KB  0.124
#define TTANA 0.03
#define VF  0.05

double sqrt(double c);
double log(double d);
double pow(double g,double h);

main()
{
   FILE *fopen(), *fp_out, *fp_in;
   char fn_out[12], fn_in[12];
   int i,j;
   int ENCRIT;
   double sref, delta, pref, delcrit;
   double KI, rp, xp, xratio;
   double pzone_tip,crack_tip, xcrit;
   double kappa,B1,C1,str_pb;
   double beta, cr_len;
   double xrtemp, str_temp, diff;
   double xr1, xr2, str1, str2;
   double f_fib, xo, yo;
   double FNUM, Z, R1, R2, R3;
   double f_fib1,f_fib2,f_fib3,f_fib4;
   double STR_BK;
```

```
/* --------- SETUP I/O FILES ------------------- */
printf ("enter name of input (strain) file: ");
scanf ("%s", fn_in);
fp_in = fopen (fn_in, "r");

      printf (" brk strain input file is %s \n", fn_in);
      fscanf (fp_in," %lf\n ", &STR_BK);
      printf (" new brk strain is %lf \n", STR_BK);

printf ("enter name of output file: ");
scanf ("%s", fn_out);
fp_out = fopen (fn_out, "w");

/* -------- INITIALIZE ARRAYS ------------------ */
  KI = 0.0;
  rp = 0.0;
  xp = 0.0;
  pzone_tip = 0.0;
  crack_tip = 0.0;

  xratio = 0.0;
  xcrit = 0.0;


/* ------ CALCULATE MATERIAL CONSTANTS ------------ */
kappa = (3.0-NU)/(1.0+NU);
B1 = (1.0/32.0)*(1.0/pow(GAMMA,2.0))*
                ((kappa+5.0)+4.0*GAMMA*(kappa+1.0))*(E/MU)-(2.0/3.0);
C1 = (1.0/32.0)*(1/pow(GAMMA,2.0))*
                (-(kappa+5.0)+2.0*GAMMA*(kappa+1.0))*(E/MU)+(2.0/3.0);
str_pb = (3.0/8.0)*(KYIELD/MU)*(kappa-(1.0/3.0));

FNUM = SWID*LAY*VF/FDIA;
Z = FLEN*KB/KA;
R1 = (FLEN/2 - Z)/TTANA;
R2 = SWID;
R3 = R2 + R1;
printf (" FNUM=%lf\t R1=%lf\t R2=%lf\t R3=%lf\n",FNUM,R1,R2,R3);

/* --------- LOCAL STRAIN (SREF,XRATIO) ----------- */
beta = 1.0;
cr_len = 4.0;
ENCRIT=0;

for (i=1; i<=600; ++i)
 {
   diff = 1.0;

   delta = i*DELINC;
   sref = E*delta/SLEN;
   pref = beta*sref*SWID;

   /* ---- CHECK ENERGY CRITERION (K=KIC; G=R) ------------- */
   KI = sref*sqrt(PI*cr_len);
   if (KI >= KIC)
      {
        KI = KIC;
        ENCRIT = 1;
      }
```

```
      else
         {
           ENCRIT = 0;
           printf (" energy criterion not satisfied ");
         }

      rp = pow(KI,2)/(2*PI*(pow(((3.0/2.0)*KYIELD),2)));
      xp = rp/GAMMA;

/*      printf( " sref=%lf\t pref=%lf\t KI=%lf\t rp=%lf\t ENC=%d\n",
           sref, pref, KI, rp, ENCRIT);     */

      if (ENCRIT = 1)
       {
         /* ------ CRITICAL X (STRAIN CRITERION) --------------- */

         xr1 = XR_LOW;
         xr2 = XR_HI;

         fscanf (fp_in, " %lf ", &STR_BK);
         printf (" new brk strain is %lf \n", STR_BK);


         while (diff > 0.001)
         {
          str1 = str_pb + (KYIELD/E)*
                    (pow(log(xr1),2.0) - B1*log(xr1)
                      - (1.0/3.0)*C1*(pow(xr1,3.0)-1.0));

          if (str1 <= STR_BK)
            {
              printf (" strain criterion not satisfied");
              xcrit = 0.0;
              break;
            }

          str2 = str_pb + (KYIELD/E)*
                    (pow(log(xr2),2.0) - B1*log(xr2)
                      - (1.0/3.0)*C1*(pow(xr2,3.0)-1.0));

          xrtemp = ((str1-STR_BK)/(str1-str2))*(xr2-xr1) + xr1;
          str_temp = str_pb + (KYIELD/E)*
                    (pow(log(xrtemp),2.0) - B1*log(xrtemp)
                      - (1.0/3.0)*C1*(pow(xrtemp,3.0)-1.0));

          if (str_temp < STR_BK)
            {
                xr2 = xrtemp;
                diff = STR_BK - str_temp;
            }
          else
            {
                xr1 = xrtemp;
                diff = str_temp - STR_BK;
            }

          if (STR_BK > str1)
           {
            xr1 = xr1/10;
           }
```

```
      xratio = xrtemp;
      xcrit = xratio*xp;

      /* ---- FIBER PULLOUT COMPONENT ------------ */
         xo = (1-beta)*SWID;

      if (xo > 0 && xo < R1)
         f_fib = TAUB*VF*LAY*xo*
                     (KA*(FLEN/2 - xo*TTANA/2)
                       - KB*(FLEN/2));
      else if (xo >= R1 && xo < R2)
         f_fib = TAUB*VF*LAY*((FLEN/2-Z)/TTANA)*
                     (KA*(FLEN/4 + Z/2)
                       - KB*(FLEN/2));
      else
         f_fib = 0;

      pref = pref + f_fib;

    }

    crack_tip = crack_tip + xcrit;
    pzone_tip = pzone_tip + xp;


   printf("delta=%lf\t pref=%lf\t f_fib=%lf\n"
           , delta, pref, f_fib);

   fprintf(fp_out,"delta=%lf\t pref=%lf f_fib=%lf\n"
           , delta, pref, f_fib);

   if (beta <= 0.1)
        {
          printf("sheet is completely failed\n");
          beta=0.0;
          delcrit = delta;
          cr_len = 12;
          i = 601;
        }
   else
        {
          beta = 1.0 - (crack_tip/SWID) - ALPHA*(xp/(beta*SWID));
          cr_len = cr_len + crack_tip;
        }
 }
printf (" matrix failed,  starting pullout only \n ");

 /* -------- FINISH PULLOUT -------------------- */
for (j=1; j<=100; ++j)
 {
   delta = j*DELINC+delcrit;
   xo = j*DELINC/TTANA + SWID;
   yo = xo*TTANA;

   f_fib = TAUB*VF*LAY*(SWID - (yo-(FLEN/2-Z))/TTANA)*
                        (KA*(FLEN/4-yo/2+SWID*TTANA/2+Z/2)
                          - KB*(FLEN/2));

   printf (" delta=%lf\t f_fib=%lf\n",
```

```
                    delta,f_fib);

      pref = f_fib;
      fprintf(fp_out,"delta=%lf\t  pref=%lf\n"
                    , delta, pref);
      if (pref < 0)
        {
          printf(" all fibers pulled out \n");
          j=101;
        }
    }


   /* ------------------ OUTPUT AND CLOSE ---------------- */

   printf ("output in file: %s\n", fn_out);
   fclose (fp_out);
   fclose (fp_in);
   exit (0);
}

/* ------------------------------------------- */
/* ---------------- ERROR FUNCTION ------------ */
/* ------------------------------------------- */
   nrerror()
    {
     printf("there was an error /n");
     exit(0);
    }
/* ---------------- END ---------------------------- */
```